

# **The Growth and Fluorescence of Organic Monolayers and Heterostructures**

**James Kerfoot**

**Thesis submitted to the University of Nottingham for the degree of  
doctor of philosophy**

**July 2018**

## Abstract

Monolayer organic thin films and heterostructures are of great interest for their optical and electronic properties and as systems which allow the interplay between the structural and functional properties of organic molecules to be investigated. In the first experimental section of this thesis, sub-monolayer coverages of perylene tetracarboxylic diimide (PTCDI) were grown on hBN substrates and found to form needle-like monolayer islands at room temperature, while higher growth temperatures gave larger monolayer islands. The molecular packing of monolayer PTCDI was confirmed, using AFM, to correspond to the canted phase. The 0-0 fluorescence peak of this structure was found to occur at  $2.208 \pm 0.002$  eV. The fluorescence of multi-layer PTCDI samples was mapped, with additional peaks measured at  $2.135 \pm 0.002$  eV ( $580.7 \pm 0.5$  nm) and  $2.118 \pm 0.002$  eV ( $585.4 \pm 0.5$  nm). Relating the morphology and fluorescence of such films using AFM and fluorescence microscopy is a promising way to investigate structural effects on the optical properties of multi-layer organic systems.

Using solution deposition techniques, the PTCDI-melamine supramolecular network and the canted phase of PTCDI were deposited on hBN. The molecular packing of both structures was confirmed using AFM and the 0-0 fluorescence peaks were measured to be  $2.245 \pm 0.002$  eV and  $2.214 \pm 0.002$  eV for the PTCDI-melamine network and PTCDI respectively. The fluorescence of sublimed PTCDI, solution deposited PTCDI, PTCDI-melamine and measurements of Me-PTCDI doped helium nano droplets (HND) were compared. A  $0.031 \pm 0.002$  eV red shift was measured from PTCDI-melamine to PTCDI while a  $0.346 \pm 0.002$  eV red shift was measured from doped HND to PTCDI on hBN. A second perylene derivative, perylene tetracarboxylic dianhydride (PTCDA), was also deposited on hBN. Comparing the fluorescence of PTCDA monolayers on various dielectric substrates suggested a large shift due to the coupling of transition dipole moments and image dipoles beneath the dielectric surface. The

shift between PTCDI and PTCDI-melamine was attributed to the coupling of transition dipole moments, for which the exciton bandstructure of both phases has been calculated with and without screening.

The growth of sublimed C<sub>60</sub> was also investigated, with monolayer islands observed for growth at room temperature and faceted bi-layer islands observed at 212 °C. The growth of PTCDI/C<sub>60</sub> heterostructures was also investigated, with C<sub>60</sub> found to form monolayer islands on monolayer PTCDI at room temperature. At higher growth temperatures, C<sub>60</sub> was found to form multilayers, with a reduced island density at PTCDI island edges, suggesting upward and downward hopping from the PTCDI surface to the second C<sub>60</sub> layer and hBN respectively. C<sub>60</sub> was found to quench the fluorescence of PTCDI and led to a  $0.032 \pm 0.02$  eV blue shift.

Finally, the growth of cyanuric acid-melamine (CA.M) on CVD graphene and CA.M/PTCDI heterostructures on hBN was investigated. Cyanuric acid-melamine was found to form monolayers with a honeycomb packing structure on CVD graphene. On monolayers of CA.M, PTCDI was found to form needle-like monolayer islands, the row direction of PTCDI is thought to have an on-axis registry with the substrate. Finally, the fluorescence of CA.M/PTCDI heterostructures on hBN was measured, with a  $0.045 \pm 0.002$  eV blue shift from PTCDI on hBN.

## **Acknowledgements**

I would like to thank my supervisor, Professor Peter Beton, for giving me the opportunity to carry out PhD research and for his wisdom and support throughout my time at Nottingham. I have thoroughly enjoyed carrying out my research within the Nottingham nanoscience group and his guidance has been central to this. I would also like to thank Dr Vladimir Korolkov, for his expertise and for helpful discussions throughout my PhD.

I would like to thank all current and former members of the Nottingham nanoscience group, particularly Dr Alex Summerfield, Manal Alkhamisi, Juan Diez Albar, Abigail Browning, James Thomas, James Wrigley, Joe Hodgkinson, Dr Simon Svatek and Dr Izabela Cebula, for making my research both productive and enjoyable.

I would like to thank Dr Nila Balakrishnan, Professor Amalia Patane, Dr Graham Rance, Dr Andrew Davies, Dr Anton Nizovtsev, Professor Nick Besley, Professor Elena Besley, Dr Alex Saywell, Ryan Jones and Professor Phil Williams, for their support, assistance and collaboration at various stages of my PhD. I would also like to thank the technical staff at the School of Physics and Astronomy, and the EPSRC for funding my PhD.

Finally I would like to thank my parents Simon and Rebecca and the rest of my family for their continual support and encouragement, and Hannah, for making every day so special.

## **Contents**

<b>1. Introduction</b>	1
1.1 Introduction	2
1.2 Overview	5
<b>2. Background</b>	7
2.1. Intermolecular Bonding and Growth modes on surfaces	8
2.2. Fullerenes	11
2.3. Perylene Derivatives: PTCDI and PTCDA	15
2.4. Cyanuric acid-Melamine	21
2.5. Hexagonal Boron Nitride and Graphene	22
2.6. Molecular Fluorescence	24
2.6.1. Gas Phase, HND and Solution	25
2.6.2. Molecular Monolayers	27
2.7. Conclusion	30
<b>3. Experimental Techniques</b>	31
3.1. Atomic Force Microscopy	32
3.2. Fluorescence and Raman Microscopy	37
3.3. Substrate Preparation	43
3.4. UHV and Sublimation	45
3.5. Conclusion	48

<b>4. PTCDI thin films on hexagonal boron nitride</b>	49
4.1. Overview	50
4.2. The Island Morphology of Sublimed PTCDI on hBN	51
4.3. The Fluorescence of Sublimed PTCDI on hBN	60
4.4. The Optical Properties of PTCDI Monolayers on hBN at Cryogenic Temperatures	68
4.5. The Morphology and Fluorescence of Multi-layer PTCDI films on hBN	72
4.6. Conclusion	76
<b>5. Chromatic shifts of organic monolayers adsorbed on insulating surfaces</b>	77
5.1. Overview	79
5.2. The PTCDI-Melamine Supramolecular Network and Solution Processed PTCDI on hBN	80
5.3. The Deposition of PTCDI on Insulating Substrates	87
5.4. Substrate Induced Chromatic Shifts: The Fluorescence of PTCDA on hBN	89
5.5. Resonant Intermolecular Interactions of PTCDI on hBN	95
5.6. The Fluorescence Shifts of PTCDI and PTCDA Monolayers on hBN	103
5.7. Conclusion	109

<b>6. C<sub>60</sub> thin films and PTCDI/C<sub>60</sub> heterostructures on hexagonal boron nitride</b>	<b>111</b>
6.1. Overview	112
6.2. The Morphology of Sub-Monolayer C <sub>60</sub> films on hBN	113
6.3 The Morphology of Sub-Monolayer C <sub>60</sub> films on hBN: Temperature Dependence	118
6.4. The Morphology of C <sub>60</sub> Thin Films on hBN: Thickness Dependence	129
6.5. The Morphology of PTCDI/C <sub>60</sub> Heterostructures	134
6.6. The Fluorescence of PTCDI/C <sub>60</sub> Heterostructures	138
6.7. Conclusion	143
<b>7. Cyanuric Acid-Melamine/PTCDI Heterostructures on Hexagonal Boron Nitride</b>	<b>145</b>
7.1. Overview	146
7.2. The Deposition of Cyanuric Acid-Melamine on Graphene from Solution	147
7.3. Cyanuric Acid-Melamine/PTCDI Heterostructures on hBN	151
7.4. Conclusion	156
<b>8. Conclusion</b>	<b>157</b>
<b>A1. Appendix 1: Optical Interference in Fluorescence Spectroscopy</b>	<b>163</b>
Measurements	
<b>A2. Appendix 2: The Fluorescence of hBN/PTCDI/hBN Heterostructures</b>	<b>170</b>
<b>References</b>	<b>182</b>



# **Chapter 1:**

## **Introduction**

## **1. Introduction**

In this chapter, the aims of this thesis are introduced in the context of current research in the fields of molecular electronics, surface science, supramolecular chemistry and fluorescence spectroscopy. The work carried out in the experimental chapters of this thesis is then briefly outlined.

### **1.1. Introduction**

In recent years, the field of molecular electronics has made many advances in the study of photoactive molecules and conductive polymers. These studies have yielded electronic devices which have many advantages compared to conventional semiconductors, particularly in terms of their mechanical properties [1]. As a result, the same functional properties exhibited by inorganic materials and devices can now be observed in organic thin films and flexible polymeric membranes with numerous practical applications [2]. The functional properties of organic materials are particularly relevant to the field of nanoscience, where nanometre-scale structural control leads to a high degree of tuneability of their optical and electronic properties.

When the placement of the building blocks of such organic systems can be controlled, arrangements promoting desirable functional properties and device architectures can be coordinated, leading to both enhanced performance and novel functionality [3]. It is the aim of this work to study the interplay between the structural and functional properties of organic thin films, where possible identifying systems which show promise for their incorporation into devices.

For many years, the surface science community has studied the adsorption of organic species at interfaces. Using scanning tunnelling microscopy (STM) under ultra-high vacuum (UHV)

conditions, ambient conditions and at the liquid-solid interface, the molecular packing of many hydrogen bonded systems has been studied [4]. On many conducting substrates, including highly oriented pyrolytic graphite (HOPG), graphene, molybdenum disulphide and noble metals, the molecular packing of a number of optically active molecules has been studied. In addition to molecular self-assemblies formed from a single species, a number of bi-component molecular self-assemblies, formed by co-depositing molecules of different species onto a surface, have been demonstrated [5,6,7].

Molecular self-assembly has also been demonstrated to form pores at interfaces, which can act as a host for a number of guest molecules. A number of studies into guest-host interactions within molecular self-assemblies have been carried out, including the adsorption of C<sub>60</sub> and coronene in the pores of the trimesic acid network at the liquid solid interface [8] and the adsorption of multiple species within the pore of the PTCDI-melamine supramolecular network [9]. In addition to controlling the lateral placement of molecules adsorbed on a surface, monolayers of different organic species can also be deposited sequentially in order to form molecular heterostructures. Often referred to as organic-organic hetero-epitaxy, the formation of molecular heterostructures has been carried out for a number of n-type and p-type molecular species, including perylene tetracarboxylic dianhydride (PTCDA) and hexa-peri-benzocoronene on HOPG [10].

By investigating the self-assembly of organic molecules on conductive substrates using STM, the surface science community has demonstrated that the relative placement of optically active molecules can be templated through a number of mechanisms. This can be achieved using hydrogen bonding within mono- and bi-component molecular networks, through guest-host interactions and through organic-organic hetero-epitaxy. The placement of molecules is expected to give rise to a number of interesting functional properties. It is difficult, however, to measure the optical and electronic properties of organic monolayers adsorbed on

conductive substrates directly. In order to measure the properties of molecular self-assemblies, wetting layers are often required to decouple a molecular self-assembly from the substrate [11].

In order to access the optical and electronic properties of molecular monolayers, dielectric substrates on which flat-lying molecular assemblies can be formed are desirable. A number of groups are currently carrying out research into molecular self-assembly on insulating surfaces, including the Grutter group (McGill) and Kühnle group (Mainz) which have carried out a number of experiments on alkali halide and calcite substrates. One drawback in the use of insulating substrates is that STM cannot be used to measure the morphology of molecular thin films on these surfaces. Instead, atomic force microscopy (AFM) is used. Recently, the resolution which can be achieved using AFM both in UHV conditions and ambient conditions has improved considerably [12], allowing the packing structure of molecular self-assemblies to be measured on both conductive and insulating substrates.

This work focuses on the fluorescent properties of organic molecules at interfaces, an area in which fresh experimental methodologies have recently been applied [13,14], notably by the Sokolowski group (Bonn) and the Fritz group (Jena). Despite a number of novel experiments which have been carried out, the mechanisms which explain the fluorescence of organic molecules are still not fully understood. This is particularly true of the fluorescence shift between ‘gas phase’ measurements and molecules at a dielectric surface, analogous to the ‘gas-to-crystal shift’ for optically active organic crystals.

The morphology and fluorescent properties of organic molecules are studied through the deposition of organic thin films and subsequent characterisation using AFM and fluorescence microscopy. For this, hBN is chosen as the substrate since it does not quench the fluorescence of organic species, promotes favourable arrangements of molecules, and its use within van

der Waals heterostructures in inorganic devices raises the potential of novel organic-inorganic hybrid structures.

The potential applications of molecular self-assemblies and heterostructures at dielectric interfaces are considerable. By influencing the relative placement and orientation of molecules within a film, it is possible to tune their optical properties [15]. The incorporation of molecular self-assemblies at the interfaces of van der Waals heterostructures is also a promising concept, since the functional properties and structure of an atomically thin molecular layer could lead to novel functionality and rapid charge transfer between layers.

## 1.2. Overview

The aim of this work is to investigate how the organisation of molecules on a surface influences their optical properties. In chapter 2, the general background and state-of-the-art investigations pertaining to the fluorescence of molecules at interfaces will be discussed. STM investigations of fluorescent species on metal surfaces are discussed, particularly where the molecular arrangement can be templated by hydrogen bonding within supramolecular networks. Molecular fluorescence is then introduced, with particular attention paid to fluorescence at interfaces. In chapter 3, an introduction to the experimental techniques used in this work are given, including; AFM, fluorescence and Raman microscopy and organic molecular beam epitaxy.

The deposition of the perylene derivative PTCDI is discussed in chapter 4. The morphology of PTCDI thin films grown on hBN at a range of substrate temperatures is shown as well as fluorescence measurements from these films. Interference effects arising from the structure of the substrate will be discussed as well as the results of low temperature fluorescence

measurements. Finally, the fluorescence of thick PTCDI films is mapped using both AFM and confocal fluorescence microscopy.

In chapter 5, the fluorescence of sublimed PTCDI on hBN is compared to solution deposited PTCDI and the PTCDI-melamine supramolecular network. Comparing the morphology and fluorescence of these monolayer films, the relative effect of the coupling of transition dipole moments, non-resonant intermolecular interactions and interactions with the substrate are discussed. This is explored further by depositing a second perylene derivative, PTCDA, onto hBN and making a comparison with measurements available in the literature.

In chapter 6, the morphology of thin films of Buckminsterfullerene ( $C_{60}$ ), grown by sublimation in vacuum for a range of coverages and substrate temperatures, is explored using AFM. The growth of PTCDI/ $C_{60}$  heterostructures on hBN was then investigated. By exploring the growth of  $C_{60}$  on both hBN and PTCDI monolayers at different substrate temperatures, quantitative and qualitative comparisons are made with investigations on alkali halide surfaces carried out by the Kühnle group at the University of Mainz. The fluorescence of PTCDI/ $C_{60}$  heterostructures is then studied and compared with results of monolayer PTCDI discussed in chapters 4 and 5.

Finally, in chapter 7, the deposition of the cyanuric acid-melamine network on graphene is discussed in addition to the growth of cyanuric acid-melamine/PTCDI heterostructures on hBN. The morphology and fluorescence of PTCDI on cyanuric acid-melamine are then compared to results of PTCDI from previous chapters.

# **Chapter 2:**

# **Background**

## **2. Background**

In this chapter, the growth of molecular thin films, on-surface molecular self-assembly and the structural and environmental factors which influence the fluorescence of organic monolayer films are introduced.

### **2.1. Intermolecular Bonding and Growth Modes on Surfaces**

Attractive forces between molecules and between a molecule and a substrate occur through a number of mechanisms, the relative strength and directionality of these forces determine the structure of molecular thin films at interfaces. One type of interaction which occurs between all atoms is the van der Waals interaction, where spontaneous dipoles within molecules induce dipoles within adjacent molecules and surfaces. The interaction of spontaneous and induced dipoles leads to an attractive force, described by the attractive component of the Lennard-Jones potential (the London dispersion force). Van der Waals bonding is typically weak compared to other mechanisms such as hydrogen bonding (discussed below) and occurs in all materials [16].

Hydrogen bonding occurs when a hydrogen atom and a second atomic species of greater electronegativity bond covalently within a molecule. The resulting chemical bond is polarised along the bond axis, leading to highly directional electrostatic interactions with hydrogen bonding groups of adjacent molecules [17]. Hydrogen bonding occurs between molecules and surfaces which are functionalised with hydrogen bonding groups. As well as the two interactions discussed, molecules can also interact through halogen bonding, metal-ligand bonding and electrostatic interactions.

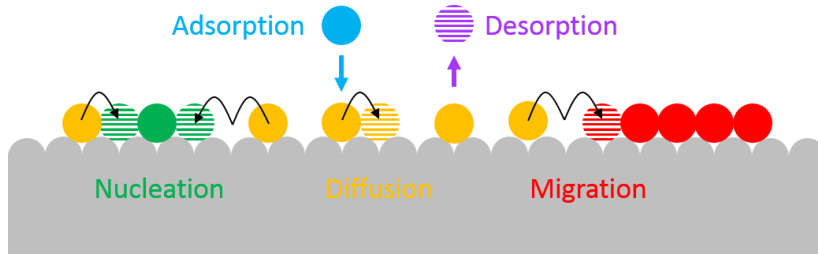


**Figure 2.1.1.** Upon adsorption on a surface, molecules can desorb, hop to adjacent binding sites, participate in nucleation events and migrate to pre-formed islands.

When deposited on a substrate, molecules are incident at random locations. Molecules can then desorb, hop to adjacent binding sites or remain localised at one site. The fraction of the deposited molecules which remain adsorbed on the surface is known as the sticking coefficient. As the substrate temperature increases, the probability that a given molecule can hop to an adjacent binding site increases. The diffusion coefficient,  $D$ , the rate at which molecules jump to the next adsorption site, is given in equation 2.2.1 where  $v$  is the attempt frequency,  $E_d$  is the potential barrier between two adjacent hopping sites and  $T$  is the substrate temperature [18].

$$D = v \exp\left(-\frac{E_d}{k_B T}\right) \quad (2.2.1)$$

Molecules typically diffuse across the substrate surface until they desorb or occupy a binding site on the surface with a greater binding energy. Such binding sites can occur at step edges and defects on the substrate, and also at the edges of pre-formed clusters (later referred to as islands) of molecules. The interaction of a number of mobile molecules can also lead to new stable clusters through nucleation events [19]. During the early stages of growth, the first molecules to reach the surface form stable clusters through nucleation. Nucleation can occur on the pristine substrate surface or at defects such as step edges. At a given temperature, the number of molecules,  $i$ , required to form a cluster which is kinetically stable, such that the rate of attachment of additional molecules exceeds the rate of detachment of molecules bound within an island, is known as the critical cluster size.

By considering,  $R$ , the rate of arrival of molecules per unit area on the surface,  $\tau_a$ , the time taken for molecules to desorb from the surface,  $\tau_n$ , the time taken for isolated molecules to cluster together in nucleation events,  $\tau_c$ , the time taken for molecules to join stable clusters on the surface and  $U_{\text{Cluster}}$ , the coalescence of pre-formed critical clusters, a pair of coupled equations can be derived for  $n_1$  and  $n_x$ , the surface concentrations of isolated molecules and critical clusters respectively [18,19,20,21].

$$\frac{dn_1}{dt} = R - \frac{n_1}{\tau_a} - \frac{n_1}{\tau_n} - \frac{n_1}{\tau_c} \quad (2.2.2)$$

$$\frac{dn_x}{dt} = \frac{n_1}{\tau_c} - U_{\text{Cluster}} \quad (2.2.3)$$

Assuming the time that isolated molecules remain bound to the surface,  $\tau_a$ , is much greater than the time taken for molecules to migrate to stable pre-formed clusters,  $\tau_c$ , the growth is said to be in the complete condensation regime. When  $\tau_a \gg \tau_c$ , equations 2.2.2 and 2.2.3 can be solved to give  $n_{\text{crit}}$ , the critical cluster density as a function  $R$ ,  $i$ ,  $E_d$ ,  $T$  and  $E_i$ , the binding energy of the cluster, see equation 2.2.4. By comparing the growth of molecular thin films of known critical cluster size,  $i$ , at different substrate temperatures during deposition, it is possible to extract the diffusion barrier,  $E_d$ , using equation 2.2.4 [19]. In subsequent chapters, equation 2.2.4 will be compared with experimentally determined island densities, for films grown at temperatures in the range of 21 °C to 250 °C.

$$n_{\text{crit}} \propto R^{\frac{i}{i+2}} \exp\left(\frac{E_i + iE_d}{(i+2)k_B T}\right) \quad (2.2.4)$$

The growth of molecular thin films is classified into three regimes; layer-by-layer growth, island growth and layer-plus-island growth [18]. Given sufficient energy to migrate to favourable binding sites, when molecules have a greater interaction with the surface than adjacent molecules, they can form a complete first layer before the formation of subsequent layers, this growth mode is called layer-by-layer or Frank-van der Merwe growth. When

molecules are bound more strongly within a 3D arrangement of adsorbate molecules than to the surface, additional layers form before the first layer is complete; this is known as island or Volmer-Weber growth. The final growth mode occurs when a full monolayer, also known as a wetting layer, is formed but subsequent layers form islands on top of the initial monolayer, this is known as layer-plus-island or Stranski-Krastanov growth. These three growth modes are illustrated in figure 2.1.2.

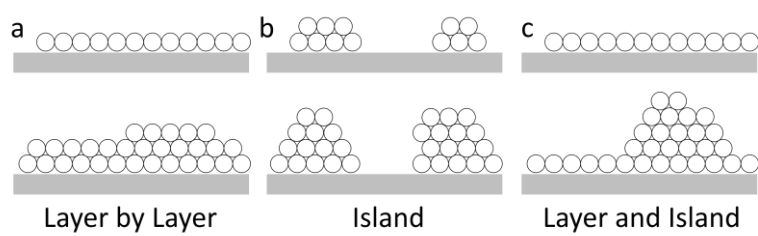


**Figure 2.1.2.** The growth of molecules (black circles) on a substrate is indicated for sub-monolayer (top) and few-layer coverages (bottom).

## 2.2. Fullerenes

Buckminsterfullerene ( $C_{60}$ ) is a spherical molecule which consists of 60 carbon atoms, which bond covalently to three neighbours in a network of hexagons and pentagons. The arrangement of atoms within a  $C_{60}$  molecule is shown in figure 2.2.1. While  $C_{60}$  is a particularly famous example, the term fullerene refers to any hollow 3 dimensional molecule formed by carbon atoms. The fullerene consisting of 20 carbon atoms ( $C_{20}$ ) is the smallest known while many other fullerenes occur naturally.  $C_{60}$  was discovered in 1985 by researchers at Rice University, Harry Kroto, Robert Curl and Richard Smalley [22], for which they were subsequently awarded the 1996 Nobel Prize in chemistry.

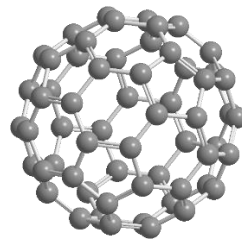


**Figure 2.2.1.** A ball and stick model of C<sub>60</sub>. Carbon atoms form a circular structure of hexagons and pentagons through the bonding of sp<sup>2</sup> hybridised molecular orbitals.

C<sub>60</sub> is synthesised from carbon plasmas, typically achieved using lasers or arc discharge [22].

C<sub>60</sub> molecules have a van der Waals diameter of 1 nm and are π-conjugated over their surface.

Fullerenes are of great interest because of their optical and electronic properties, fullerene derivatives are important in the field of photovoltaics [23], while charge transfer through a single C<sub>60</sub> molecule has also been investigated [24].

C<sub>60</sub> forms a bulk crystal through van der Waals bonding. Above 249 K, C<sub>60</sub> adopts a face centred cubic packing arrangement with no orientational alignment between molecules. Below 249 K, C<sub>60</sub> has a simple cubic unit cell with C<sub>60</sub> molecules aligned with one another [25]. C<sub>60</sub> molecules arrange in a configuration which maximises the strength of intermolecular van der Waals interactions. When deposited on a substrate in sub-monolayer doses, C<sub>60</sub> interacts with the surface and also with neighbouring molecules. On many surfaces, this leads to a 2D hexagonal close packed structure. C<sub>60</sub> has been deposited on a range of surfaces by sublimation in vacuum and characterised using surface science techniques including low energy electron diffraction (LEED) [26], scanning tunnelling microscopy (STM) [27] and non-contact atomic force microscopy (NC-AFM).

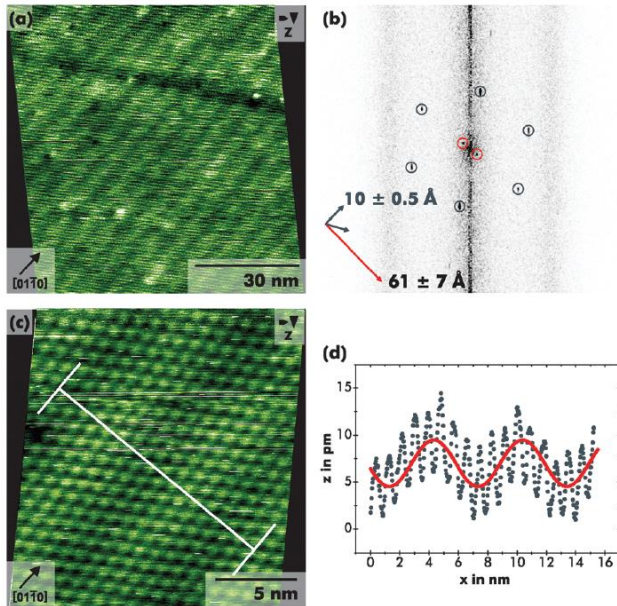


**Figure 2.2.2.** High resolution non-contact AFM images of  $C_{60}$  on  $\text{CaCO}_3$ . From a large scale image showing hexagonal packing and a large moiré pattern (a) and its 2D Fourier transform (b), a lattice parameter of  $1.0 \pm 0.05 \text{ nm}$  and a moiré period of  $6.1 \text{ nm} \pm 0.07 \text{ nm}$  are extracted. Image c shows a high resolution image with a line profile (d) showing the periodicity of  $C_{60}$  molecules and the moiré pattern. Taken from [28].

The molecular self-assembly group at the University of Mainz have published a number of studies on  $C_{60}$  adsorbed on insulating surfaces, investigated using non-contact AFM. The packing of  $C_{60}$  molecules was observed to depend on the structure of the substrate surface. Rhombic packing arrangements have been observed on the rutile  $\text{TiO}_2$  (110) surface [29] while hexagonal packing is observed on many alkali halide surfaces. A hexagonal packing arrangement was observed for  $C_{60}$  on calcium carbonate [28], see figure 2.2.2. As well as resolving the molecular packing within monolayers, with an extracted lattice constant of  $1.00 \pm 0.05 \text{ nm}$ , a moiré pattern was observed for  $C_{60}$  on calcium carbonate. Moiré patterns occur when there is a mismatch between the lattice parameters of the substrate and the adsorbate. The moiré period is the spatial separation of adsorbate molecules situated at equivalent adsorption sites on the substrate.

The observation of different island morphologies has been made for C<sub>60</sub> thin films on many insulating substrates. While noble metal substrates such as Au (111) give rise to layer-by-layer growth of C<sub>60</sub>, where sub-monolayer coverages give monolayer islands, multi-layers have been reported on many insulating substrates [30]. Studies of C<sub>60</sub> on calcium fluoride (CaF<sub>2</sub>), carried out by the Mainz molecular self-assembly group and the Maass group at Osnabrück, have investigated the morphology of islands with increasing substrate temperature, see figure 2.2.3 [30]. Samples grown at 319 K form triangular bi-layer structures while at 308 K, hexagonal islands with bi-layer edges and cavities within islands are observed. At 297 K, predominantly monolayer islands with a dendritic extra layer are seen.

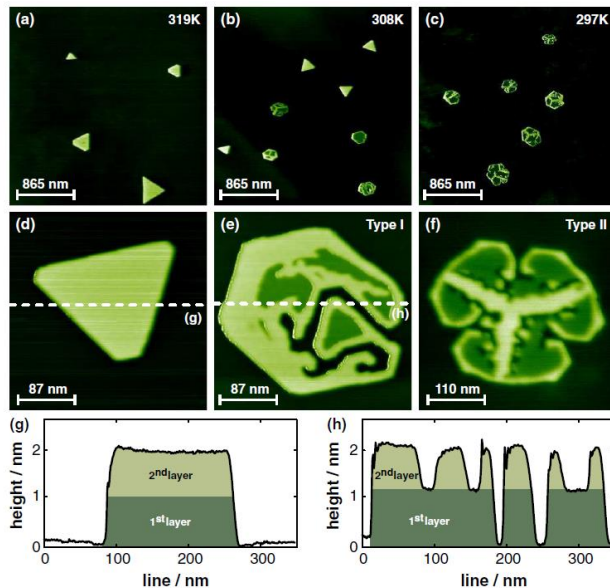


**Figure 2.2.3.** Non-contact AFM images are shown for C<sub>60</sub> deposited onto calcium fluoride (CaF<sub>2</sub>) at 319 K (a), 308 K (b) and 297 K (c). Higher resolution images of each sample (d,e and f) and line profiles (g and h) show islands with different morphologies. Taken from [30].

The morphology of C<sub>60</sub> islands on potassium bromide (KBr) and sodium chloride (NaCl) surfaces were also studied by the Grüter group at McGill University. C<sub>60</sub> was found to simultaneously form faceted monolayer structures with additional layers at edges as well as multi-layers with dendritic extra layers [31].

The observation of different morphologies and layer numbers of C<sub>60</sub> islands on insulating substrates was attributed to kinetics. The kinetic growth of C<sub>60</sub> films on CaF<sub>2</sub> was modelled

using a Monte Carlo simulation by Korner et al [30]. While  $C_{60}$  bi-layers are often energetically favourable due to stronger intermolecular interactions than molecule-substrate interactions, the mechanisms which enable molecules to migrate to energetically favourable sites are kinetically suppressed at lower temperatures. Upward hopping of  $C_{60}$  molecules, where molecules migrate from the substrate to the second layer of  $C_{60}$ , is controlled by the Ehlich-Schwoebel barrier [32,33,34].

The morphology of  $C_{60}$  thin films is dependent upon the relative strength of intermolecular and molecule-substrate interactions, as well as the threshold for thermally activated processes such as diffusion and upward hopping. Figure 2.2.4 shows the island morphology of sub-monolayer coverages of  $C_{60}$  on a range of substrates with different surface energies. As the surface energy increases, a transition from three dimensional island growth to layer-by-layer growth is observed.

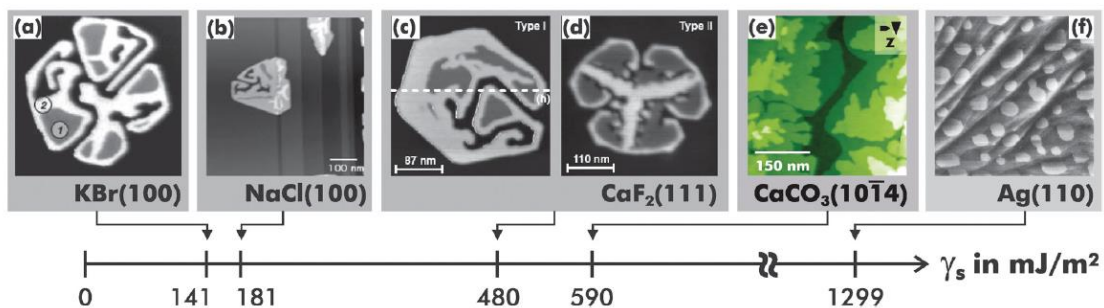


**Figure 2.2.4.** The morphology of  $C_{60}$  thin films on a range of substrates, determined using scanning probe microscopy (SPM) techniques. The surface energy of each substrate is indicated on the axis below. Taken from [28].

### 2.3. Perylene Derivatives: PTCDI and PTCDA

Perylene is a molecule consisting of 20  $sp^2$  hybridised carbon atoms which form a  $\pi$ -conjugated structure. The molecule consists of five covalently bonded benzene rings, which are terminated by hydrogen atoms. Perylene can be functionalised by adding anhydride

groups to the peri-positions of the molecule to give perylene tetracarboxylic dianhydride (PTCDA) [35]. Perylene can also be functionalised with the addition of imide groups, giving perylene tetracarboxylic diimide (PTCDI). The structures of perylene, PTCDA and PTCDI are given in figure 2.4.1. PTCDA, PTCDI and their derivatives were first used as synthetic dyes but are now also commonly used in organic electronics. Perylene derivatives are still studied extensively to this day for their optical and electronic properties while the morphology of thin films of these molecules have been investigated on a range of substrates using both STM and AFM.

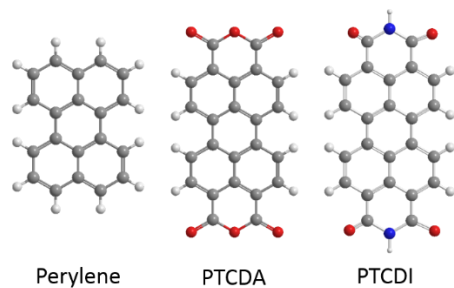


**Figure 2.3.1.** The structure of perylene, PTCDA and PTCDI are shown. Carbon molecules are denoted by grey, hydrogen: white, oxygen: red and nitrogen: blue.

The direction, placement and number of functional groups within a molecule can be controlled through rational synthesis. The synthesis of molecules with specific structure can be used to direct their self-assembly into a range of 2D packing arrangements, see figure 2.3.2 [36]. Templing the structure of a molecular thin film in this way could be used to change the morphology and functional properties of a film. The packing of fluorescent molecules within a thin film can influence its optical properties, an effect which will be discussed in greater detail in section 2.6.

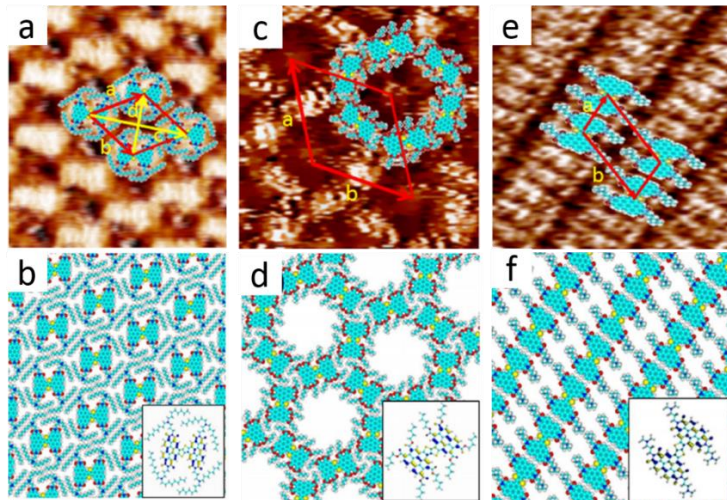


**Figure 2.3.2.** The self-assembly of three perylene-bithiophene-perylene derivatives on HOPG was investigated using STM. STM images of each derivative on HOPG (a,c,e) are shown in addition to diagrams showing the molecular packing (b,d,f). Taken from [36].

PTCDI and PTCDA have both been deposited onto the Ag-Si (111)-v3xv3 surface and studied using STM in UHV conditions by the Nottingham nanoscience group [37]. Sublimed PTCDA forms flat-lying monolayers on Ag-Si (111)-v3xv3, these flat-lying monolayers can arrange in square or herringbone phases, see figure 2.3.3 [37,38]. The herringbone phase consists of rows of molecules where subsequent rows are canted by 90°, the unit cell of this structure is rectangular and contains two molecules. Swarbrick et al extracted the unit cell dimensions of the herringbone phase of PTCDA on Ag-Si (111)-v3xv3 ( $2.00 \pm 0.02$  nm and  $1.16 \pm 0.02$  nm) from STM images. The herringbone phase has also been observed on Ag-Si (111)-v3xv3 by Gustafsson et al [38] in addition to gold [39], graphite [40] and molybdenum disulphide substrates [41].

In the square phase, PTCDA molecules have a square unit cell with molecules at one corner and the centre, the two basis molecules are counter rotated by 90°. An STM image elucidating both the herringbone and square PTCDA phases on Ag-Si (111)-v3xv3 is shown in figure 2.3.3, in this image, PTCDA molecules are resolved as two bright lobes, owing to the distribution of electrons within the HOMO state.

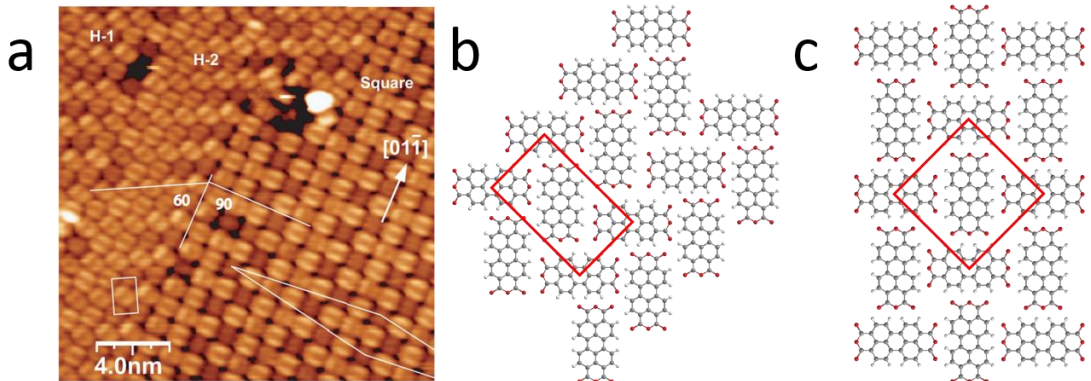


**Figure 2.3.3.** PTCDA deposited on Ag-Si (111)- $\sqrt{3}\times\sqrt{3}$  under UHV conditions, studied using STM, was found to form both a herringbone and square phase (indicated). The STM image above shows an area with both the herringbone and square phase as well as the boundary between the two phases, the unit cells of which are shown in white. Diagrams showing the structure of the herringbone (b) and square phase (c) of PTCDA are also shown, with unit cells indicated in red. Image (a) taken from [38].

Using non-contact AFM, PTCDA has been found to form herringbone, brick wall and square phases on a number of alkali halide substrates including NaCl [42] and KCl [14]. By annealing pre-formed monolayer PTCDA islands in-situ after growth, the thin film morphology was found to undergo a transition from monolayer to large multilayer islands, see figure 2.3.4. Similar de-wetting effects have also been reported for PTCDI on NaCl [43].

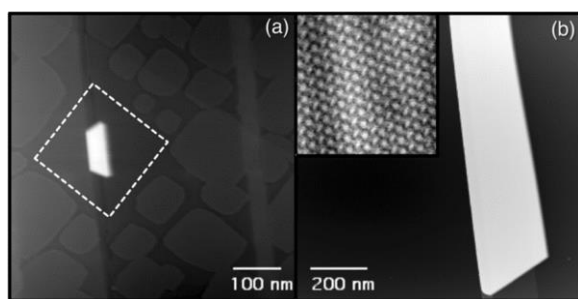


**Figure 2.3.4.** Upon annealing to 150 °C, de-wetting from the NaCl substrate was found to lead to a transition from metastable monolayer to multi-layer PTCDA islands. The herringbone packing of PTCDA molecules within multi-layer islands is also shown, inset (b). Images were acquired using NC-AFM. Taken from [42].

PTCDI has also been studied extensively using both STM and AFM on a range of substrates [37, 41, 43, 44] while many more studies have been carried out on PTCDI derivatives. On two dimensional surfaces such as highly oriented pyrolytic graphite (HOPG) and molybdenum

disulphide ( $\text{MoS}_2$ ), PTCDI molecules have been found to form a canted structure. In this arrangement, PTCDI molecules are aligned in rows where molecules are counter rotated by  $12^\circ$  from the intra-row lattice vector in order to maximise the strength of intra-row hydrogen bonding. Alternating rows are rotated in the opposite direction, which gives a greater packing efficiency, see figure 2.3.5 [41].

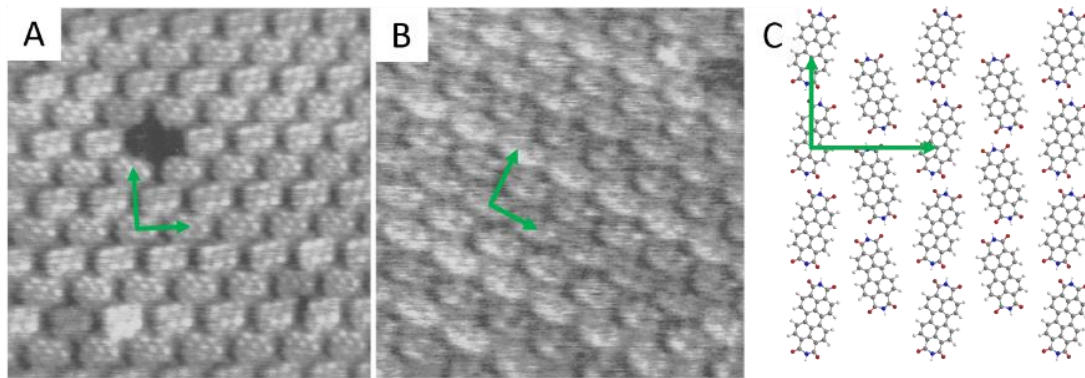


**Figure 2.3.5.** The molecular packing of PTCDI on molybdenum disulphide and graphite surfaces has been studied by Ludwig et al. On both molybdenum disulphide (a) and HOPG (b), a canted arrangement of PTCDI molecules is observed. A schematic of this molecular arrangement is also shown (c), PTCDI molecules arrange in rows to maximise intra-row hydrogen bonding, with adjacent rows counter rotated by  $\pm 12^\circ$  from the row direction. Images a and b taken from [41].

PTCDI also forms a bi-component supramolecular network when co-deposited with melamine [5]. Hydrogen bonding between melamine and PTCDI molecules on the surface stabilises a junction between one melamine molecule and three PTCDI molecules. This junction forms the basis of the PTCDI-melamine honeycomb network, which occurs due to stronger coupling between PTCDI and melamine (hetero-coupling) than between two molecules of the same species (homo-coupling), see figure 5.3.6.

This network was studied by the Nottingham nanoscience group [5] by first depositing sub-monolayer coverages of PTCDI onto the Ag-Si (111)- $\sqrt{3}\times\sqrt{3}$  surface by sublimation in vacuum. Melamine was then deposited onto the surface held at  $100^\circ\text{C}$ , leading to the formation of the

PTCDI-melamine network which could be studied using in-situ STM. The PTCDI-melamine network forms a hexagonal array with a period of 3.5 nm on the Ag-Si (111)- $\sqrt{3}\times\sqrt{3}$  surface.

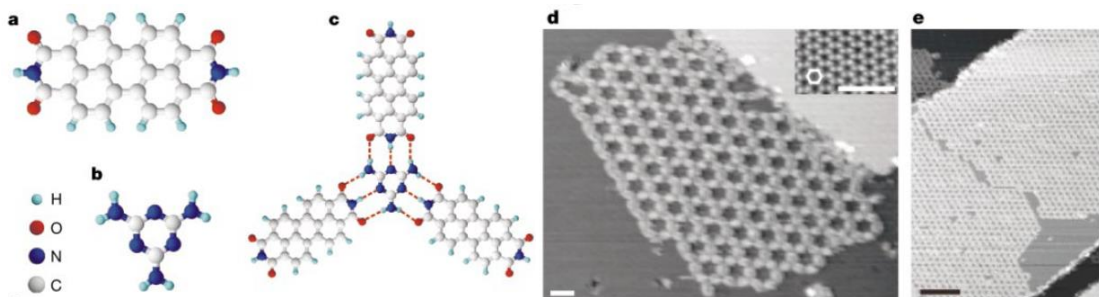


**Figure 2.3.6.** A representation of PTCDI (a), melamine (b) and the hydrogen bonding junction between melamine and 3 PTCDI molecules (c) is shown. Both PTCDI and melamine were deposited onto the Ag-Si (111)- $\sqrt{3}\times\sqrt{3}$  surface by sublimation in vacuum and studied using UHV STM (d,e). Images d and e have scale bars of 3 and 20 nm respectively. Taken from [5].

One feature of the PTCDI-melamine supramolecular network is that the pores created by the hexagonal network can act as a host for the deposition of further molecular species. The Nottingham nanoscience group have incorporated heptamers of  $C_{60}$  into the PTCDI-melamine network by both sublimation in vacuum [5] and electrospray deposition [45]. The PTCDI-melamine supramolecular network has also been deposited from solution. This was first demonstrated on the Au (111) surface by the Buck group at the University of St Andrews using a solution of PTCDI and melamine in dimethylformamide. This solution deposited supramolecular network was studied using STM and used to template the growth of thiol self-assembled monolayers (SAMs) [6]. More recently, the PTCDI-melamine network has been deposited from solution onto HOPG, molybdenum disulphide and hexagonal boron nitride (hBN) by the Nottingham nanoscience group [46].

## 2.4. Cyanuric Acid-Melamine

Bulk melamine-cyanurate crystals, extended hydrogen bonded networks of melamine and cyanuric acid, have industrial applications as flame retardant materials. More recently, these materials have been studied for their on-surface self-assembly. Like PTCDI and melamine, cyanuric acid and melamine form a supramolecular network. The adsorption of cyanuric acid-melamine on surfaces has been studied by a number of groups, including the Nottingham nanoscience group, using both sublimation and solution deposition techniques [47,48]. One example is cyanuric acid-melamine on Au (111) [49]. On the Au (111) surface, cyanuric acid and melamine have distinct packing structures. Upon co-adsorption, a hexagonal arrangement is observed at room temperature, see figure 2.4.1, and also a chiral structure with longer spatial periodicity.

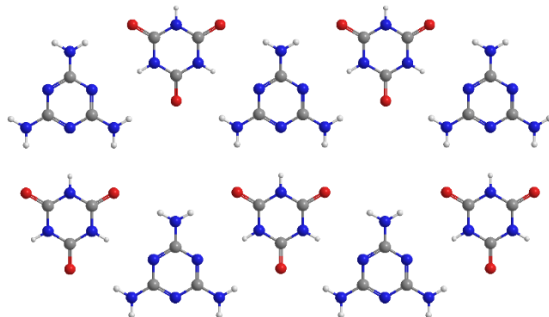


**Figure 2.4.1.** The honeycomb structure of the cyanuric acid-melamine network is shown. This packing structure has a basis consisting of one cyanuric acid and one melamine molecule.

The adsorption of cyanuric acid-melamine has also been studied by solution deposition onto HOPG and mica substrates [50]. Depending upon the concentration of the cyanuric acid-melamine solution and the deposition time, the coverage of cyanuric acid–melamine can be tuned to give a range of coverages from monolayer islands to 3D crystal growth [50]. For monolayer coverages of cyanuric acid–melamine on HOPG, moiré patterns are observed due to the differing spatial periodicities of the substrate and adsorbate [51].

The large bandgap of both cyanuric acid and melamine and the ease with which films of monolayer thickness can be processed make the cyanuric acid-melamine network interesting for a number of applications. Recently, the Nottingham nanoscience group used cyanuric acid-melamine to passivate black phosphorus [52]. The incorporation of cyanuric acid-melamine into van der Waals heterostructures is also of interest, since the network could be used to modify the interface between two layers or act as a dielectric spacer layer.

## 2.5. Hexagonal Boron Nitride and Graphene

Graphene, an allotrope of carbon, is a single atom thick sheet of  $sp^2$  hybridised carbon atoms which form a honeycomb arrangement [53]. The unique structure of graphene gives rise to its exceptional transport and mechanical properties [54,55]. The electronic properties of graphene can be described using the tight binding model, from which features such as its linear bandstructure close to the Dirac point, and resulting zero effective mass can be explained. Depositing adsorbates on the surface of graphene, in order to produce a superstructure, offers a potential route to tune its electrical properties [56]. The synthesis of one- and two-dimensional  $sp^2$  hybridised films by the on-surface polymerisation of organic precursors is also a promising route to form functional layers with analogous structures to graphene [57].

Graphene can be produced by a number of methods including mechanical exfoliation, chemical vapour deposition (CVD), molecular beam epitaxy (MBE) and chemical exfoliation. When sufficiently clean, graphene can be used as a substrate for molecular self-assembly experiments [58]. The isolation of single layer graphene by Geim and Novoselov led to renewed interest in many two-dimensional crystals including transition metal dichalcogenides and hexagonal boron nitride (hBN). hBN is isostructural to graphene and

consists of boron and nitrogen atoms forming a honeycomb network. The structures of both graphene and hBN are shown in figure 2.5.1.

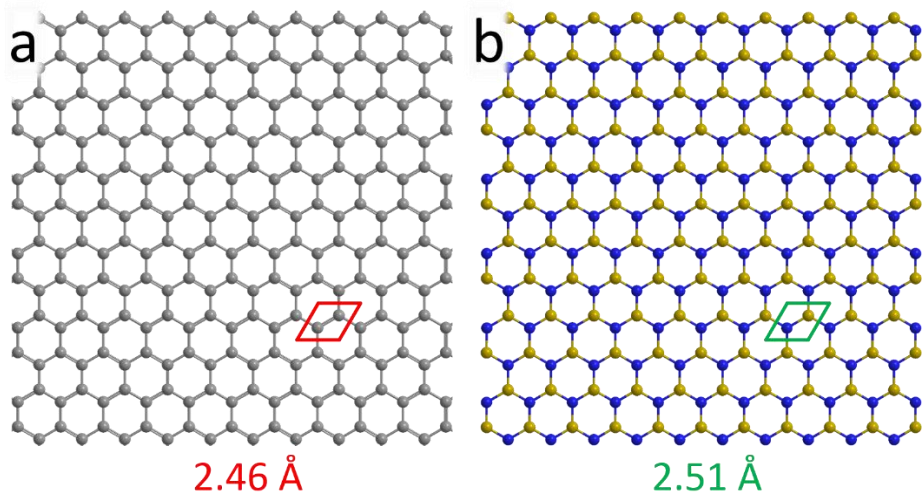


**Figure 2.5.1.** The structures of both graphene (a) and hBN (b) are shown with the unit cells indicated. Grey, blue and yellow are used to denote carbon, nitrogen and boron atoms respectively.

Recently, hBN has been investigated as a substrate for graphene and other 2D materials as well as for its incorporation into van der Waals heterostructures, where layers of 2D materials are vertically stacked in order to fabricate novel electronic devices [59,60]. hBN is seen as a promising substrate for graphene because it has an atomically flat surface, is a wide band-gap semiconductor and is weakly interacting. On hBN substrates, graphene has a higher carrier mobility ( $1.4 \times 10^5 \text{ cm}^2 \text{ V}^{-1} \text{ s}^{-1}$ ) [61], comparable with free standing suspended graphene ( $1.9 \times 10^5 \text{ cm}^2 \text{ V}^{-1} \text{ s}^{-1}$ ) [62]. By comparison, interactions with the substrate give rise to electron-hole ‘puddles’ on conventional  $\text{SiO}_2$  substrates, which occur due to shifts of the Fermi level of graphene [63].

The insulating properties of hBN, arising from its large bandgap of 6.0 eV [64] and its atomically flat surface, make it a particularly interesting substrate on which to study organic thin films and their optical properties. Because hBN is isostructural to graphene with no

dangling bonds, it interacts weakly with the functional groups of a molecular adsorbate. This favours an adsorption geometry where planar molecules lie parallel to the hBN surface in order to maximise van der Waals interactions. The large bandgap and insulating properties of hBN also allow fluorescence spectroscopy to be carried out on adsorbed organic thin films. This is not possible on conductive substrates, which quench fluorescence.

## 2.6. Molecular Fluorescence

Molecular fluorescence occurs when a molecule absorbs a photon and undergoes a transition from the ground state to an excited electronic state. The molecule then relaxes to the lowest vibrational level of the excited electronic state before decaying back to the electronic ground state through emission of a photon. Fluorescence occurs at a longer wavelength than the excitation source and is distinct from phosphorescence, where intersystem crossing causes the molecule to undergo a transition to an excited triplet state. Relaxation from the excited triplet state back to the ground state has a much longer lifetime [65].

The energy at which fluorescence occurs is influenced by the separation between the highest occupied molecular orbital (HOMO) and the lowest unoccupied molecular orbital (LUMO) of a molecule, in addition to a correction due to the electron-hole interaction energy [66]. The fluorescence of isolated molecules can be measured using techniques involving molecules in the gas phase or doped helium nano-droplets (HND). In different chemical environments such as in solution, within crystals and on surfaces, resonant and non-resonant interactions give rise to dramatic changes in the fluorescent properties of organic molecules.

### **2.6.1. Gas Phase, HND and Solution**

In order to study the optical properties of isolated fluorescent molecules, spectroscopy can be carried out on sublimed molecules in the gas phase. Gas phase measurements are carried out by annealing molecules in an oven with an inert gas, commonly helium. The gas and sublimed organic molecules are then passed through an aperture into a vacuum chamber which causes the expansion and cooling of the mixture. Fluorescence spectroscopy is then carried out in the region of the expanding gas [67]. An example of such an experiment is that carried out by Fitch et al on the fluorescence of free base phthalocyanine molecules [68].

Another way in which the fluorescence spectra of isolated molecules can be studied is by subliming molecules onto helium nano-droplets (HND), a process referred to as doping [69]. Wewer and Stienkemeier have carried out HND fluorescence measurements on both PTCDA and functionalised PTCDI molecules (Me-PTCDI). Me-PTCDI has methyl groups attached to both imide positions [70,71]. Fluorescence spectra of both PTCDA and Me-PTCDI from [70,71] are shown in figure 2.6.1.1. Fluorescence measurements of doped HND are often taken to correspond very closely to gas phase measurements, since shifts arising from resonant and non-resonant interactions within noble gasses at cryogenic temperatures are small compared to shifts due to solvation and surface adsorption. For the free base phthalocyanine molecule, a red shift of approximately 0.005 eV was measured from gas phase to doped HND measurements [68,72].

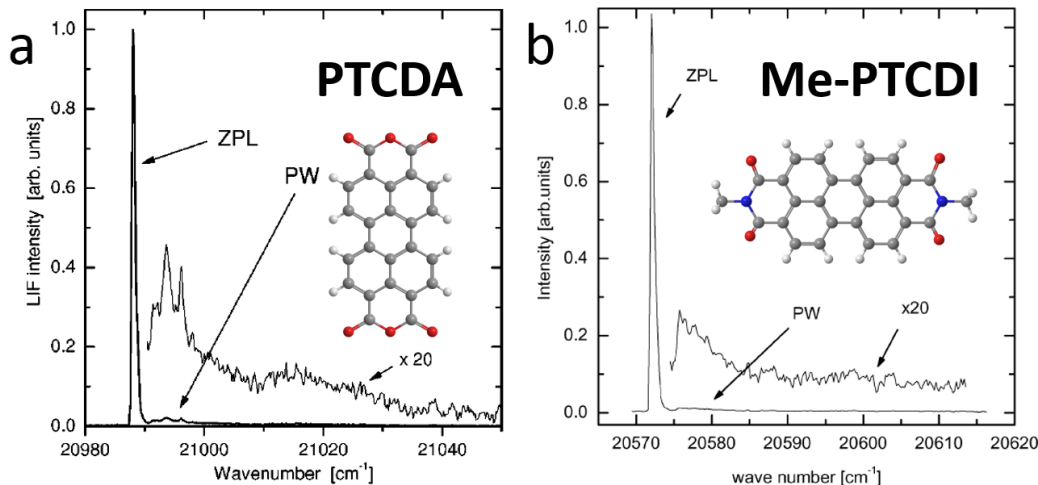


**Figure 2.6.1.1.** The fluorescence spectra of PTCDA (a) and Me-PTCDI (b) doped helium nanodroplets are shown, vibronic sidebands are shown with a 20x enhancement. The 0-0 fluorescence peaks of PTCDA and Me-PTCDI occur at  $2.6022 \pm 0.0001$  eV and  $2.5506 \pm 0.0001$  eV respectively. Taken from [70,71].

Upon solvation, solvatochromic shifts affect the fluorescence of organic molecules. In solution, solute molecules are typically surrounded by solvent molecules and so do not interact with other molecules of the same species, as they would within a bulk crystal. In the absence of a fluorescence quenching species, a strong 0-0 peak is observed in the fluorescence of many molecules in solution. Solvatochromic shifts, first explained by Bayliss [73], are shifts which arise from the interaction of the transition dipole moment of a fluorescent molecule with an induced charge distribution within a non-polar solvent. The strength of interaction depends on the polarisability of the solvent, leading to a shift which is greater for solvents of greater refractive index.

## 2.6.2. Molecular Monolayers

There are a number of possible mechanisms which give rise to fluorescence shifts from the gas phase to flat-lying molecular monolayers. Fluorescence shifts can arise from both non-resonant and resonant interactions. Non-resonant interactions have been observed in systems where interactions between a fluorescent molecule and its environment perturb the electronic states within a molecule. Such a shift was observed by the Nottingham nanoscience group, where the fluorescence of monolayer films of tetra carboxyl phenyl porphyrin (TCPP) on hBN were shifted due to the interaction of the molecule with the substrate [74].

Resonant interactions occur due to the delocalisation of excitons across a number of molecules. The fluorescence of such structures is explained by considering the coupling of transition dipole moments. In ‘The Theory of Molecular Excitations’ [75] Davydov presented a model of transition dipole coupling in molecular fluorescence which is still used to describe the shifts of both organic monolayers and crystals. Both the Sokolowski group at the University of Bonn and the Fritz group at the University of Jena have studied the optical properties of organic monolayers, particularly PTCDA on alkali halide surfaces, in great detail. The Sokolowski group at Bonn measured the fluorescence of flat-lying isolated PTCDA molecules and two packing arrangements of monolayer PTCDA on NaCl [13]. When deposited on NaCl held at 20 K, with a coverage of much less than one monolayer, molecules are flat-lying and isolated on the NaCl surface (this is referred to as the dilute phase in the literature). On NaCl, PTCDA also forms both a square and a herringbone (rectangular) packing structure. The packing of these phases and their fluorescence spectra are shown in figure 2.6.2.1.

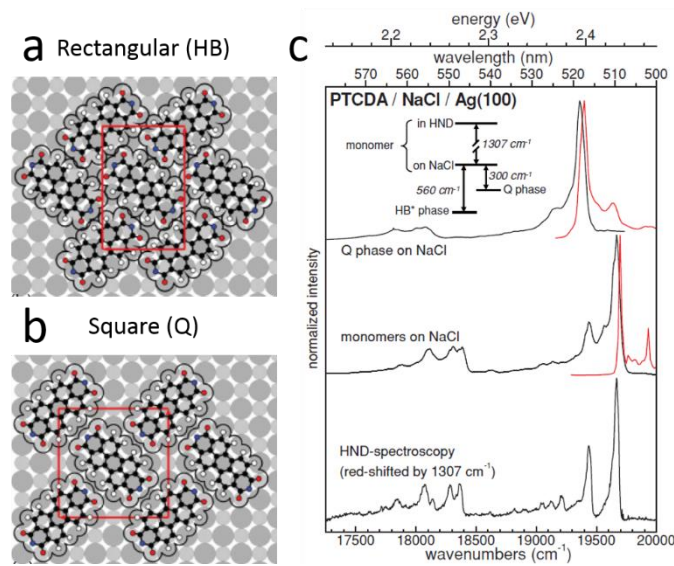


**Figure 2.6.2.1.** The structure of both the herringbone (rectangular, HB) (a) and square (Q) (b) phases of PTCDA on NaCl are shown. The fluorescence spectra of the square and rectangular close packing arrangements and isolated PTCDA molecules (dilute phase) are shown. Taken from [13].

The Sokolowski group have also published a similar study of PTCDA on KCl substrates [76], where a  $0.1215 \pm 0.0001$  eV red shift was measured from PTCDA doped HND to isolated molecules on the surface, with a further  $0.0496 \pm 0.0001$  eV red shift due to aggregation into a monolayer brick wall phase. In reference [13,76], the origin of the shift of the fluorescence peak of aggregated PTCDA compared to isolated PTCDA on alkali halide surfaces is attributed, in part, to the on-surface coupling of neighbouring transition dipole moments. The coupling of transition dipole moments was modelled and used to calculate the exciton bandstructure of each PTCDA phase. In general, the fluorescence shift from gas phase measurements of a close packed organic monolayer,  $\Delta E_{\text{tot}}$ , is made up of a shift due to interactions with the surface,  $\Delta E_{g-s}$ , and a shift due to intermolecular interactions,  $\Delta E_{\text{int}}$ .

$$\Delta E_{\text{tot}} = \Delta E_{g-s} + \Delta E_{\text{int}} \quad (2.6.2.1)$$

Earlier, the Fritz group at Jena had measured the fluorescence of the same brick wall phase of PTCDA monolayers on KCl using differential reflectance spectroscopy (DRS) [14]. The brick wall phase of PTCDA on KCl was observed at room temperature for sub-monolayer coverages using

non-contact AFM, while the herringbone (rectangular) phase was observed as the coverage was increased. The narrow peak width of PTCDA on KCl, compared to monolayers on mica and PTCDA in solution, was attributed to the registry of molecules and the substrate.

In addition to conventional spectroscopy measurements, STM induced luminescence (STML) can also provide insights into the delocalisation of excitons and their influence on molecular fluorescence [77,78,79]. For example, Zhang et al [78] used STM to investigate zinc-phthalocyanine molecules adsorbed on a thin NaCl layer on silver, see figure 2.6.2.2. Clusters of two, three and four molecules were formed using sample manipulation with the STM tip. The luminescence of monomers and oligomers, induced through excitation by the STM tip, was measured, with a red-shift observed for larger clusters. The observed shifts were found to agree with descriptions involving the coupling of transition dipole moments [75,80].

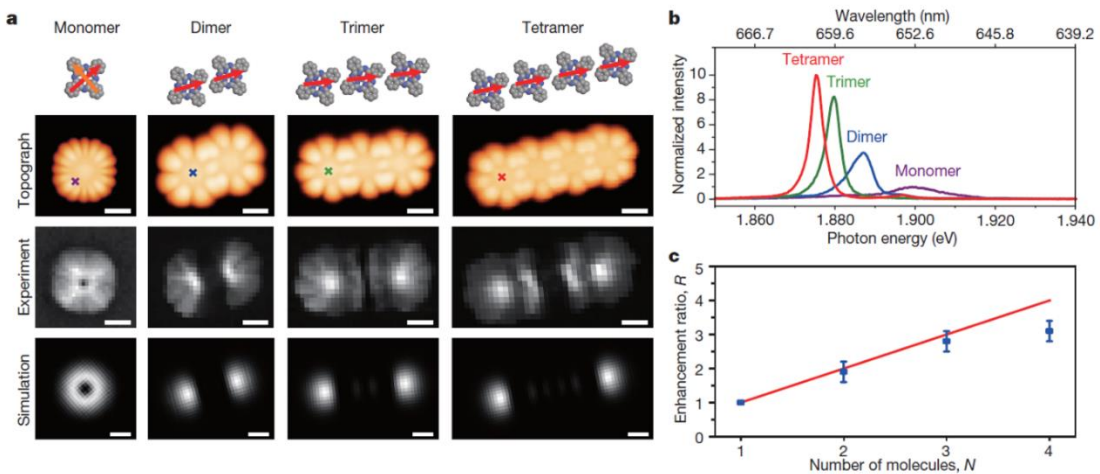


**Figure 2.6.2.2.** A schematic representation of phthalocyanine monomers and oligomers is shown in addition to STM images and experimental and theoretical photon images, all scale bars are equal to 1 nm (a). STML spectra, extracted from the positions indicated in the STM images are shown (b) in addition to the enhancement factor for monomers and oligomers. Taken from [78].

More recently, the Fritz group has measured DRS spectra for PTCDA on monolayer hBN on Pt (111) and Rh (111) surfaces as well as PTCDA on graphene (on silicon carbide), gold and silver surfaces [81]. In this work they observe very similar adsorption peak positions, extracted from

fitted DRS spectra, on hBN on Pt(111), graphene on SiC and on gold and silver surfaces. In the case of PTCDA on hBN on Rh(111), they observe a different peak position which is attributed to the trapping of PTCDA monomers within pores on the substrate surface. The relative position of the peaks is explained in terms of the on-surface coupling of the transition dipole moments of PTCDA molecules, with reference to the calculated exciton bandstructure of the observed herringbone packing arrangement [13].

In their paper, the Fritz group also discuss similarities between the DRS spectra of PTCDA on substrates with different refractive indices and extinction coefficients, and go on to suggest that the dielectric properties of the substrate have little effect on the fluorescence of molecular monolayers. While chromatic shifts between different molecular packing structures and isolated molecules on surfaces can be explained in terms of resonant coupling of transition dipole moments, the role of the substrate and the mechanisms behind shifts from ‘gas phase’ (doped HND) measurements are still not fully understood.

## 2.7. Conclusion

This chapter has provided an overview of the growth of molecular thin films on surfaces. The adsorption of C<sub>60</sub> was discussed as well as a brief review of hydrogen bonded arrays and supramolecular networks based on perylene derivatives, cyanuric acid and melamine. The two-dimensional materials, graphene and hBN, were then introduced with reference to their importance to molecular self-assembly. Finally, molecular fluorescence was discussed with an emphasis on the physical interactions pertinent to monolayer organic thin films.

# **Chapter 3:**

# **Experimental Techniques**

### **3. Experimental Techniques**

In this chapter, the techniques used to study molecular thin films on hBN are discussed. The two main techniques used in this work are atomic force microscopy (AFM) and fluorescence microscopy. AFM is used to study the morphology of molecular thin films while their optical properties can be measured using fluorescence microscopy and Raman spectroscopy. Sample fabrication procedures including mechanical exfoliation, substrate cleaning and sublimation of organic material in vacuum are then discussed.

#### **3.1. Atomic Force Microscopy**

In 1982, Gerd Binnig and Heinrich Rohrer invented the scanning tunnelling microscope (STM) [82]. By mapping the tunnelling current between an atomically sharp tip and a sample, images of the topography of a conductive surface can be acquired. The tunnelling current is dependent upon the tip-sample separation and the tip-sample bias. Conventionally, the tip-sample bias is held constant while the position of the tip above the sample is controlled using piezoelectric crystals. The tip height can then be kept fixed during mapping, as in constant height STM, or changed by feedback control in order to maintain a constant tunnelling current [83]. STM was first used in order to study metal and semiconductor surfaces with atomic resolution and is now used in a number of fields, including atomic manipulation [84], molecular self-assembly [85] and single molecule electronics [86].

On insulating substrates, the tunnelling current leads to a build-up of charge and an unstable tip-sample bias, therefore STM can only be carried using conductive substrates. To overcome this limitation, the atomic force microscope (AFM) was invented by Gerd Binnig, Christoph Gerber and Calvin Quate. AFM can be used to study the morphology of both insulating and conducting surfaces [87]. When an atomically sharp tip is placed at the end of a cantilever,

forces experienced by the tip cause a deflection of the cantilever. Measuring the deflection of a cantilever of known stiffness allows the force between the tip and sample to be extracted using Hooke's law, given by equation 3.1.1, where the deflection,  $\Delta x$ , due to an applied force,  $F$ , is determined by the spring constant,  $k$ , of the cantilever [88]. By mapping the interaction between the tip and sample laterally across the surface, an image can be produced.

$$k = \frac{F}{\Delta x} \quad (3.1.1)$$

When the tip approaches the sample surface, interactions with the substrate lead to attractive or repulsive forces depending upon the tip-sample separation. The interaction between two atoms can be modelled by the Lennard-Jones potential [16], given in equation 3.1.2 where  $r$  is the separation,  $\sigma$  is the separation at which the potential is zero and  $\varepsilon$  is the maximum attractive potential. At separations larger than  $\sigma$ , the interaction between instantaneous and induced dipoles (London forces) leads to an attractive force, modelled by the second term in equation 3.1.2. At small separations, the overlap of electronic wave functions leads to a repulsive force due to the Pauli principle. The deflection of a cantilever due to interactions with a substrate is shown in figure 3.1.1.

$$V(r) = 4\varepsilon \left( \left(\frac{\sigma}{r}\right)^{12} - \left(\frac{\sigma}{r}\right)^6 \right) \quad (3.1.2)$$

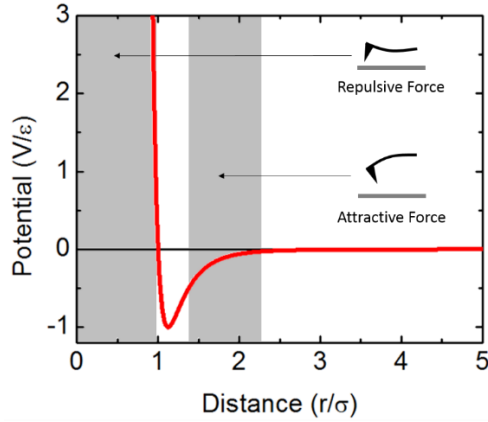


**Figure 3.1.1.** The Lennard-Jones potential is used to model the potential between two atoms. For separations ( $r$ ) smaller than  $\sigma$ , the tip experiences a repulsive force and is deflected away from the surface. For separations greater than  $\sigma$ , the tip experiences an attractive force and deflects towards the surface.

Using calibrated piezoelectric crystals, the position of the tip above the sample surface can be controlled with sub-nanometer precision. When a voltage is applied across a piezoelectric crystal, ions within the unit cell of the crystal respond to the potential. This leads to a small change in the dimensions of the unit cell and a small contraction or extension of the whole crystal [89]. The piezoelectric crystals used in modern commercial AFM instruments have a maximum range in the order of  $100 \mu\text{m}$ , allowing large scale images of the substrate morphology to be acquired.

In order to measure the topography of a sample, the tip is scanned along the surface in a raster pattern. Forces between the tip and sample lead to deflections of the cantilever. Early AFM techniques measured the deflection of the cantilever using a tunnelling current between the cantilever and an STM probe. Modern AFM techniques measure the deflection of the cantilever by projecting a laser onto the side opposite the tip and recording the position of the reflected beam using a photodetector [90], see figure 3.1.2.

In AFM, the position of the tip is controlled using piezoelectric crystals while the tip sample interaction can be monitored by measuring the deflection of the cantilever. By measuring the response of the cantilever continuously, the tip-sample separation can be changed in order to

maintain a constant force using feedback control, this is known as constant force imaging. The use of feedback control enables AFM to be used in a number of modes, using different feedback parameters. In this work, both contact mode and AC mode (also known as tapping mode and non-contact mode) are used. The configuration used for AFM measurements in both AC and contact mode is shown in figure 3.1.2.

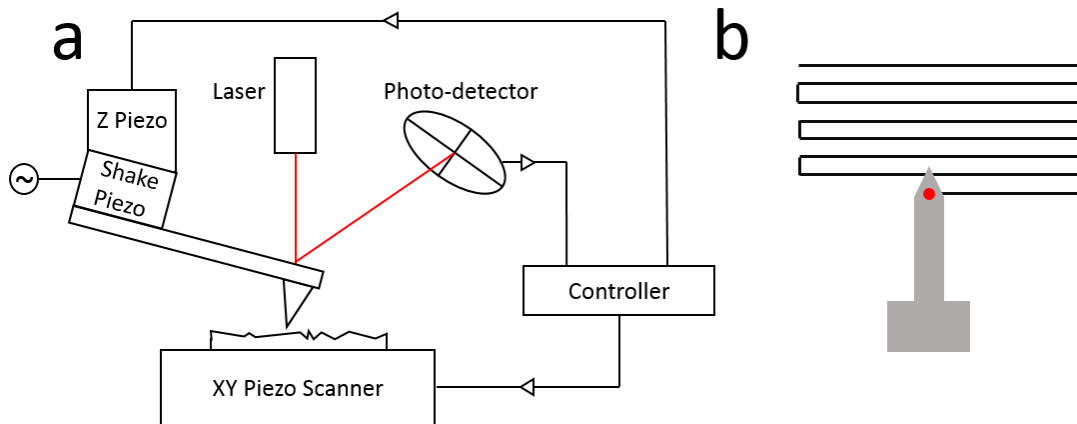


**Figure 3.1.2.** The conventional setup of an AFM instrument, which can be used in either AC mode or contact mode (a). The response of the cantilever is monitored by measuring the deflection of a laser, projected onto the back of the cantilever. The deflection or amplitude of oscillation of the cantilever can then be used as a feedback parameter. The raster pattern made by the tip as it moves laterally across the sample is also shown (b).

In contact mode AFM, the tip is moved towards the surface and the deflection of the cantilever is measured. The deflection of the cantilever corresponds to a force exerted on the tip which can be calculated, using Hooke's law, for cantilevers of known stiffness. The tip is lowered towards the surface by extending the z-piezo until a setpoint is reached. The setpoint is a user-specified deflection value which is maintained by lowering or retracting the tip during scanning.

Contact mode enables the surface topography of samples to be measured more quickly and often with greater resolution than in other imaging modes, but the tip-sample interaction can lead to the tip becoming blunt and also damage weakly bound molecular layers. For these reasons, contact mode is only typically used for high resolution scans of substrate surfaces

and small scans of molecular monolayers, where damage is limited to a very small area of the sample.

In AC mode AFM, the tip is driven on-resonance using a piezo crystal known as the excitation piezo. When far above the sample surface, the cantilever oscillates at the free air amplitude. As the cantilever approaches the sample surface, repulsive forces between the sample and tip lead to a reduction in the amplitude of the cantilever. The amplitude of the cantilever is used as the feedback parameter, with a setpoint below the free-air amplitude. The equation of motion of a cantilever with a spring constant,  $k$ , is given by equation 3.1.3, where  $x$  is the displacement of the cantilever,  $\gamma$  is the damping of the cantilever,  $F_{TS}$  is the force between the tip and sample and  $F_d$  and  $\omega_d$  are the amplitude and frequency at which the cantilever is driven [91]. By solving equation 3.1.3, quantities such as the resonant frequency and amplitude of the cantilever in air can be calculated.

$$\frac{d^2}{dt^2}x + \gamma \frac{d}{dx}x + kx = F_{TS} + F_d \cos \omega_d t \quad (3.1.3)$$

In this work, AC mode is used to acquire all large scale AFM images. Though slower than contact mode, the reduced interaction between the tip and sample means that molecular layers are not strongly affected during scanning and the degradation in the tip will not occur as quickly.

When using feedback to acquire images of the surface topography, the response of the system to an offset is controlled by the gain [89]. It is important to pick appropriate values for the gain since if the gain is set too low, the response to features in the topography will be slow, reducing the resolution of AFM images. If gains are set too high, the response will be too large and lead to a greater offset than in the previous loop, introducing noise due to the system repeatedly over-shooting the setpoint. Both proportional and integral gain are commonly used in AFM.

In addition to the gain, a number of parameters can be changed to improve the quality of AFM images. Increasing the speed at which the tip is scanned across the surface reduces the effect of thermal drift but requires sophisticated supporting electronics to enable rapid execution of feedback control. The number of pixels per image can also be increased and allows large areas to be mapped in detail. The resolution of AFM is ultimately limited by the geometry of the tip as well as thermal and acoustic noise. Carrying out measurements in ultra-high vacuum (UHV) at cryogenic temperatures with tips functionalised with carbon monoxide allows modern AFM techniques to achieve sub-molecular resolution [12].

AFM can be used under ambient conditions to acquire images of the morphology a sample, without the use of laborious ultra-high vacuum (UHV) procedures. Studying samples under ambient conditions using AFM also allows the stability of molecular thin films to be confirmed, an important factor when considering the practical applications of such samples. In this work, images were acquired under ambient conditions using the Asylum research MFP-3D and Cypher S with standard silicon cantilevers from Budget Sensors.

### **3.2. Fluorescence and Raman Microscopy**

Photoluminescence is the emission of light from a material as a consequence of absorbing light from an external source. When a photoluminescent molecule absorbs light with sufficient energy, it will undergo a transition from the ground state to an excited electronic state. Once in the excited electronic state, the molecule can relax to other accessible states by various means. This work focuses on relaxation from excited singlet states to the ground state by the emission of a photon, the phenomenon known as fluorescence [65].

In the case of fluorescent molecules, the ground state is typically the highest occupied molecular orbital (HOMO). Upon absorption of a photon of sufficient energy, the molecule

undergoes a transition to an excited state with the same or greater energy than the lowest unoccupied molecular orbital (LUMO). The distance between HOMO and LUMO states, the HOMO-LUMO gap, is analogous to the bandgap of an inorganic semiconductor and is an important factor in the optical and electronic properties of organic molecules. For many fluorescent molecules, an extended  $\pi$  conjugated state is the HOMO while the  $\pi^*$  state is the LUMO. As the spatial extent of the delocalised system increases, the HOMO-LUMO gap and the fluorescence energy typically decrease [65].

As well as electronic states, molecules have vibrational levels which can be excited upon interaction with a photon. These vibrational energy levels correspond to linear, rotational and torsional perturbations across individual bonds or extended structures within molecules. The energy of vibrational states is typically of the order 0.1 eV, corresponding to infra-red and microwave frequencies [92,93]. Each electronic state has an associated set of vibrational levels. A jump between states within a fluorescent material can be described using a Jablonski diagram [92], shown in figure 3.2.1.

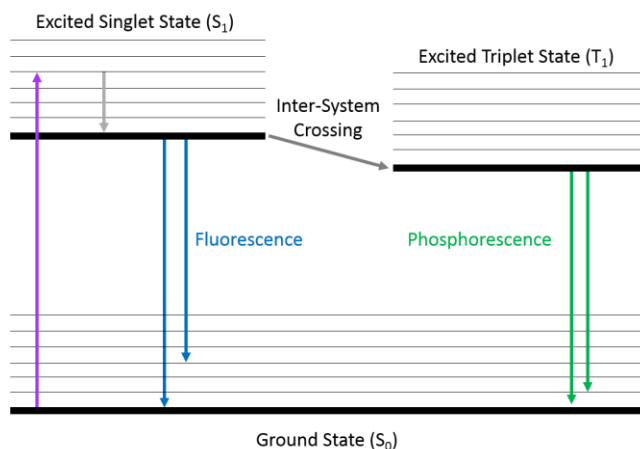


**Figure 3.2.1.** The electronic energy levels (bold) and vibrational energy levels (grey) are shown as horizontal lines on the Jablonski diagram. When absorbing a photon of sufficient energy, a molecule can change from a lower energy singlet state ( $S_0$ ) to an excited singlet state ( $S_1$ ). Molecules can relax to the vibrational ground state of the excited electronic state quickly and non-radiatively before decaying back to some vibrational state associated with the ground electronic state by emission of a photon. It is also possible for molecules to switch to an excited triplet state through inter-system crossing.

The electronic states of a molecule can be singlet or triplet in character. When all electrons can be paired with another electron of opposite spin, the total spin of the system is zero and the molecule is in a singlet state. When there are two unpaired electrons with the same spin, the particle is in a triplet state, since three degenerate spin states exist. While the alignment of electronic spins often causes the energy of a triplet state to be lower than a corresponding singlet state, a transition between the two states is forbidden and can only occur by inter-system crossing [65].

From the lowest vibrational level of the excited electronic singlet state, the molecule can undergo a transition to the electronic ground state by the emission of a photon. Alternatively the molecule can jump to the triplet state by inter-system crossing, a process involving the coupling of the spin and orbital angular momentum of electrons in the excited state, before relaxing back to the electronic ground state by emission of a photon; this is known as phosphorescence. The lifetime of fluorescence states is typically much shorter than phosphorescence states.

Using Raman spectroscopy, the vibrational states of organic molecules can be studied. Raman spectroscopy uses the same experimental configuration as fluorescence spectroscopy but instead measures peaks due to photons undergoing Raman scattering. Inelastic scattering of photons by organic molecules leads to a transfer of energy corresponding to a difference between vibrational energy levels of the sample, the resulting shift is measured as a wavenumber ( $\text{cm}^{-1}$ ). Raman spectroscopy is a useful tool in measuring the structure of molecules and the presence of strain, but the low cross sections for Raman scattering mean that it is difficult to measure Raman spectra without damaging monolayers of organic molecules.

Fluorescence can be studied using spectroscopic techniques which measure the intensity and wavelength of light emitted from a sample. In order to produce excited states within a sample, a source of photons with energy greater than the excitation energy of the sample is required. This can be achieved using lasers, which are a source of coherent and monochromated light with a narrow spatial distribution. In diffraction-limited systems, lasers can be projected onto a sample surface with spot sizes of less than 1  $\mu\text{m}$ . The power and monochromation of lasers can be further controlled using filters. One drawback of using a laser excitation source is that the emission wavelength is commonly fixed. In this work, frequency doubled ND-YAG (532 nm), argon ion (488 nm), and delta diode (405 nm) lasers have been used as excitation sources.

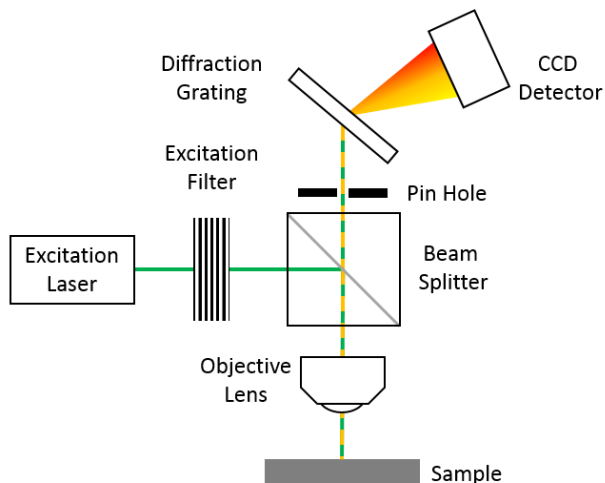


**Figure 3.2.2.** In fluorescence microscopy, an excitation laser is filtered using a high pass filter and directed onto a sample using a beam splitter. The light is focused onto the sample using an objective lens which also collects light from the sample surface. The reflected light from the sample is then directed on to a diffraction grating. The position of the diffraction grating is calibrated so that light within a given wavelength interval lands on each pixel of the CCD detector.

To measure fluorescence spectra, light from an excitation source is directed onto the sample through a beam splitter and focussed using an objective lens. Fluorescent light from the sample is collected by the objective and passed to a spectrometer via the beam splitter and a pin hole. The rudimentary configuration of a spectrometer is shown in figure 3.2.2. In order to measure the fluorescence spectra exclusively from the sample surface, a confocal system

is necessary. Confocal microscopy techniques use pinholes at the focal point of the objective lens in order to exclude light that does not originate from the focal plane of the objective. The use of pin holes in fluorescence microscopy yields a greater degree of surface specificity and offers the possibility of depth profile measurements.

In the arrangement used in this thesis, reflected light from the sample is directed to a spectrometer, typically a series of reflective diffraction gratings. By changing the orientation of the diffraction grating, the wavelength of light incident on a particular area of a CCD detector can be controlled. By calibrating the grating position so that the wavelength of light incident on each CCD pixel is known, it is possible to measure fluorescence spectra. Important parameters that must be optimised in the acquisition of fluorescence spectra are the laser power, excitation energy and acquisition time (the time the CCD detector accumulates counts for each grating position). In this work, a Horiba LabRAM HR spectrometer with an excitation wavelength of 532 nm was used to acquire fluorescence spectra. The laser power was restricted to values of the order of 10  $\mu$ W to reduce sample burning over acquisition times of between 5 and 10 seconds.

Using a cryostat, fluorescence spectra can be measured at low temperatures. At low temperatures, the width of fluorescence peaks decreases due to reduced thermal line-broadening. By comparing fluorescence measurements taken at room temperature and cryogenic temperatures, the temperature dependence of fluorescence can also be investigated. In this work two different cryostats, using liquid nitrogen and liquid helium respectively, were used in conjunction with a Horiba LabRAM HR spectrometer fitted with long working distance objective lenses.

Fluorescence microscopy can also be used to map fluorescence laterally across a sample surface. One way this can be done is by measuring fluorescence spectra from multiple positions across the sample using a motorised stage. Information such as the fluorescence

intensity within a given interval or the position of peaks can then be used to build a false-colour image of the sample. This method is useful since full spectra are acquired at each image pixel, however the technique is very slow. Depending upon the size of the map and the time taken to acquire single spectra, a map can take over 12 hours to acquire.

Fluorescence can also be mapped laterally using confocal scanning fluorescence microscopy. Confocal scanning fluorescence microscopy uses a mirror to modulate the position of a laser spot. By controlling the position of the mirror, the laser can be made to quickly and accurately to scan over the sample surface. Fluorescent light from the sample is collected by the objective lens and directed to a spectrometer via a beam splitter and pin-hole. The spectrometer is calibrated so that only light within a specified bandwidth is transmitted to a photomultiplier tube, used to measure weak and rapidly fluctuating fluorescence signals. The setup of a confocal scanning fluorescence microscope is shown in figure 3.2.3. Using confocal scanning fluorescence microscopy, fluorescence spectra can be extracted from multiple images acquired at a sequence of bandwidths. In appendix 2, a Leica TCS SP confocal scanning fluorescence microscope has been used to map the distribution of fluorescent molecules on hBN and record their spectra.

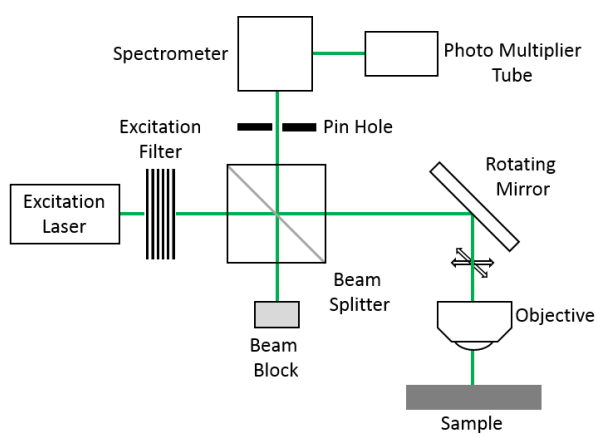


**Figure 3.2.3.** Confocal scanning fluorescence microscopy is used to project a laser spot onto a surface using a motorised mirror. By altering the deflection of the mirror, the position of the laser spot can be controlled. Light from the sample is collected by an objective lens. The spectrometer is used as a filter so that only wavelengths within a specified range reach a photomultiplier tube.

### 3.3. Substrate Preparation

In this work, hBN is used as a substrate for the growth of organic thin films. In order to grow high-quality and flat lying thin films of organic molecules, hBN substrates must be atomically flat and free from contamination. Hexagonal boron nitride (hBN) can be synthesised in a high temperature-high pressure environment, producing sub-millimetre sized crystallites [94]. In this work, hBN crystallites are mechanically exfoliated and deposited onto various substrates. In order to mechanically exfoliate hBN, a small amount of material is placed on Scotch<sup>TM</sup> tape. The tape is then repeatedly adhered to itself and peeled away, causing the mechanical cleavage of the hBN crystallites. The hBN loaded tape is adhered to the desired substrate before being peeled away to leave hBN flakes on the surface, the mechanical exfoliation process is shown in figure 3.3.1.

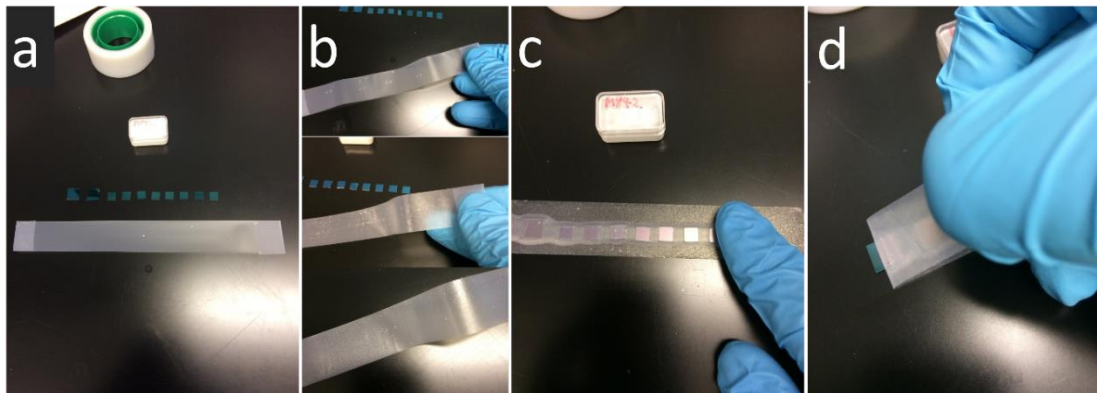


**Figure 3.3.1.** The mechanical exfoliation of hBN. A small amount of hBN is placed on Scotch<sup>TM</sup> tape (a) before it is mechanically exfoliated (b). The tape is then applied to scribed 300 nm SiO<sub>2</sub>/Si substrates (c) before the tape is very slowly peeled away (d).

hBN flakes, mechanically exfoliated and deposited onto thermally oxidised 300 nm silicon dioxide on silicon (300 nm SiO<sub>2</sub>/Si) are large enough to be seen using optical microscopy, with typical lateral dimensions of between 10 and 100 µm and thicknesses ranging from approximately 5 to 100 nm. The apparent colour of individual hBN flakes is due to interference effects from the hBN/Air, hBN/SiO<sub>2</sub> and SiO<sub>2</sub>/Si interfaces [95]. Using optical microscopy, the

presence of tape residue as well as cracks and wrinkles of flakes can be checked. An optical image of a hBN flake on 300 nm SiO<sub>2</sub>/Si is shown in figure 3.3.2. Where necessary, the coverage of hBN flakes may be increased by exfoliating onto SiO<sub>2</sub>/Si substrates held at elevated temperatures or by plasma treating substrates prior to exfoliation.

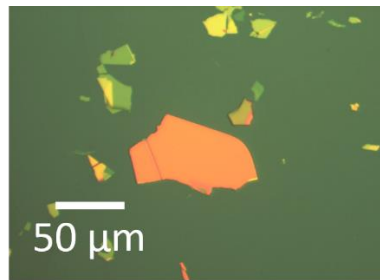


**Figure 3.3.2.** An image of a hBN flake on 300 nm SiO<sub>2</sub>/Si acquired using optical microscopy.

After mechanical exfoliation and deposition, substrates with hBN flakes must be cleaned in order to remove residue from the Scotch<sup>TM</sup> tape. This can be done using two different methods; flame-annealing and furnace-cleaning. Flame-annealed samples are heated from the reverse (non-polished) face of the SiO<sub>2</sub>/Si substrate using a butane gas torch. Furnace-cleaned samples are placed in toluene for 12 hours before they are dried with a nitrogen gun and placed inside a tube furnace. The tube furnace heats samples to 400 °C for 8 hours in an atmosphere of 5% hydrogen: 95% argon, the cleanliness of hBN substrates can then be checked using AFM. Figure 3.3.3 shows the morphology of a mechanically exfoliated hBN flake before and after flame-annealing, the roughness seen in the second image of cleaned hBN is due to topography of the underlying SiO<sub>2</sub> substrate.

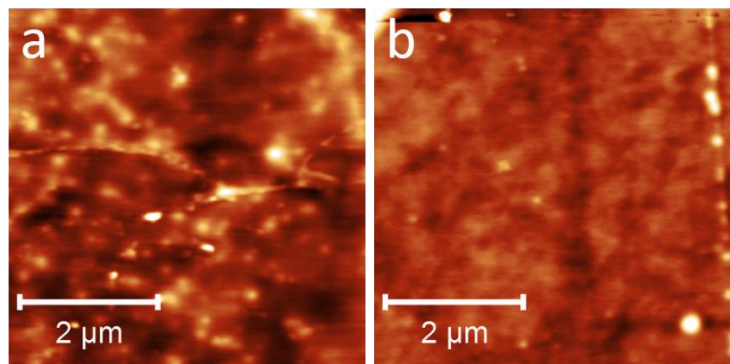


**Figure 3.3.3.** AFM images, shown with the same scale height scale (2 nm), of a mechanically exfoliated hBN flake on 300 nm SiO<sub>2</sub>/Si before (a) and after (b) flame-annealing.

As well as 300 nm SiO<sub>2</sub>/Si substrates, differing SiO<sub>2</sub> thicknesses (including native silicon dioxide), mica, thermally evaporated chromium on SiO<sub>2</sub> and gold on mica have been used as substrates for hBN flakes. In the case of the native oxide surface of silicon and thermally evaporated chromium, low tack semiconductor dicing tape is used in order to obtain a higher coverage of flakes. In the case of exfoliable surfaces such as mica and gold on mica, Scotch™ tape loaded with hBN flakes was applied to the surface before being placed in toluene for 12 hours. Through immersion in toluene, the Scotch™ tape adhesive was dissolved, leaving hBN flakes which could be cleaned by flame-annealing or furnace-cleaning.

### 3.4. UHV and Sublimation

By heating organic material in ultra-high vacuum (UHV), organic and metallic thin films may be grown on surfaces. Pressures in the ultra-high vacuum (UHV) range are required to produce high quality films, in order to reduce the incorporation of contaminant species in the film, to ensure there is an uninterrupted path to the substrate surface and to prevent chemical reactions of the source material. In this work, an ion pump, a turbo molecular pump and a scroll pump were used to pump the deposition apparatus to a base pressure of approximately  $1 \times 10^{-8}$  mbar.

The vacuum chamber used in this work contained a sample holder, two Knudsen cells, a quartz crystal microbalance (QCM) and a shutter. The sample holder, mounted on a 6" flange, could be removed after venting the chamber in order to replace the sample. Flanges housing two Knudsen cells were situated on the opposing side of the vacuum chamber. A retractable shutter was placed directly in-between the sample and Knudsen cells in order to control the amount of material deposited onto the sample surface. The deposition rate of organic molecules was measured using the QCM, placed above the sample in a position unobscured by the shutter. The configuration of the apparatus is depicted in figure 3.4.1.

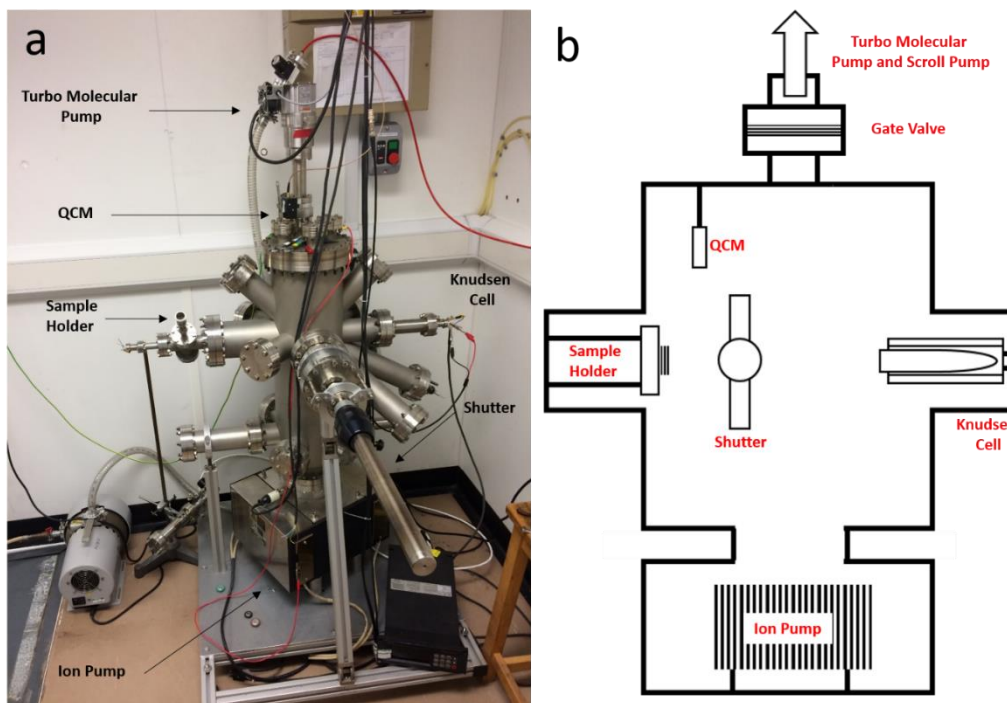


**Figure 3.4.1.** A photograph of the UHV deposition system (a), with the positions of the sample holder, Knudsen cell, QCM and shutter shown in addition to the ion pump and turbo molecular pump. On the right, a diagram shows the configuration of the components within the chamber (b).

In order to deposit a monolayer of organic molecules, clean hBN on SiO<sub>2</sub> samples were loaded onto the sample holder before the system was pumped down to its base pressure overnight. Once the system had reached  $1 \times 10^{-7}$  mbar, the sample was annealed to approximately 450 °C by passing a current through a tantalum strip beneath the sample. The sample temperature

was measured using a type C thermocouple, the configuration of the sample holder is shown in figure 3.4.2.

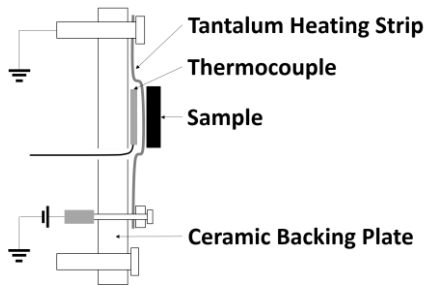


**Figure 3.4.2.** The sample holder used in the vacuum chamber consists of a ceramic plate which holds a tantalum strip. One half of the tantalum strip is connected to a power supply while the other is connected to the chamber walls, which are earthed. The temperature is measured by a thermocouple below the tantalum strip.

Annealing the sample in vacuum before the growth of organic thin films was carried out to remove any contaminant species from the substrate surface. Figure 3.4.3 shows a hBN on  $\text{SiO}_2$  substrate with a coverage of 0.4 ML of sublimed PTCDI, deposited without prior annealing in vacuum. The surface morphology suggests PTCDI has formed aggregated structures on the surface. For pre-annealed hBN, monolayer PTCDI islands were observed, see chapter 4.

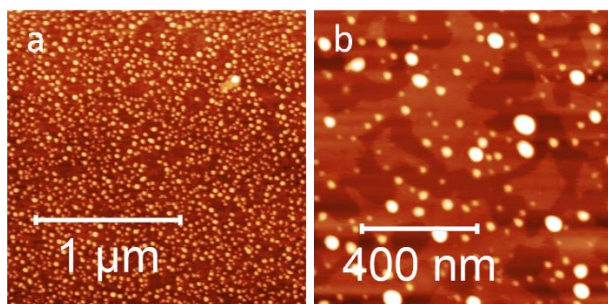


**Figure 3.4.3.** Furnace-cleaned hBN on  $\text{SiO}_2$  was placed in vacuum and a coverage of 0.4 ML of PTCDI was sublimed onto the surface without prior annealing in vacuum. Images of the sample morphology were acquired using AFM.

After annealing to 450 °C in vacuum, substrates were cooled to a specified temperature, which was maintained during growth. A Knudsen cell was heated to a stable temperature in order to give a constant deposition rate, suitable for the growth of sub-monolayer coverages of

organic molecules. Knudsen cells were held at 442 °C for the deposition of PTCDI and 374 °C for C<sub>60</sub>. The deposition rate was measured using a quartz crystal microbalance (QCM). A shutter was used to control the dose of sublimed material reaching the sample surface.

Since the QCM and sample holder are at different positions of the vacuum chamber relative to the two Knudsen cells, a tooling factor must be calculated to convert rate measured by the QCM to the rate at which material is deposited on to the substrate. This is done by depositing a thick film onto a clean SiO<sub>2</sub> substrate and comparing the thickness measured by the QCM to heights extracted from AFM images of the film. Once a stable deposition rate is reached, typically one monolayer every 5 minutes, the shutter is opened for the amount of time required to deposit the desired dose of material. Once material has been deposited onto the sample, the chamber is left to cool to room temperature before it is vented to nitrogen.

### **3.5. Conclusion**

In this chapter, the experimental methods used to acquire results in later chapters are described. The principles of AFM, used to measure the morphology of organic thin films, are described. The phenomena of fluorescence and Raman scattering are then introduced before the instrumentation used to measure these effects is discussed. The preparation of hBN samples is then described in addition to a brief introduction to the growth of organic thin films by sublimation in UHV.

# **Chapter 4:**

# **PTCDI Thin Films on Hexagonal Boron Nitride**

## **4. PTCDI Thin Films on Hexagonal Boron Nitride**

In this chapter, the growth of PTCDI on hBN substrates by sublimation in vacuum will be explored. The morphology of sub-monolayer coverages of PTCDI, deposited onto substrates held at a range of temperatures has been investigated using AFM under ambient conditions. The fluorescence of monolayer PTCDI films on hBN has been measured and a variation in the lineshape of the fluorescence spectra due to optical interference has been observed. Low temperature fluorescence and Raman measurements of PTCDI monolayers are shown and are compared to computational results available in the literature. Finally, the fluorescence of higher coverage PTCDI thin films is related to their morphology through AFM and fluorescence mapping.

### **4.1 Overview**

The perylene derivative; perylene tetracarboxylic diimide (PTCDI) has been studied by the Nottingham nanoscience group and the surface science community at large for over a decade. Monolayer PTCDI has been studied using both STM and AFM on a range of substrates, with both canted and brick wall phases reported in addition to a bi-component network, the PTCDI-melamine supramolecular network [5,38,44]. The use of conductive substrates, a requirement in the application of STM, has prevented the measurement of the fluorescence of organic thin films studied using this technique, since the fluorescence at the surface would be quenched by the underlying metal/semiconductor.

In order to study the fluorescence of molecular thin films at interfaces, an insulating substrate and a technique capable of measuring the molecular packing are required. The second requirement has been satisfied with advances in the resolution of AFM carried out under

ambient conditions, which can now be used to determine the packing of molecular monolayers on both insulating and conducting substrates.

While interest in insulating substrates for investigations of on-surface molecular self-assembly is increasing [30,32], the choice of substrates is still limited to a small number of materials including mica, alkali halides and hBN. In this work, hBN is used since it promotes the adsorption of flat-lying molecular aggregates and is atomically flat. hBN is also of great interest since it can be incorporated into van der Waals heterostructures of 2D materials, the interfaces of which could be separated or functionalised through molecular self-assembly. Finally, unlike many alkali halide substrates, hBN is not hygroscopic, so does not dissolve upon exposure to ambient conditions or water. While the adsorption of atmospheric molecules is thought to occur, the surface itself is unchanged. This is important for the academic and technological relevance of such systems, where the fabrication routes to molecular adsorbates on hBN and their stability are key considerations. In this chapter, the deposition of PTCDI on hBN by sublimation in vacuum will be discussed.

## 4.2. The Island Morphology of Sublimed PTCDI on hBN

In order to study the growth of sublimed PTCDI on hBN, mechanically exfoliated hBN on SiO<sub>2</sub> substrates were prepared using the method outlined in section 3.3. Clean hBN on SiO<sub>2</sub> was loaded into a UHV chamber fitted with a Knudsen cell, quartz crystal microbalance (QCM), shutter and a heated sample holder. In this experiment, commercially available PTCDI powder was used as a source material. Once the vacuum system had reached its base pressure (approximately  $1 \times 10^{-8}$  mbar) the Knudsen cell was heated to 442 °C, which gave a deposition rate of approximately  $1.7 \pm 0.3$  ML/min. The hBN substrate was also annealed in vacuum to 450 °C in order to remove any adsorbed contaminants due to exposure to ambient conditions.

For more details of the deposition procedure, see section 3.4.

Sublimed PTCDI grown on flame-annealed hBN at room temperature was found to form needle-like monolayer islands. This was confirmed by AFM images, from which a coverage of  $0.43 \pm 0.04$  ML and a mean major island dimension of  $1.1 \pm 0.4$   $\mu\text{m}$  were extracted, see figure 4.2.1. The  $0.3 \pm 0.1$  nm island height extracted from AFM height profiles confirms that PTCDI islands are monolayers. The fraction of the surface covered by monolayer PTCDI is in good agreement with the dose measured using the QCM. On  $\text{SiO}_2$ , PTCDI was found to aggregate into amorphous three dimensional structures.

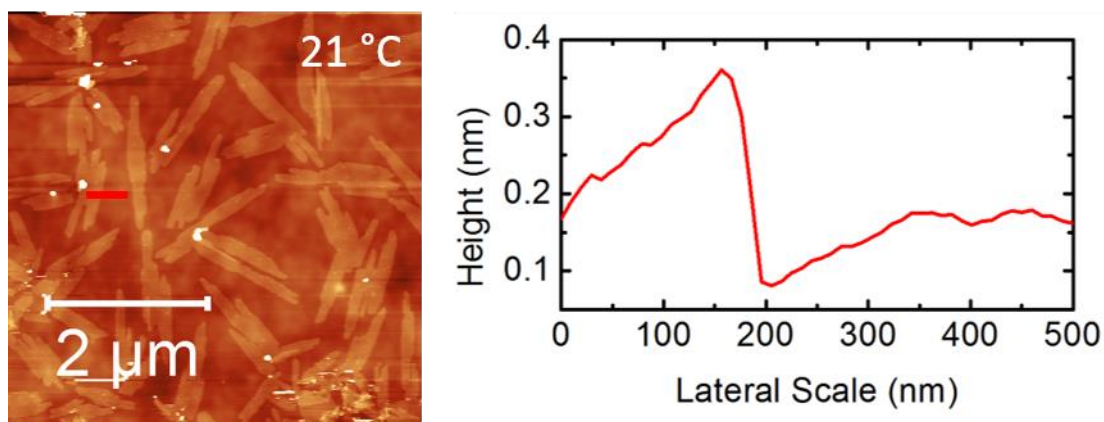


**Figure 4.2.1.** An AFM image of PTCDI grown on flame-annealed hBN on  $\text{SiO}_2$  by sublimation in vacuum. A line profile extracted from the AFM image, indicated by a red line on the AFM image (left), shows that the PTCDI islands have a height of  $0.3 \pm 0.1$  nm, corresponding to one monolayer.

One procedure which was critical in obtaining reproducible PTCDI island morphologies was to anneal the sample in vacuum prior to deposition. When this was not carried out, PTCDI was found to aggregate on the hBN surface with no observable monolayer islands. This is thought to be a consequence of exposure to ambient conditions after cleaning the sample by either flame-annealing or furnace-cleaning. The morphology of PTCDI on hBN without prior annealing in vacuum was very similar to the morphology of PTCDI on  $\text{SiO}_2$ . This suggests contaminant species, present under ambient conditions, were also present on the hBN surface and inhibited the formation of flat-lying islands of PTCDI.

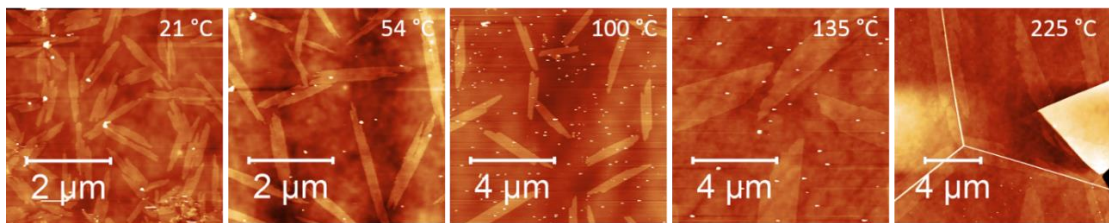


**Figure 4.2.2.** AFM images of PTCDI deposited onto flame-annealed hBN on SiO<sub>2</sub> by sublimation in vacuum for a range of substrate temperatures during deposition. As the growth temperature increases, PTCDI islands are more likely to be nucleated by folds and terraces on the hBN substrate. For the sample grown at 225 °C, folds of the hBN substrate appear as white lines in the AFM image.

In order to investigate the effect of the growth temperature on the morphology of sub-monolayer PTCDI films, a series of films were grown on flame-annealed hBN substrates at a range of temperatures, see figure 4.2.2. The dose of sublimed material was held constant across all samples, this corresponded to a coverage of approximately 0.4 ML for substrates held at room temperature. As the substrate temperature during deposition was increased, the size of PTCDI islands was found to increase while features such as the appearance, aspect ratio and the occurrence of additional layers of PTCDI did not change.

As the temperature was further increased, the sticking coefficient, the amount of material observed on the surface upon formation of a thin film relative to the amount deposited, decreased. Nucleation at defects such as on-surface contamination, terraces, folds and creases of the hBN substrate was found to be more significant at higher temperature. Comparing the morphology of PTCDI grown on both flame-annealed and furnace-cleaned substrates, slight differences in the appearance of monolayer PTCDI islands were observed but the mean major island dimension ( $1.3 \pm 0.4 \mu\text{m}$ ) of PTCDI grown at room temperature on furnace-cleaned samples was found to be comparable. The morphology of PTCDI films, with a coverage of 0.4 ML, on furnace-cleaned hBN on SiO<sub>2</sub>, grown at room temperature and 142 °C are shown in figure 4.2.3.

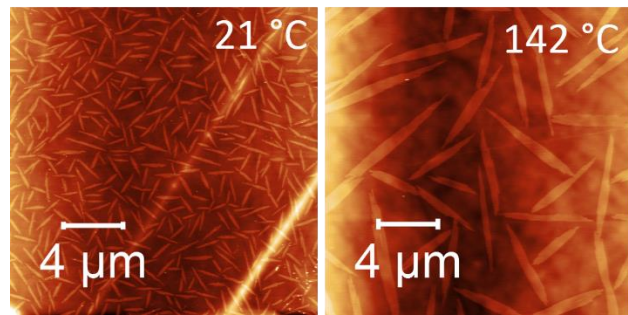


**Figure 4.2.3.** AFM images of PTCI grown by sublimation in vacuum on furnace-cleaned hBN on  $\text{SiO}_2$ , held at room temperature and 142 °C.

Differences in the morphology of islands on furnace-cleaned and flame-annealed substrates are thought to occur due to differing cleaning procedures, see figure 4.2.2 and 4.2.3, the presence of contamination or damage to the surface would introduce defects from which islands could be nucleated.

By comparing samples grown at a range of temperatures using the two cleaning techniques, differences due to sample preparation were found to be smaller than differences arising from depositing films with the substrate held at elevated temperatures. Figure 4.2.4 shows the mean major and minor island dimensions of films on both furnace-cleaned and flame-annealed substrates, all films were grown with 0.4 ML coverage. Comparing the major and minor island dimensions of monolayer PTCI gives an aspect ratio of  $0.15 \pm 0.06$  which had no discernible temperature dependence over the range considered in this investigation.

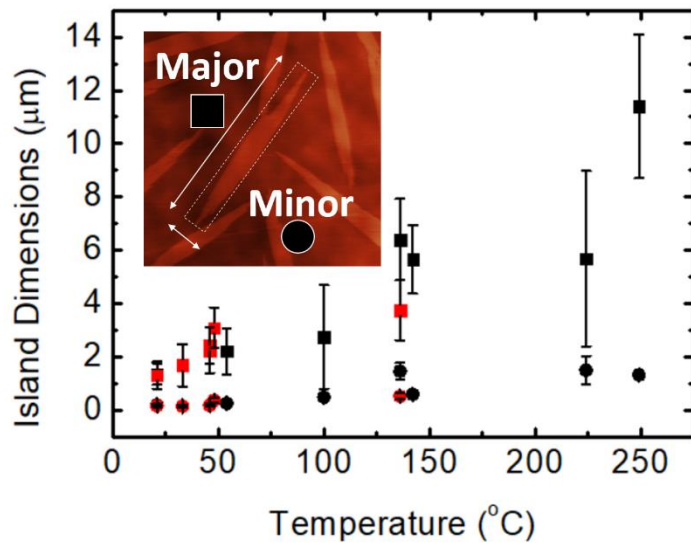


**Figure 4.2.4.** The mean major (squares) and minor (circles) dimensions of PTCDI islands was extracted from AFM images of samples grown at a range of temperatures on both flame-annealed (black) and furnace-cleaned (red) substrates. The major and minor (length and width) dimensions are also indicated (inset).

In figure 4.2.5, both the coverage and island density are plotted for a range of substrate temperatures during deposition, this was carried out for both flame-annealed and furnace-cleaned samples. As the substrate temperature increases, a reduction of the coverage is observed, the island density was also found to decrease, see figure 4.2.5b.

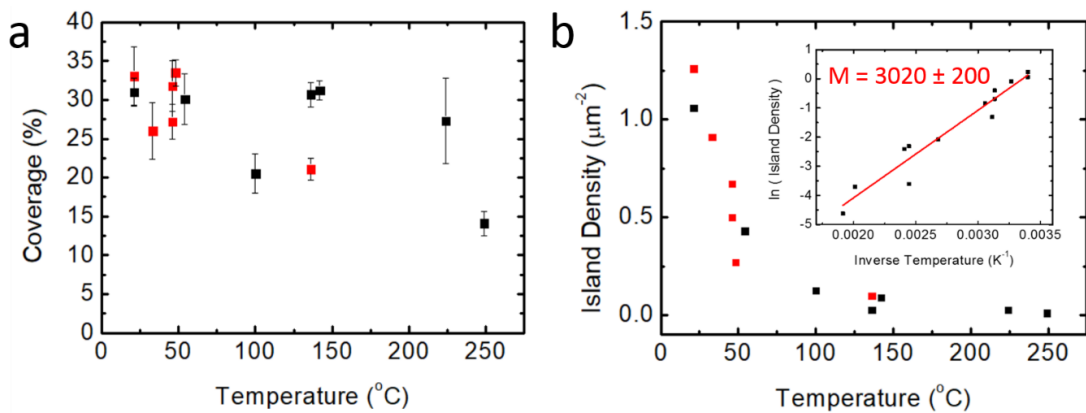


**Figure 4.2.5.** The coverage (a) and island density (b) of PTCDI islands was extracted from AFM images of samples grown at a range of temperatures on both flame-annealed (black) and furnace-cleaned (red) hBN substrates.

The island morphology of sub-monolayer coverages of organic molecules is influenced by a number of parameters including the adsorption energy and diffusion barrier for a molecule on the substrate, the binding energy of molecular aggregates and the energy available to molecules to overcome these barriers, which is directly related to the substrate temperature. The sticking coefficient of PTCDI on hBN is thought to be close to 1 at room temperature, the growth is therefore said to be in the complete condensation regime, in which molecules remain bound on the surface for a time,  $\tau_a$ , much greater than the capture time,  $\tau_c$ , the average time for molecules to diffuse to join stable pre-formed islands.

By solving the rate equations, discussed in section 2.2, for isolated molecules and clusters on a substrate surface, the functional dependence of the nucleation density on parameters such as substrate temperature and the diffusion barrier can be established. In the complete condensation regime ( $\tau_a \gg \tau_c$ ), the nucleation density,  $n$ , is given by equation 4.2.1, where  $R$  is the deposition rate,  $E_d$  is the diffusion barrier,  $E_i$  is the critical cluster energy,  $i$  is the critical cluster size and  $T$  is the substrate temperature [18].

$$n = R^{\frac{i}{i+2}} \exp\left(\frac{E_i + iE_d}{(i+2)k_B T}\right) \quad (4.2.1)$$

Assuming a constant deposition rate, critical cluster size and diffusion barrier, the decrease in the island density at higher temperatures is in good qualitative agreement with the expected behaviour for sub-monolayer films in the complete condensation regime, see figure 4.2.5b. By fitting the island density plotted in figure 4.2.5b with a function of the form of equation 4.2.1, an estimate for the term  $(E_i + iE_d)/(i+2)$  of  $0.26 \pm 0.02$  eV was extracted. Assuming a critical cluster size of 2, in which PTCDI dimers are stable at room temperature, a diffusion barrier of  $0.27 \pm 0.02$  eV is extracted. This calculation was carried out using calculated values for the intra-row binding energy of PTCDI molecules (-0.5 eV), available in reference [44]. Unfortunately, in this work, it was not possible to determine the critical cluster size experimentally.

Equation 4.2.1 does not include the effect of features such as contamination and step edges, which have been shown to act as nucleation sites for PTCDI grown at higher temperatures, see figure 4.2.2. These features are only significant at higher temperatures, where the nucleation density is thought to be comparable to the density of inhomogeneities on the surface, which dominate nucleation.

The increase in both the major and minor island dimensions at higher temperature, see figure 4.2.4, is a consequence of the decreased nucleation density. For PTCDI on hBN, it is assumed that the capture time is much smaller than the corresponding nucleation and adsorption times. In this regime, the nucleation density of the film is established during the initial stages of growth. Any subsequently deposited molecules are then more likely to diffuse to pre-formed islands than form new islands through nucleation events. Lower nucleation densities at higher temperatures therefore lead to larger islands for a given dose of material.

In order to understand the growth of PTCDI monolayers on hBN, the effect of both intermolecular interactions and interactions with the substrate must be considered. In many cases, molecules have preferred binding sites and orientations with respect to the substrate [43]. Measuring the relative orientation of both the substrate and an adsorbate can be done through diffraction techniques such as transmission electron microscopy (TEM) or low energy electron diffraction (LEED), as well as STM and AFM. Since hBN flakes are insulating, of the order of tens of microns in size, not continuous over a surface and placed upon a substrate, it was not possible to measure the island orientation through diffraction techniques. Instead, the orientation of the major axis of PTCDI islands on a single crystal was extracted from AFM images and plotted as a histogram with a bin size of 5°, the distribution of island orientations from PTCDI deposited onto furnace-cleaned hBN at room temperature is shown in figure 4.2.6.

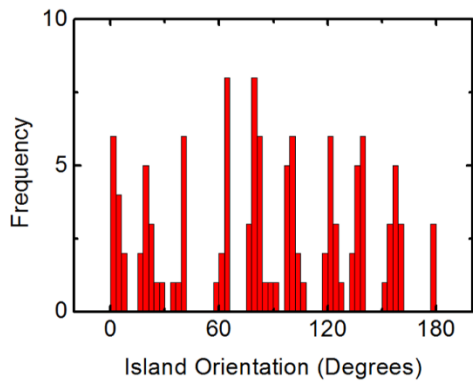


**Figure 4.2.6.** The orientation of the major axis of needle-like PTCDI islands grown on furnace-cleaned hBN on SiO<sub>2</sub> at room temperature is shown. The distribution uses values extracted from AFM images and binned into channels with a width of 5°.

Assuming that both the individual islands and the underlying hBN substrate were single crystals and that the direction of the major axis of needle-like PTCDI islands was a manifestation of the crystal structure of the aggregate, the presence of 9 distinct peaks in the orientation distribution indicates a number of preferred adsorption sites for PTCDI on hBN. This could arise due to both on-axis and off-axis alignments of PTCDI with respect to the underlying hBN substrate.

In order to understand the morphology of sublimed PTCDI islands on hBN, it is important to consider their molecular packing, which can be determined using AC-mode AFM under ambient conditions, see figure 4.2.7. Initially, contact mode AFM was used but PTCDI was found to be removed from the surface due to the interaction with the tip.

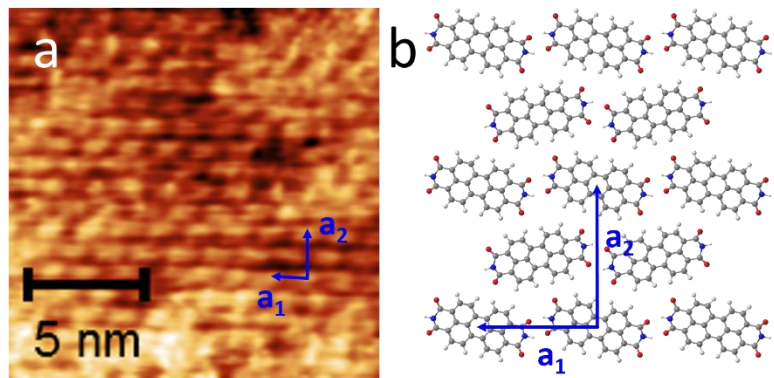


**Figure 4.2.7.** A high resolution AFM image of PTCDI on hBN on  $\text{SiO}_2$  (a), the intra- ( $a_1$ ) and inter- ( $a_2$ ) row lattice vectors are indicated in blue. A diagram showing the structure of the canted PTCDI phase is also shown with lattice vectors indicated (b).

From the AFM images, obtained with the assistance of Dr Vladimir Korolkov and shown in figure 4.2.7, lattice parameters of  $1.4 \pm 0.1$  nm ( $a_1$ ) and  $1.8 \pm 0.1$  nm ( $a_2$ ) were extracted for the intra-row and inter-row separations respectively. The packing structure observed on hBN is in good agreement with the canted structure of PTCDI described by Mura et al [44], with lattice parameters of 1.38 nm (1.45 nm) and 1.67 nm (1.75 nm), extracted from STM measurements on Au (111) (values in parentheses are the corresponding DFT estimates from the same work).

The high resolution images of sublimed PTCDI on hBN show some areas of lower resolution. These features have a higher topography which suggests additional material is present on the surface of PTCDI islands. Possible origins of this material include additional layers or disordered PTCDI, contamination from ambient conditions, or material displaced due to interactions with the tip. Comparing multiple AFM images showing the internal structure of sublimed PTCDI islands, areas of an island where the monolayer appears uncovered are much more abundant than areas with additional material. In chapter 5 it will also be shown that similarities in the fluorescence spectra of sublimed and solution deposited PTCDI imply the additional material does not affect the fluorescent properties of the PTCDI monolayer.

The needle-like island morphology of sublimed PTCDI is expected to occur due to the relative interaction energy of inter-row and intra-row bonding. Intra-row bonding is much stronger in the canted PTCDI structure as it is primarily facilitated by hydrogen bonding of adjacent carboxyl-diimide groups [44]. A needle-like morphology is seen since PTCDI molecules are able to diffuse to intra-row binding sites with stronger interaction energy.

### 4.3. The Fluorescence of Sublimed PTCDI on hBN

The optical properties of sub-monolayer PTCDI films on hBN, deposited by sublimation in vacuum, were studied using fluorescence microscopy, as described in section 3.2. In this section, all samples were grown on hBN at room temperature with a coverage of 0.4 ML, which gave monolayer islands. The fluorescence of PTCDI on hBN on a thermally oxidised 300 nm SiO<sub>2</sub>/Si substrate, measured using a 532 nm excitation laser, is shown in figure 4.3.1. The fluorescence spectra of sublimed PTCDI monolayers on hBN share many similarities with those of PTCDI monomers and monomer derivatives, both in solution and in helium nano-droplets (HND) [71,96].

Similarities between the spectral features of PTCDI monolayers and monomers suggests that phenomena such as collective excitations and coupling of electronic and vibrational modes do not have a significant effect on the lineshape of the spectrum [97]. The peak at  $2.208 \pm 0.002$  eV is attributed to the 0-0 transition, with the satellite peak at  $2.045 \pm 0.002$  eV, the 0-1 vibronic peak. Upon further comparison of the fluorescence of PTCDI monolayers on hBN with measurements of dimethyl-PTCDI (Me-PTCDI) doped helium nano droplets (HND) carried out by Wewer and Stienkemeier [71], a red shift of  $0.342 \pm 0.002$  eV is determined between measurements of Me-PTCDI doped HND and sublimed PTCDI monolayers. Given the weak polarisability of superfluid HND, fluorescence measurements of doped HND are taken to be

'gas phase' measurements. The origin of this red shift will be examined in greater detail in chapter 5.

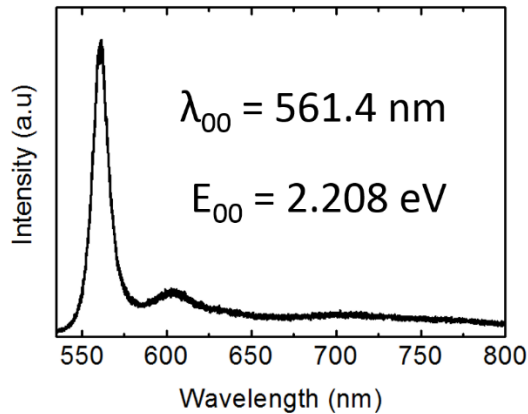


**Figure 4.3.1.** Fluorescence spectra of PTCDI grown on flame-annealed hBN on SiO<sub>2</sub> at room temperature. Acquired using a 532 nm excitation laser.

When comparing the fluorescence spectra of PTCDI monolayers on different hBN flakes on SiO<sub>2</sub>/Si, a variation in the lineshape of PTCDI was observed. On different hBN flakes, the ratio between the main peak at  $2.208 \pm 0.002 \text{ eV}$  ( $561.4 \pm 0.5 \text{ nm}$ ) and the vibronic peak at  $2.045 \pm 0.002 \text{ eV}$  ( $606.3 \pm 0.5 \text{ nm}$ ) was found to vary. While the fluorescence lineshape of PTCDI monolayers was found to vary on different hBN flakes, the island morphology on a range of flakes was investigated using AFM and found to be comparable.

Comparing measurements from different hBN flakes, a correlation between the lineshape of PTCDI and the colour of the flake was observed. Mechanically exfoliated hBN flakes have a distribution of flake heights which range from a few nanometres to hundreds of nanometres. Though transparent in the visible region of the spectrum, interference at the top and bottom surfaces cause hBN flakes to exhibit an apparent colour [95]. The apparent colour of a particular flake is dependent upon its thickness and the optical properties of the underlying substrate.

Figure 4.3.2 shows normalised fluorescence spectra from monolayer PTCDI islands from a range of hBN flakes on 300 nm SiO<sub>2</sub>/Si. All fluorescence spectra in this section will be plotted

against wavelength, in units of nm, in order to give a more intuitive comparison with interference effects.

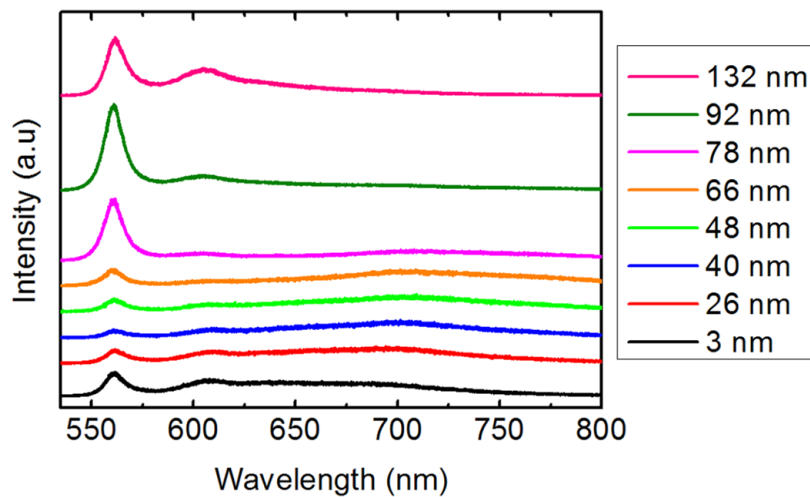


**Figure 4.3.2.** Normalised fluorescence spectra of monolayer PTCDI islands grown on hBN on  $\text{SiO}_2$  at room temperature, acquired using a 532 nm excitation laser. The normalised spectra are shown for a range of hBN flake heights, determined using AFM.

Comparing normalised spectra obtained from different hBN flakes on 300 nm  $\text{SiO}_2/\text{Si}$ , as in figure 4.3.2, the variation in the lineshape is apparent. By measuring fluorescence spectra from a range of flakes and extracting the height of each flake from AFM images, the effect of the flake height on the fluorescence lineshape could be investigated. A variation was seen between hBN flakes of different thickness, while similar fluorescence lineshapes and intensities were observed from flakes of comparable thickness.

In order to investigate the effect of optical interference on the fluorescence of PTCDI monolayers on hBN, flakes were also deposited onto thermally evaporated chromium, 50 nm  $\text{SiO}_2/\text{Si}$ , silicon and mica. Normalised fluorescence spectra from monolayer PTCDI islands on hBN on chromium, recorded from multiple flakes, are shown in figure 4.3.3. The variation in the lineshape of the fluorescence spectra on hBN on chromium substrates is much less apparent than that of 300 nm  $\text{SiO}_2/\text{Si}$  within the range of flake heights (5 nm - 150 nm) observed here.

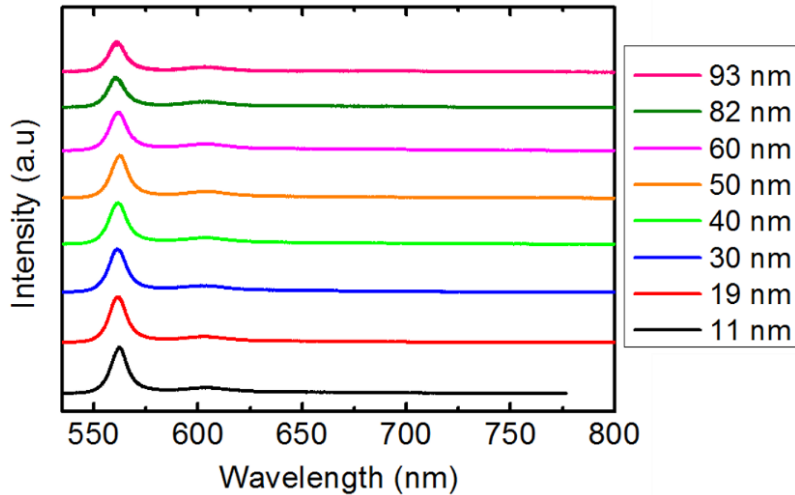


**Figure 4.3.3.** Normalised fluorescence spectra, acquired using a 532 nm excitation laser, of PTCDI on furnace-cleaned hBN on chromium were measured from hBN flakes with a range of thicknesses, determined using AFM.

In order to explain the variation in the fluorescence lineshape due to interference effects on a range of substrates, both direct calculations and the transfer matrix model were used. The structure of substrates with two (a) and three (b) interfaces is shown in figure 4.3.4. Where the structure of the substrate gave rise to two interfaces, direct calculations were used to calculate the intensity of a given wavelength of light at the hBN surface. The amplitude of the first reflected wave is given in equation 4.3.1, where  $t_{ij}$  and  $r_{ij}$  represent the transmission and reflection coefficients of the interface between the  $i^{\text{th}}$  and  $j^{\text{th}}$  layers,  $d$  is the layer thickness,  $k$  is the wave vector of light within the medium ( $2\pi n/\lambda_0$ ) and  $\phi$  is the phase change of the wave upon reflection. By summing the total amplitude of the incident wave and all multiply reflected waves, it is possible to calculate the amplitude at the hBN surface using a recursive sum. Evaluating this sum gives equation 4.3.2a and b; the total amplitude at the hBN surface as a function of the flake thickness, the wave vector and the transmission and reflection coefficients of the interfaces [98].

$$r_1 = t_{12} r_{23} t_{21} e^{i(2kd + \phi)} \quad (4.3.1)$$

$$r_{\text{total}} = 1 + r_{12} + \frac{t_{12} t_{21}}{r_{21}} \left( \frac{s}{1-s} \right) \quad (4.3.2a)$$

$$s = r_{21}r_{23}e^{i(2kd+\phi)} \quad (4.3.2b)$$

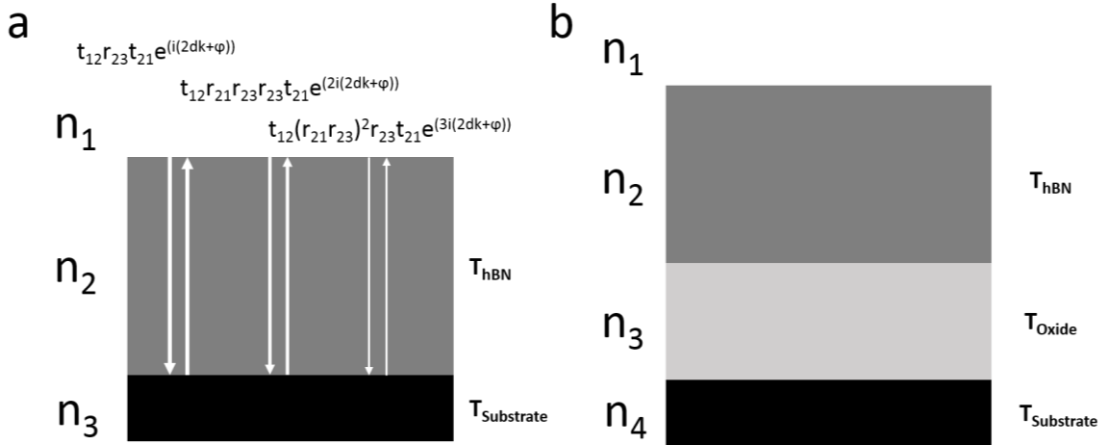


**Figure 4.3.4.** In this work, hBN has been mechanically exfoliated onto a range of substrates. In order to model the effects of optical interference, both recursive sums and the transfer matrix model were used. The structure of the cavity formed by hBN on a reflective or bulk substrate (e.g. mica) is shown by (a) while silicon dioxide substrates, containing an additional oxide layer, are illustrated by (b).

In the case of three interfaces, such as hBN on silicon dioxide, it is more complicated to form a recursive sum of all optical paths since reflections could occur within the first layer (hBN), within the second layer (silicon dioxide) or across both. The intensity was instead calculated by defining transfer matrices for each layer [98], as shown in equation 4.3.3, where  $d$  is the layer thickness,  $n$  is the refractive index of the layer and  $k$  is the wavevector of the incident light within the medium. The substrate is then described by the product of the two transfer matrices, corresponding to media with different thicknesses and refractive indices. The reflectivity of the substrate is then given by equation 4.3.4, where  $t_{ij}$  is the element  $(i,j)$  of the total transfer matrix,  $n_a$  is the refractive index of air and  $n_b$  that of the underlying substrate (in this case silicon).

$$T = \begin{pmatrix} \sin(kd) & \frac{i}{n} \sin(kd) \\ i n \sin(kd) & \cos(kd) \end{pmatrix} \quad (4.3.3)$$

$$r_{\text{total}} = 1 + \frac{2n_b t_{11} - 2t_{21}}{n_b(n_a t_{12} - t_{11}) + t_{21} - n_a t_{22}} \quad (4.3.4)$$

The intensity of the fluorescence peak of PTCDI is modelled by calculating the product of the intensity (the square of 1 plus the reflection coefficient) at the fluorescence wavelength ( $561.4 \pm 0.5$  nm) and the wavelength of the excitation source. The lineshape of PTCDI is modulated by the interference intensity across the spectral range. Characterising the lineshape by the ratio of the main and vibronic peaks at  $561.4 \pm 0.5$  nm and  $606.3 \pm 0.5$  nm, it is possible to compare the modelled and experimentally observed lineshape variation. Figure 4.3.5a shows the expected variation in absolute intensity of a fluorescence peak at 560 nm measured using a 532 nm excitation laser, while figure 4.3.5b shows the ratio of two peaks at 560 nm and 610 nm for hBN on  $\text{SiO}_2/\text{Si}$  with 300 nm, 50 nm and 5 nm oxide thicknesses.

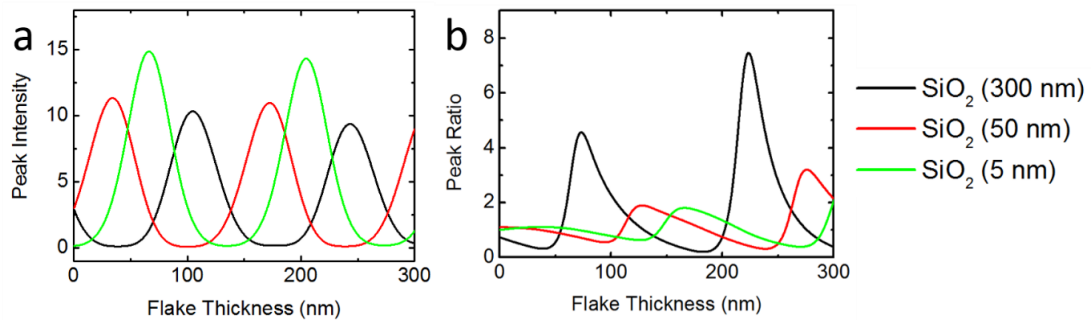


**Figure 4.3.5.** The intensity of a fluorescence signal of wavelength 560 nm and excited by a 532 nm source was modelled using transfer matrices. The layers modelled consisted of fluorescent molecules on hBN on a set thickness of  $\text{SiO}_2/\text{Si}$ . The intensity of the 560 nm signal (a) and the ratio between peaks at 560 and 600 nm (b) are plotted for 5 nm, 50 nm and 300 nm oxide thicknesses.

The intensity and lineshape variation of PTCDI monolayers on hBN was investigated by measuring fluorescence spectra from a number of flakes on a range of substrates. For each sample, acquisition parameters such as the laser power, acquisition time and accumulation were kept constant while low laser powers (in the range of units and 10s of  $\mu\text{W}$ ) were chosen to reduce sample damage and photo bleaching. In this investigation, 532 nm and 405 nm lasers were used in conjunction with long working distance 50X objective lenses. The area of the sample illuminated by a maximally focused laser is diffraction-limited, the minimum spot

size,  $D$ , is given by equation 4.3.5, where  $\lambda$  is the wavelength of the laser and  $NA_{Obj}$  is the numerical aperture of the objective lens. In this experiment, spot sizes in excess of  $1 \mu\text{m}$  were used.

$$D = \frac{0.61\lambda}{NA_{Obj}} \quad (4.3.5)$$

In order to minimise the impact of variations in the signal due to local variations in the coverage of monolayer PTCDI islands, all samples were grown at room temperature. This was done in order to utilise the higher island density seen in these samples. The fluorescence intensity of the  $561.4 \pm 0.5 \text{ nm}$  peak as well as the ratio of the main and vibronic peaks were extracted by fitting fluorescence spectra to sets of Lorentzian curves. Figure 4.3.6 shows the variation of the fluorescence intensity and peak ratio of PTCDI on hBN on  $300 \text{ nm SiO}_2/\text{Si}$  with hBN flake height.

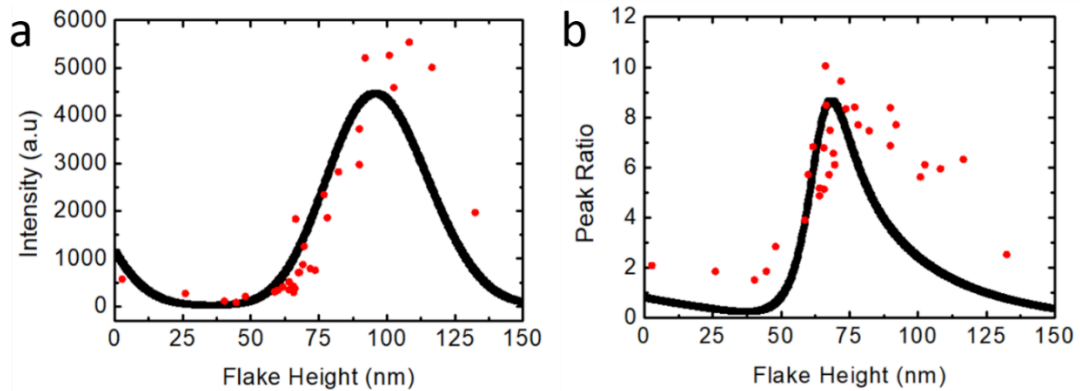


**Figure 4.3.6.** Fluorescence spectra of PTCDI grown on hBN on  $300 \text{ nm SiO}_2/\text{Si}$  were acquired using a  $532 \text{ nm}$  excitation laser. The Peak properties were then extracted by fitting to multiple Lorentzian curves. The 0-0 peak intensity is shown plotted against the hBN flake height (a) as is the ratio between the 0-0 and 0-1 vibronic peaks (b). Flake heights were extracted from AFM images.

For PTCDI on hBN on  $300 \text{ nm SiO}_2/\text{Si}$ , the dependence of the intensity of the  $561.4 \pm 0.5 \text{ nm}$  fluorescence peak and peak ratio upon the flake height was plotted and fitted to the modelled intensity variation (calculated using the transfer matrix method). The dependence of the peak height of the fluorescence spectra on the height of hBN flakes is in good agreement with that

predicted by the transfer matrix model. While there is good agreement between analytical calculations and experimental measurements of the flake height at which the maximum peak ratio is observed, the agreement is poor for flake heights below 50 nm. This is thought to occur due to the poor signal to noise ratios at peak heights below 50 nm.

Substrate	Flake Height At Maximum Intensity: Experiment (nm)	Flake Height At Maximum Intensity: Model (nm)
<b>300 nm SiO<sub>2</sub>/Si *</b>	106 ± 10	104.3
<b>50 nm SiO<sub>2</sub>/Si *</b>	21 ± 10	33.9
<b>Si (native oxide) **</b>	57 ± 5	63.1
<b>Mica</b>	129 ± 5	128.4
<b>Chromium</b>	33 ± 5	54.6 ***

\*All SiO<sub>2</sub>/Si substrates were thermally deposited commercially available wafers with a 5% tolerance.  
\*\* Silicon wafer had a native oxide thickness which was not considered in the interference model.  
\*\*\*The interference model did not take into account the error in flake height measurement due to surface reactions during substrate preparation.

**Table 4.3.1.** The fitted experimental results (acquired using a 532 nm laser) and models of the hBN flake heights which give the greatest intensity of the  $561.4 \pm 0.5$  nm PTCDI monolayer peak are shown for various substrates. The transfer matrix method was used for SiO<sub>2</sub> substrates while the analytical model was used for all others.

The dependence on the fluorescence intensity and lineshape was also investigated for 50 nm SiO<sub>2</sub>/Si, Si, mica and chromium substrates. These results are discussed in detail in appendix 1 and summarised in table 4.3.1. Taking into account significant sources of error such as variations in the height of flakes themselves, variations in the thickness of thermally oxidised SiO<sub>2</sub> substrates and changes to the surface topography due to a reactive surface (chromium), experimentally determined variations in the fluorescence intensity with hBN flake height are in good agreement with interference models. Similarly, optical interference has been shown to account for the variation of the lineshape observed in these samples, for further discussion of these results, see appendix 1. This effect is distinct from reported changes in the ratio of

the 0-0 and vibronic peaks due to H- and J-aggregation [99] or  $\pi$ -stacking [100,101] of fluorophores.

Interference effects have been demonstrated to affect the intensity of fluorescence in a number of systems. In reference [74], the Nottingham nanoscience group observed a similar flake height dependence for the fluorescence intensity of a porphyrin derivative on hBN, due to interference of both 532 nm and 660 nm excitation lasers. The variation in the fluorescence lineshape of PTCDI on hBN on SiO<sub>2</sub>/Si cannot be explained by optical interference of the laser source alone, and is caused by a continuous modulation of both the laser and the fluorescence signal across all points of the spectrum. Buscema et al observed the same interference effect in 2D van der Waals heterostructures containing molybdenum disulphide [102], which could be explained by comparing optical interference at both the excitation and emission wavelengths.

#### **4.4. The Optical Properties of PTCDI Monolayers on hBN at Cryogenic Temperatures**

In order to investigate the fluorescence of monolayer PTCDI on hBN more thoroughly, measurements were carried out under cryogenic conditions. Due to the fluorescent species being adsorbed at the surface of the sample, it was necessary to carry out measurements in high vacuum in order to prevent the accumulation on ice of the sample surface. Such ice build-up was observed during initial measurements with a liquid nitrogen cryostat at ambient pressures. Using a high vacuum cryostat cooled by liquid helium, fluorescence measurements were carried out using a long working distance objective through a window in the cryostat. All cryogenic measurements in this section were carried out within the Semiconductor Quantum Nanostructures group at the University of Nottingham with the assistance of Dr Nilanthy Balakrishnan.

The fluorescence of PTCDI (of 0.4 ML coverage) on hBN on chromium was measured at ambient temperatures before and after cooling. Chromium substrates were chosen given the less pronounced variation in the fluorescence lineshape between hBN flakes. Figure 4.4.1 shows fluorescence spectra from the same hBN flake for a range of temperatures. In all low temperature spectra, features at approximately 690 nm were due to the cryostat window.

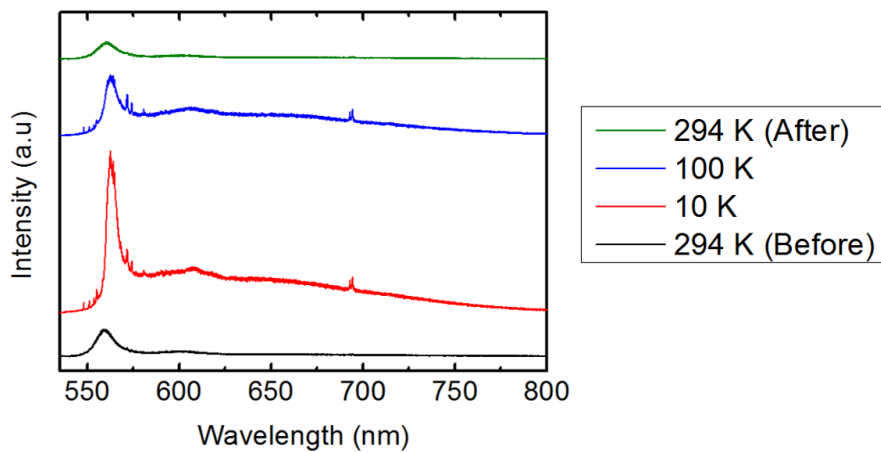


**Figure 4.4.1.** Fluorescence spectra of PTCDI on hBN on chromium, grown at room temperature, were measured using a 532 nm excitation laser. The sample temperature was controlled using a liquid helium cooled, high vacuum cryostat. At cryogenic temperatures, the fluorescence peak of PTCDI is shifted and Raman lines are observed.

Once initial measurements at room temperature were taken outside of the cryostat, samples were cooled to 10 K over approximately 2 hours to establish a stable temperature. Upon cooling to 10 K, the fluorescence peak due to the PTCDI monolayer increased in intensity and was red shifted by  $3.4 \pm 0.5$  nm ( $0.014 \pm 0.002$  eV). The full width half maximum of the main fluorescence peak was reduced to  $6.2 \pm 0.5$  nm from  $11.6 \pm 0.5$  nm. Despite the reduction in the width of the peak, phenomena such as Davydov splitting were [103] not observed; sharp lines in the fluorescence spectra were attributed to Raman modes of PTCDI. It was also noted that the structure of the vibronic side bands was modified upon cooling.

The fluorescence of the sample was measured under ambient conditions before and after cooling. The 0-0 fluorescence peak was shifted from  $559.8 \pm 0.5$  nm before to  $560.9 \pm 0.5$  nm after, and reduced in intensity by 41 % during the cooling cycle. This suggests samples were not significantly affected by cooling but, since spectra were acquired from the same area of each flake, may have been bleached by the higher laser powers required to overcome reflections and scattering from the cryostat window. As mentioned earlier, Raman peaks were observed for monolayer PTCDI islands on hBN at 10 K and 100 K. Figure 4.4.2 shows the Raman spectrum of PTCDI on hBN at 100 K, measured with increased laser power.

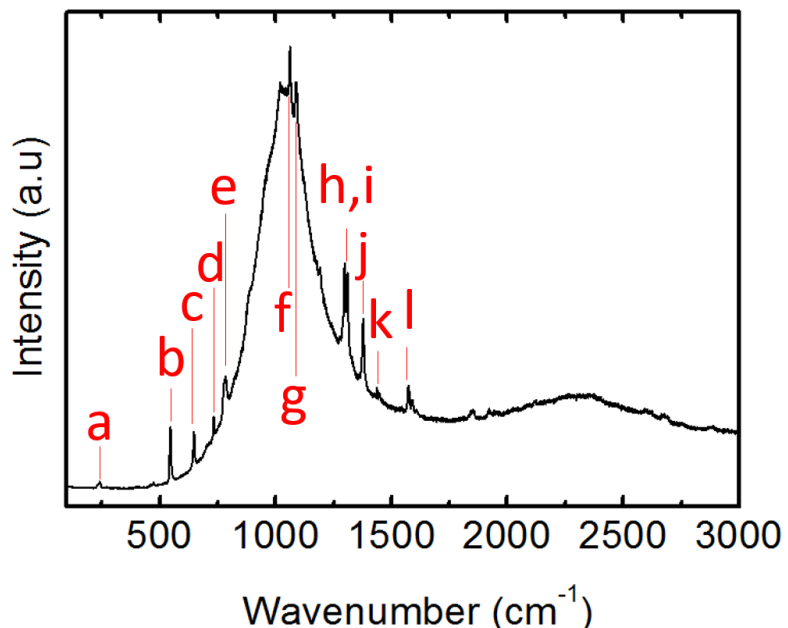


**Figure 4.4.2.** Raman spectroscopy was carried out using a 532 nm laser on PTCDI on hBN on chromium held at 100 K in a liquid helium cooled cryostat. In addition to the red-shifted PTCDI fluorescence peak, Raman lines corresponding to PTCDI are observed.

The positions of Raman peaks in figure 4.4.2 are labelled a-l and shown in table 4.4.1 alongside computational results by Chis et al [104]. Comparing the values of the Raman peaks obtained from monolayer PTCDI on hBN samples with experimental and density functional theory (DFT) investigations by Chis et al, gives good agreement for all but one of the experimentally observed peaks. All of the Raman peaks of PTCDI powder measured by Chis et al could be compared to peaks of PTCDI monolayers on hBN, which had additional peaks at 733, 782, 1089

and  $1439\text{ cm}^{-1}$ . Peaks at  $733$ ,  $782$ ,  $1089\text{ cm}^{-1}$  were comparable to calculated modes from DFT by Chis et al which were not observed experimentally in PTCDI powder, this could be due to interactions with the hBN surface.

Peak	Wavenumber: This work ( $\text{cm}^{-1}$ )	Wavenumber: Chis et al [104] ( $\text{cm}^{-1}$ )
A	232 and 242	<b>247 {252}</b> Outer Rings Rocking
B	546	<b>551 {550}</b> Lateral Stretch
C	647	<b>654 {656}</b> Central Ring Stretch
D	<b>733</b>	{733} CNC
E	<b>782</b>	{781} ring deformation
F	1062	<b>1066 {1042}</b> CH + ring deformation
G	<b>1089</b>	{1085} inner ring deformation
H	1298	<b>1285 {1275}</b> CH + CC
I	1311	<b>1302 {1290}</b> Central Ring Stretch + CH
J	1378	<b>1377 {1367}</b> CN + CH
K	1439	
L	1573 and 1590	<b>1572 &amp; 1585 {1554 &amp; 1574}</b> CC + CH & CC

**Table 4.4.1.** The values of the Raman peaks corresponding to the labels on figure 4.4.2 are shown as well as results from Chis et al [104] where experimental results, obtained from PTCDI powder, are shown in addition to DFT results, in parentheses. Values shown in red are peaks not observed in measurements of PTCDI powder by Chis et al, but are present for PTCDI monolayers on hBN and in DFT calculations.

The observation of Raman peaks was only possible under cryogenic, high vacuum conditions using higher laser powers. Such laser powers were not used under ambient conditions as they would damage the sample. The increased laser power could be the reason for the observation of Raman lines in PTCDI monolayers at  $10\text{ K}$  and  $100\text{ K}$ . While PTCDI Raman lines were observed, Raman peaks from the hBN were not seen. This is thought to be due to the relative intensities of the hBN and PTCDI Raman peaks under the conditions considered in this experiment.

## 4.5. The Morphology and Fluorescence of Multi-Layer PTCDI Films on hBN

The effect of the coverage of PTCDI on the thin film morphology was also investigated. PTCDI thin films were grown by sublimation in vacuum on flame-annealed hBN on SiO<sub>2</sub> substrates held at 135 °C for a range of coverages. After growth, samples were removed from vacuum and images of the morphology were acquired using AFM. The morphology of a range of coverages of PTCDI on hBN grown at 135 °C is shown in figure 4.5.1. As the coverage of PTCDI is increased, second layers of PTCDI form on existing islands before the completion of the first layer.

At a coverage of 0.7 ML, significant second layer regions of PTCDI are observed on top of existing islands. At coverages of 1.4 ML and 2.1 ML, islands with third layers are observed with areas of uncovered hBN in between. At coverages of 3.6 ML, four-layer islands are observed while the hBN surface is covered by a complete monolayer of PTCDI

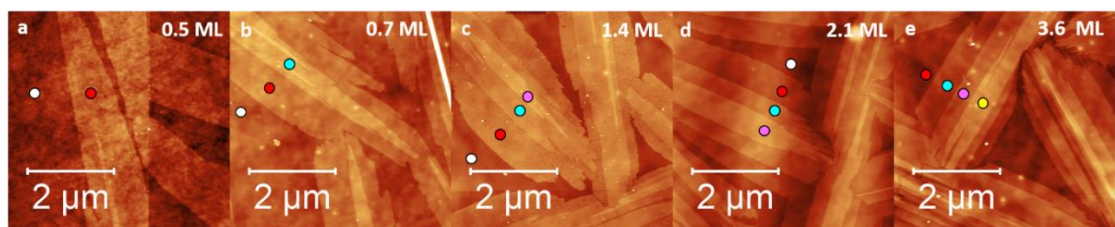


**Figure 4.5.1.** A range of coverages of PTCDI were grown on flame-annealed hBN on SiO<sub>2</sub> held at 135 °C during deposition. At 135 °C, PTCDI forms a second layer before the completion of the initial layer. Areas of hBN (white), monolayer (red), bi-layer (light blue), third layer (pink) and fourth layer PTCDI (yellow) are indicated by coloured circles.

The fluorescence of multi-layer molecular thin films at interfaces has been studied by a number of groups [101,105]. In such studies, the fluorescence spectra are acquired over a large area. The fluorescence of thin films is then related to their morphology. In this work, the fluorescence of PTCDI is mapped spatially in order to relate the spectral features of the fluorescence to structures within the films. Monolayers and multi-layers of PTCDI on hBN grown at 135 °C have features such as areas of monolayer or second layer PTCDI with a spatial

extent of up to 5  $\mu\text{m}$ . Using a confocal fluorescence microscope, the Horiba LabRAM HR, with a 50X objective lens, it was possible to obtain a laser spot size of approximately 1  $\mu\text{m}$ . The fluorescence microscope was also equipped with a scanning stage which enabled the fluorescence of PTCDI thin films to be mapped.

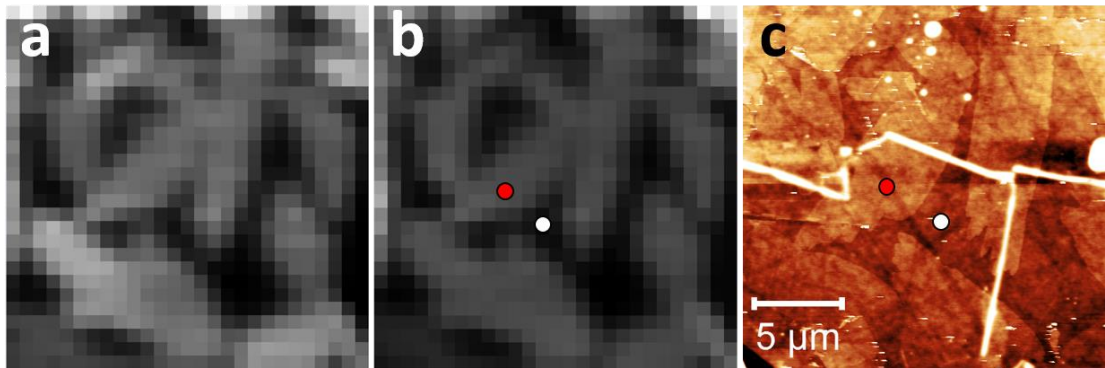


**Figure 4.5.2.** PTCDI was deposited, with a 0.7 ML coverage, on flame-annealed hBN on  $\text{SiO}_2$  by sublimation in vacuum at 135 °C. Fluorescence spectra were acquired for a grid of 27 points with a 1  $\mu\text{m}$  step size. The integrated intensity of the spectra within the intervals of 550 nm-560 nm (a) and 590 nm-620 nm (b) was used to build up an image. An AFM image of the same area of the surface is shown (c). The same monolayer PTCDI island and an area of hBN are indicated in both the AFM image and a fluorescence map by red and white circles respectively.

Fluorescence maps are produced by measuring fluorescence spectra at fixed intervals. The sample is mapped in a raster pattern, an image is then generated by extracting spectral features such as the integrated intensity within a given spectral range in order to assign pixel values. A 27  $\mu\text{m}$  fluorescence map of a PTCDI film with a coverage of 0.7 ML on hBN on 300 nm  $\text{SiO}_2/\text{Si}$  is shown in figure 4.5.2 alongside AFM images from the same area. This sample was found to contain monolayer islands. Spectra from all pixels were in good agreement with the spectra of sublimed PTCDI monolayers discussed in section 4.3. The fluorescence map was compared to AFM images of the same area where the shapes of individual islands could be resolved. Comparing spectra from different areas of the sample and different areas of the same island, no significant variations in the fluorescence peak position or lineshape were observed. The fluorescence peaks from different PTCDI islands are comparable, suggesting

that the orientation of islands with respect to the substrate had little effect on either the peak position or width.

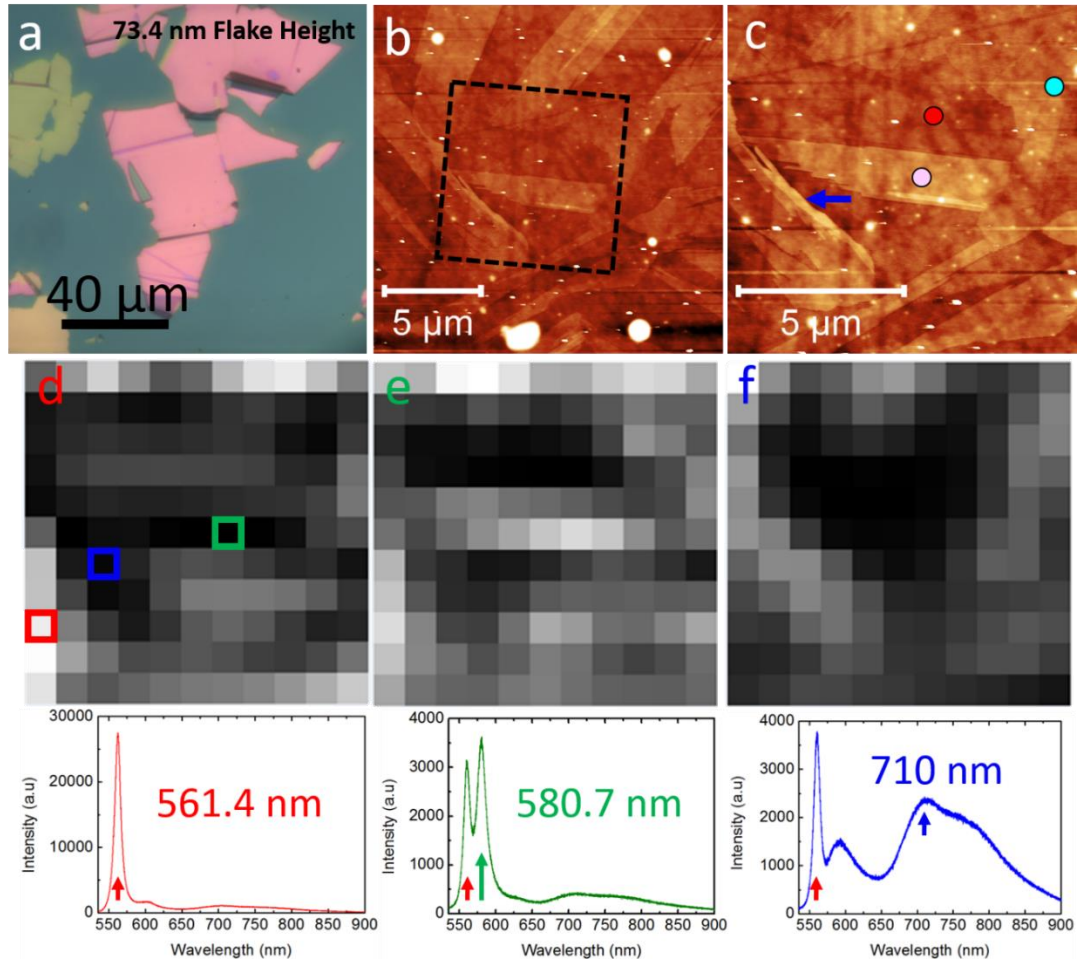


**Figure 4.5.3.** A map of PTCI (2.1 ML coverage) on flame-annealed hBN on SiO<sub>2</sub>. The flake from which the map was taken is shown (a) alongside two AFM scans from the centre of the flake (b,c) where monolayer, bi-layer and tri-layer areas are indicated by red, light blue and pink circles, and a region of thicker multi-layer PTCI is indicated by a blue arrow. A 10 μm fluorescence map, indicated by a black square overlaid on AFM image b, was acquired from the same area and shows three distinct peaks. Images d,e and f show the integrated intensity over spectral regions of 555-565 nm, 575-585 nm and 650-850 nm respectively. Below, spectra from individual pixels, indicated in map d, are shown.

Fluorescence maps were also acquired for a 2.1 ML coverage of PTCI on hBN on 300 nm SiO<sub>2</sub>/Si grown at 135 °C. The island morphology of PTCI was investigated using AFM, with monolayers, bi-layers and tri-layers observed. Figure 4.5.3 shows a map from one flake on the hBN surface where a thicker region of aggregated PTCI was also observed. The fluorescence map from this region of the hBN flake contained three distinct spectral lineshapes, the

positions of these features were successfully compared to features in the AFM map of the sample. In addition to the typical monolayer peak at  $561.4 \pm 0.5$  nm, a peak at  $580.7 \pm 0.5$  nm and a much broader feature at approximately 710 nm were observed. The broad peak at 710 nm in figure 4.5.3 is thought to be due to aggregates of PTCDI consisting of 4 or more stacked layers, this is comparable to the fluorescence of the bulk PTCDI powder at  $708.0 \pm 0.5$  nm. The peak at  $561.4 \pm 0.5$  nm was observed in spectra from all pixels, this could be due to regions of monolayer PTCDI being present within the region illuminated by the laser spot at each pixel. Alternatively, PTCDI molecules within bi-layers and tri-layers could fluoresce at the same wavelength as a monolayer of PTCDI on hBN. It is thought that the presence of the  $561.4 \pm 0.5$  nm peak occurs due to regions of monolayer PTCDI rather than multi-layers, since additional layers of PTCDI molecules would be expected to lead to shifts due to resonant and non-resonant interactions between the first and higher layers. The peak at  $580.7 \pm 0.5$  nm is thought to occur due to the presence of bi-layer PTCDI, this was investigated further through the acquisition of a second 24  $\mu\text{m}$  fluorescence map from the same sample, see figure 4.5.4.

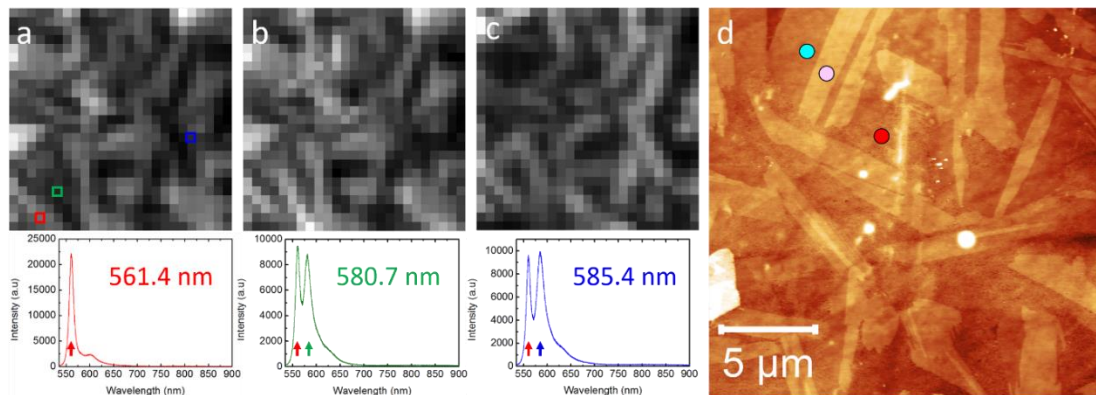


**Figure 4.5.4.** A second 24  $\mu\text{m}$  fluorescence map (a,b,c) of a different flake from the sample shown in figure 4.5.3 was acquired as well as an AFM image (d) from the same flake, where monolayer, bi-layer and tri-layer areas are again indicated by red, light blue and pink circles respectively. The map shows the relative distribution of integrated signals within the range 550-570 nm (a), 570-585nm (b) and 585-600 nm (c). The fluorescence spectra from three different pixels (denoted by colour) are shown and display three distinct peak positions at  $561.4 \pm 0.5$  nm,  $580.7 \pm 0.5$  nm and  $585.4 \pm 0.5$  nm.

In addition to peaks at  $561.4 \pm 0.5$  nm and  $580.7 \pm 0.5$  nm, a further peak at  $585.4 \pm 0.5$  nm was observed from a larger fluorescence map acquired from a different hBN flake. Peaks at  $580.7 \pm 0.5$  nm and  $585.4 \pm 0.5$  nm are thought to arise due to the presence of bi-layer and tri-layer regions of PTCDI. As a consequence of both the close spectral separation and spatial distribution of these fluorescence peaks, samples would need to be studied with greater spatial resolution than was possible in this experiment in order to assign spectral features to individual structures on the surface with confidence. Single fluorescence spectra were also measured from a range of coverages of PTCDI on hBN on chromium, the same fluorescence peaks were observed but it was not possible to attribute individual fluorescence peaks to structural features.

#### **4.6. Conclusion**

In this chapter, the morphology and fluorescence of sublimed PTCDI on hBN has been discussed. Firstly the temperature dependence of the morphology of monolayer PTCDI islands was investigated. Needle-like monolayer islands were observed at room temperature, an increase in the size of islands was seen with increasing growth temperature. The fluorescence of monolayer PTCDI on hBN was measured and interference effects in the fluorescence spectra from various substrates were observed. These interference effects were explained using analytical and transfer matrix models. The fluorescence of PTCDI on hBN was measured at low temperature with Raman lines corresponding to PTCDI observed. Finally, higher coverages of sublimed PTCDI were investigated. By mapping the PTCDI thin films both optically and using AFM, features in the fluorescence spectra can be related to structural properties of thin films.

# **Chapter 5:**

## **Chromatic Shifts of Organic Monolayers Adsorbed on Insulating Substrates**

## **5. Chromatic Shifts of Organic Monolayers Adsorbed on Insulating Substrates.**

In this chapter, the origins of the chromatic shifts of molecular monolayers are explored for the case of two perylene derivatives; perylene tetracarboxylic diimide (PTCDI) and perylene tetracarboxylic dianhydride (PTCDA). The fluorescence of the PTCDI-melamine supramolecular network on hBN is discussed and compared to measurements of the canted phase of PTCDI. The shift between the two monolayer PTCDI phases is explained in terms of resonant interactions between neighbouring transition dipole moments, for which the exciton bandstructure of each phase is calculated. A larger shift of both phases with respect to fluorescence measurements from doped helium nano-droplets (HND) is attributed to interactions with the hBN substrate. Efforts to produce flat-lying PTCDI monolayers on various insulating substrates are then discussed. In order to investigate the role of the substrate, PTCDA was deposited onto hBN and its fluorescence compared to measurements carried out in other studies. The fluorescence of these perylene molecules is discussed in terms of ubiquitous resonant and non-resonant interactions, which have been modelled using time dependent density functional theory (TD-DFT) and numerical calculations.

## 5.1. Overview

The fluorescence of molecular monolayers on surfaces is currently of great interest given the importance of the organic-inorganic interface in molecular electronics and the absence of a unified description of the fluorescent properties of monolayers at insulating surfaces. In recent years, a number of novel investigations involving fluorescent monolayers have been conducted, particularly layers formed from PTCDA [13,14,76,81]. Concurrently, scanning tunnelling microscopy induced luminescence (STM-L) studies of porphyrin and phthalocyanine derivatives have provided an insight into charge transfer between molecular dimers on alkali halide bi-layers [78,79].

A number of accounts discussing the electronic and optical properties of monolayer molecular aggregates are available in the literature, and several mechanisms have been proposed to account for the fluorescence shifts from gas phase measurements which have been observed experimentally. These include: the coupling of transition dipoles; substrate induced deformation of fluorophores; interactions with a polarisable substrate; and non-resonant intermolecular interactions. In general, the fluorescence shift between gas-phase measurements and monolayers adsorbed on surfaces,  $\Delta E_{\text{tot}}$ , is comprised of a shift due to the adsorption of isolated molecules on the substrate,  $\Delta E_{g-s}$ , and intermolecular interactions,  $\Delta E_{\text{int}}$ , see equation 5.1.1. Given the complex nature of the fluorescence phenomenon and the interactions giving rise to fluorescence shifts, it is a very difficult task to encapsulate all of the mechanisms listed above in a single computational model.

$$\Delta E_{\text{tot}} = \Delta E_{g-s} + \Delta E_{\text{int}} \quad (5.1.1)$$

One particularly interesting study was carried out by Müller et al at the University of Bonn [76]. A novel observation in this work was a distinction between isolated and aggregated molecules on a potassium chloride (KCl) substrate. A red shift from fluorescence measurements of PTCDA doped helium nano-droplets,  $\Delta E_{g-s}$ , of  $0.122 \pm 0.001$  eV is measured

upon adsorption of isolated molecules on KCl. A further red shift of  $0.050 \pm 0.001$  eV is seen upon aggregation of isolated molecules into a close packed brick wall phase. While the shift between isolated and aggregated molecules on the surface has been attributed to on-surface coupling of transition dipole moments in a number of systems, the exact role of the substrate and the interplay between molecule-substrate and intermolecular interactions is still not fully understood.

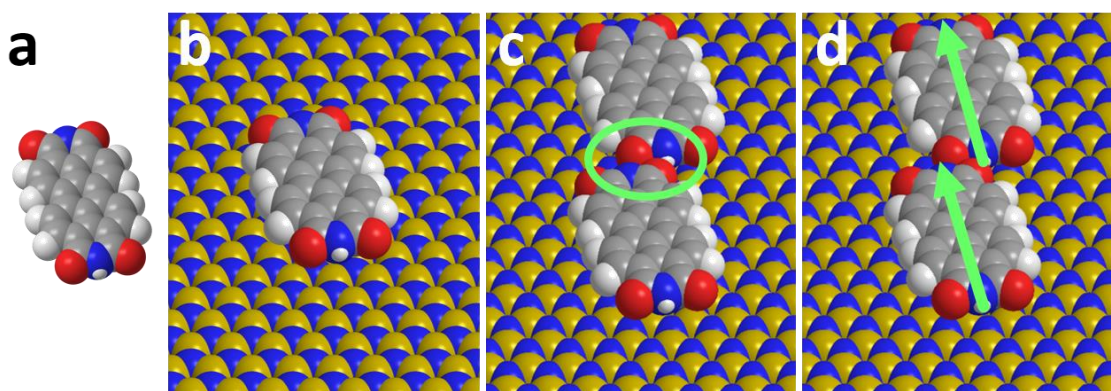


**Figure 5.1.1.** Different chemical environments influence mechanisms leading to chromatic shifts in the fluorescence of organic molecules. A PTCDI molecule (a) is shown as well as isolated PTCDI (b) on hBN. Hydrogen bonding (c) and the placement of transition dipole moments (d) are also indicated for two nearest neighbours of PTCDI on hBN.

## 5.2. The PTCDI-Melamine Supramolecular Network and Solution

### Processed PTCDI on Hexagonal Boron Nitride

In addition to the canted structure, discussed in chapter 4, PTCDI forms a honeycomb supramolecular network when co-deposited with melamine [5]. Using a solution deposition technique, PTCDI-melamine was deposited onto hBN substrates [46]. Deposition of PTCDI-melamine and the acquisition of high-resolution AFM images was carried out by Dr Vladimir Korolkov. The deposition of PTCDI-melamine was optimised to give full monolayer coverage, used for all such samples in this chapter. From high resolution AFM images, a lattice parameter of  $3.5 \pm 0.1$  nm was extracted, in good agreement with previous STM investigations of the

same structure on metal and HOPG surfaces [5,6]. The PTCDI-melamine network was deposited onto both flame-annealed hBN on 300 nm SiO<sub>2</sub>/Si and furnace-cleaned hBN on chromium substrates. The fabrication steps for both substrates are described in section 3.3.

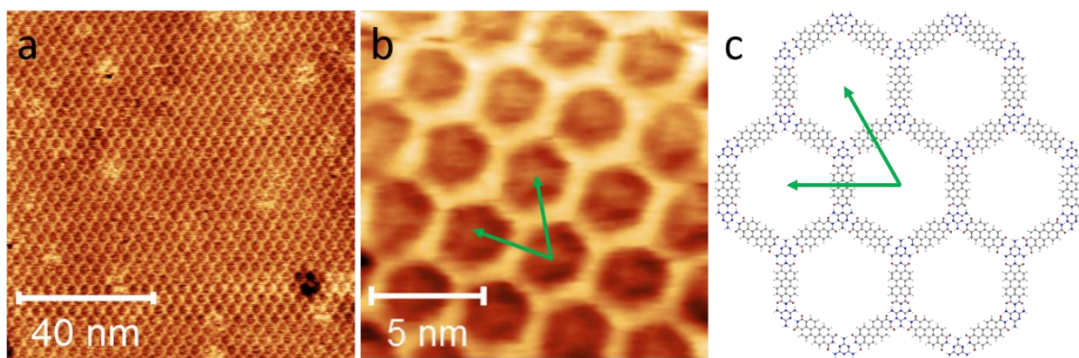


**Figure 5.2.1.** A monolayer of the PTCDI-melamine supramolecular network was deposited onto flame-annealed hBN on SiO<sub>2</sub> from solution. The morphology of the PTCDI-melamine network was determined using AFM (a,b), from which a lattice constant of  $3.5 \pm 0.1$  nm was extracted. A diagram of the arrangement of PTCDI and melamine molecules within the network is also shown (c). Deposition of the PTCDI-melamine network from solution and acquisition of high-resolution AFM images was carried out by Dr Vladimir Korolkov.

Fluorescence spectra of the PTCDI-melamine supramolecular network were measured using the Horiba LabRAM HR spectrometer with a 532 nm excitation laser. In order to prevent sample damage and photo-bleaching, filters were used to decrease the laser power. The PTCDI-melamine films were found to degrade over a few days, thought to be due to exposure to moisture under ambient conditions. Spectra were therefore acquired immediately after deposition from solution in order to reduce the effect of sample degradation.

As with sublimed PTCDI on hBN on 300 nm SiO<sub>2</sub>/Si, discussed in section 4.3, the lineshape of the PTCDI-melamine fluorescence was found to vary between hBN flakes of different thickness. Fluorescence spectra of PTCDI-melamine on hBN on 300 nm SiO<sub>2</sub>/Si were acquired from a number of flakes, see figure 5.2.2. The height of the underlying hBN flakes was extracted from AFM images and compared to fluorescence spectra. The relative intensity of the fluorescence peaks was found to change with the height of the underlying hBN flake; this was attributed to interference effects. In order to explore this effect further, fluorescence

spectra were modelled using the transfer matrix model and direct calculations introduced in section 4.3.

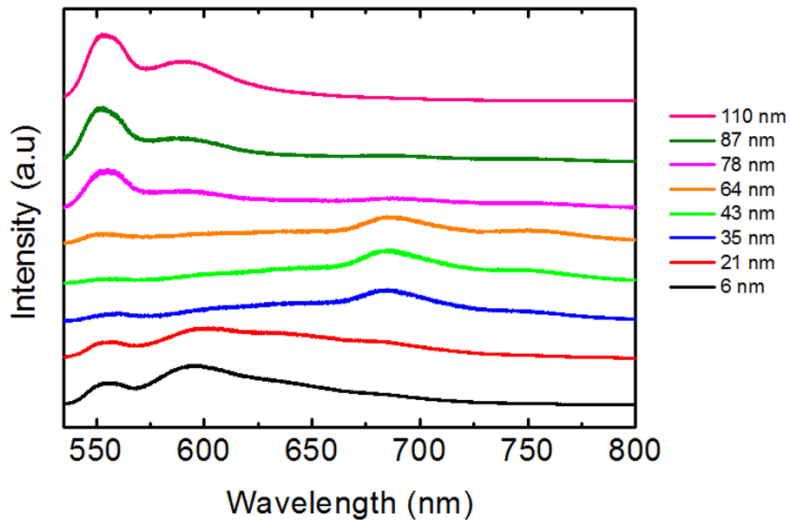


**Figure 5.2.2.** Fluorescence spectroscopy of the PTCDI-melamine network on hBN on 300 nm SiO<sub>2</sub>/Si was carried out using a 532 nm excitation laser. Normalised fluorescence spectra are shown for a range of hBN flake thicknesses, extracted from AFM images and indicated in the legend.

By fitting the fluorescence spectra of PTCDI-melamine to a series of Lorentzian curves, the intensities and positions of the 0-0 ( $2.235 \pm 0.002$  eV /  $554.8 \pm 0.5$  nm) and 0-1 ( $2.082 \pm 0.002$  eV /  $595.4 \pm 0.5$  nm) peaks of PTCDI-melamine were extracted. In figure 5.2.2, spectra taken from flakes with heights of 35 nm, 43 nm and 64 nm show a broad fluorescence peak between 675 nm and 750 nm, the prominence of this broad peak is explained in terms of optical interference.

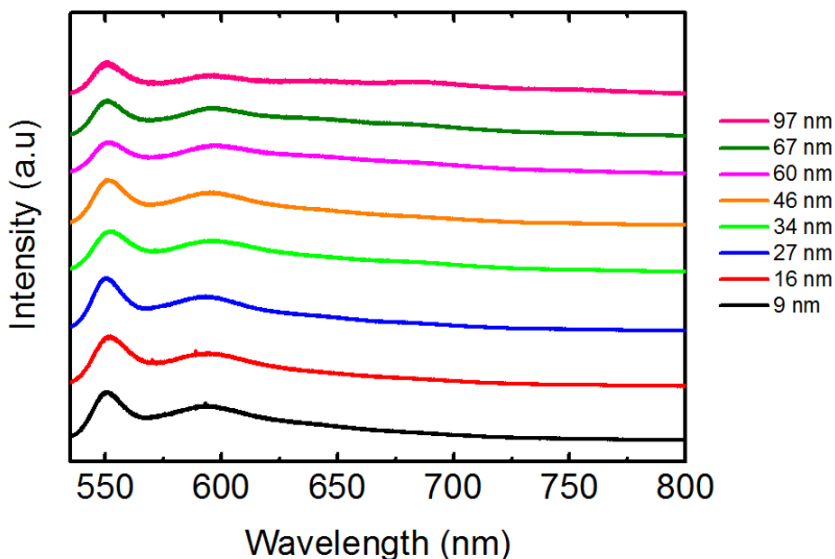


**Figure 5.2.3.** Fluorescence measurements of the PTCDI-melamine network deposited onto furnace-cleaned hBN on chromium. Measurements were carried out using a 532 nm excitation laser while the flake heights were extracted from AFM images.

In order to reduce the variation in the fluorescence line shape between hBN flakes, PTCDI-melamine was also deposited onto furnace-cleaned hBN on chromium. Fluorescence spectra of PTCDI-melamine on hBN on chromium were acquired from a range of hBN flakes and are shown plotted in figure 5.2.3. On hBN on chromium, the fluorescence lineshape was found to be more consistent (as observed for sublimed PTCDI, see section 4.3).

On hBN on chromium, the 0-0 and 0-1 peaks of PTCDI-melamine were measured to be  $(2.245 \pm 0.002 \text{ eV} / 552.3 \pm 0.5 \text{ nm})$  and  $(2.085 \pm 0.002 \text{ eV} / 594.7 \pm 0.5 \text{ nm})$  respectively. The ratios between the 0-0 and 0-1 peaks were extracted from fluorescence spectra and modelled using analytical methods. By comparing the fitting parameters of interference models, the ratio between the 0-0 and 0-1 peaks was found to decrease by a factor of  $4.5 \pm 0.2$  between sublimed PTCDI and PTCDI-melamine on hBN on chromium, see section 4.3 and appendix 1.

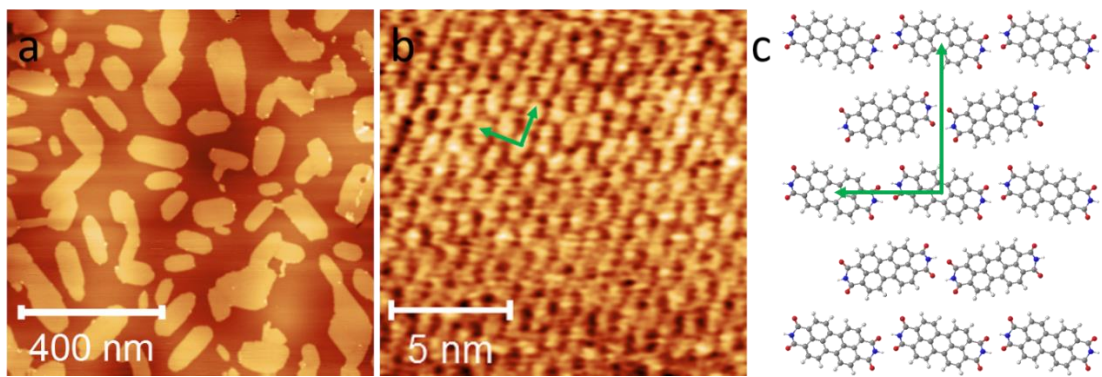


**Figure 5.2.4.** By immersing the PTCDI-melamine supramolecular network on hBN in water, melamine is removed and insoluble PTCDI molecules re-organise on the surface. AFM was used to acquire images of the resulting PTCDI sample showing the island morphology (a) and molecular packing (b) of PTCDI. A diagram showing the canted structure of PTCDI is also shown (c). Solution processing of PTCDI films and acquisition of high-resolution AFM images was carried out by Dr Vladimir Korolkov.

The canted PTCDI phase can be formed by immersing the pre-formed PTCDI-melamine network in ultra-pure water to remove the soluble melamine species. PTCDI films on hBN were fabricated in this way by Dr Vladimir Korolkov, prior to the acquisition of images of the sample using AFM. PTCDI was found to rearrange into monolayer islands on the hBN surface, while high-resolution AFM images of the islands revealed a canted molecular packing structure which was also observed for sublimed PTCDI, see section 4.2. The lattice constants of solution processed PTCDI were found to be  $1.5 \pm 0.1$  nm and  $1.7 \pm 0.1$  nm, in good agreement with values extracted from AFM images of sublimed PTCDI on hBN, see chapter 4, and STM images of PTCDI on gold by Mura et al [44]. The island morphology and molecular packing of solution processed PTCDI are shown in figure 5.2.4.

The fluorescence of solution processed PTCDI on hBN on chromium was found to be comparable to sublimed PTCDI films, see figure 5.2.5. The variation in the fluorescence lineshape of solution processed PTCDI monolayers on hBN on chromium was found to be similar to that of sublimed PTCDI monolayers. Comparing the fluorescence spectra of sublimed PTCDI, solution processed PTCDI and PTCDI-melamine on hBN on chromium substrates, a small red shift of  $0.006 \pm 0.002$  eV was observed between solution-deposited

and sublimed PTCDI. This difference is attributed to the preparation of the two films, sublimed molecular films can exhibit areas of additional material on top of islands while solution-processed films may also be affected by the presence of excess solvent molecules or residual melamine.

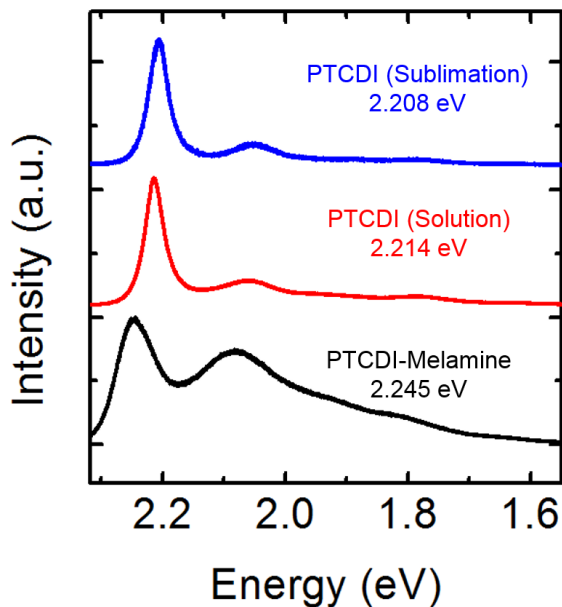


**Figure 5.2.5.** Normalised fluorescence spectra taken from sublimed PTCDI (blue), solution processed PTCDI (red) and the PTCDI-melamine supramolecular network (black) on hBN. Measurements were taken from hBN flakes of height 48 nm, 48 nm and 49 nm respectively, with an excitation wavelength of 532 nm.

A red shift of  $0.031 \pm 0.002$  eV was observed between PTCDI-melamine and solution processed PTCDI, much larger than the difference between the 0-0 peaks of sublimed and solution-processed PTCDI monolayers. The similarities between the fluorescence spectra of solution processed and sublimed monolayer PTCDI films suggests that the different deposition routes to the canted structure of PTCDI has little effect on the fluorescence of the film. This is the basis for the assumption that differences in the fluorescence spectra between PTCDI and PTCDI-melamine on hBN are a consequence of the structure of the film, rather than any external factors such as the presence of excess solvent molecules. This assumption is supported further by AFM results, where images of the morphology of all samples have been

acquired with lattice resolution. A larger red shift,  $\Delta E_{\text{tot}}$ , of  $0.342 \pm 0.002$  eV, was observed between HND measurements of Me-PTCDI ( $2.5506 \pm 0.0001$  eV) and solution deposited PTCDI on hBN ( $2.214 \pm 0.002$  eV) [71].

Aggregate	0-0 Peak Position (nm/eV)	0-0 Peak Width (nm/eV)	0-1 Peak Position (nm/eV)
PTCDI-melamine (hBN-Cr)	552.3 / 2.245	15.1 / 0.061	594.7 / 2.085
PTCDI-melamine (hBN-SiO <sub>2</sub> -Si)	554.8 / 2.235	19.5 / 0.079	595.4 / 2.082
PTCDI (hBN-Cr) (Sublimed)	561.5 / 2.208	9.8 / 0.039	602.2 / 2.059
PTCDI (hBN-SiO <sub>2</sub> -Si) (Sublimed)	561.4 / 2.208	11.3 / 0.043	606.3 / 2.045
PTCDI (hBN-Cr) (Solution Processed)	560.1 / 2.214	9.6 / 0.038	599.9 / 2.067
Me-PTCDI [71] (HND)	486.2 / 2.550	-	-

**Table 5.2.1.** The position and width of the main and vibronic peaks of solution deposited PTCDI-melamine, sublimed PTCDI and solution processed PTCDI thin films on hBN are shown for a range of substrates. The 0-0 peak of Me-PTCDI doped helium nano-droplets [71] is shown for comparison.

The fluorescence peak positions and widths of both PTCDI and PTCDI-melamine on hBN are shown in table 5.2.1. Slight variations in the peak positions and peak widths between substrates were attributed to interference effects. This was seen in plots of the peak position, extracted from fitting, against the hBN flake height, see appendix 1. For hBN on 300 nm SiO<sub>2</sub>/Si substrates, a small modulation of the peak position in the range of 0.008 eV (2 nm) was observed with changing flake height. All comparisons between the fluorescence of PTCDI and PTCDI-melamine phases on hBN are drawn from hBN on chromium substrates, this is because the lineshape and peak positions of spectra did not vary as much between hBN flakes. In this section, the close packing structure and fluorescence of PTCDI-melamine and solution processed PTCDI have been determined experimentally, these results will be discussed further in section 5.5 and 5.6.

### 5.3. The Deposition of PTCDI on Insulating Substrates

In order to investigate the effect of the substrate upon the fluorescence of monolayer PTCDI films, sub-monolayer coverages of PTCDI were grown on a range of substrates by sublimation in vacuum. The deposition of PTCDI was first studied on two alkali halide substrates; potassium chloride (KCl) and calcium fluoride ( $\text{CaF}_2$ ). Alkali halide substrates were produced by mechanical cleavage before being placed in vacuum. Alkali halide samples were annealed in vacuum to approximately  $450\text{ }^\circ\text{C}$  and cooled to room temperature prior to the deposition of a 0.4 ML coverage of PTCDI from a Knudsen-cell, see section 4.2. The morphology of a sub-monolayer coverage of PTCDI on KCl (a,b) and  $\text{CaF}_2$  (c,d) is shown in figure 5.3.1. After the vacuum chamber containing the sample was vented, the morphology of these films was investigated using AFM.

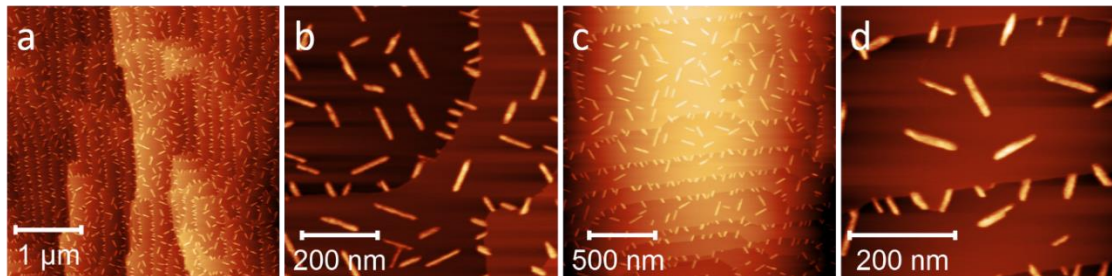


**Figure 5.3.1.** PTCDI was deposited onto two alkali halide surfaces, potassium chloride (a,b) and calcium fluoride (c,d). Alkali surfaces were cleaved in ambient conditions before annealing in vacuum prior to the deposition of 0.4 ML of PTCDI, substrates were held at room temperature during deposition. Images of the morphology of PTCDI films were acquired using AFM.

From AFM images of the surface morphology of KCl and  $\text{CaF}_2$ , a series of flat planes and terraces of height  $0.3\text{ nm} \pm 0.1\text{ nm}$  were observed. Following the deposition of PTCDI, needle-like islands with a typical length of 94 nm and a distribution of heights in the range of 1.1 nm to 1.5 nm were seen on  $\text{CaF}_2$ . On KCl, islands with a typical length of 76 nm and a distribution of heights between 0.8 nm and 1.6 nm were observed. The distribution of island heights in

addition to the observation of steps in the AFM height profiles of islands suggests they were composed of multiple layers of flat lying PTCDI molecules, rather than molecules standing up.

The multi-layer islands are expected to arise due to de-wetting effects which have previously been reported for both PTCDI and PTCDA on NaCl surfaces by the Grütter group at McGill University [42,43]. These effects could possibly be exacerbated by the exposure of the hygroscopic alkali halide surfaces to ambient conditions. The acquisition of AFM images of epitaxial thin films of PTCDI on alkali halide substrates in-situ would be of interest in order to check the effect of exposure to ambient conditions on the thin film morphology. Given the absence of flat-lying monolayer islands on these two alkali halide surfaces, at least under the conditions considered in this experiment, the fluorescence of these thin films is not explored in the context of substrate mediated fluorescence shifts. For multi-layers of PTCDI, interactions between layers would be expected to lead to further resonant and non-resonant shifts, introducing difficulties in making a direct comparison between substrates.

PTCDI was also deposited onto a range of other substrates, notably; SiO<sub>2</sub>, glass, poly methyl methacrylate (PMMA) (both before and after annealing) and sapphire. As before, samples were loaded into vacuum in order to deposit a sub-monolayer coverage of PTCDI. With the exception of PMMA films, all samples were annealed to 450 °C in vacuum and cooled prior to the deposition of PTCDI. In all cases, no distinct island morphology was observed and instead regions of aggregated material were seen.

The absence of well-defined structures, formed by PTCDI, on this collection of substrates is thought to be due to the three-dimensional morphology of these samples. The nature of the bonding within these materials leads to inhomogeneities on the surface, which inhibit the formation of monolayer PTCDI islands, where molecules bond to each other through hydrogen bonding and to the surface through van der Waals interactions. The morphology of sub-monolayer coverages of PTCDI on a range of substrates was investigated using AFM under

ambient conditions and is shown in figure 5.3.2. In the case of sapphire, the surface morphology resembled that of unreconstructed sapphire. Given its large refractive index and bonding structure, reconstructed sapphire would be an interesting substrate for future investigations [106]. In this experiment however, a convenient method of annealing sapphire to the required temperature was not available.

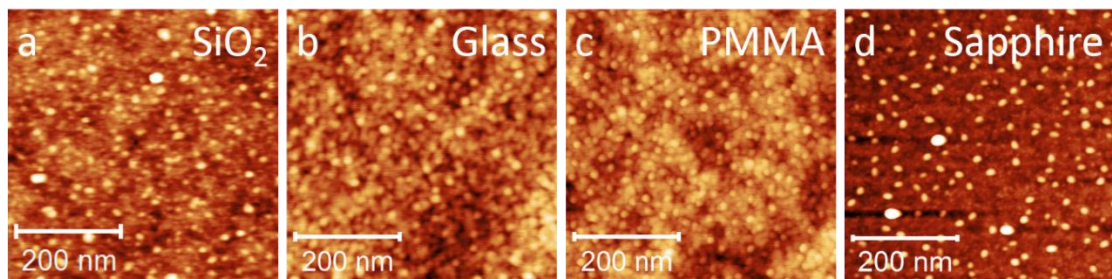


**Figure 5.3.2.** PTCDI was sublimed onto SiO<sub>2</sub> (a), glass (b), PMMA (c) and sapphire (d) surfaces under UHV conditions. With the exception of PMMA, all substrates were annealed in vacuum prior to the deposition of PTCDI onto a substrate held at room temperature. All images were acquired using AFM.

## 5.4. Substrate Induced Chromatic Shifts: The Fluorescence of PTCDA on hBN

In order to explore the effect of the substrate on the fluorescence of perylene derivatives adsorbed on dielectric substrates, a second perylene derivative, PTCDA, was investigated. By depositing PTCDA monolayers onto hBN substrates, the fluorescence was measured and compared with published data on flat-lying PTCDA adsorbed on various substrates. PTCDA was first sublimed onto hBN substrates under UHV conditions (the method used was the same as was carried out for PTCDI, described in section 4.2 and 3.4). In order to deposit a 0.4 ML coverage, a Knudsen cell was heated to 335 °C, giving a deposition rate of 1.7 ± 0.2 ML/min. Images of the morphology of sublimed PTCDA films grown at room temperature and 135 °C on flame-annealed hBN on SiO<sub>2</sub> were acquired using AFM, see figure 5.4.1.

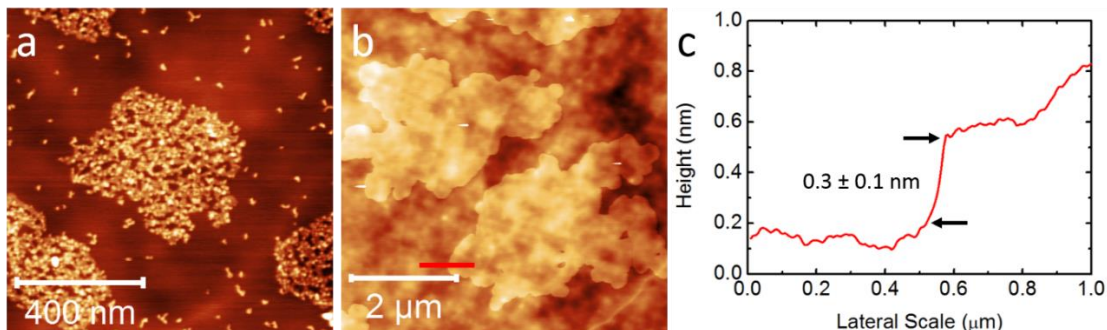


**Figure 5.4.1.** PTCDA was sublimed onto flame-annealed hBN on  $\text{SiO}_2$  substrates held at room temperature (a) and 135 °C (b). A line profile (c) taken from image b confirms that PTCDA forms a monolayer on hBN when deposited at 135 °C.

In the case of PTCDA grown at room temperature, monolayer regions are observed in addition to regions of aggregated material. At higher temperatures, irregular monolayer islands with no additional layers are observed. The irregular morphology of PTCDA islands is thought to be due to the intermolecular bonding structure of a number of reported phases of monolayer PTCDA [37]. The presence of monolayer islands of PTCDA grown at 135 °C was confirmed by the  $0.3 \text{ nm} \pm 0.1 \text{ nm}$  step height of islands, extracted from AFM images. Variations in the line profile in figure 5.5.1c are attributed to the roughness of the underlying  $\text{SiO}_2$  substrate.

PTCDA was also deposited from solution on flame-annealed hBN substrates on  $\text{SiO}_2$ . The deposition of PTCDA thin films and subsequent structural determination using AFM was carried out by Dr Vladimir Korolkov. AFM images showing the island morphology and molecular packing of this sample are shown in figure 5.4.2. By depositing PTCDA from solution, uniform monolayer islands were obtained. Using high-resolution AFM under ambient conditions, the molecular packing was found to be that of the square phase. A square packing structure has previously been reported by Gustaffson et al [38] and Swarbrick et al [37] on the Ag-Si (111)- $\sqrt{3}\times\sqrt{3}$  surface. The lattice constant,  $1.62 \pm 0.02 \text{ nm}$ , reported in these STM

investigations is in good agreement with the lattice parameter,  $1.6 \pm 0.1$  nm, extracted from AFM images of PTCDA on hBN in this thesis.

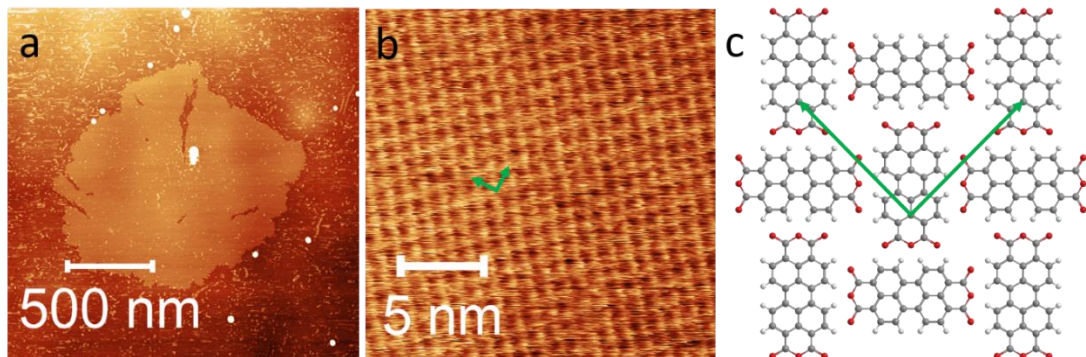


**Figure 5.4.2.** PTCDA was deposited onto flame-annealed hBN on  $\text{SiO}_2$  from solution. The island morphology (a) and molecular packing (b) were determined using AFM. A diagram showing the packing of the square phase of PTCDA is shown (c). Solution deposition and acquisition of high-resolution AFM images were carried out by Dr Vladimir Korolkov.

Fluorescence spectra acquired from solution deposited and sublimed PTCDA films, of sub-monolayer coverage, have 0-0 fluorescence peaks at  $2.234 \pm 0.002$  eV and  $2.247 \pm 0.002$  eV respectively, see figure 5.4.3. The red shift of  $0.013 \pm 0.002$  eV from sublimed PTCDA films to solution deposited films is attributed to differences in the sample preparation. The presence of excess solvent molecules in solution deposited films could account for an additional shift between the two samples. Since the molecular packing of sublimed PTCDA on hBN could not be determined using AFM under ambient conditions, it is not possible to rule out two different phases of PTCDA, leading to a shift due to two different close packing arrangements. For this reason, fluorescence measurements from solution deposited PTCDA will be used for the purpose of comparison with other results in this work and in the literature. In reference [70], Wewer and Steinkemeier measured the 0-0 fluorescence peak of PTCDA doped HND to be  $2.6022 \pm 0.0001$  eV, implying a red shift,  $\Delta E_{\text{tot}}$ , of  $0.368 \pm 0.002$  eV to the square phase of PTCDA on hBN, deposited from solution.

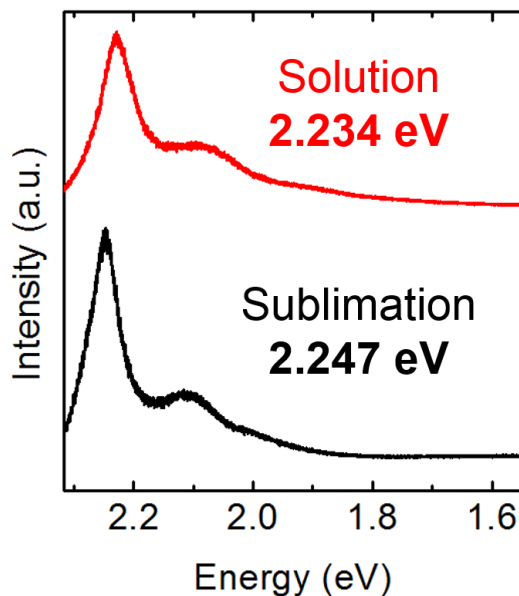


**Figure 5.4.3.** The fluorescence spectra of solution deposited and sublimed PTCDA monolayers on hBN were measured using a 532 nm excitation laser. Normalised fluorescence spectra from hBN flakes are shown for both samples, as well as the position of the main peak.

In reference [13], Müller et al measured a red shift,  $\Delta E_{g-s}$ , of  $0.162 \pm 0.001$  eV from measurements of PTCDA doped HND to isolated molecules on the NaCl surface. A further red shift,  $\Delta E_{int}$ , of  $0.037 \pm 0.001$  eV was measured upon formation of a closed packed square phase. The shift upon formation of a square phase was attributed to the coupling of transition dipole moments of neighbouring molecules.

The experimentally observed red shift,  $\Delta E_{tot}$ , of  $0.368 \pm 0.002$  eV from PTCDA doped HND [70] to the square phase of PTCDA on hBN, is greater than those reported in the literature, for both isolated PTCDA molecules and monolayer aggregates on alkali halide surfaces. The comparable square packing arrangements of PTCDA on NaCl and hBN substrates, which led to a  $0.037 \pm 0.001$  eV red shift,  $\Delta E_{int}$ , from isolated molecules on NaCl [13], suggests that interactions with the hBN substrate dominate the observed overall red shift.

The fluorescence of monolayer PTCDA and isolated PTCDA molecules on a range of substrates are available in the literature [13,14,76,101,107]. The shifts from HND measurements [70] are

shown plotted against the refractive index of the substrate in figure 5.4.4. With the exception of measurements of isolated molecules on KCl [76] and NaCl [13], all measurements were taken from close packed monolayers of PTCDA. The red shifts for close packed monolayers include a shift due to the substrate in addition to shifts arising from resonant and non-resonant intermolecular interactions. Assuming that interactions with the substrate dominate the fluorescence shift of close packed PTCDA monolayers, the shift due to the substrate appears to be correlated with the refractive index of the substrate, see figure 5.4.4.

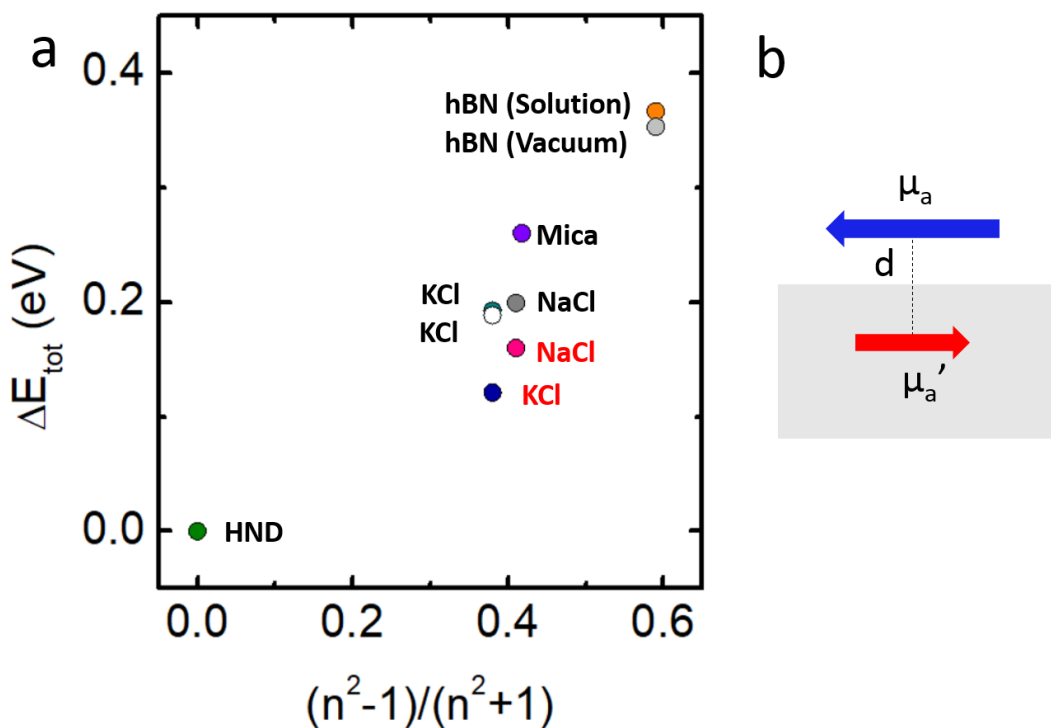


**Figure 5.4.4.** The fluorescence shifts, from doped HND [70], of PTCDA on various substrates are plotted for measurements of flat-lying aggregates available in the literature (a). The KCl [76] and NaCl [13] values in red are for isolated molecules at 20 K while all other points are for monolayer aggregates on KCl [76,107], NaCl [13], mica [101] and hBN (this work). A diagram depicting the position of a transition dipole moment above the surface and the image dipole below is also shown (b).

At dielectric interfaces, a charge distribution outside the dielectric induces image charges within the material. For  $\mu$ , a transition dipole moment above a surface,  $\mu'$ , the image dipole, will be oriented in the opposite direction below the dielectric surface. The magnitude of  $\mu'$  is

given by equation 5.4.1, where  $n$  is the refractive index of the substrate. Assuming the transition dipole moment and its image can be approximated as classical point dipoles, their interaction energy is given by equation 5.4.2, where  $r_{ij}$  is the vector representing the separation of transition dipoles  $\mu_i$  and  $\mu_j$ . The interaction energy of the transition dipole moment and its image at a dielectric surface is then given by equation 5.4.3, where  $r$  is the absolute magnitude of the separation between the transition dipole moment and its image. It has been assumed that the transition dipole moment and its image are oriented parallel to one another and perpendicular to the displacement vector between them.

$$\mu' = -\frac{n^2-1}{n^2+1} \mu \quad (5.4.1)$$

$$V_{ij} = \frac{1}{4\pi\epsilon_0} \left( \frac{\mu_i \cdot \mu_j}{r_{ij}^3} - 3 \frac{(\mu_i \cdot r_{ij})(\mu_j \cdot r_{ij})}{r_{ij}^5} \right) \quad (5.4.2)$$

$$V_{ii} = -\frac{n^2-1}{n^2+1} \frac{\mu^2}{4\pi\epsilon_0 r^3} \quad (5.4.3)$$

In equation 5.4.3, an additional factor of  $1/2$ , which is present in derivations of the classical interaction energy of a point dipole and its image dipole, has been omitted. This factor is not present in quantum mechanical calculations of the fluorescence shift of a two-level system placed close to a dielectric surface (based upon Greens functions) carried out by Ryan Jones and Beatriz Olmos-Sanchez at the School of Physics and Astronomy at the University of Nottingham. The plotted fluorescence shift from doped HND, see figure 5.4.4, shows the expected dependence on the refractive index with the form of equation 5.4.3, suggesting that the interaction of transition dipole moments with the dielectric surface contributes to the observed fluorescence shift. Deviation from a linear dependence in figure 5.4.4 is attributed to additional shifts due to phenomena such as the coupling of transition dipole moments.

A number of assumptions are made in the assertion that the interaction of transition dipole moments accounts for a large fluorescence shift,  $\Delta E_{g-s}$ , due to interactions with the substrate.

Firstly, that the interaction of the two transition dipole moments can be modelled by the point dipole approximation. When the charge separation across the dipole is greater than the separation between dipoles, there is a reduction in the interaction energy of the two charge distributions. This effect could be particularly prominent in fluorophores with a greater macrocycle, since the charge of the dipole moment is spread over a greater area. Secondly, it is assumed that no non-resonant shifts occur due to the interaction of fluorescent molecules with the substrate. In the case of large molecules such as porphyrin, deformation upon adsorption has been found to lead to a significant non-resonant shift in the fluorescence of monolayers [74]. In section 5.6, these assumptions will be examined in greater detail, where the mechanisms which give rise to fluorescence shifts of PTCDA and PTCDI on hBN are discussed.

## 5.5. Resonant Intermolecular interactions of PTCDI on hBN

In chapter 4 and section 5.2, the molecular packing and fluorescence spectra of monolayers of sublimed PTCDI, solution processed PTCDI and PTCDI-melamine on hBN were determined experimentally. The red shift,  $\Delta E_{\text{int}}$ , of  $0.031 \pm 0.002$  eV, between the 0-0 fluorescence peaks of PTCDI and PTCDI-melamine was suggested to be a consequence of the structure of the two films. There are three major differences between the two PTCDI phases which could account for the shift observed. The first is that the different hydrogen bonding environments, arising from heterogeneous PTCDI-melamine and homogenous PTCDI-PTCDI hydrogen bonding junctions, would affect the fluorescence. Secondly, templated assembly would lead to a difference in the registry between PTCDI molecules and the hBN substrate. Thirdly, the different arrangements of PTCDI molecules would affect the interaction of molecular transition dipole moments on the surface. In order to ascertain the importance of molecular

packing in the coupling of transition dipole moments, the exciton band structure of both phases of PTCDI was calculated using the Wolfram Mathematica graphical software package.

As a molecule decays from the first excited electronic state to the ground state by emission of a photon, the molecule exhibits a transition dipole moment, arising from the change from the charge distribution of the excited electronic state to that of the ground electronic state. When the transition dipole moments of adjacent molecules couple, the interaction energy is approximated by the classical point dipole interaction energy shown in equation 5.4.2; where  $\mu_i$  and  $\mu_j$  are the transition dipole moments (in vector form) of two molecules and  $r$  is the displacement vector between the two dipoles.

From numerical calculations, accounts of which are available in the literature [108], the transition dipole moment of PTCDI has been found to be oriented along the major axis of symmetry of the molecule, as indicated in figure 5.5.1.a. The relative orientations and separations of molecules within the canted phase of PTCDI and the honeycomb PTCDI-melamine network give rise to different interaction energies between neighbouring molecules. The arrangement of molecules within the canted PTCDI structure is shown in figure 5.5.1.b, along with the vectors indicating the displacement to neighbouring molecules.

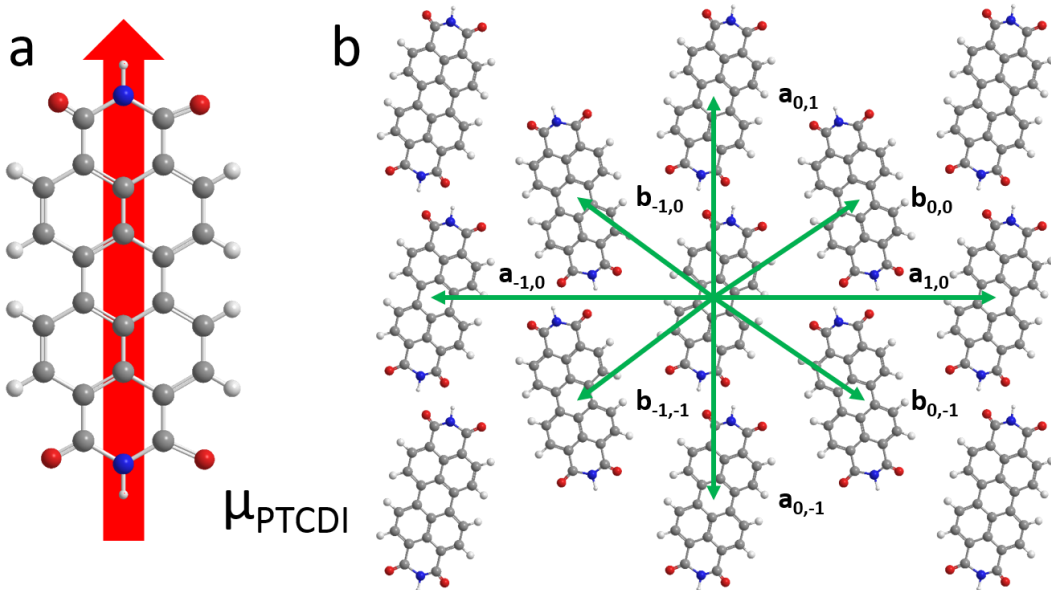


**Figure 5.5.1.** The PTCI molecule and the direction of its transition dipole moment is shown (a) in addition to the vectors from one central PTCI molecule to neighbouring molecules within the canted PTCI structure (b). The labels a and b are used to denote molecules occupying equivalent or non-equivalent basis sites, the corresponding interaction energies are shown in table 5.5.1.

Neighbour	Shift ( $E_{\text{dip}}$ )
$\mathbf{a}_{0,1}, \mathbf{a}_{0,-1}$	$-0.711 \pm 0.152$
$\mathbf{a}_{-1,0}, \mathbf{a}_{1,0}$	$0.187 \pm 0.040$
$\mathbf{b}_{-1,-1}, \mathbf{b}_{0,-1}, \mathbf{b}_{-1,0}, \mathbf{b}_{0,0}$	$-0.137 \pm 0.029$

**Table 5.5.1.** The interaction energies of two adjacent transition dipole moments occupying specified positions (shown in figure 5.5.1b) of the canted PTCI structure are given in units of  $E_{\text{dip}}$ , the energy of two parallel transition dipole moments with a separation of 1 nm, equivalent to  $0.624 \text{ meV}/\mu^2$ .

The lattice vectors  $\mathbf{a}_{ij}$  and  $\mathbf{b}_{ij}$  refer to equivalent and inequivalent basis sites in the unit cell at coordinates  $(i,j)$ , (note the canted PTCI structure has a unit cell containing two molecules which are counter rotated by a canting angle to the intra-row lattice vector). The canting angle of PTCI has been extracted from STM images of PTCI adsorbed on a number of substrates [37,41,44] and found to be approximately  $12^\circ$ . The interaction energies of the 8 nearest neighbours of a central molecule within a canted packing arrangement are given in table 5.5.1. The same procedure was also carried out for the PTCI melamine network, which has a basis

consisting of three PTCDI molecules and an angle of  $60^\circ$  between lattice vectors. The vectors  $a_{ij}$ ,  $b_{ij}$  and  $c_{ij}$  denote vectors to the three basis molecules within the unit cell at position  $(i,j)$ . Lattice parameters were extracted from AFM images of the PTCDI-melamine network on hBN ( $3.5 \pm 0.1$  nm).

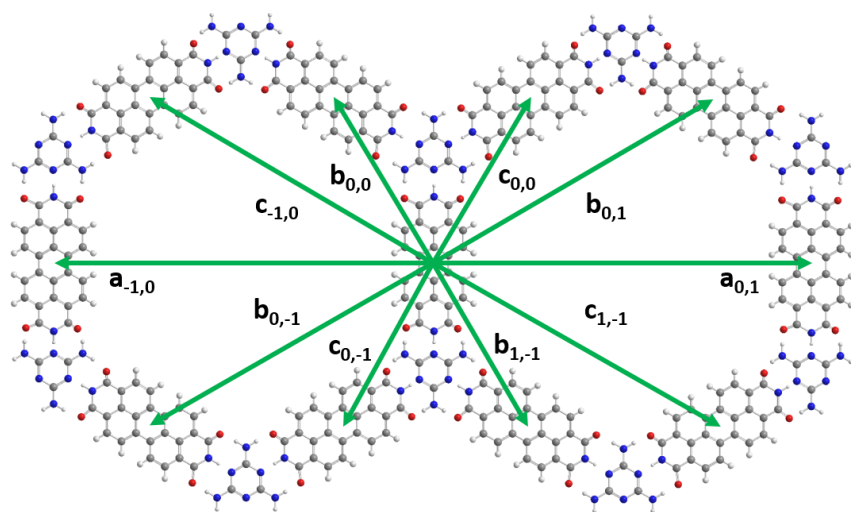


**Figure 5.5.2.** The vectors from one central PTCDI molecule to neighbouring molecules within the PTCDI-melamine supramolecular network are indicated. The labels a, b and c denote interactions with neighbouring molecules occupying each of the three basis sites, the corresponding interaction energies are shown in table 5.5.2.

Neighbour	Shift ( $E_{\text{dip}}$ )
<b>b<sub>0,0</sub>,c<sub>0,0</sub>,b<sub>1,-1</sub>,c<sub>0,-1</sub></b>	-0.327 ± 0.029
<b>c<sub>-1,0</sub>,b<sub>0,1</sub>,b<sub>0,-1</sub>,c<sub>1,-1</sub></b>	0.045 ± 0.004
<b>a<sub>0,1</sub>,a<sub>-1,0</sub></b>	0.023 ± 0.002

**Table 5.5.2.** The interaction energies of nearest neighbours within the PTCDI-melamine network, indicated in figure 5.5.2, are calculated using the classical point dipole equation and are shown in units of  $E_{\text{dip}}$ , the energy of two parallel transition dipole moments with a separation of 1 nm, equivalent to  $0.624 \text{ meV}/\mu^2$ .

The interaction energy of a central molecule and all other molecules within an aggregate of 10,000 unit cells was calculated for both the canted PTCDI phase and the PTCDI-melamine network. The interaction energy is taken to approximate the eigenvalue of the corresponding quantum mechanical operator, given in equation 5.5.1, where  $\psi^0$  and  $\psi^*$  are the wave functions of the ground and excited electronic states and  $V_{na,mb}$  is the interaction energy of

the transition dipole moments of molecules na and mb (the subscript na denotes the a<sup>th</sup> basis site within the n<sup>th</sup> unit cell), approximated to be point dipoles, see equation 5.4.2. The exciton bandstructure is calculated from a weighted sum of the transition dipole moment interaction energies between molecules, given by equation 5.5.2, where k is the wavevector in k-space and  $\chi_{00}$  is the Franck-Condon factor of the 0-0 optical transition [80].

$$M_{na,mb}^* = \langle \psi_{na}^0 \psi_{mb}^* | V_{na,mb} | \psi_{mb}^0 \psi_{na}^* \rangle \quad (5.5.1)$$

$$L_{ab}^*(k) = \chi_{00}^{-2} \sum_{m,n} M_{na,mb}^* e^{i(k.(m-n))} \quad (5.5.2)$$

In references [13] and [76], the Sokolowski group at Bonn calculated the exciton bandstructure for a number of PTCDA phases on alkali halide substrates. The bandstructure of the brick wall phase of PTCDA on KCl from [76] and the square phase observed on NaCl [13] were calculated using the model presented in this thesis and found to be in good agreement.

In this thesis, screening from the dielectric substrate has also been considered. At dielectric interfaces, dipoles induce an image dipole with the same spatial dimensions as the original charge distribution, but with a reduced magnitude, as discussed above. The magnitude of the image dipole ( $\mu'$ ) induced by a dipole ( $\mu$ ) above a dielectric of refractive index n is given by equation 5.4.1. The arrangement of a transition dipole moment, its image dipole and a neighbouring transition dipole above a dielectric surface is given in figure 5.5.3.

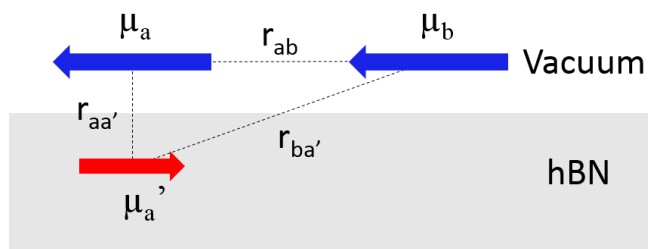


**Figure 5.5.3.** Transition dipole moments above a dielectric substrate will induce image dipoles below the surface. The screening of transition dipole moments by image dipoles beneath the dielectric is illustrated above.

By considering the interaction of image dipoles with transition dipole moments above a dielectric surface, a reduction in the interaction energy of a central transition dipole moment with neighbouring molecules is calculated. Where the separation of neighbouring transition dipole moments is much greater than the separation of transition dipoles and their image dipoles, the dipoles are approximated to be screened point dipoles, given by equation 5.5.3. In general, the interaction energy is the sum of the object-object and object-image transition dipole interactions, dependent upon the separation between the object dipole and its image.

$$\mu_{\text{Screened}} = \mu_i - \mu_r = \frac{2}{n^2 + 1} \mu \quad (5.5.3)$$

The exciton bandstructures of PTCDI (a) and PTCDI-melamine (b) are shown in figure 5.5.4, with the Brillouin zones inset. In both cases, the lowest energy band corresponding to unscreened (black) and screened dipoles (red) is shown. The chromatic shift arising from the coupling of transition dipole moments is given by the value of the lowest energy eigenvalue of the exciton band structure. In these systems, this occurs at the  $\Gamma$  point, corresponding to a direct transition. Using the experimentally measured transition dipole moment of Me-PTCDI ( $6.8 \pm 0.7$  D) from reference [109] and a calculated Franck-Condon factor for the 0-0 transition of PTCDI from reference [100], the expected shifts of both PTCDI and PTCDI-melamine on hBN due to transition dipole moment coupling have been calculated, see table 5.5.3.

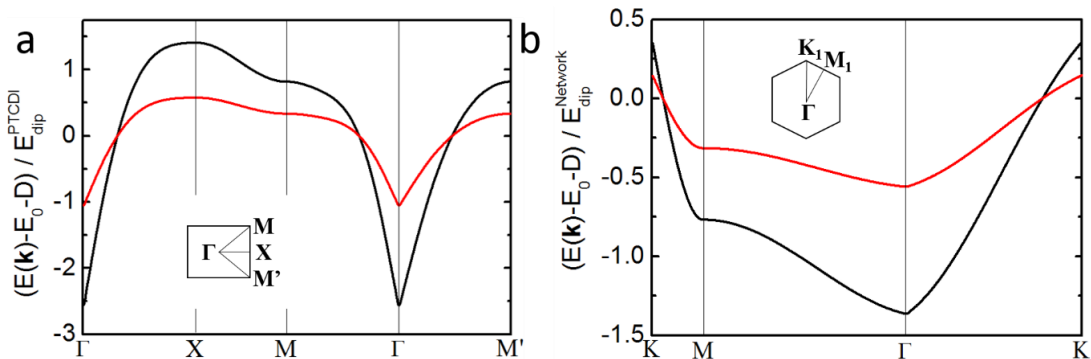


**Figure 5.5.4.** The calculated exciton bandstructures of PTCDI and the PTCDI-melamine supramolecular network are shown plotted in units of  $E_{\text{dip}}$ , the energy of two parallel transition dipole moments with a separation of 1 nm, equivalent to  $0.624 \text{ meV}/\mu\text{m}^2$ . Both calculations were carried out for an aggregate size of 10,000 unit cells both without screening (black) and with screening (red). The Brillouin zones of each aggregate are shown inset.

Structure	Shift (eV) No FC Factor No Screening	Shift (eV) FC Factor No Screening	Shift (eV) FC Factor Screened
<b>PTCDI</b>	$-0.089 \pm 0.019$	$-0.050 \pm 0.011$	$-0.020 \pm 0.004$
<b>PTCDI-melamine</b>	$-0.039 \pm 0.003$	$-0.022 \pm 0.002$	$-0.009 \pm 0.001$
<b>Relative Shift</b>	<b><math>-0.050 \pm 0.019</math></b>	<b><math>-0.028 \pm 0.011</math></b>	<b><math>-0.011 \pm 0.004</math></b>

**Table 5.5.3.** The calculated chromatic shifts from isolated molecules on the hBN surface to molecules within the canted and honeycomb structures of PTCDI and PTCDI-melamine are shown. The effect of screening due to the dielectric surface and the Franck-Condon factor are also included.

Including the Franck Condon factor [100], the calculated red shift (un-screened) between PTCDI-melamine and PTCDI is  $-0.028 \pm 0.011$  eV. This is comparable to the experimentally observed red shift of  $-0.031 \pm 0.002$  eV. The calculated shift between PTCDI and PTCDI-melamine has a large degree of uncertainty due to errors in the experimentally calculated transition dipole moment of PTCDI and uncertainty surrounding an appropriate value of the Franck-Condon factor, in general this could depend upon a number of structural and environmental factors.

Including screening due to the dielectric substrate, a shift of  $-0.011 \pm 0.004$  eV is expected, lower than the experimental result. This value is in fact a lower bound for shift since the approximated screening is only valid when the separation of neighbouring transition dipoles,  $r_{ij}$ , is greater than the separation between a transition dipole moment and its image,  $r_{ii'}$ , ( $r_{ij} > r_{ii'}$ ), see figure 5.5.3.

In table 5.5.3, a red-shift is calculated for both PTCDI and PTCDI-melamine, with a larger red shift for PTCDI. The band structures of both packing arrangements also have a minimum at the  $\Gamma$  point. This suggests that both structures are J aggregates and that the canted phase of PTCDI more closely resembles an ‘ideal’ J aggregate. In section 5.2, the ratio between the 0-0 and 0-1 peaks of PTCDI and PTCDI-melamine were determined, and found to be much larger for PTCDI. In reference [99], Spano discusses the effect of H and J aggregation on the vibronic structure of fluorescence and adsorption spectra of optically active molecules. J-aggregates exhibit a dominant 0-0 peak while the 0-0 peak of ‘ideal’ H-aggregates is suppressed since the optical transition from the minimum of the exciton bandstructure is forbidden. The difference between the peak ratios of PTCDI and PTCDI-melamine is therefore further evidence that the canted PTCDI phase more closely resembles that of an ‘ideal’ J-aggregate.

Full determination of the relative intensity and position of vibronic sidebands requires calculation of the Franck-Condon factors for each optical transition. Such investigations are available in the literature for bulk materials and oligomers [97], while the vibrational structure of PTCDA on alkali halide substrates was investigated both experimentally and computationally by Hochheim et al [110].

From the calculated exciton bandstructures and experimental results of PTCDI and PTCDI-melamine, it is concluded that the coupling of transition dipoles accounts partially towards the experimentally observed red shift. In section 5.6, shifts arising from intermolecular hydrogen bonding and the adsorption of PTCDI and PTCDA on the substrate are discussed with

reference to calculations carried out by collaborators within the department of Chemistry at the University of Nottingham.

## 5.6. The Fluorescence Shifts of PTCDI and PTCDA Monolayers on hBN

In sections 5.2 and 5.4, the 0-0 fluorescence peaks of solution processed PTCDI, PTCDI-melamine and solution deposited PTCDA were determined and compared to gas phase measurements, see table 5.6.1. In order to better understand the contribution of the substrate and intermolecular hydrogen bonding to the observed shifts, both PTCDA and PTCDI were modelled using time-dependent density functional theory (TD-DFT) by Anton Nizovtsev working with Elena Besley and Nicholas Besley at the School of Chemistry of the University of Nottingham.

	Fluorescence Energy (eV)		Fluorescence Shift: $\Delta E_{\text{tot}}$ (eV)
	hBN (this work)	Doped HND	
PTCDI	$2.214 \pm 0.002$	2.550** [71]	-0.336
PTCDI-Melamine	$2.245 \pm 0.002$	N/A	-0.305
PTCDA	$2.234 \pm 0.002$	2.600 [70]	-0.366

\*\*Measurements carried out for Me-PTCDI doped HND.

**Table 5.6.1.** The experimentally determined energies of the 0-0 fluorescence peaks of solution processed PTCDI, PTCDI-melamine and solution deposited PTCDA on hBN are compared to measurements of doped HND, taken to be gas phase measurements.

TD-DFT was carried out by Dr Anton Nizovtsev using the Q-Chem software package. The modelled adsorption geometry of PTCDI and PTCDA was optimised using the hybrid  $\omega$ B97X-D functional in addition to the cc-pVDZ basis set. The hBN surface was modelled for an array of 65 unit cells, each containing a boron and nitrogen atom. Using TD-DFT at the TD- $\omega$ B97X-D/cc-pVDZ// $\omega$ B97X-D/cc-pVDZ level of theory, the gas phase fluorescence emission energies of PTCDI and PTCDA were calculated to be  $2.41 \pm 0.02$  eV and  $2.43 \pm 0.02$  eV respectively.

Considering the systematic errors often present in TD-DFT calculations of the absolute transition energy, differences between calculations and the experimentally determined fluorescence of Me-PTCDI and PTCDA doped HND are to be expected [71,71]. By modelling the effect of surface adsorption and intermolecular hydrogen bonding in TD-DFT calculations, the shifts arising from these interactions can be calculated and compared to experimental results. Despite the differences between calculations and experimental results, it is anticipated that calculated shifts due to adsorption on a surface and intermolecular bonding are less susceptible to systematic errors, so can be directly compared to experimentally measured shifts. For all shifts calculated using TD-DFT, the error is thought to be in excess of 20 meV.

The calculated shift due to interactions with the surface were considered in two ways. Firstly; the molecule was modelled with the hBN surface included. When the surface is considered in the calculation, both non-resonant interactions due to bonding with the substrate as well as interactions arising from the polarisability of the surface are included. By calculating the geometry of the molecule on the surface, and extracting the fluorescence energy of an isolated molecule in this conformation, the effect of non-resonant interactions with the substrate can be found. In order to consider non-resonant interactions and interactions due to the polarisability of the substrate separately, the shift calculated in the substrate geometry is taken to be the shift due to non-resonant molecule-substrate interactions. From the results of TD-DFT calculations, bonding with the substrate is not expected to lead to a significant fluorescence shift, see table 5.6.2.

Molecule	Transition Dipole Moment (D)	Fluorescence Shift: (eV)	
Notes	Surface Conformation	Adsorption on the Surface	Surface Conformation (Free Space)
<b>PTCDI</b>	8.84	-0.10 ± 0.02	0.00 ± 0.02
<b>PTCDA</b>	8.66	-0.10 ± 0.02	0.00 ± 0.02

**Table 5.6.2.** Transition dipole moments of PTCDI and PTCDA are shown in addition to the calculated fluorescence shifts between the gas phase and molecules adsorbed on hBN and in the surface conformation (gas phase). Values were calculated at the TD- $\omega$ B97X-D/cc-pVDZ// $\omega$ B97X-D/cc-pVDZ level of theory. TD-DFT was carried out by Dr Anton Nizovtsev.

In reference [109], Hoffmann et al measured the transition dipole moments of Me-PTCDI and PTCDA to be  $6.8 \pm 0.7$  D and  $7.4 \pm 0.7$  D respectively. In this work, TD-DFT was used to calculate transition dipole moments, returning values of 8.84 D and 8.66 D for PTCDI and PTCDA in the surface conformation. Later calculations in this section will use calculated TD-DFT values to predict shifts due the coupling of transition dipoles and the polarisability of the surface.

In addition to interactions with the substrate, intermolecular hydrogen bonding is also expected to lead to a fluorescence shift. Using TD-DFT at the TD- $\omega$ B97X-D/cc-pVDZ// $\omega$ B97X-D/cc-pVDZ level of theory, the shifts arising from the formation of different hydrogen bonding junctions were calculated. The first junction considered was PTCDI bonded to two melamine groups. The second was PTCDI bonded to two naphthalene tetracarboxylic diimide (NTCDI) molecules, this molecule was used instead of PTCDI since it forms very similar hydrogen bonding junctions but does not contain a perylene core, which would lead to an additional shift in the calculation due to resonant intermolecular interactions. The calculated shifts due to intermolecular hydrogen bonding are summarised in table 5.6.3.

Junction Type	Calculated Shift: $\Delta E_{\text{int}}$ (eV)
Melamine-PTCDI-melamine	+0.04 ± 0.02
NTCDI-PTCDI-NTCDI	+0.03 ± 0.02

**Table 5.6.3.** The shift due to the formation of hydrogen bonding junctions of PTCDI with melamine and NTCDI molecules were calculated using TD-DFT at the TD- $\omega$ B97X-D/cc-pVDZ// $\omega$ B97X-D/cc-pVDZ level of theory. TD-DFT was carried out by Dr Anton Nizovtsev.

The calculated shifts due to intermolecular hydrogen bonding suggest a relative 0.01 eV blue-shift from PTCDI-melamine to PTCDI, which does not agree with the experimentally observed 0.031 eV red shift. This suggests that the experimentally observed shift occurs due to the coupling of transition dipole moments, discussed in section 5.5. Using estimates for the transition dipole moment of PTCDI calculated using TD-DFT in table 5.6.2, shifts of 0.047 eV and 0.019 eV are calculated for un-screened and screened interactions. Using estimates for the transition dipole moment of PTCDI from TD-DFT gives better agreement with the experimentally measured shift for screened transition dipole moments.

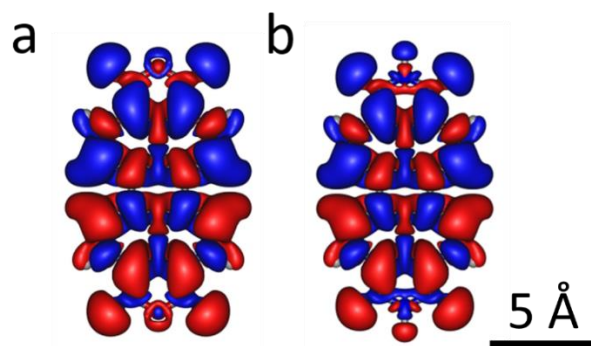


**Figure 5.6.1.** The charge distribution of PTCDA (a) and PTCDI (b) during the 0-0 transition were calculated using TD-DFT at the OT-TD- $\omega$ B97X-D/cc-pVDZ level of theory. Isosurfaces for a charge of ±0.00025 e are shown, where blue and red surfaces correspond to positive and negative charge respectively. Produced by Dr Anton Nizovtsev

In section 5.4, shifts arising due to the polarisability of the substrate were considered. In the model presented, both the transition dipole moment and its image were taken to be point dipoles. Since the expected separation of transition dipole moments with their image dipoles is smaller than the charge distribution of the transition dipole moment, the point dipole approximation does not hold.

Using TD-DFT, the charge distributions of the transition dipole moments of PTCDI and PTCDA were calculated, see figure 5.6.1. Using Wolfram Mathematica, the calculated charge distributions were read and used to calculate the interaction energy,  $\Delta E_{\text{image}}$ , of the charge distribution and its image using equation 5.6.1, where  $q$  is the charge contained within each voxel of the transition dipole moment charge distribution,  $r$  is the separation between voxels and subscripts a and b denote voxels within the three dimensional charge distribution of a transition dipole moment and its image, see table 5.6.4. The separation of the transition dipole moment and its image dipole were taken to be the distance between adsorbed PTCDI molecules and the hBN surface, 0.31 nm, calculated using TD-DFT at the (MOM-)  $\omega$ B97X-D/cc-pVDZ level of theory.

$$\Delta E_{\text{image}} = \frac{1}{4\pi\epsilon_0} \frac{n^2-1}{n^2+1} \sum_{a,b} \frac{q_a q_b}{r_{ab}} \quad (5.6.1)$$

From table 5.6.4, it is seen that for a 0.31 nm separation between dipoles, the point dipole approximation returns a much larger shift than is measured experimentally. When the charge distribution of transition dipole moments is taken into account, the shift is reduced by approximately an order of magnitude. The calculated shifts, introduced in this section and section 5.5, are compared to experimental results in table 5.6.5.

Molecule	Interaction Energy: $\Delta E_{g-s}$ (eV)	
	Point Dipole	Calculated Distribution
PTCDI	0.966 (-0.572)	-0.095
PTCDA	0.927 (-0.677)	-0.095

**Table 5.6.4.** The interaction energies of PTCDI and PTCDA transition dipole moments and their images were calculated for a substrate with a refractive index of 1.97. The separation between the transition dipole moment and its image was 0.31 nm. The interaction of point dipoles was calculated using transition dipole moments calculated using TD-DFT in addition to experimental values available in the literature [109], which are shown in parentheses. The interaction energy of the calculated transition dipole charge distribution with its image was calculated using Wolfram Mathematica. TD-DFT was carried out by Dr Anton Nizovtsev.

Comparing the experimentally observed shifts to each of the interactions considered, it is seen that the polarisability of the substrate and the coupling of transition dipole moments both contribute towards the large experimentally observed red shifts,  $\Delta E_{tot}$ . Comparing the fluorescence of PTCDI and PTCDI-melamine to the calculated exciton bandstructure of each phase, a red shift due to the coupling of transition dipole moments has been confirmed. Intermolecular hydrogen bonding, calculated using TD-DFT, is expected to lead to a blue shift between PTCDI-melamine and PTCDI. It is therefore concluded that the shift due to intermolecular interactions,  $\Delta E_{int}$ , is dominated by transition dipole moment coupling.

The experimentally determined shift from HND,  $\Delta E_{tot}$ , is much larger than the calculated shift due to the coupling of transition dipole moments. In the case of PTCDI and PTCDA, a larger shift due to interactions with the substrate is thought to occur,  $\Delta E_{g-s} > \Delta E_{int}$ . It is thought that the substrate shift,  $\Delta E_{g-s}$ , is due to interactions with the dielectric surface. Evidence that the polarisability plays a role in the fluorescence shift of molecular aggregates on surfaces comes from the trend seen in figure 5.4.4, in addition to TD-DFT calculations, which predict that the non-resonant shifts due to adsorption on the surface is small compared to the experimentally observed shift. Considering calculated charge distributions instead of point dipoles leads to a

reduction in the interaction energy, see table 5.6.4. Considering the terms in equation 5.4.3, small changes in the value of the transition dipole moment and transition dipole moment-image dipole separation could lead to dramatic changes in the estimated shift,  $\Delta E_{g-s}$ . These factors are expected to account for the differences between the experimental and calculated shifts.

Shift	PTCDI	PTCDI-Melamine	PTCDA
<b>Experimental HND (eV)</b>	2.550 [71]	N/A	2.600 [70]
<b>Experimental hBN (eV)</b>	2.214	2.245	2.234
<b>Experimental Red Shift: <math>\Delta E_{tot}</math> (eV)</b>	-0.336	-0.305	-0.366
<b>Dipole Coupling: <math>\Delta E_{int}</math> (eV)</b>	-0.084 (-0.034)	-0.037 (-0.015)	-0.019 (-0.008) [13]
<b>Hydrogen Bonding: <math>\Delta E_{int}</math> (eV)</b>	+0.04	+0.03	N/A
<b>Surface Adsorption: <math>\Delta E_{g-s}</math> (eV)</b>	0.00 (-0.10)	0.00 (-0.10)	0.00 (-0.10)
<b>Polarisable Substrate: <math>\Delta E_{g-s}</math> (eV)</b>	-0.095	-0.095	-0.095

**Figure 5.6.5.** The fluorescence of Me-PTCDI and PTCDA doped HND are compared to experimental measurements of solution deposited monolayers on hBN. Shifts due to resonant intermolecular interactions were calculated from exciton bandstructures, values in parentheses include screening. Calculated shifts due to intermolecular hydrogen bonding are also included. The calculated shift for a molecule in the surface geometry is shown, with the value for surface adsorption in parentheses. Finally, shifts due to the interaction of transition dipole moments with image dipoles beneath the dielectric were calculated using charge distributions from TD-DFT and a separation of 0.31 nm.

In reference [81], Forker et al discuss the similar optical transition energies measured from PTCDA on noble metal surfaces, monolayer graphene on SiC and monolayer hBN on Pt (111). The results presented in this thesis are interpreted differently to those measured by Forker et al, who discount effects arising from the polarisability of the substrate and discuss shifts due to intermolecular interactions,  $\Delta E_{int}$ , which are in good agreement with previous studies by the Sokolowski group [13]. Exploring the effect of interstitial layers such as monolayers of hBN or a molecular wetting layer on the fluorescence of organic molecules, as was carried out by

Forker et al, would be a good way to test current understanding of molecular fluorescence at interfaces, one such experiment is discussed in chapter 7.

## 5.7. Conclusions

In this chapter, the fluorescence of monolayers of the perylene derivatives PTCDI and PTCDA at dielectric interfaces has been discussed. Firstly, a large red shift is observed due to adsorption of flat lying molecules on a dielectric hBN substrate. This shift is thought to occur due to the interaction of transition dipole moments with image dipoles beneath the dielectric hBN surface. Secondly, resonant and non-resonant intermolecular interactions have been calculated for the canted PTCDI phase and PTCDI-melamine on hBN. A red shift between PTCDI-melamine and PTCDI is described in terms of resonant coupling of transition dipole moments, due to differences between the two packing structures. By considering TD-DFT calculations of the charge distributions of the transition dipole moments, fluorescence shifts of PTCDA and PTCDI due to adsorption on the hBN surface and the formation of hydrogen bonding junctions, significant contributions to the measured fluorescence shifts due to non-resonant interactions were discounted. Instead it is thought that the shifts arise due to the coupling of screened transition dipole moments and interactions with the polarisable substrate.

## **Chapter 6:**

# **$C_{60}$ Thin Films and PTCDI/ $C_{60}$ Heterostructures on Hexagonal Boron Nitride**

## **6. C<sub>60</sub> Thin Films and PTCDI/C<sub>60</sub> Heterostructures on Hexagonal Boron Nitride**

In this chapter, the deposition of Buckminsterfullerene (C<sub>60</sub>) on hBN by sublimation in vacuum will be discussed. The morphology of C<sub>60</sub> on hBN will be investigated for sub-monolayer coverages grown at a range of substrate temperatures during deposition and compared to published results for C<sub>60</sub> adsorbed on other insulating surfaces. The coverage dependence of the morphology of C<sub>60</sub> thin films will also be considered. Finally, the growth of C<sub>60</sub>/PTCDI molecular heterostructures by sublimation in vacuum will be discussed.

### **6.1. Overview**

Fullerenes are commonly studied for their functional properties, which have particular relevance to the field of molecular electronics. A range of fullerene structures can be synthesised and functionalised to further tailor their structural, electronic and optical properties. C<sub>60</sub> is commonly studied by the surface science community, where the morphology of sublimed and solution deposited C<sub>60</sub> thin films can be investigated using SPM techniques on a range of substrates [30,31].

The study of the morphology of C<sub>60</sub> thin films on insulators is interesting for a number of reasons. Firstly, investigating molecular self-assembly on insulating substrates has recently become more accessible through advances in non-contact mode AFM, as well as AFM carried out under ambient conditions. Secondly, insulating surfaces also allow the electronic and optical properties of C<sub>60</sub> thin films to be explored in a way not previously possible using conducting substrates. C<sub>60</sub> is also of interest for its use in organic electronic devices, where the interface between C<sub>60</sub> and other functional layers is critical to their performance.

The incorporation of C<sub>60</sub> into molecular heterostructures is also a promising avenue for further research. The morphology of co-deposited C<sub>60</sub> and PTCDI was studied on an alkali halide substrate by Loske et al [111], while several accounts of molecular hetero-epitaxy are available in the literature [10,11,112]. The study of molecular heterostructures on both insulating and conductive substrates could lead to the refinement and development of a number of electronic devices. Molecular layers could be used as wetting layers to decouple layers within heterostructures [11] or as charge transfer complexes consisting of stacked n-type and p-type molecular layers [113].

## 6.2. The Morphology of Sub-Monolayer C<sub>60</sub> films on hBN

C<sub>60</sub> was sublimed onto hBN substrates using the same experimental configuration described in sections 3.4 and 4.2. hBN flakes were deposited onto 300 nm SiO<sub>2</sub>/Si substrates by mechanical exfoliation before cleaning using flame-annealing and furnace-cleaning procedures outlined in section 3.3. hBN samples were annealed in vacuum prior to deposition of C<sub>60</sub> from a Knudsen cell held at 374 °C. For all depositions, a rate of 0.23 ± 0.06 ML/min was used. The deposition was calibrated by producing a thick film of C<sub>60</sub> on SiO<sub>2</sub> and comparing the thickness of the film, extracted from AFM results, to the thickness measured using a quartz crystal microbalance (QCM).

The morphology of sub-monolayer coverages of C<sub>60</sub> was investigated by depositing a 0.4 ML coverage onto flame-annealed hBN held at room temperature. Images of the C<sub>60</sub> film were acquired using AFM under ambient conditions, see figure 6.2.1. Islands of C<sub>60</sub> had an irregular shape and had additional higher layers. In order to identify the number of layers of C<sub>60</sub> present within islands, height profiles were extracted from AFM images. This was not straightforward, since height profiles were different between images and samples of C<sub>60</sub>, as discussed below.

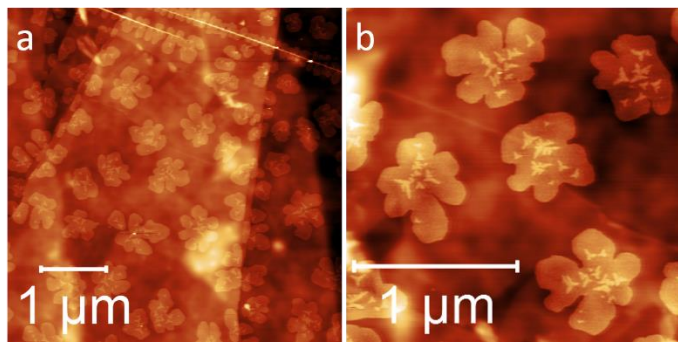


**Figure 6.2.1.** AFM images of a 0.4 ML coverage of sublimed C<sub>60</sub>. Deposition was carried out at room temperature on flame-annealed hBN on SiO<sub>2</sub>. The island morphology is shown in 5 μm (a) and 2 μm images (b), where both the irregular island shape and additional layers of C<sub>60</sub> can be seen.

The height of C<sub>60</sub> islands, extracted from AFM images, was found to vary between samples although there were no differences in the dose of C<sub>60</sub> or the island morphology. The measured height of islands was found to vary between 1 nm and 3 nm. Initially it was thought that C<sub>60</sub> formed multi-layers on hBN, leading to a variation in the island height, but this idea was discarded for a number of reasons. Firstly, the deposition of C<sub>60</sub> had been calibrated using AFM measurements of a thick film. The expected surface coverage is in good agreement with the coverage of sub-monolayer films grown at room temperature, assuming monolayer islands. Secondly, though areas of second layer C<sub>60</sub> were observed on top of islands, no other indicative features of multi-layers, such as step edges, were observed. Overall, the variation in the island height between samples of similar coverage and morphology is suggestive of artefacts in the AFM height measurement.

The presence of artefacts in AFM results, leading to an error in the measurement of the height of islands, was investigated by acquiring a series of AFM images from the same area using different acquisition parameters. In this work, the morphology of molecular layers is studied using AFM in AC mode (also known as tapping mode or non-contact mode). When using AFM in this mode, the cantilever is driven on-resonance with a user-specified amplitude. The amplitude of the cantilever in air is referred to as the free air amplitude. AC mode AFM uses

a feedback loop to maintain the amplitude of the cantilever at a user-specified setpoint, see section 3.1. As the tip is lowered towards the sample, its amplitude is reduced due to tip-sample interactions. Deflections of the cantilever are detected by measuring the position of a reflected laser spot using a photodetector. The deflection is therefore expressed as the voltage measured by the detector, this quantity can be used to calculate the amplitude of a cantilever, given its optical sensitivity [114].

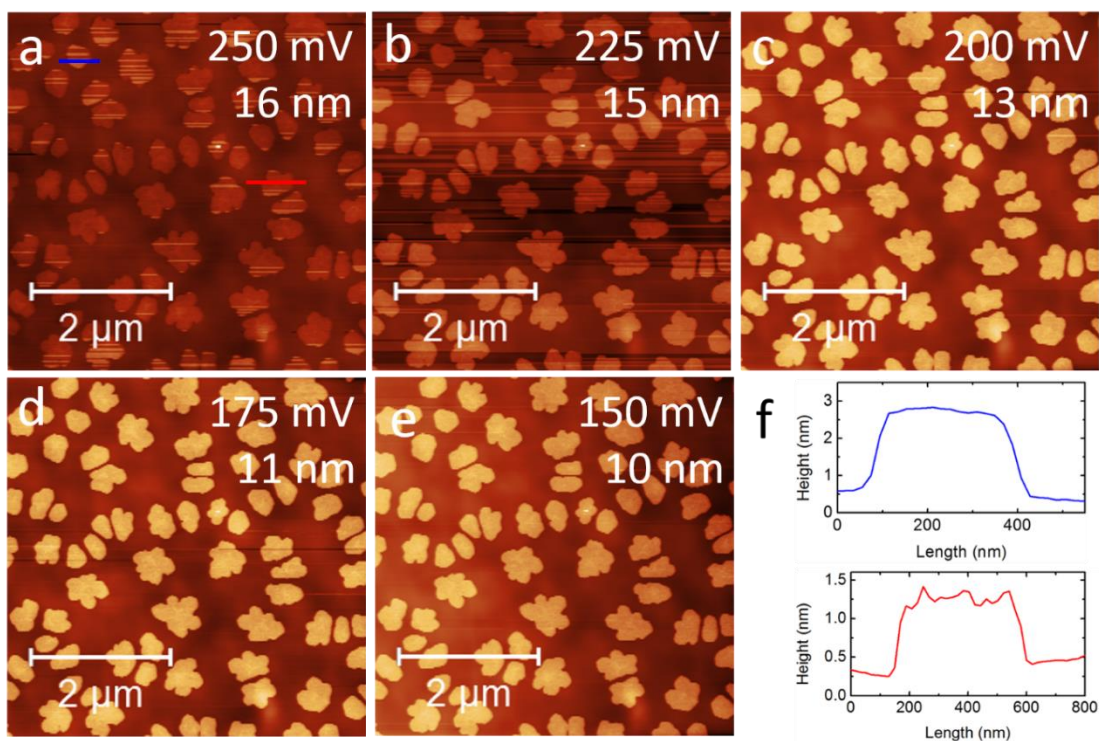


**Figure 6.2.2.** AFM images of C<sub>60</sub> on hBN were acquired from the same area. Images (a-e) were acquired at a range of set points for a cantilever driven at a frequency of 69.30 kHz and with a 500 mV (33 nm) free air amplitude. Setpoints are shown inset, in addition to the oscillation amplitude, calculated using the optical sensitivity (65 nm/V) of the type of cantilevers used. Two line profiles from image (a) indicate two apparent island heights.

By acquiring a sequence of AFM images from the same area with a series of setpoints, the effect of the tip-sample separation on the apparent height of C<sub>60</sub> islands was investigated. At lower setpoints, a stronger repulsive force between the tip and sample is required to reduce the amplitude of the cantilever.

Images of C<sub>60</sub> grown at room temperature are shown in figure 6.2.2 for a range of AC-mode AFM setpoints; all other imaging parameters were kept constant. These images were acquired using a standard silicon cantilever from Budget Sensors, driven on resonance at a frequency of 69.30 kHz and with a free-air amplitude of 500 mV (33 nm). Using a setpoint of 250 mV, the C<sub>60</sub> islands were observed to have a height of  $1.0 \pm 0.1$  nm, which is comparable to the height of monolayer C<sub>60</sub> islands on a range of substrates [115]. Bands of higher topography were also observed over islands, in the direction of the tip rastering. As the setpoint was reduced below 225 mV, the apparent height of islands increased. The apparent height of C<sub>60</sub> islands grown at room temperature, extracted from AFM images acquired at a range of setpoints, are shown in table 6.2.1.

AFM Set point (mV)	Apparent Height (nm)
250 (a)	1.0 and 2.4
225 (b)	2.7
200 (c)	2.9
175 (d)	2.9
150 (e)	2.9

**Table 6.2.1.** The apparent island heights observed at the different AFM setpoints used in figure 6.2.2 are shown. At 250 mV, two apparent island heights are observed, the 1.0 nm value corresponds to monolayer C<sub>60</sub>.

Lateral variations in the tip-sample interaction at short distances, in this case between C<sub>60</sub> islands and the hBN substrate, could lead to variations in the sample topography with changing setpoint. The effect of the tip-sample interaction has also been studied using non-contact AFM in UHV conditions with similar results [29,115,116]. In reference [115], Sadewasser and Lux-Steiner observed bias-dependent contrast variation for C<sub>60</sub> on HOPG, while inverted contrast was seen by Loske et al for C<sub>60</sub> islands on calcite [29].

In this investigation, a number of factors could potentially account for the observed height variation of islands. These include mobile C<sub>60</sub> adsorbed on the tip, the exchange of a C<sub>60</sub>

molecule between islands and the tip at island edges and a difference in the tip-sample interaction between C<sub>60</sub> islands and hBN. The bands of higher topography over islands, in the direction of the scan suggest that the tip state changes during scanning, see figure 6.2.2a. The morphology of the islands did not change over successive scans, which suggests that the transfer of molecules between the tip and sample did not occur at island edges. Instead, it is thought that C<sub>60</sub> could be present and mobile over the surface of the tip in response to the tip-sample potential, see figure 6.2.3. At reduced tip-sample distances, the tip-sample potential could cause a C<sub>60</sub> molecule to migrate to the tip when above islands, leading to an increase in the island height extracted from AFM images.

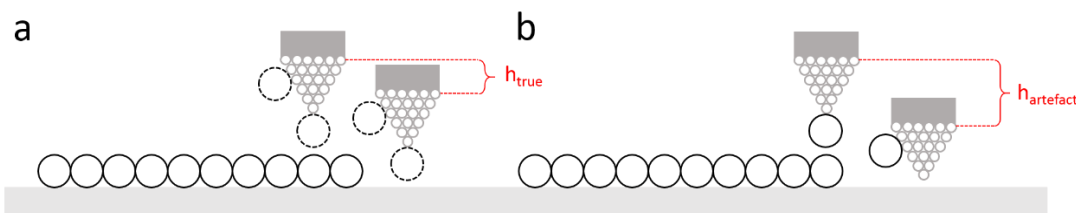


**Figure 6.2.3.** The position of the tip at the minimum tip-sample separation above islands and the hBN substrate is illustrated for the case of a stable tip (a) and for a tip which changes state due to a mobile C<sub>60</sub> molecule (b). In (a), two possible positions for C<sub>60</sub> molecules on the tip are indicated.

The values extracted from AFM images acquired at the greatest tip-sample distances were taken to be ‘true’ height measurements without artefacts. At the largest tip-sample separations, island heights of  $1.0 \pm 0.1$  nm are measured for 0.4 ML coverages of C<sub>60</sub> grown at room temperature. These values are in good agreement with published results for C<sub>60</sub> monolayers [30]. The measured island height as well as the agreement between the surface coverage and dose of C<sub>60</sub> suggests islands grown at room temperature are monolayers. This conclusion is further supported by results shown in section 6.3, where the morphology of C<sub>60</sub> grown at a range of substrate temperatures is explored.

In addition to flame-annealed hBN, the morphology of C<sub>60</sub> deposited on furnace-cleaned hBN substrates was also investigated, see figure 6.2.4. On furnace-cleaned hBN, an increase in the island density to  $10 \pm 3 \text{ } \mu\text{m}^{-2}$ , compared to  $2.7 \pm 0.6 \text{ } \mu\text{m}^{-2}$  for flame-annealed hBN was observed. The overall appearance of C<sub>60</sub> islands was found to be comparable on both flame-annealed and furnace cleaned substrates. A possible reason for the difference between furnace-cleaned and flame-annealed hBN substrates could be the presence of contamination, which could act as a nucleation site for C<sub>60</sub> islands.

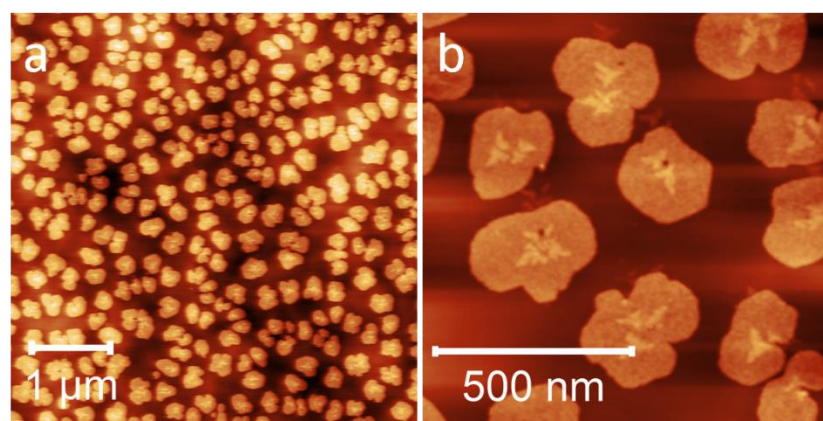


**Figure 6.2.4.** Sub-monolayer coverages of C<sub>60</sub> were deposited by sublimation in vacuum on furnace-cleaned hBN on SiO<sub>2</sub> held at room temperature. Images of the sample surface were acquired using AFM with 10  $\mu\text{m}$  (a) and 1  $\mu\text{m}$  scales (b).

### 6.3. The Morphology of Sub-Monolayer C<sub>60</sub> films on hBN: Temperature Dependence

The effect of the growth temperature on the morphology of sub-monolayer coverages of C<sub>60</sub> on hBN was investigated by growing a series of C<sub>60</sub> films, of 0.4 ML coverage, for a range of substrate temperatures during deposition. The total surface coverage, extracted from AFM images, can be affected by the number of layers within islands and the sticking coefficient. The morphology, as determined using AFM, of C<sub>60</sub> films grown at a range of temperatures on flame-annealed hBN on SiO<sub>2</sub> is shown in figure 6.3.1.

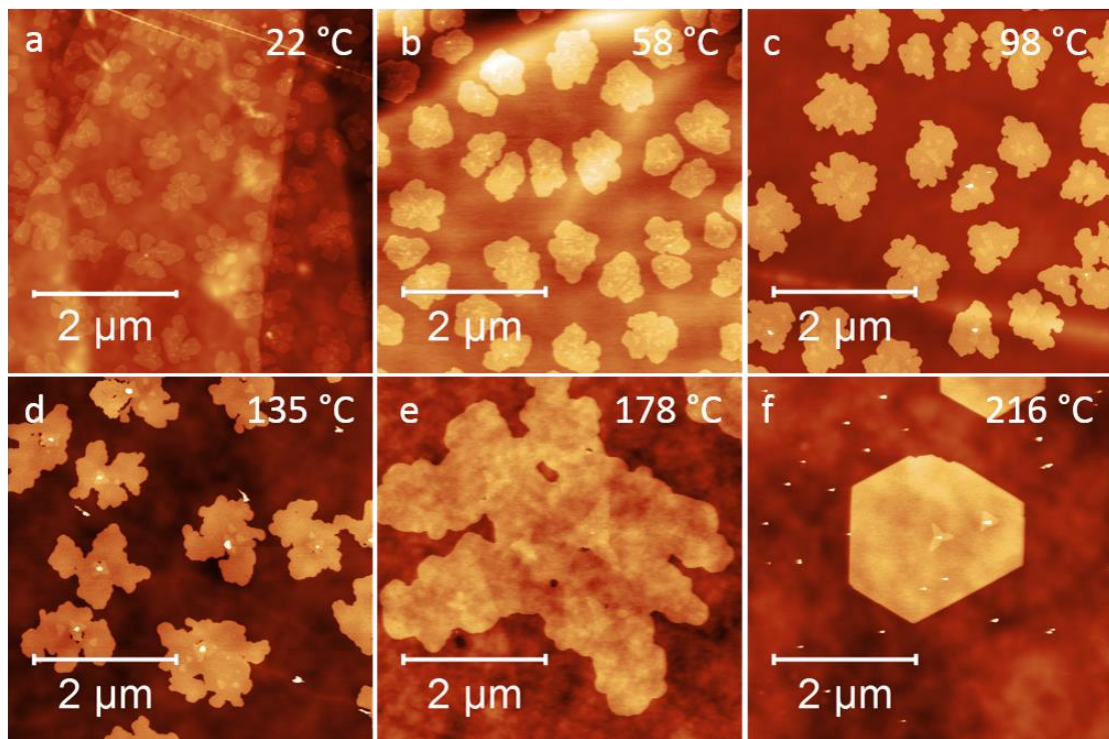


**Figure 6.3.1.** The deposition of sub-monolayer coverages of C<sub>60</sub> by sublimation in vacuum onto flame-annealed hBN substrates yields a range of island morphologies, depending upon the substrate temperature during deposition. AFM images of C<sub>60</sub> deposited onto flame-annealed hBN on SiO<sub>2</sub> at different temperatures are shown (a-f).

In the previous section, it was established that C<sub>60</sub> forms monolayer islands on hBN substrates held at room temperature. Such C<sub>60</sub> islands had no discernible facets and instead had a dendritic island shape with irregular edges, second layers were also observed on top of monolayer islands. The morphology of C<sub>60</sub> films grown at 58 °C and 98 °C, shown in figure 6.3.1b and c, was similar to that of films grown at room temperature. The island density decreased and island size increased with increasing substrate temperature between these three samples. All islands had an irregular shape and contained fractal-like second layers, see figure 6.3.2.

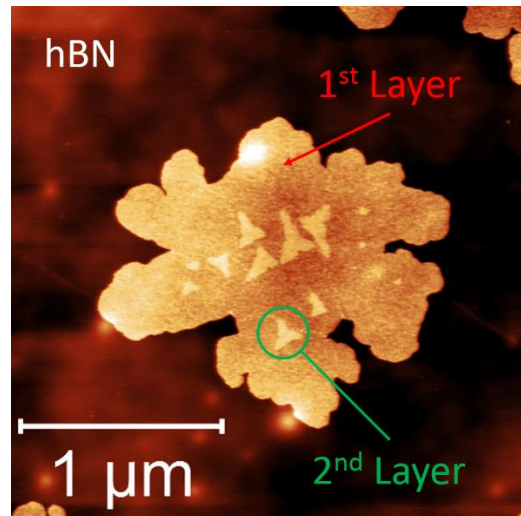


**Figure 6.3.2.** An image, acquired using AFM, of a C<sub>60</sub> island grown on flame-annealed hBN on SiO<sub>2</sub> at 58 °C. The substrate, monolayer and second-layer regions are indicated.

A C<sub>60</sub> film grown at 135 °C was also found to form monolayers with an irregular island morphology, but the size of dendritic features relative to the size of islands increased, see figure 6.3.1d. The amount of second layer C<sub>60</sub> on top of monolayers also decreased. At 178 °C, C<sub>60</sub> was found to form dendritic monolayer islands, seen in figure 6.3.1e and figure 6.3.3. The aspect ratio, the ratio of the maximum and minimum diameters of islands, was greater for dendritic monolayer islands grown at 178 °C than for samples grown at lower temperatures. In addition to monolayer islands, bi-layer islands with distinctive faceted structure were also found to co-exist on the surface, see figure 6.3.3. The morphology of the sample grown at 178 °C provides further evidence that layers grown at temperatures of 135 °C and below have monolayer height since the monolayer and bi-layer regions can easily be distinguished.

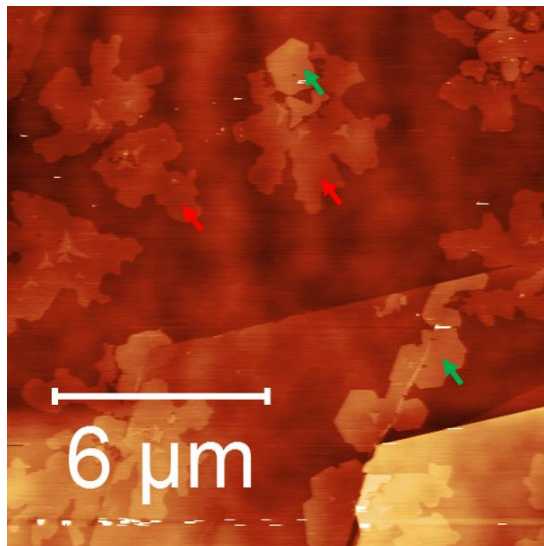


**Figure 6.3.3.** A 15  $\mu\text{m}$  AFM image of a sub-monolayer coverage of  $\text{C}_{60}$  grown at 178  $^{\circ}\text{C}$ . At 178  $^{\circ}\text{C}$ ,  $\text{C}_{60}$  on hBN has been observed to form both dendritic monolayer and faceted bi-layer islands. Monolayer and bi-layer islands are indicated by red and green arrows respectively.

At 216  $^{\circ}\text{C}$ , only faceted bi-layer  $\text{C}_{60}$  islands were observed, see figure 6.3.1f. The facets of bi-layer  $\text{C}_{60}$  islands are oriented at multiples of 60 $^{\circ}$ . While facets were not observed in monolayer islands, second layers were seen with a triangular fractal-like structure, these additional layers had similar facet orientations across individual monolayer islands, see figure 6.2.1b and 6.3.2. The faceted structure of bi-layer islands and second layer regions on top of monolayers is a consequence of the hexagonal close packing geometry expected for  $\text{C}_{60}$  thin films on a variety of substrates [117].

The presence of bi-layers at 216  $^{\circ}\text{C}$  was confirmed by again carrying out AC mode AFM at a series of setpoints, as described in section 6.2. Images of the same  $\text{C}_{60}$  island were acquired using a second cantilever, driven on-resonance at 67.33 kHz, with a drive amplitude of 37.2 mV and a free air amplitude of 500 mV (33 nm). A sequence of AFM images are shown in figure 6.3.4, while the apparent island heights, extracted from AFM images, are shown in table 6.3.1. At 375 mV, lines of higher topography were observed in the direction of the scan, this gave rise to two apparent island heights of  $1.8 \pm 0.1$  nm and  $3.1 \pm 0.1$  nm.

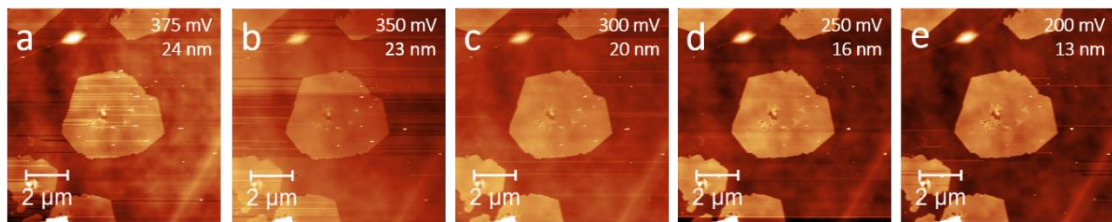


**Figure 6.3.4.** Successive AFM images, acquired from  $C_{60}$  on hBN on  $\text{SiO}_2$  grown at  $216\text{ }^\circ\text{C}$  with decreasing setpoints (a-e) show a similar behaviour to that seen in figure 6.2.2. Table 6.3.1 shows the apparent height of islands, extracted from AFM images taken at each setpoint, with the  $1.8\text{ nm}$  measurement taken at  $375\text{ mV}$  corresponding to bi-layer  $C_{60}$ . The cantilever, its frequency, drive amplitude and free air amplitude were maintained for each of the images. The value below the setpoint is the amplitude of the cantilever, calculated using the optical sensitivity ( $65\text{ nm/V}$ ) for the type of cantilevers used.

Set point (mV)	Height (nm)
375 (a)	1.8 & 3.1
350 (b)	2.0 & 3.3
300 (c)	3.3
250 (d)	3.2
200 (e)	3.3

**Table 6.3.1.** The apparent height of bi-layer islands, extracted from AFM images acquired at different setpoints are shown, see figure 6.3.4. At  $375\text{ mV}$ , two apparent island heights are measured, with  $1.8 \pm 0.1\text{ nm}$  corresponding to bi-layer  $C_{60}$ .

The measured island height of  $1.8 \pm 0.1\text{ nm}$ , acquired at the maximum tip-sample separation, is in good agreement with previous measurements of bi-layer  $C_{60}$ , where molecules sit above hollow sites in the first layer [30], see figure 6.3.5. As the setpoint was decreased further, the apparent height of islands was observed to increase. The greater island heights measured at lower setpoints are thought to be a consequence of imaging artefacts, discussed in section 6.2.

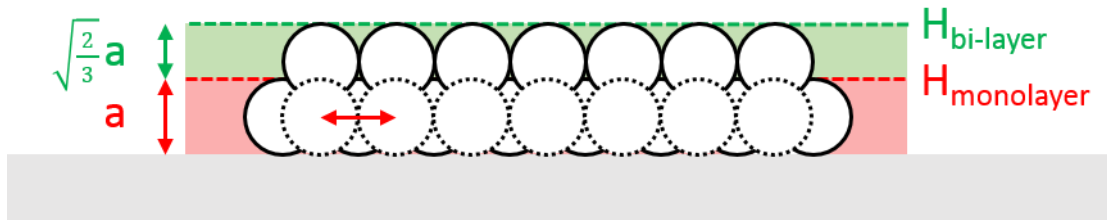


**Figure 6.3.5.** For spherical molecules in a hexagonal close packing arrangement, second-layer molecules occupy hollow sites of the first layer. The occupation of hollow sites leads to a reduction in the height of the second layer compared to that of the monolayer.

The maximum size, coverage and density of C<sub>60</sub> islands was extracted from AFM images of films grown at a range of temperatures. These values are plotted in figure 6.3.6, and where repeated, were highly reproducible. In figure 6.3.6.a, the island size is shown to increase with increasing substrate temperature during deposition up to 216 °C. The decrease in the island size and coverage at 216 °C was due to the formation of bi-layer islands, which contain twice the amount of C<sub>60</sub> for a given coverage. The reduction in coverage of approximately 50 % upon the transition to solely faceted islands at 216° is further evidence that C<sub>60</sub> formed only monolayer islands below 135 °C and only bi-layer islands at temperatures of 216 °C.

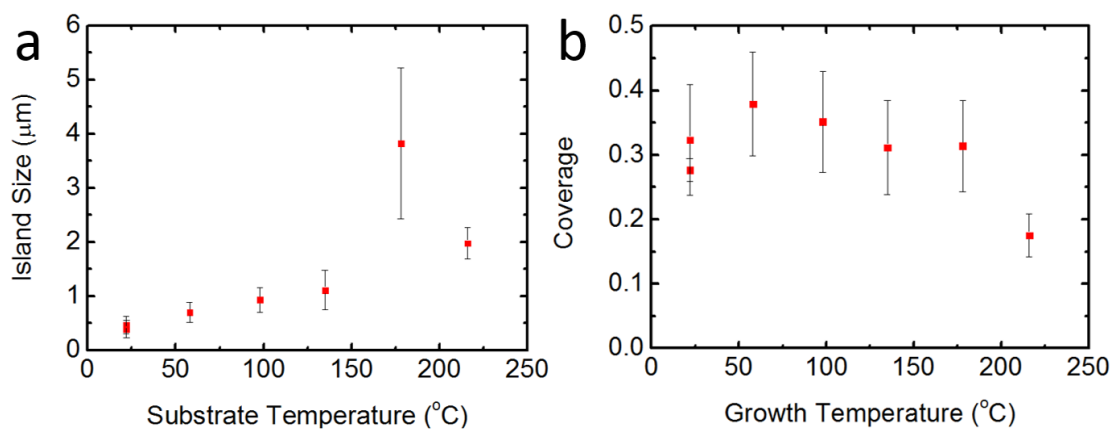


**Figure 6.3.6.** The dependence of island size (a) and coverage (b) on the growth temperature for C<sub>60</sub> deposited on flame-annealed hBN substrates is shown. In each case the same (sub-monolayer) amount of material, measured using a QCM, was deposited. The island properties were extracted from AFM images.

The morphology of C<sub>60</sub> on hBN at room temperature is comparable to that reported by Yamamoto et al on molybdenum disulphide [118]. With increasing temperature, up to 178 °C, the size of monolayer islands was observed to increase while the island density was found to decrease. The density of critical islands, n, for growth in the complete condensation regime, is dependent upon, R, the deposition rate, T, the substrate temperature, E<sub>i</sub>, the critical cluster binding energy and, E<sub>d</sub>, the diffusion barrier, see equation 6.3.1.

$$J \propto R \exp\left(\frac{E_i + iE_d}{(i+2)k_B T}\right) \quad (6.3.1)$$

The decrease in the island density with increasing growth temperature is in good qualitative agreement with equation 6.3.1 [19]. By fitting the island densities plotted in figure 6.3.7, a value for the exponent of equation 6.3.1, (E<sub>i</sub>+iE<sub>d</sub>)/(i+2), of 0.17 ± 0.01 eV was extracted. In this thesis, it was not possible to experimentally determine the critical cluster size, i, in order to measure the diffusion barrier. Using a value of 0.27 eV for the C<sub>60</sub>-C<sub>60</sub> intermolecular bonding energy, available in the literature [119,120,121], a critical cluster size of i=2 returned the most realistic estimate for the diffusion barrier, 0.21 ± 0.01 eV. For comparison, a previous study by Loske et al, measured the diffusion barrier, E<sub>d</sub>, of C<sub>60</sub> on calcium fluoride (CaF<sub>2</sub>) to be 0.21 ± 0.02 eV [21].

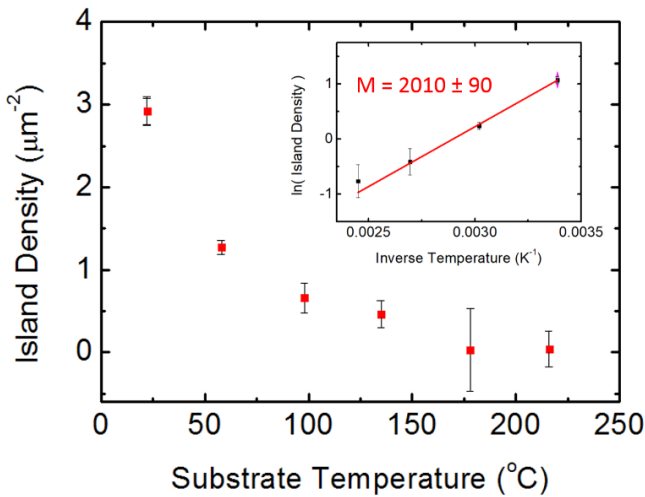


**Figure 6.3.7.** The dependence of the island density on the substrate temperature was extracted from AFM images and is plotted above. The island density was also plotted on a logarithmic scale (inset) and fitted in order to extract an estimate for the quantities in equation 6.3.1.

In order to investigate the morphology of  $\text{C}_{60}$  islands further, the orientation of island edges was extracted from AFM images of samples grown at room temperature and  $216^{\circ}\text{C}$ , a histogram of the island orientations is shown in figure 6.3.8 with a bin size of  $5^{\circ}$ . At room temperature, no preferred orientations were observed for edges across a sample of islands over a region of a monocrystalline hBN. The presence of 6 preferred orientations of  $\text{C}_{60}$  bi-layers implies that they have two preferred alignments with respect to the hBN substrate. This could occur either through two misaligned arrangements of  $\text{C}_{60}$ , at an angle of  $\pm 15^{\circ}$  to the lattice direction of hBN, or one aligned arrangement and a second arrangement misaligned by  $30^{\circ}$ .

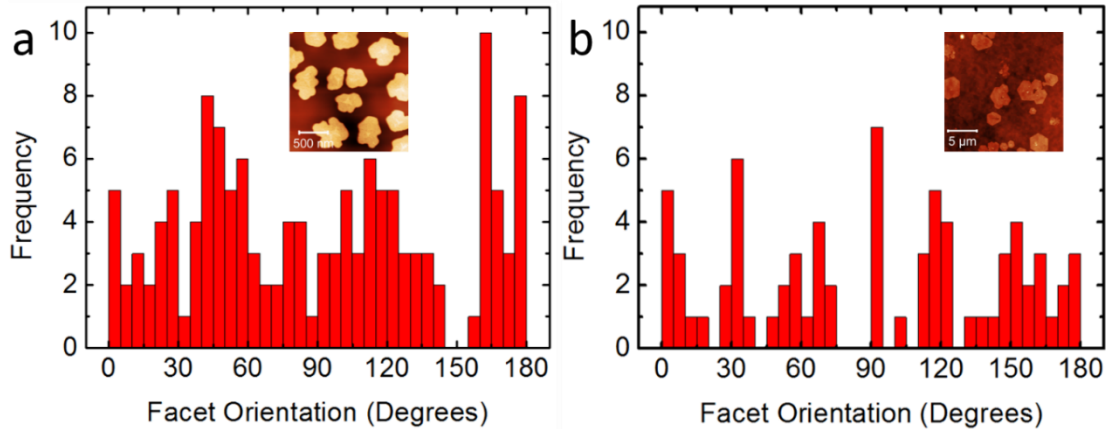


**Figure 6.3.8.** For sub-monolayer coverages of C<sub>60</sub> on flame-annealed hBN on SiO<sub>2</sub> grown at room temperature (a) and 216 °C (b), the orientation of facets were extracted from AFM images (examples inset) and plotted as a histogram.

The morphology of C<sub>60</sub> has been studied extensively on alkali halide and calcite substrates, where the interplay between hopping from the substrate surface to the top of the C<sub>60</sub> monolayer and diffusion lead to a range of thin film morphologies [28,30,31], these processes are illustrated in figure 6.3.9. In [30], Körner et al used a Monte Carlo simulation to model the growth of two different monolayer island morphologies and a faceted bi-layer morphology. In the model, the rate at which C<sub>60</sub> molecules diffuse across an alkali halide substrate is considered, in addition to the rate of upward hopping from the alkali halide surface to a second C<sub>60</sub> layer. The rate of upward hopping is determined by the Ehrlich-Schwoebel barrier, which is dependent upon the adsorption energy of substrate, second layer and intermediate binding sites.

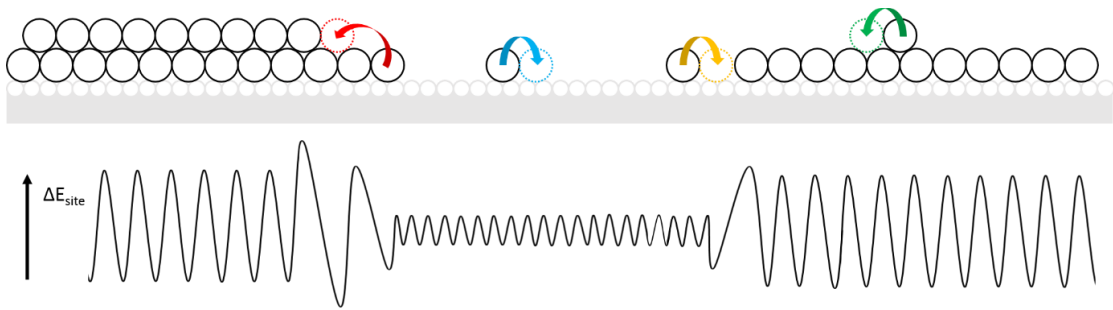


**Figure 6.3.9.**  $C_{60}$  molecules, denoted by black circles, can move between different binding sites on the surface by diffusion across the substrate and upwards hopping to the second layer. Diffusion across the surface (blue), diffusion across a  $C_{60}$  island (green), diffusion to an island edge (yellow) and hopping to the second layer (red) are shown in addition to the potential (below).

Comparison of images of  $C_{60}$  grown on hBN with the literature suggests that at substrate temperature  $T_s > 178$  °C, thermally activated upwards hopping from the hBN surface to the second  $C_{60}$  layer, which is controlled by the Ehrlich Schwoebel barrier, occurs at a similar rate to the addition of molecules at the edges of pre-formed islands [33,34]. Molecules at an island edge can therefore hop from the hBN surface and form a complete second layer of  $C_{60}$  during island formation. Bi-layer  $C_{60}$  islands have been observed on a number of substrates, where multi-layers are energetically favourable due to a greater interaction energy between  $C_{60}$  molecules than with the substrate. On many substrates, upward hopping is kinetically suppressed at lower temperatures, leading to monolayer island morphologies below a specific threshold temperature. The observations of bi-layers at  $T_s > 178$  °C suggests that this is also the case for hBN.

At  $T_s = 178$  °C, the presence of monolayer and bi-layer  $C_{60}$  islands could be due to local variations in the rate at which molecules diffuse to island edges. If the rate of upwards hopping and diffusion to island edges occur on a similar time scale, different island morphologies may be seen at temperatures close to the thermal activation temperature of upwards hopping.

The growth of sub-monolayer  $C_{60}$  films was also investigated on potassium chloride (KCl). Commercially available KCl crystals were mechanically cleaved, loaded into the vacuum deposition system and annealed in vacuum to approximately 450 °C. The sample was then cooled to room temperature prior to the deposition of 0.4 ML of  $C_{60}$ , before venting to nitrogen. The morphology of sublimed  $C_{60}$  on KCl, of which images were acquired using AFM under ambient conditions, is shown in figure 6.3.10. It is surprising that it was possible to determine the morphology of sublimed  $C_{60}$  on KCl under ambient conditions, given that KCl is a hygroscopic surface.

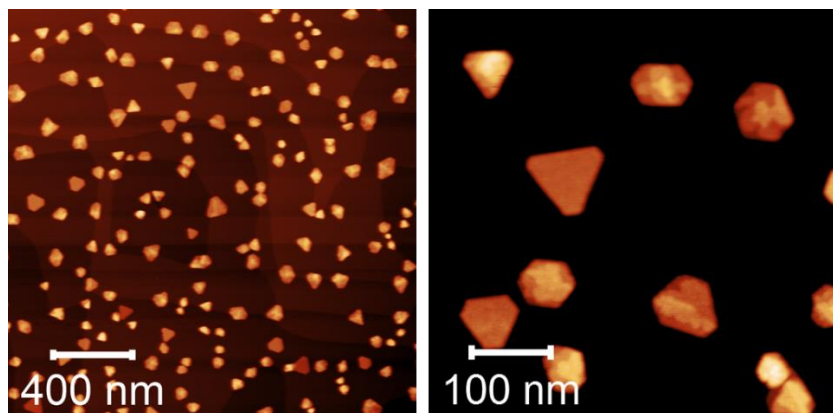


**Figure 6.3.10.** AFM images of a sub-monolayer coverage of  $C_{60}$ , deposited on mechanically cleaved KCl substrates held at room temperature during deposition. Images were acquired immediately after removal from vacuum.

From AFM images, three distinct island morphologies were observed in addition to terraces of the KCl substrate, measured to have a height of  $0.3 \pm 0.1$  nm. In addition to bi-layer triangular islands, multi-layer triangular islands and compact hexagonal islands were observed. These multi-layer islands appeared to have a complete bi-layer and partially completed 3<sup>rd</sup> and 4<sup>th</sup> layers. The observation of islands with a distribution of heights between 2 and 4 layers is corroborated by the surface coverage (13%), extracted from AFM images. While the same increase in the apparent height of islands due to artefacts, as discussed in section 6.2, was observed, the number of layers could be found since step edges of  $C_{60}$  layers were easily identified. The presence of multi-layer islands suggests that the Ehrlich-Schwoebel

barrier for C<sub>60</sub> on KCl substrates is sufficiently low that C<sub>60</sub> molecules can make upward transitions to form multi-layers at room temperature. The morphology of C<sub>60</sub> on KCl is comparable to observations on other alkali halide surfaces carried out under UHV conditions [30,31].

#### **6.4. The Morphology of C<sub>60</sub> Thin Films on hBN: Thickness Dependence**

The effect of the film thickness on the morphology of C<sub>60</sub> on hBN was investigated by producing a series of samples of increasing coverage at both room temperature and 216 °C. The morphology of C<sub>60</sub> films deposited at room temperature is shown in figure 5.4.1. As the coverage of C<sub>60</sub> is increased, islands increase in size while the island density was found to be constant. The amount of C<sub>60</sub> on top of the first layer also increases with increasing coverage, the fractal-like appearance of these second layers is similar to those of sub-monolayer coverages. In this case, the second layer is expected to be formed from C<sub>60</sub> which is deposited onto a pre-formed island during deposition, rather than due to upwards hopping from the surface. This idea is supported by the absence of second layer regions at island edges. At higher coverages, further fractal-like layers increase in size and islands begin to merge. At a coverage of 1.2 ML, incomplete second and third layers are observed.

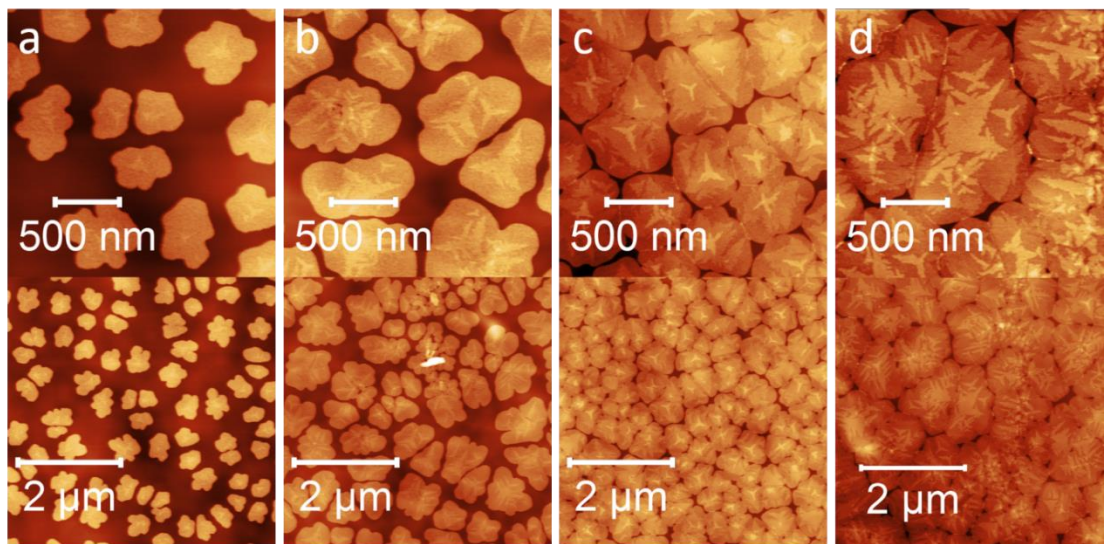


**Figure 5.4.1.** C<sub>60</sub> was deposited onto hBN held at room temperature for a range of film thicknesses. AFM images of 0.4 ML (a), 0.8 ML (b), 1.2 ML (c) and 1.6 ML (d) coverages of C<sub>60</sub> are shown.

The coverage dependence was also investigated for C<sub>60</sub> films grown at 216 °C. As the coverage was increased, the size of C<sub>60</sub> islands increased. At a coverage of 2.1 ML, third layers of C<sub>60</sub> were observed with a triangular morphology. The facets of 3<sup>rd</sup> layer C<sub>60</sub> on bi-layer islands were found to share preferred orientations relative both to one another and the facets of the underlying bi-layer island, this is expected to be a consequence of the hexagonal close packing of C<sub>60</sub>. Given the absence of third layers of C<sub>60</sub> at bi-layer island edges, the origin of the third layer is attributed to C<sub>60</sub> deposited onto pre-formed islands.

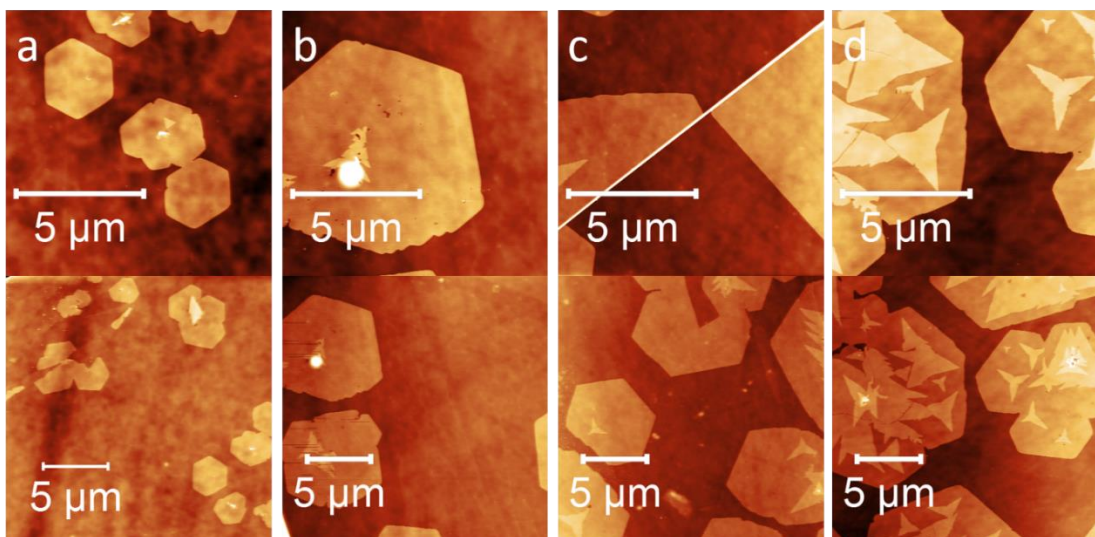


**Figure 5.4.2.**  $C_{60}$  was deposited onto flame-annealed hBN held at 216 °C with a range of coverages. AFM images of 0.4 ML (a), 0.9 ML (b), 1.5 ML (c) and 2.1 ML (d) coverages of  $C_{60}$  are shown. The apparent coverage of  $C_{60}$  is lower than expected due to the reduced sticking coefficient of  $C_{60}$  on hBN at 216 °C relative to room temperature.

Comparing the coverage of the thicker films grown at room temperature and 216 °C, the coverage appears higher than anticipated for room temperature growth and lower than anticipated for samples grown at 216 °C. This difference is attributed to a slight underestimate in the amount of material on the surface, arising from errors in the calibration and the measurement of the amount of bi-layer  $C_{60}$  present on top of monolayers. The second layer was found to have a coverage of  $0.19 \pm 0.05$  ML on top of monolayer islands with 0.4 ML surface coverage. Taking into account the presence of bi-layers in both cases, the sticking coefficient was found to decrease by  $24 \pm 5\%$  between room temperature and 216 °C, this was measured by comparing films of 0.4 ML and 0.8 ML coverage grown at both room temperature and 216 °C. Considering both the presence of the additional-layer on monolayer islands and a reduction in the sticking coefficient, the amount of material observed on the surface of each sample was as-expected.

Using conventional optical microscopy, images of hBN flakes containing  $C_{60}$  bi-layers were acquired. Under standard acquisition parameters, the contrast between areas of  $C_{60}$  and hBN

was such that islands could be seen on flakes of certain thickness. Figure 5.4.3 shows images acquired using an optical microscope of a 1.5 ML coverage of C<sub>60</sub> grown at 216 °C. The observed island morphology of C<sub>60</sub> was the same in both AFM and optical microscopy images. While individual C<sub>60</sub> islands could be resolved using optical microscopy, the contrast obtained was dependent upon the thickness of the underlying hBN flake. The effect of the height of the hBN flake on the contrast of C<sub>60</sub> is anticipated to be due to interference effects, similar to effects reported for graphene on SiO<sub>2</sub> substrates [122].

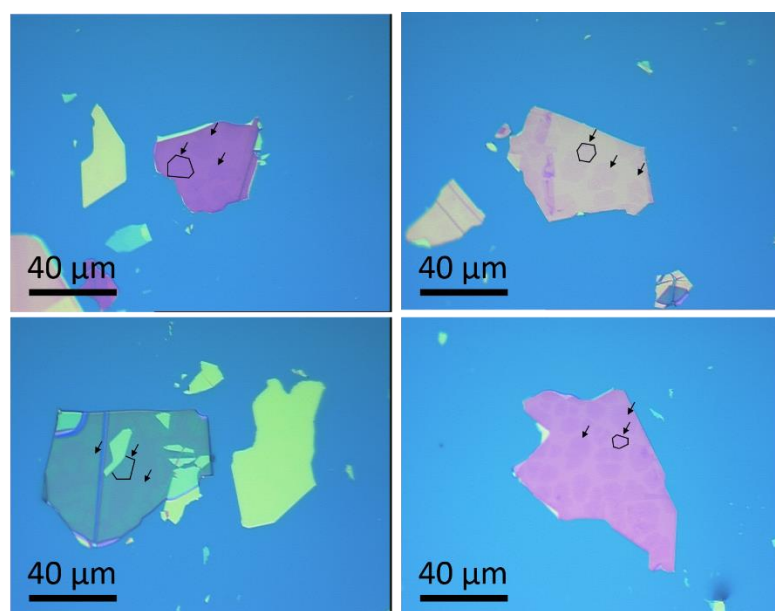


**Figure 5.4.3.** Optical images of a 1.5 ML coverage of C<sub>60</sub> grown at 216 °C on hBN on 300 nm SiO<sub>2</sub>. Different flake heights lead to different optical contrast of C<sub>60</sub> bi-layers. On each flake, the perimeter of an individual island has been outlined, in addition to arrows indicating the position of further islands.

Fluorescence and Raman measurements were carried out for C<sub>60</sub> thin films of various thicknesses on hBN using the Horiba LabRAM HR spectrometer. For coverages below 6.3 ML (5 nm), both the fluorescence and Raman signals were too weak to measure using excitation laser powers which would not damage the sample under ambient conditions. The morphology of two thicker films of sublimed C<sub>60</sub> on hBN on SiO<sub>2</sub> was determined using AFM and is shown in figure 5.4.4.

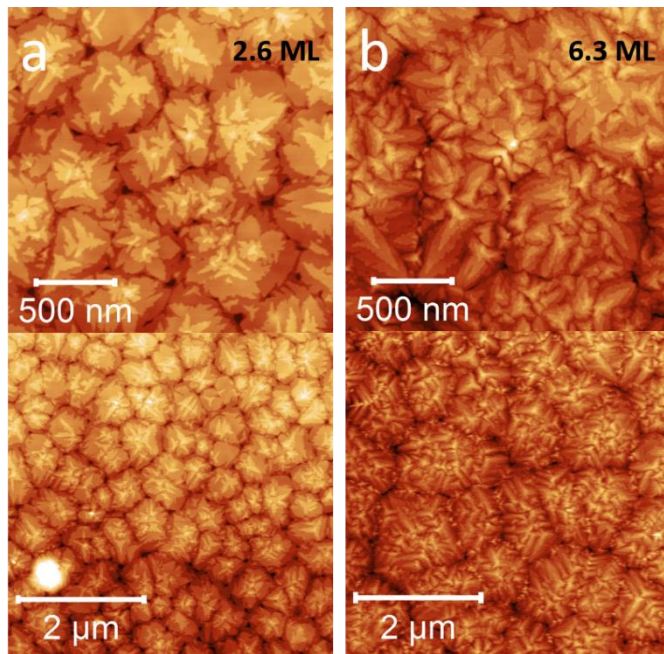


**Figure 5.4.4.**  $C_{60}$  films, with thicknesses of 2.6 ML (2.1 nm) (a) and 6.3 ML (5 nm) (b), were grown on hBN at room temperature by sublimation in vacuum and studied using AFM.

The morphology of 2.6 ML (2.1 nm) and 6.3 ML (5.0 nm) thick films of  $C_{60}$  on hBN was found to be three dimensional, with terraces present at island edges, comparable to accounts of thicker films on HOPG and potassium bromide substrates [123,124]. While it was not possible to measure fluorescence or Raman spectra from  $C_{60}$  films with a thickness of 2.6 ML (2.1 nm) and below, spectra were measured for 6.3 ML (5.0 nm) and 26.5 nm thick films on hBN on  $SiO_2$ . The fluorescence and Raman spectra of these films, acquired using a 532 nm excitation laser, are shown in figure 5.4.5.

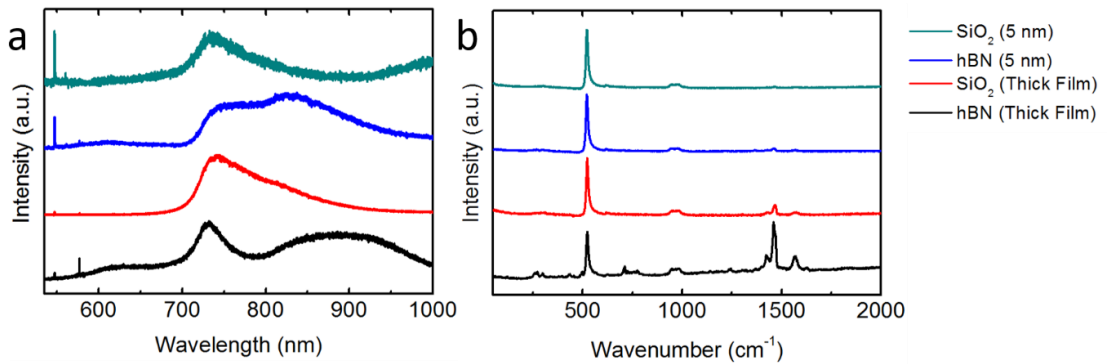


**Figure 5.4.5.** Normalised fluorescence (a) and Raman (b) spectra were acquired from a thick  $C_{60}$  film and a (6.3 ML) 5 nm film, see figure 5.4.4. Both films were deposited by sublimation in vacuum onto hBN on  $SiO_2$  held at room temperature during deposition. Fluorescence was acquired both on hBN flakes and the  $SiO_2$  substrate.

The fluorescence spectra of  $C_{60}$  films were measured both on hBN flakes and on  $SiO_2$ . The spectra were normalised and sharp features close to the excitation wavelength were shown to be the Raman lines of the silicon substrate. The broad fluorescence peak at approximately 750 nm was in good agreement with the spectra of bulk  $C_{60}$ , available from various sources in the literature [125]. Differences in the fluorescence spectra of  $C_{60}$  on hBN due to interference effects from the substrate were observed, an effect discussed in chapter 4 and appendix 1. The Raman spectra of thin films were comparable to that of bulk  $C_{60}$ , with distinct peaks at 1423, 1460 and 1570  $cm^{-1}$  corresponding to  $H_g$ ,  $A_g$  and  $H_g$  peaks respectively [126,127].

## 6.5. The Morphology of PTCDI/ $C_{60}$ Heterostructures

In this section, molecular heterostructures of  $C_{60}$  on PTCDI on hBN were produced, their morphology and fluorescence was studied using AFM and fluorescence microscopy. Heterostructures were produced by sequential deposition of PTCDI and  $C_{60}$ . A 0.4 ML coverage of PTCDI was deposited onto hBN held at 135 °C, as described in section 4.2. A deposition temperature of 135 °C was chosen since islands grown at a higher temperature have a larger area over which the morphology of sequentially deposited  $C_{60}$  could be investigated. Growing PTCDI at elevated temperatures also allowed samples to be taken out of vacuum, returned to

vacuum and then annealed to slightly below the initial substrate temperature during deposition without changing the island morphology of PTCDI.

Samples were cooled to room temperature prior to the deposition of C<sub>60</sub> by sublimation from a second Knudsen cell. C<sub>60</sub> films with 0.4, 0.8 and 1.2 ML coverages were deposited onto pre-formed PTCDI monolayers. The morphology of these films was acquired using AFM under ambient conditions, see figure 6.5.1.

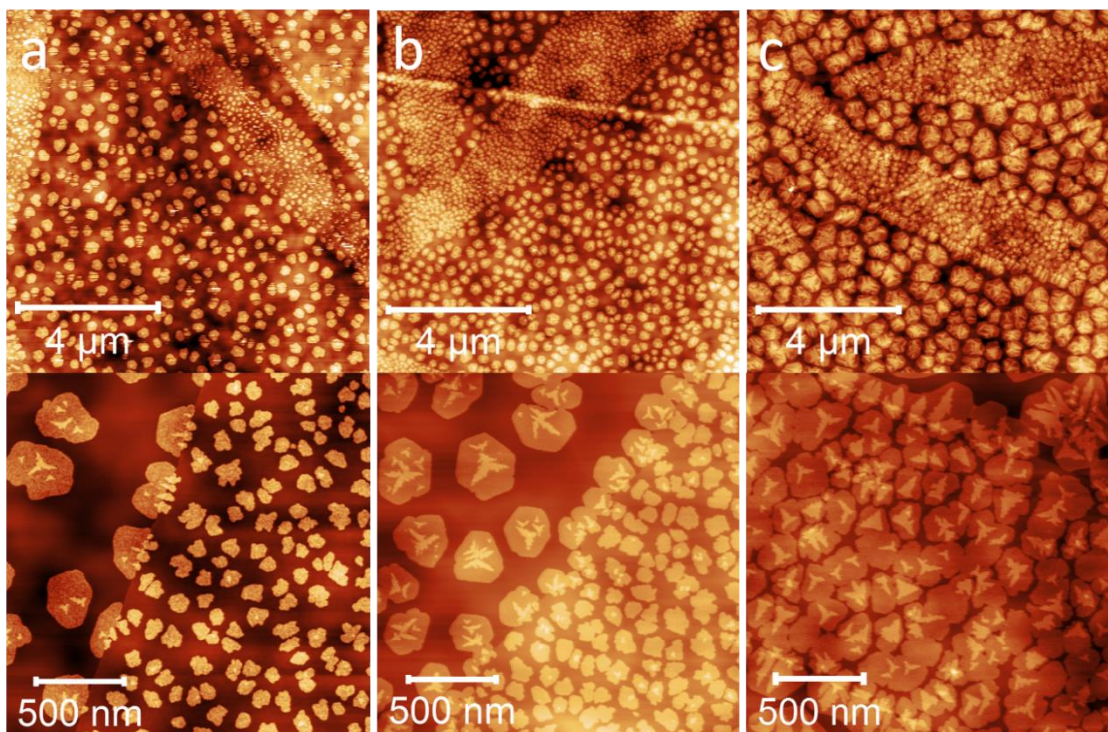


**Figure 6.5.1.** C<sub>60</sub>/PTCDI heterostructures on hBN were produced by depositing 0.4 (a), 0.8 (b) and 1.2 ML coverages of C<sub>60</sub> on monolayer PTCDI islands at room temperature. Images were acquired using AFM under ambient conditions.

The morphology of PTCDI islands, deposited by sublimation in vacuum onto hBN held at 135 °C, is in good agreement with the results of chapter 4, where needle-like monolayer islands were observed. Upon the deposition of C<sub>60</sub>, monolayers were observed to form both on pre-formed PTCDI islands and on the exposed hBN substrate. The island morphology of C<sub>60</sub> on bare hBN was comparable to samples grown without prior deposition of PTCDI. On pre-formed PTCDI islands, monolayer C<sub>60</sub> islands were observed with an island density of

$45 \pm 8 \mu\text{m}^{-2}$ , a significant increase compared to  $\text{C}_{60}$  on flame-annealed hBN ( $2.7 \pm 0.6 \mu\text{m}^{-2}$ ).

The size of islands ( $110 \pm 30 \text{ nm}$ ) was also smaller for  $\text{C}_{60}$  on PTCDI, compared to hBN ( $440 \pm 40 \text{ nm}$ ). The increase in the nucleation density suggests that the diffusion barrier for  $\text{C}_{60}$  on PTCDI is greater than on hBN, see equation 6.3.1. By comparing the island density of  $\text{C}_{60}$  on PTCDI and hBN, a  $0.07 \pm 0.01 \text{ eV}$  increase in the value of  $(E_i + iE_d)/(i+2)$  is estimated, assuming that quantities such as the attempt frequency and the critical island size,  $i$ , are the same on both substrates, see section 2.1 and equation 6.3.1. This increase could occur due to a higher diffusion barrier or differing critical cluster size for  $\text{C}_{60}$  on PTCDI, a consequence of the differing electrostatic charge distribution across the hydrogen bonded canted PTCDI phase compared to hBN.

Comparing  $\text{C}_{60}$  films of 0.4 and 0.8 ML coverage on PTCDI to hBN, the amount of second-layer  $\text{C}_{60}$  on top of monolayer islands was lower on PTCDI. The absence of second layer regions of  $\text{C}_{60}$  on films with coverages of 0.4 and 0.8 ML suggests that molecules deposited onto pre-formed  $\text{C}_{60}$  islands made a downwards transition to the PTCDI surface. Given that  $\text{C}_{60}$  islands on PTCDI are much smaller than on hBN, it could be that the diffusion length of  $\text{C}_{60}$  molecules on top of the  $\text{C}_{60}$  monolayer is greater than the size of islands, enabling migration to island edges, from which downward hopping occurs.

To investigate the morphology of  $\text{C}_{60}$  deposited on PTCDI at elevated temperatures, a sub-monolayer coverage of PTCDI was deposited by sublimation in vacuum at  $139^\circ\text{C}$  and vented to nitrogen. An AFM image of the island morphology of PTCDI is shown in figure 6.5.2.a. The PTCDI sample was then placed back in the vacuum system and annealed to  $120^\circ\text{C}$  prior-to and during the deposition of a 0.4 ML coverage of  $\text{C}_{60}$ . AFM images from the same hBN flake were acquired before and after the deposition of  $\text{C}_{60}$ . In figure 6.5.2 part a and b, the size, shape and position of PTCDI islands is unchanged upon a further pumping cycle and the deposition of  $\text{C}_{60}$  at  $120^\circ\text{C}$ . On regions of hBN, the morphology of  $\text{C}_{60}$  is comparable to results

in section 5.2. On top of PTCDI islands,  $C_{60}$  forms bi-layers and multi-layers at 120 °C, the density of  $C_{60}$  islands was  $4.5 \pm 0.6 \mu\text{m}^{-2}$ , while the mean island size was  $180 \pm 20 \text{ nm}$ . The presence of bi-layers and multi-layers of  $C_{60}$  on PTCDI suggests that molecules make a thermally activated upward transition from PTCDI to the top of  $C_{60}$  monolayers at substrate temperatures of 120 °C.

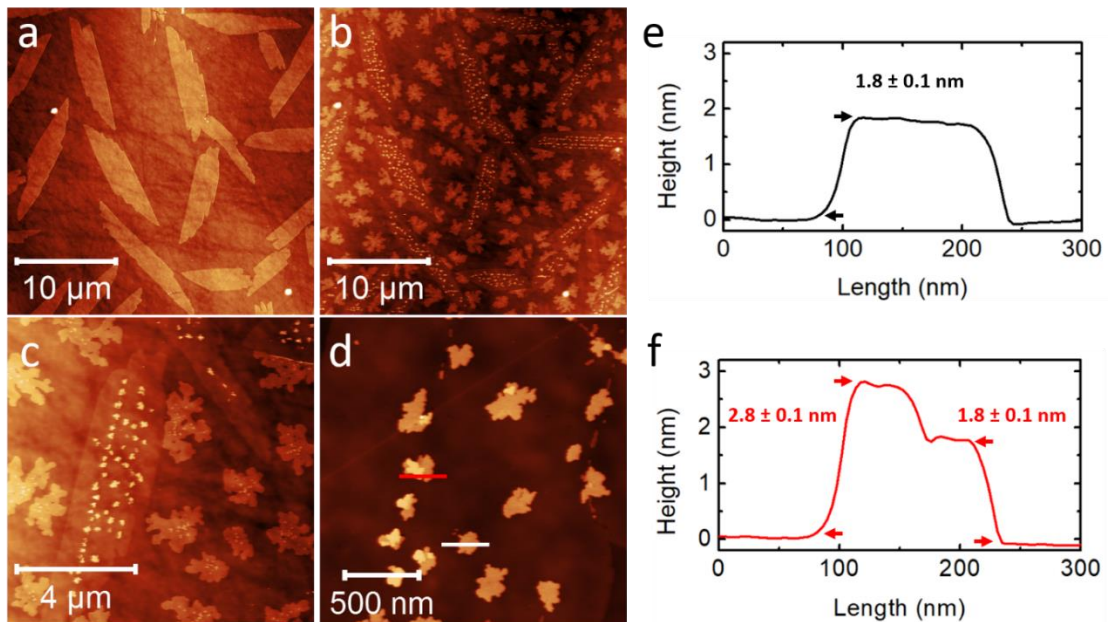


**Figure 6.5.2.** PTCDI was deposited onto flame-annealed hBN on  $\text{SiO}_2$  at 139 °C and studied using AFM (a). The sample was then placed back into the vacuum chamber and a coverage of 0.4 ML of  $C_{60}$  was deposited on the surface (b,c,d). The sample was annealed in vacuum to 120 °C prior to and during the deposition of  $C_{60}$ . Line profiles were extracted from image (d) for the white (e) and red (f) paths indicated.

Comparing the morphology of  $C_{60}$  on PTCDI grown at room temperature and 120 °C, a change from monolayers to bi-layers is observed. This suggests that upward hopping of  $C_{60}$  molecules from PTCDI to a second layer of  $C_{60}$  is thermally activated, in order to give multi-layer islands at 120 °C.  $C_{60}$  bi-layers are only observed on hBN for growth temperatures of 178 °C and above, which suggests that the Ehrlich-Schwoebel barrier for the upward hopping of  $C_{60}$  is lower on the PTCDI surface. At 120 °C,  $C_{60}$  islands are absent from the edges of pre-formed PTCDI islands while at room temperature,  $C_{60}$  islands are located close to islands edges. This suggests that

at 120 °C, molecules migrate from PTCDI to exposed hBN by thermally activated downwards hopping.

Comparison between a similar non-contact AFM study of C<sub>60</sub>/PTCDI heterostructures on calcium fluoride by Loske et al [111] was difficult since de-wetting of PTCDI, seen on calcium fluoride and many other alkali halide substrates, leads to multilayer structures rather than monolayer islands. hBN is a particularly promising substrate for investigations into molecular heterostructures, since behaviours such as molecular de-wetting and multi-layer growth occur less frequently than on many other insulating substrates [32]. The large monolayer and bi-layer islands exhibited by many optically active molecules on hBN is also encouraging in the search for functional molecular heterostructures with novel electronic and optical properties.

## 6.6. The Fluorescence of PTCDI/C<sub>60</sub> Heterostructures

The effect of a C<sub>60</sub> ad-layer on the fluorescence of PTCDI monolayers was investigated using AFM and fluorescence microscopy. A 0.4 ML coverage of PTCDI was deposited on flame-annealed hBN on SiO<sub>2</sub>. The morphology of PTCDI on two different hBN flakes was determined using AFM, before fluorescence spectra were acquired from a further 10 flakes. PTCDI on hBN was then loaded back into the vacuum chamber and annealed to 123 °C prior-to and during the deposition of a 0.4 ML coverage of C<sub>60</sub>. The process of measuring the morphology and fluorescence was repeated for 4 subsequent deposition cycles. The morphology of C<sub>60</sub> on PTCDI after each deposition cycle was determined using AFM and is shown in figure 6.6.1.

C<sub>60</sub> deposited on PTCDI monolayers on hBN at 123 °C was found to form monolayer, bi-layer and tri-layer islands on the PTCDI surface, see the lower image of figure 6.6.1b. This is a further example of the multi-layer growth behaviour discussed in section 6.5. As the coverage of C<sub>60</sub> was increased, further C<sub>60</sub> islands were nucleated, with a distribution of layer orders observed.

Small areas where PTCDI had desorbed or was displaced by C<sub>60</sub> were also observed but were much less frequent than areas of PTCDI or C<sub>60</sub> on PTCDI. After each deposition cycle the fluorescence of the sample was measured, fluorescence spectra from the same flake are shown plotted in figure 6.6.2.

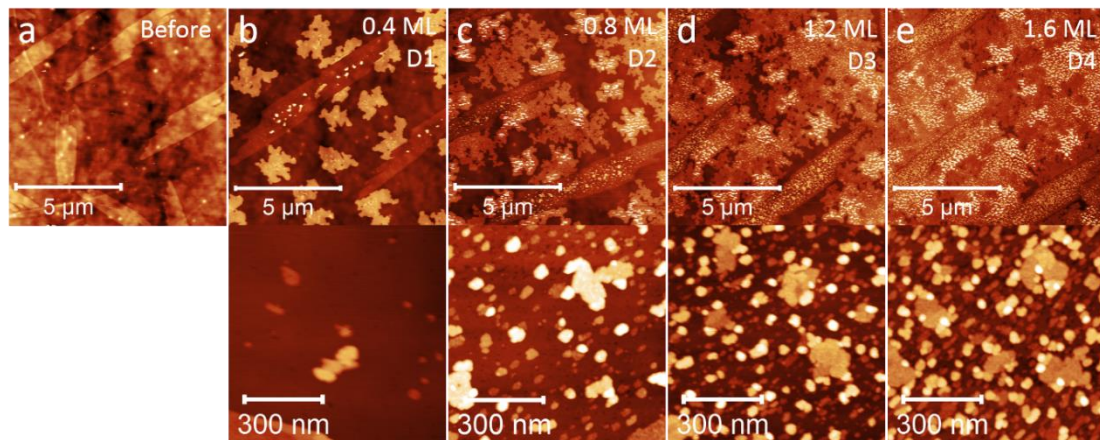


**Figure 6.6.1.** PTCDI on hBN on SiO<sub>2</sub>, grown at 135 °C, was first studied using AFM (a). The sample was then placed back into the vacuum system and annealed to 123 °C prior-to and during the deposition of a 0.4 ML coverage of C<sub>60</sub>. The sample was then removed from vacuum and images of the morphology were acquired from the same area using AFM (b), this process was repeated a further three times (c,d,e). The lower images (b,c,d,e) show the morphology of sublimed C<sub>60</sub> on PTCDI islands.

After the first deposition cycle of C<sub>60</sub>, the intensity and wavelength of the 0-0 fluorescence peak decreased. Further decreases in intensity were observed upon further depositions of C<sub>60</sub>, up to a total coverage of 1.6 ML. Fluorescence spectra from 10 flakes were acquired after each deposition. The peak heights, positions and widths were extracted by fitting spectra to a series of Lorentzian curves. The quenching was defined as the ratio of the signal before the deposition of C<sub>60</sub> to each subsequent cycle, the ratio was then averaged over all flakes and is shown in figure 6.6.3. The quenching and 0-0 peak position were plotted against the true surface coverage on PTCDI islands, extracted from AFM images. This was lower than the expected coverage, thought to occur due to a reduction in the sticking coefficient and migration from PTCDI to exposed hBN through thermally activated downwards hopping. The

total amount of material on top of PTCDI islands, extracted from AFM images, was found to be  $30 \pm 10\%$  lower than the expected surface coverage.

The intensity of PTCDI monolayers on hBN can also be affected by the laser power, photo-bleaching effects, interference effects from the underlying substrate and the distribution of PTCDI islands. The 405 nm laser used for these measurements was used with a selection of filters which reduced the laser power to a level where there was no sample degradation.

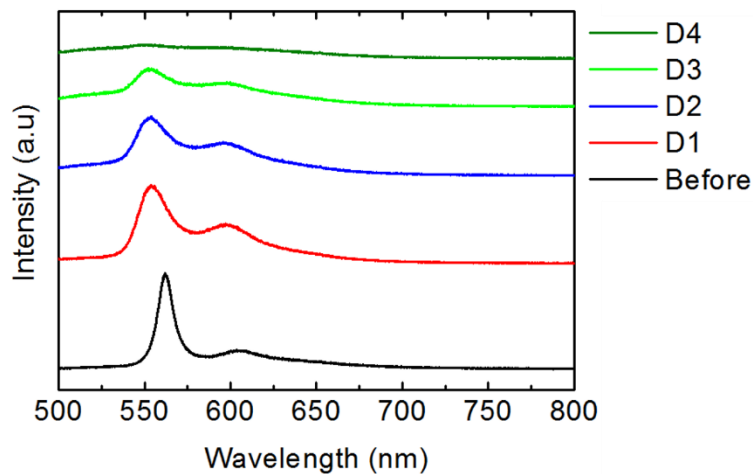


**Figure 6.6.2.** Fluorescence spectra were acquired from the sample shown in figure 6.6.1, prior to the deposition of C<sub>60</sub> and after each subsequent C<sub>60</sub> deposition cycle. The spectra shown above are from the same area of the same flake, and were taken with the same acquisition parameters. A 405 nm excitation laser was used.

The lateral distribution of PTCDI islands was also found to cause a variation in intensity across a hBN flake. In this investigation, a long working distance 50X objective lens was used and gave an estimated laser spot size of 5  $\mu\text{m}$ . By recording the exact position of the laser spot on the flake, the orientation of the underlying flake and using a lens which gave a large laser spot size, the effect of lateral variations of the PTCDI island density was reduced. This was further reduced by averaging across multiple flakes.

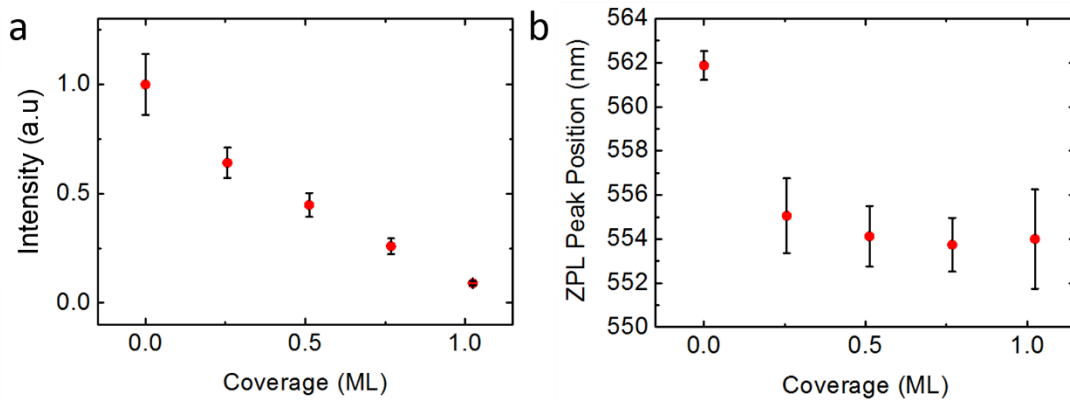


**Figure 6.6.3.** Before and after each deposition cycle of C<sub>60</sub>, the fluorescence spectra of PTCDI was measured from the same positions on 10 different hBN flakes. The quenching was quantified by the mean reduction in the fluorescence after each cycle, relative to the initial intensity, and is shown plotted against coverage (a). The peak position was also extracted by fitting the fluorescence spectra to a series of Lorentzian curves and is also shown plotted against C<sub>60</sub> coverage (b).

As the coverage of C<sub>60</sub> increased, the fluorescence intensity of the underlying PTCDI monolayers decreased. At a total coverage of 1.6 ML, the fluorescence of the underlying PTCDI was almost completely quenched. This indicates that C<sub>60</sub> is able to effectively quench the fluorescence of PTCDI. This experiment is believed to be the first example of such a measurement, where fluorescence quenching in a molecular heterostructure is directly related to the sample morphology. In this system, the fluorescence of PTCDI is believed to be quenched by resonant energy transfer from excited PTCDI molecules to C<sub>60</sub>.

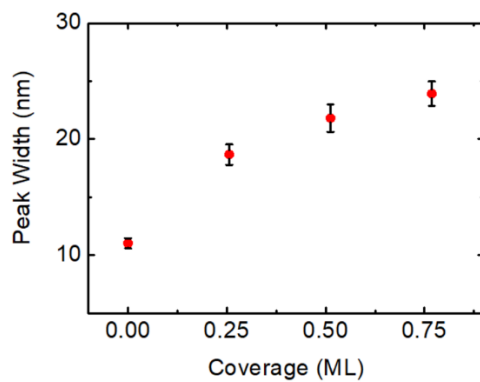


**Figure 6.6.4.** The peak width of the 0-0 transition of PTCDI/C<sub>60</sub> heterostructures on hBN was extracted by fitting spectra to a set of Lorentzian curves. The peak width is plotted against the coverage of C<sub>60</sub>.

Surprisingly, as the coverage of C<sub>60</sub> increased, the fluorescence peak of PTCDI was blue shifted while its width increased, see figure 6.6.3b and 6.6.4. This was unexpected since the absolute surface coverage of C<sub>60</sub> upon the initial deposition was low ( $0.25 \pm 0.09$  ML). Since C<sub>60</sub> quenches the fluorescence of PTCDI, resonant or non-resonant shifts due to any local arrangement of C<sub>60</sub> and PTCDI molecules would not be observed, since the fluorescence would be quenched. It is proposed that a possible origin of the shift could be due to competition between the coupling of transition dipole moments of PTCDI molecules within the canted arrangement, and energy transfer between PTCDI and C<sub>60</sub> molecules. The fluorescence could therefore be dominated by emission from regions of PTCDI where the number of neighbouring PTCDI molecules which can interact through the coupling of transition dipole moments was reduced, possibly due to defects or local disorder. As shown in chapter 5, the in-plane coupling of PTCDI transition dipole moments within a canted arrangement is thought to lead to screened and unscreened shifts of -0.020 eV and -0.050 eV respectively, this is comparable to the blue shift of  $0.032 \pm 0.02$  eV observed due to the adsorption of C<sub>60</sub>.

The fluorescence is more strongly blue shifted by the initial deposition of C<sub>60</sub> than subsequent cycles. Since the strongest interactions would occur between adjacent molecules on the surface, resonant transfer of excitons between PTCDI and C<sub>60</sub> molecules is unlikely to account for the shift as described, unless either excitons or C<sub>60</sub> molecules have significant diffusion lengths. This is because, without diffusion, interactions between adjacent molecules would only be interrupted at high coverages of aggregated C<sub>60</sub>. It is possible that C<sub>60</sub> could be mobile across the PTCDI surface. Were C<sub>60</sub> molecules mobile across the surface, they could limit the coupling of transition dipoles even at low coverages. Alternatively, the diffusion of excitons across the surface could also lead to resonant energy transfer at low concentrations of C<sub>60</sub> [128].

Given the number of control parameters, the conclusions of this experiment are subject to a number of caveats. Firstly it is assumed that the fluorescence of PTCDI is unchanged by the process of cycling and annealing in vacuum. Secondly, that factors such as burning and bleaching did not accumulate over multiple cycles to become significant compared to the quenching due to C<sub>60</sub>. Finally, effects such as optical interference and the distribution of islands add a source of error in the measurement of the fluorescence intensity, such effects were minimised through methods outlined above. The approach used in this investigation was chosen as it enabled the best comparison of the fluorescence and morphology upon subsequent depositions, while removing errors due to interference effects, since measurements were taken from the same flakes.

Given the correlation between the fluorescence spectra and sample morphology; it was concluded that the fluorescence of PTCDI was quenched and blue-shifted by C<sub>60</sub>. In order to investigate the hypothesis that mobile C<sub>60</sub> molecules or excitons lead to a reduction in the in-plane coupling of transition dipole moment, a more rigorous experimental setup is needed. By depositing C<sub>60</sub> onto pre-formed PTCDI islands and measuring the fluorescence and morphology in-situ, it would be possible to remove uncertainty due to multiple pumping and annealing cycles. A much smaller coverage increment could therefore be used, allowing the dependence of the quenching and fluorescence peak position to be investigated with greater precision. Optical techniques such as scanning near-field optical microscopy (SNOM) could also be used to measure the optical properties of molecular heterostructures with nanometre scale resolution. Finally, by controlling the substrate temperature down to the cryogenic range, the presence and influence of mobile C<sub>60</sub> molecules could be tested.

## 6.7. Conclusion

In this chapter, the morphology of C<sub>60</sub> thin films on both hBN and PTCDI has been investigated.

On hBN at room temperature, monolayer islands with irregular shape are observed while faceted C<sub>60</sub> bi-layers are seen at sample temperatures of 178 °C and above. An apparent stretching of the contrast of C<sub>60</sub> islands was also observed in AC-mode AFM images acquired with low setpoints, this was attributed to artefacts in the AFM height profiles. While bi-layer C<sub>60</sub> islands were seen using optical microscopy, no fluorescence was observed for C<sub>60</sub> films thinner than (6.3 ML) 5 nm. The morphology of PTCDI/C<sub>60</sub> heterostructures on hBN was also investigated with a transition from monolayers to multilayers occurring at lower temperatures on PTCDI than on hBN. Finally, C<sub>60</sub> was found to quench the fluorescence of PTCDI monolayers and induce a  $0.032 \pm 0.02$  eV blue shift. This shift is believed to be due to a suppression of the interaction of on-surface transition dipole moments.

## **Chapter 7:**

# **Cyanuric Acid-Melamine/PTCDI Heterostructures on Hexagonal Boron Nitride**

## **7. Cyanuric Acid-Melamine/PTCDI Heterostructures on Hexagonal Boron Nitride**

In this chapter, PTCDI thin films have been sublimed onto solution deposited cyanuric acid-melamine (CA.M) on hBN under UHV conditions. The deposition of CA.M on graphene, produced by chemical vapour deposition (CVD), will be investigated before the growth of PTCDI on CA.M on hBN is explored. The morphology of PTCDI films on CA.M was investigated for a range of growth temperatures and coverages. The fluorescence of these films has also been measured.

### **7.1. Overview**

In molecular electronics, the arrangement of molecules at interfaces is critical to device performance. In this chapter, the morphology of PTCDI on the cyanuric acid-melamine supramolecular network (CA.M) is investigated. The CA.M network has been studied by the scanning probe microscopy (SPM) community for over a decade [47,48,49]. Both cyanuric acid and melamine have a large HOMO-LUMO gap which limits their potential use as functional layers within organic electronic devices. The bulk form of CA.M, melamine-cyanurate, is used industrially for its flame retardant properties. Recently, CA.M has been used by the Nottingham nanoscience group to produce molecular heterostructures [112] and to passivate the surface of black phosphorus [52].

By depositing CA.M from solution, full monolayer coverages can be achieved on hBN and graphitic surfaces, see figure 7.1.1. By changing the deposition parameters, thicker layers can also be grown. The ease and relative cheapness of fabricating CA.M layers, which range in

thickness from monolayers to tens of nanometres, make them an attractive area of study. In this work, the morphology and fluorescence of PTCDI/CA.M molecular heterostructures on hBN is considered. In the literature, a number of investigations into organic-organic heteroepitaxy have been conducted [10,11], with particular attention paid to the interface between layers of donor and acceptor molecules.

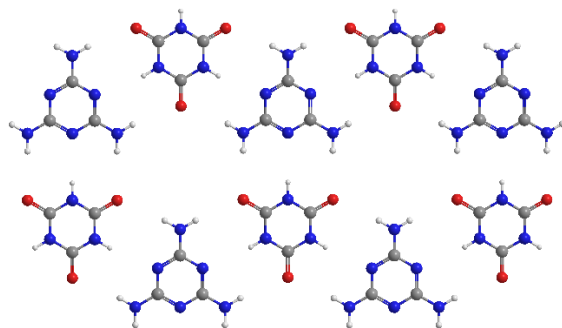


**Figure 7.1.1.** The arrangement of cyanuric acid and melamine molecules within the honeycomb cyanuric acid-melamine supramolecular network is shown.

In molecular electronics, CA.M has two interesting potential applications. Firstly, CA.M could be used as a wetting layer in order to template the growth of further organic layers. Secondly, CA.M could be used as a spacer layer at interfaces. Such interfacial layers could be used to tune phenomena such as tunnelling, quenching and charge transfer between layers. The interfaces in question include those of organic materials, van der Waals heterostructures and organic-inorganic heterojunctions.

## 7.2. The Deposition of Cyanuric Acid-Melamine on Graphene from Solution

In order to investigate CA.M as a potential spacer layer in hybrid heterostructures, it was deposited onto graphene produced by chemical vapour deposition (CVD). CVD graphene on copper, from the Wilson group at the University of Warwick, was transferred to SiO<sub>2</sub> using a

wet transfer technique [129], see figure 7.2.1. Commercially available poly methyl methacrylate (PMMA) solution was spin coated onto one side of CVD graphene on copper at 4 krpm and left to dry for 12 hours. The copper foils with graphene on both sides were then floated onto ferric chloride copper etch for 1 minute, with the PMMA coated side facing upwards. Foils were then transferred to water, in order to remove graphene from the bottom foil surface. Foils were placed back into ferric chloride for 5 minutes to etch the remaining copper. Graphene-PMMA films were then transferred to ultra-pure water using a glass plate, a process repeated five times at 10 minute intervals.

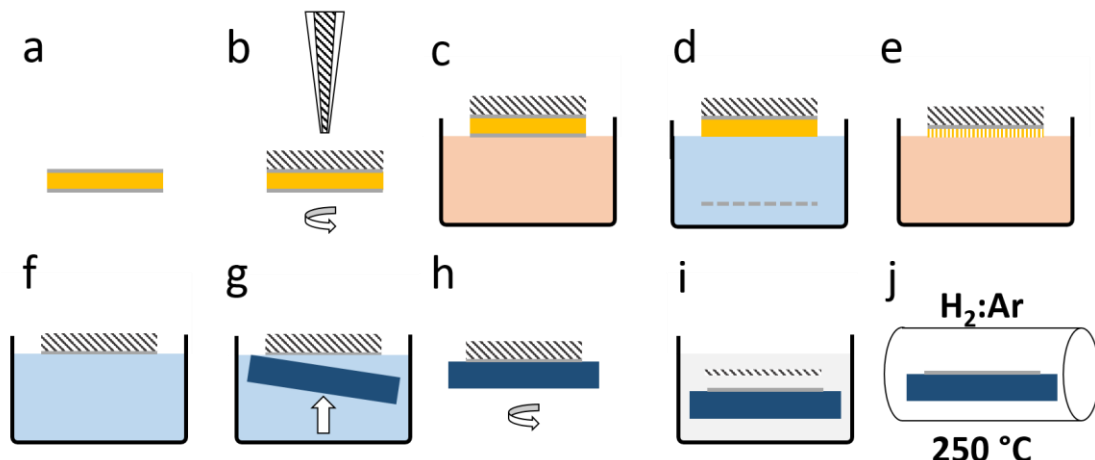


**Figure 7.2.1.** The steps in the transfer of CVD graphene on copper (a) to silicon dioxide substrates are shown and include; application and spin coating of PMMA (b), etching in ferric chloride for 1 minute (c), transfer to water to remove the lower graphene layer (d), placing the sample back into ferric chloride until the copper is fully etched (e), transfer to water to remove contamination (f), picking up the graphene/PMMA layer with the target substrate (g), spinning and drying the substrate (h), removing PMMA in toluene (i) and furnace cleaning in an atmosphere of hydrogen and argon (j).

After cleaning in water, graphene-PMMA films were floated onto 300 nm SiO<sub>2</sub>/Si substrates and immediately spun to 4 krpm for 1 minute using a spin coater, a procedure believed to reduce wrinkles in the graphene film. Substrates were left to dry for 24 hours prior to immersion in toluene for a further 12 hours to remove the PMMA. After removal from toluene, samples were dried with a nitrogen gun and annealed in an atmosphere of hydrogen and argon (5%:95%) for 4 hours at 250 °C. The morphology of CVD graphene on 300 nm SiO<sub>2</sub>/Si

was determined using AFM, see figure 7.2.2a and b. Transferred CVD graphene on  $\text{SiO}_2$  was found to contain flat-lying regions, in-between wrinkles. Wrinkles had a typical height of between 1 and 5 nm and a lateral separation of approximately 500 nm.

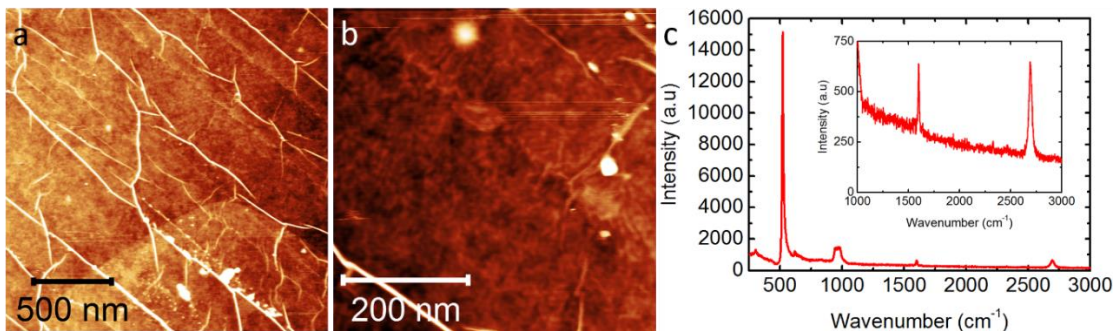


**Figure 7.2.2.** CVD graphene on copper was transferred to  $\text{SiO}_2$  by etching in ferric chloride on a PMMA support. After transfer, the samples were cleaned using solvents and annealing in an atmosphere of hydrogen and argon. AFM images of the graphene surface reveal wrinkles in the graphene with clean and flat areas in between (a,b). The sample was also studied using Raman spectroscopy, using a 532 nm excitation laser (c), confirming that the sample is likely to be monolayer graphene.

Raman spectra of CVD graphene samples were measured using a 532 nm excitation laser, see figure 7.2.2.c. While a number of peaks were attributed to the  $\text{SiO}_2/\text{Si}$  substrate, the G and 2D peaks of graphene were present and measured to occur at  $1599 \text{ cm}^{-1}$  and  $2693 \text{ cm}^{-1}$  respectively. The ratio of the noise subtracted G and 2D peaks (2D/G) was found to be  $1.4 \pm 0.1$ , which is suggestive of monolayer graphene [130]. After characterisation using AFM and Raman spectroscopy, metal contacts were applied to graphene. This was done by depositing 10 nm of titanium and 100 nm of gold on the graphene surface through a shadow mask.

STM was carried out on CVD graphene on  $\text{SiO}_2/\text{Si}$  using a tunnelling current of approximately 1 nA and a setpoint of approximately 0.1 V. The samples were found to have a roughness of approximately 0.1 nm over a 5 nm STM image. This roughness was attributed to the roughness of the  $\text{SiO}_2$  substrate but could also be a consequence of contamination or water trapped between graphene and  $\text{SiO}_2$ . A lattice constant of  $0.26 \pm 0.05 \text{ nm}$  was extracted from STM

images. Accounting for factors such as thermal drift, this value is in good agreement with the expected lattice constant of monolayer graphene [131]. In figure 7.2.3.a and b, STM images of CVD graphene on  $\text{SiO}_2$  (300 nm) are shown.

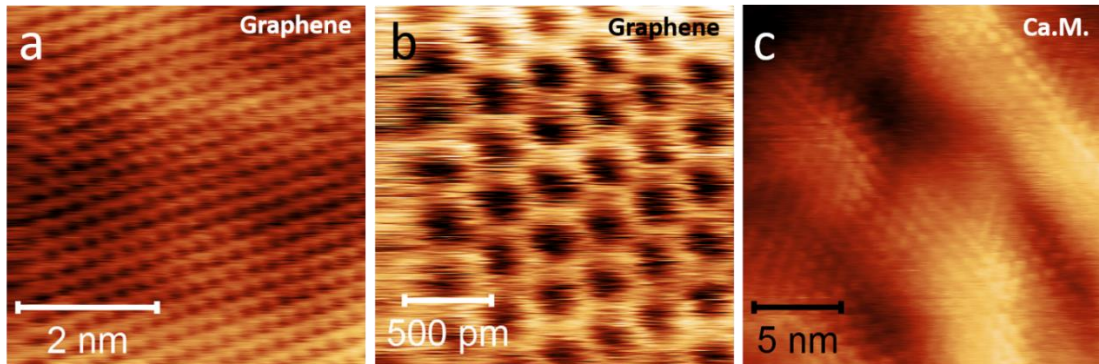


**Figure 7.2.3.** Gold contacts were thermally evaporated onto graphene on  $\text{SiO}_2$  in order to study the sample using STM. STM images a and b were obtained using acquisition parameters of (1 nA, 0.096 V) and (1.104 nA, 0.1 V) respectively. CA.M was then deposited from solution onto the graphene surface and investigated using STM (c) with acquisition parameters of (0.077 nA, 0.64 V).

CA.M was deposited onto CVD graphene on  $\text{SiO}_2$  from solution. A solution containing 0.01  $\mu\text{g}/\text{ml}$  of both cyanuric acid and melamine in water was prepared from two 1  $\mu\text{g}/\text{ml}$  concentrated stock solutions. Graphene on  $\text{SiO}_2$  substrates were then dipped into the solution of cyanuric acid and melamine for 1 minute. Samples were immediately dried with a nitrogen gun after removal from solution. AFM images of CA.M on graphene confirmed full monolayer coverage. The molecular packing of CA.M was subsequently determined using STM with a tunnelling current of approximately 0.01 nA and a bias voltage of approximately 0.5 V. CA.M was found to form a honeycomb packing arrangement with a lattice constant of  $1.04 \pm 0.05$  nm, in good agreement with previous studies of CA.M on HOPG [50].

### 7.3. Cyanuric Acid-Melamine/PTCDI Heterostructures on hBN

In addition to CVD graphene, CA.M was also deposited onto flame-annealed hBN on SiO<sub>2</sub> substrates by Dr Vladimir Korolkov [48], the same molecular packing structure as on graphene and HOPG was observed. By optimising the deposition of CA.M on hBN from solution, full monolayers of the network were produced. These samples were then used as substrates for the further deposition of PTCDI by sublimation in vacuum. Deposition of PTCDI by sublimation in vacuum was carried out using the same method outlined in section 4.2, but without annealing the substrate to 450 °C prior to deposition.

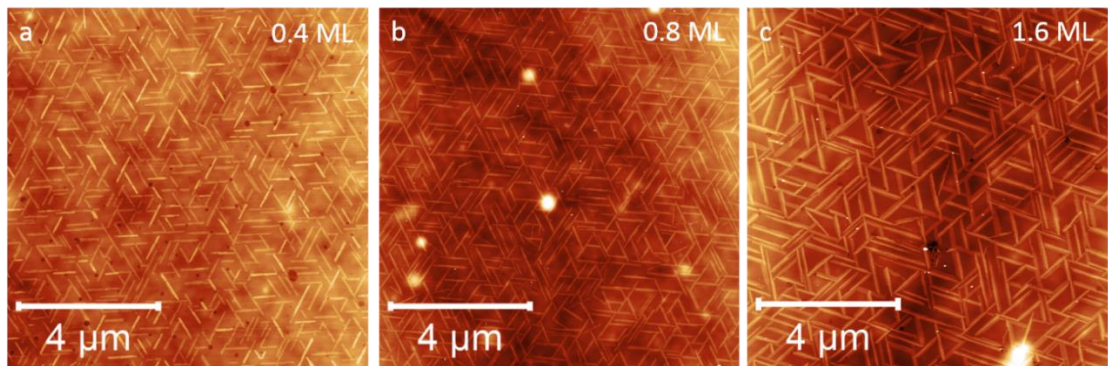


**Figure 7.3.1.** A monolayer of CA.M was deposited onto hBN on SiO<sub>2</sub> from solution. The sample was then loaded into a vacuum system and PTCDI was deposited by sublimation. AFM images are shown for 0.4 ML (a), 0.8 ML (b) and 1.6 ML (c) coverages of PTCDI on monolayer CA.M. Images were acquired with the assistance of Dr Vladimir Korolkov.

Coverages of approximately 0.4 ML, 0.8 ML and 1.6 ML of PTCDI were grown on CA.M on hBN by sublimation in vacuum, substrates were held at room temperature during deposition. Images of the CA.M/PTCDI heterostructures on hBN, acquired using AFM, are shown in figure 7.3.1. As on hBN, needle like islands of PTCDI were observed. For a 0.4 ML coverage, PTCDI islands formed monolayer islands with some bi-layer regions. Islands were observed to lie along three orientations on the surface, suggesting preferential adsorption sites on CA.M. As the coverage was increased, the size of islands and the occurrence of bi-layers increased.

The orientation of PTCDI islands grown on CA.M at room temperature with a 0.8 ML coverage was extracted from AFM images acquired under ambient conditions. The distribution of island orientations was then plotted as a histogram with a bin size of 1°. The distribution of island orientations and the AFM image from which orientations were extracted are shown in figure 7.3.2. The orientation of PTCDI islands on CA.M suggests that the row-axis of the canted phase of PTCDI is aligned to the axis of the substrate.

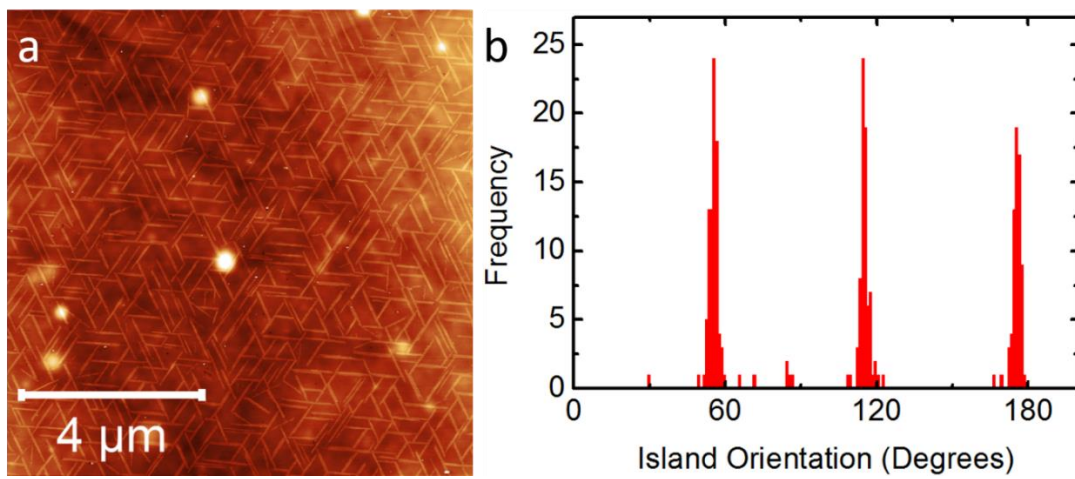


**Figure 7.3.2.** PTCDI was deposited by sublimation in vacuum onto a monolayer of CA.M on hBN. The coverage was 0.8 ML, while the substrate was held at room temperature during deposition. The sample morphology was determined using AFM (a) while the orientation of the major axis of PTCDI islands was extracted from the same image and plotted as a histogram (b).

PTCDI was also deposited onto CA.M on hBN at elevated temperatures. As the temperature was increased, the size of islands increased while the island density decreased. Figure 7.3.3 shows the island morphology, determined using AFM, of a 0.8 ML coverage of PTCDI grown on CA.M at 52 °C. At elevated temperatures, the orientation of islands still appears to be directed by the substrate but with a greater proportion of islands not oriented along the three principal directions. At higher substrate temperatures during deposition, CA.M was found to desorb from the hBN surface. This led to the nucleation of PTCDI islands at the edges of the remaining CA.M domains.

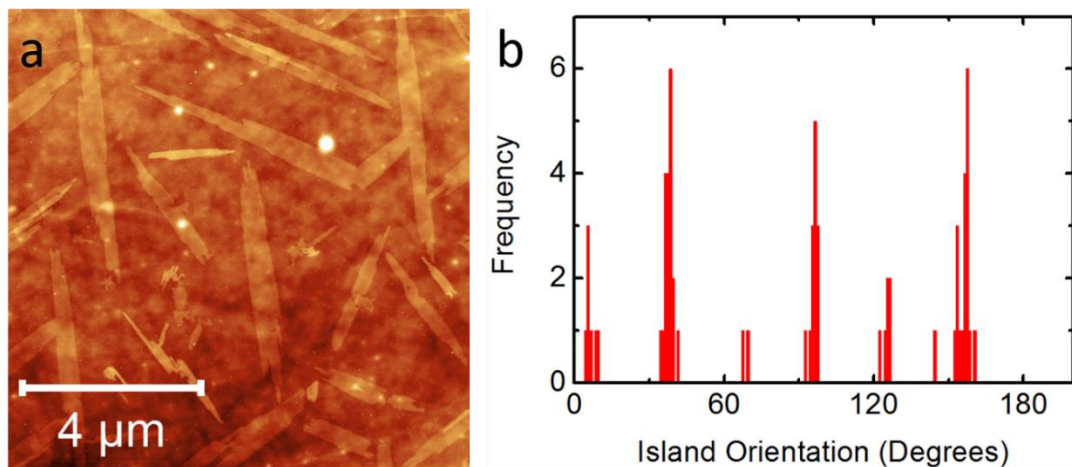


**Figure 7.3.3.** As in figure 7.3.2, PTCDI was deposited by sublimation in vacuum onto a monolayer of CA.M on hBN. The coverage was 0.8 ML, while the substrate was held at an elevated temperature of 52 °C during deposition. The sample morphology was determined using AFM (a) while the orientation of the major axis of PTCDI islands was extracted from the same image and plotted as a histogram (b).

The fluorescence of PTCDI on CA.M on hBN was measured using the Horiba LabRAM HR spectrometer with a 532 nm excitation laser. This was carried out for two samples; the first was a 0.4 ML coverage of PTCDI grown at room temperature on monolayer CA.M on hBN. The second film was grown using the same deposition conditions but on a multi-layer film of CA.M. The deposition of CA.M was again carried out by Dr Vladimir Korolkov, multi-layer samples were produced by deposition from a solution with higher concentration. The thickness of the multi-layer sample was found to vary across a hBN flake, seen in AFM and optical images. In general, the film thickness was in the order of a few nanometres across the sample surface. The morphology of PTCDI grown on mono-layer and multi-layer CA.M was determined using AFM and is shown in figure 7.3.4.

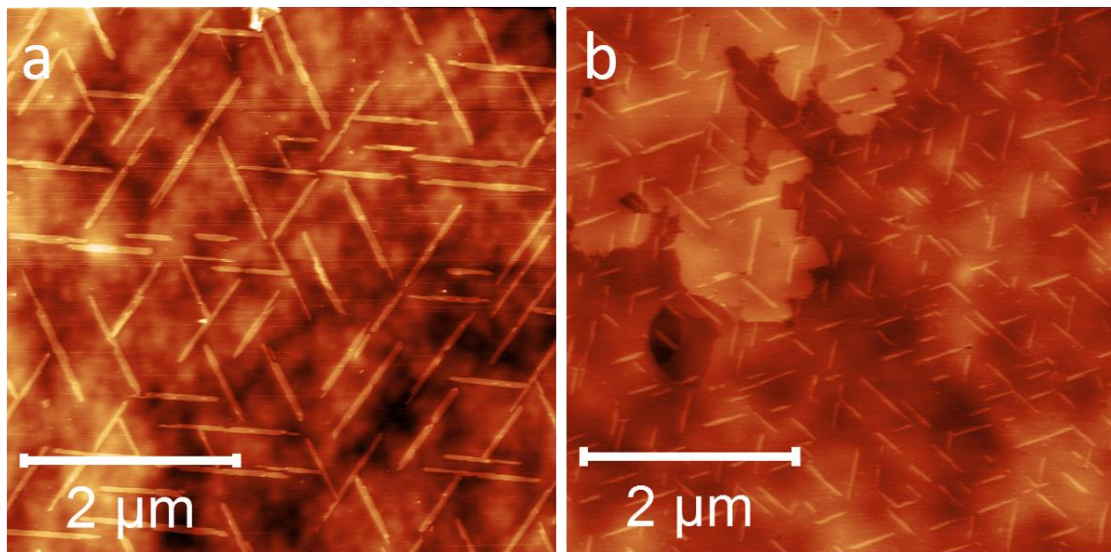


**Figure 7.3.4.** PTCDI, of 0.4 ML coverage, was deposited on solution deposited CA.M by sublimation in vacuum. The morphology of PTCDI on monolayer CA.M on hBN (a), and multi-layer CA.M on hBN (b) was determined using AFM.

For both mono-layer and multi-layer CA.M samples, a 0.4 ML coverage of PTCDI was found to form predominantly monolayer islands. As before, the islands were orientated at multiples of 60° to one another, thought to occur due to an on-axis registry with the substrate. The fluorescence spectra of PTCDI monolayers on monolayer and multi-layer CA.M is shown in figure 7.3.5. Comparing the fluorescence spectra of PTCDI on monolayer and multi-layer CA.M reveals a  $0.005 \pm 0.002$  eV blue shift to the thicker film. Comparing the shift between PTCDI on monolayer and thicker CA.M layers to the shift observed between gas phase measurements and PTCDI on hBN suggests the thickness of the film has little effect on the fluorescence. This could be interpreted in two ways; firstly, that effects due to the polarisability of the substrate are dominated by the dielectric properties of the topmost layer. This is relevant to the conclusions of chapter 5, where the shifts in monolayer PTCDI were attributed, at least partially, to the polarisability of the substrate. Secondly, the underlying CA.M substrate could give rise to modified screening, resonant and non-resonant interactions, leading to further fluorescence shifts.

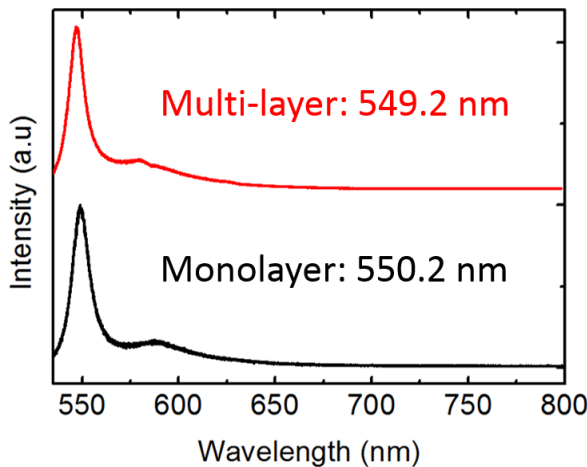


**Figure 7.3.5.** The fluorescence spectra of monolayer PTCDI on both monolayer (black) and multi-layer (red) CA.M, acquired using a 532 nm excitation laser, are shown.

A blue shift of  $0.045 \pm 0.002$  eV was observed from PTCDI monolayers on hBN to CA.M on hBN. Assuming the shift occurs due to the polarisability of the substrate, the refractive index of the CA.M thin film on hBN is calculated to be  $1.38 \pm 0.1$ . This value was estimated by comparing the shifts between PTCDI on hBN and CA.M substrates, and the calculated shift due to the interaction of the charge distribution of the transition dipole moment of PTCDI with a dielectric surface, see table 5.6.4. For comparison, the refractive index of bulk melamine cyanurate powder is 1.57 [132].

The adsorption of PTCDI on CA.M could influence other mechanisms which lead to fluorescence shifts. Firstly, the lower refractive index of the substrate, compared to hBN, could lead to a reduction in the screening of transition dipole moments on the surface, leading to stronger coupling of on-surface transition dipole moments. Secondly, preferential alignments of PTCDI islands along three directions with respect to the substrate suggests a different molecule-substrate interaction than on hBN. This could lead to a non-resonant fluorescence shift due to the interaction of PTCDI molecules with the substrate.

An interesting extension to this investigation would be to measure the fluorescence of PTCDI between two molecular layers. In an attempt to produce molecular heterostructures with

PTCDI encapsulated between two CA.M layers, CA.M was deposited onto pre-formed PTCDI on CA.M on hBN. It was not possible to produce encapsulated PTCDI islands in this way, since the solution deposition of a further layer of CA.M was found to remove PTCDI from the first layer. Depositing CA.M by sublimation in vacuum could be a promising method to allow such structures to be produced in future.

#### **7.4. Conclusion**

In this chapter, the deposition of CA.M on CVD graphene has been studied using AFM and STM. The deposition of CA.M from solution onto hBN, graphene and other 2D materials is a promising route to control the adsorption of ordered organic layers. CA.M could be used as a dielectric layer of tuneable thickness in order to study tunnelling, quenching and charge transfer effects in a range of nanoscale architectures. CA.M on hBN was also used as a substrate for PTCDI, leading to fluorescent molecular heterostructures. Molecular heterostructures provide interesting environments which allow hypotheses about molecular fluorescence at interfaces to be investigated systematically.

# **Chapter 8:**

## **Conclusion**

## 8. Conclusion

In this work, the morphology and fluorescent properties of PTCDI and PTCDA have been measured in a variety of structural conformations. This has been realised through supramolecular self-assembly and multi-layer growth of fluorescent molecules on dielectric surfaces. The same techniques have also been applied to studying the growth and fluorescence of PTCDI and PTCDA on a range of substrates and within molecular heterostructures. Based upon these experiments, the role of intermolecular and molecule-substrate interactions in the fluorescence of molecular monolayers has been discussed. It has been demonstrated that by templating the relative position and orientation of fluorophores at interfaces, the optical properties of an organic thin film can be influenced.

In chapter 4, PTCDI was deposited onto mechanically exfoliated hBN flakes by sublimation in vacuum. A 0.4 ML coverage, deposited onto hBN held at room temperature, was found to give needle like monolayer islands. By heating the sample during growth, larger monolayers of PTCDI with sizes of the order of 10s of  $\mu\text{m}$  were formed. The lattice constants of sublimed PTCDI were extracted from high resolution AFM images, acquired under ambient conditions. The molecular packing was found to correspond to the canted structure of PTCDI, reported in a number of STM investigations available in the literature.

The fluorescence of monolayer PTCDI films was measured using fluorescence microscopy, with the 0-0 peak of PTCDI on hBN observed at  $2.208 \pm 0.002$  eV. The lineshape of the PTCDI fluorescence was found to vary with the height of the underlying hBN flake, this effect was studied for PTCDI on hBN on a range of substrates and was attributed to interference effects. The fluorescence of sublimed PTCDI monolayer films was also measured down to temperatures of 10 K, where a  $0.014 \pm 0.002$  eV red shift of the 0-0 peak was observed in addition to PTCDI Raman lines.

Increasing the dose of sublimed material, PTCDI was found to form bi-layers and tri-layers before the completion of the initial monolayer. The island morphology and fluorescence of multi-layer films was investigated using AFM and fluorescence mapping. The presence of PTCDI monolayers, bi-layers and tri-layers was confirmed by AFM images while fluorescence spectra contained peaks at  $2.209 \pm 0.002$  eV,  $2.135 \pm 0.002$  eV and  $2.118 \pm 0.002$  eV. It was demonstrated that islands of PTCDI can be grown on an insulating substrate with sufficient spatial extent to be mapped using confocal fluorescence microscopy techniques.

Fluorescence maps were related to AFM images of the same area of the sample, but the resolution of fluorescence mapping was insufficient to assign the  $2.135 \pm 0.002$  eV and  $2.118 \pm 0.002$  eV peaks to structural features of the film. In the case of bi-layers and tri-layers, different layers of PTCDI could fluoresce at different energies due to stronger interactions with the substrate, it is necessary to eliminate the possibility of a signal from surrounding monolayer PTCDI. Mapping the fluorescence in this manner is interesting since it provides a way to study the effect of parameters such as the layer height and registry with the substrate on molecular fluorescence.

In chapter 5, the effect of the substrate and molecular packing on the fluorescence of organic monolayers is investigated using both PTCDI and PTCDA. A monolayer of the PTCDI-melamine supramolecular network and the canted phase PTCDI on hBN were produced by solution deposition. The morphology and fluorescence of films was determined using AFM and fluorescence microscopy. Comparing the structure and fluorescence of solution deposited films to sublimed PTCDI monolayers discussed in chapter 4, and measurements from Me-PTCDI doped HND from reference [71], the effect of molecule-substrate and intermolecular interactions are considered. Firstly, a red shift of  $0.031 \pm 0.002$  eV was observed between PTCDI-melamine and the canted phase of PTCDI on hBN. Secondly, the fluorescence of PTCDI on hBN was red shifted by  $0.342 \pm 0.002$  eV from doped HND.

Since the fluorescence shift between PTCDI and PTCDI-melamine was much smaller than the shift from isolated molecules on hBN to a close packed arrangement, the effect of the substrate was investigated further. Monolayers of PTCDA were deposited on hBN and compared to fluorescence measurements of PTCDA on various dielectric substrates available in the literature. The fluorescence of monolayer PTCDA films was compared to the refractive index of the substrate. As the refractive index of the substrate increased, the red shift in the fluorescence from PTCDA doped HND measurements was observed to increase.

The shift due to the coupling of on-surface transition dipole moments, both screened and unscreened, was estimated from the calculated exciton bandstructures of the canted PTCDI structure and the honeycomb PTCDI-melamine network. TD-DFT, carried out by Dr Anton Nizovtsev, was also used to calculate the expected non-resonant shifts due to adsorption on the hBN surface and intermolecular hydrogen bonding. Finally, the interaction of spatially distributed transition dipole moments, calculated using TD-DFT, with a dielectric substrate was considered. By comparing computational and experimental results, it was concluded that the red shift between PTCDI-melamine and PTCDI was a consequence of the coupling of transition dipole moments, while the substrate induced red-shifts of PTCDI and PTCDA were attributed to interactions with a polarisable substrate.

In chapter 6, the growth of C<sub>60</sub> by sublimation in vacuum is investigated. For sub-monolayer coverages of C<sub>60</sub> grown at room temperature, monolayer islands with irregular shape are observed. At a growth temperature of 214 °C, faceted bi-layer structures are observed. The growth of C<sub>60</sub> is explained in terms of kinetic growth and shares similarities with previous investigations on alkali halide substrates [30]. Imaging artefacts were also found to affect the apparent height of monolayer and bi-layer C<sub>60</sub> islands, extracted from AFM height profiles. This was investigated by acquiring AC-mode AFM images for a range of setpoints.

$C_{60}$  was also deposited onto pre-formed PTCDI monolayer islands, and found to form monolayers at room temperature and multi-layers at 139 °C. Following the deposition of  $C_{60}$ , the fluorescence of PTCDI was found to be quenched. The fluorescence of PTCDI was also found to be blue-shifted by  $0.032 \pm 0.002$  eV. The measured blue shift is thought to occur due to a suppression in the coupling of transition dipole moments of PTCDI. Possible mechanisms accounting for this include the diffusion of  $C_{60}$  molecules or exciton diffusion. A promising potential investigation would be to measure the fluorescence and morphology of molecular heterostructures in-situ during growth. Controlling the substrate temperature during growth down to the cryogenic range would also be advantageous, as the fluorescence of isolated molecules on the substrate could be investigated. Scanning near-field optical microscopy (SNOM) could also be used to measure the optical properties of  $C_{60}$  islands on PTCDI with nanometre scale spatial resolution.

In chapter 7, the deposition of the cyanuric acid-melamine network on CVD graphene was investigated using AFM and STM. On graphene, cyanuric acid-melamine was found to form monolayers with a hexagonal packing structure comparable to previous reports on both HOPG and noble metal surfaces. Cyanuric acid-melamine was also deposited onto hBN and used as a substrate for the growth of PTCDI. PTCDI was found to form monolayers on cyanuric acid-melamine, with islands oriented at multiples of  $60 \pm 1^\circ$  relative to both one another and the underlying cyanuric acid-melamine. The fluorescence of monolayer PTCDI islands on monolayer and multi-layer cyanuric acid melamine on hBN was measured, with 0-0 peaks observed at  $2.253 \pm 0.002$  eV and  $2.258 \pm 0.002$  eV for monolayer and multi-layer cyanuric acid-melamine respectively. The small blue-shift due to a thicker cyanuric acid-melamine layer suggests the initial monolayer dominates the interaction of transition dipole moments with a polarisable substrate.

In this thesis, molecular self-assembly, organic-organic hetero-epitaxy and the formation of organic-inorganic heterostructures have been investigated and demonstrated to influence the fluorescent properties of organic thin films. By controlling the structure and environment of organic thin films in this way, their optical properties can be tuned. The experimental methods used in this thesis are immediately applicable to molecular heterostructures containing both donor and acceptor species, measuring the fluorescent properties of guest host systems and the formation of more complicated organic-inorganic hybrid heterostructures. Such systems provide an opportunity to test and refine our current understanding in the field of molecular fluorescence in addition to providing structures which could be used to develop novel optical and electronic devices.

# **Appendix 1:**

## **Optical Interference in**

## **Fluorescence Spectroscopy**

## **Measurements**

## A1. Optical Interference in Fluorescence Spectroscopy Measurements

In chapters 4 and 5, the fluorescence of PTCDI and the PTCDI-melamine supramolecular network on hBN was discussed. Comparing fluorescence spectra from hBN flakes of different thicknesses, both the fluorescence intensity and lineshape were found to depend upon the flake thickness. In order to explore this effect; the position, width and intensity of the 0-0 and 0-1 fluorescence peaks of PTCDI and PTCDI-melamine on hBN on various substrates were extracted by fitting to a series of Lorentzian curves and compared to the hBN flake thickness.

Theoretical models were used to calculate the expected fluorescence intensity due to interference. Direct calculations, see equation 4.3.2, and the transfer matrix model, see equation 4.3.4, were used to calculate intensity of reflected light,  $r$ , at the hBN/air interface, see figure 4.3.4. The reflected intensity is dependent upon the dielectric properties of each layer, the wavelength of the incident laser light,  $\lambda_{\text{Laser}}$ , and the fluorescence wavelength. The variation in the intensity of a given fluorescence peak, here  $I_{0-0}$  and  $I_{0-1}$  represent the intensity of the 0-0 and 0-1 peaks respectively, was found to depend upon the interference of the laser light,  $\lambda_{\text{laser}}$ , and the fluorescent light,  $\lambda_{0-0}$  and  $\lambda_{0-1}$ . The total intensity of the 0-0 peak and the 0-0/0-1 peak ratio are given by equations A1.1 and A1.2 respectively.

$$I_{(0-0)} = ((r(\lambda=\lambda_{0-0})+1) (r(\lambda=\lambda_{\text{Laser}})+1))^2 \quad (\text{A1.1})$$

$$\frac{I_{(0-0)}}{I_{(0-1)}} = \left( \frac{r(\lambda_{0-0})+1}{r(\lambda_{0-1})+1} \right)^2 \quad (\text{A1.2})$$

For hBN flakes, a value of 2.13 was used for the refractive index normal to the hBN surface in theoretical models [133]. The experimentally determined fluorescence peaks,  $\lambda_{0-0}$  and  $\lambda_{0-1}$ , were used to calculate the proportional change in the fluorescence intensity, which was scaled by fitting to experimental results.

The intensity of the 0-0 fluorescence peak and the 0-0/0-1 peak ratio was plotted against the height of the hBN flake from which fluorescence was measured. This was first done for a 0.4 ML coverage of PTCDI on hBN on 300 nm SiO<sub>2</sub>/Si, fluorescence measurements were acquired using a 532 nm excitation laser, see figure 4.3.5. The same experiment was also carried out for a 0.4 ML coverage of PTCDI on hBN on 300 nm SiO<sub>2</sub>/Si using a 405 nm excitation laser, see figure A1.1.

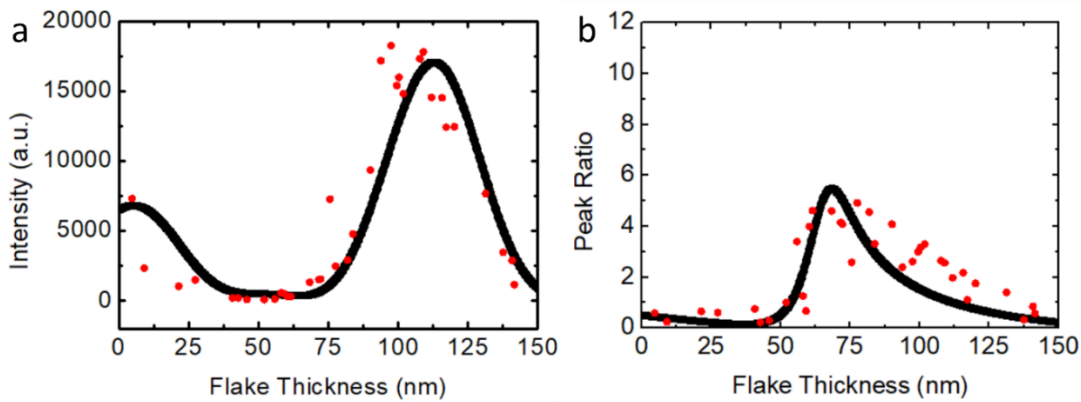


**Figure A1.1.** The fluorescence of sublimed monolayer PTCDI islands on hBN on 300 nm SiO<sub>2</sub>/Si was measured using a 405 nm excitation laser. The intensity of the 0-0 peak and the 0-0/0-1 peak ratio (red) were extracted by fitting spectra to a series of Lorentzian curves and plotted against the height of the hBN flake from which measurements were taken. The variation in the fluorescence intensity and peak ratio was also modelled using the transfer matrix model, which was fitted to experimental results (black).

Using a 532 nm excitation laser, the fluorescence of a 0.4 ML coverage of PTCDI on hBN on various substrates was measured. The intensity of fluorescence peaks and the 0-0/0-1 peak ratio is shown plotted against the thickness of the underlying hBN flake, determined from AFM images, see figure A1.2. As in figure 4.3.5, the effect of the flake thickness on the fluorescence intensity was modelled using the transfer matrix model and direct calculations.

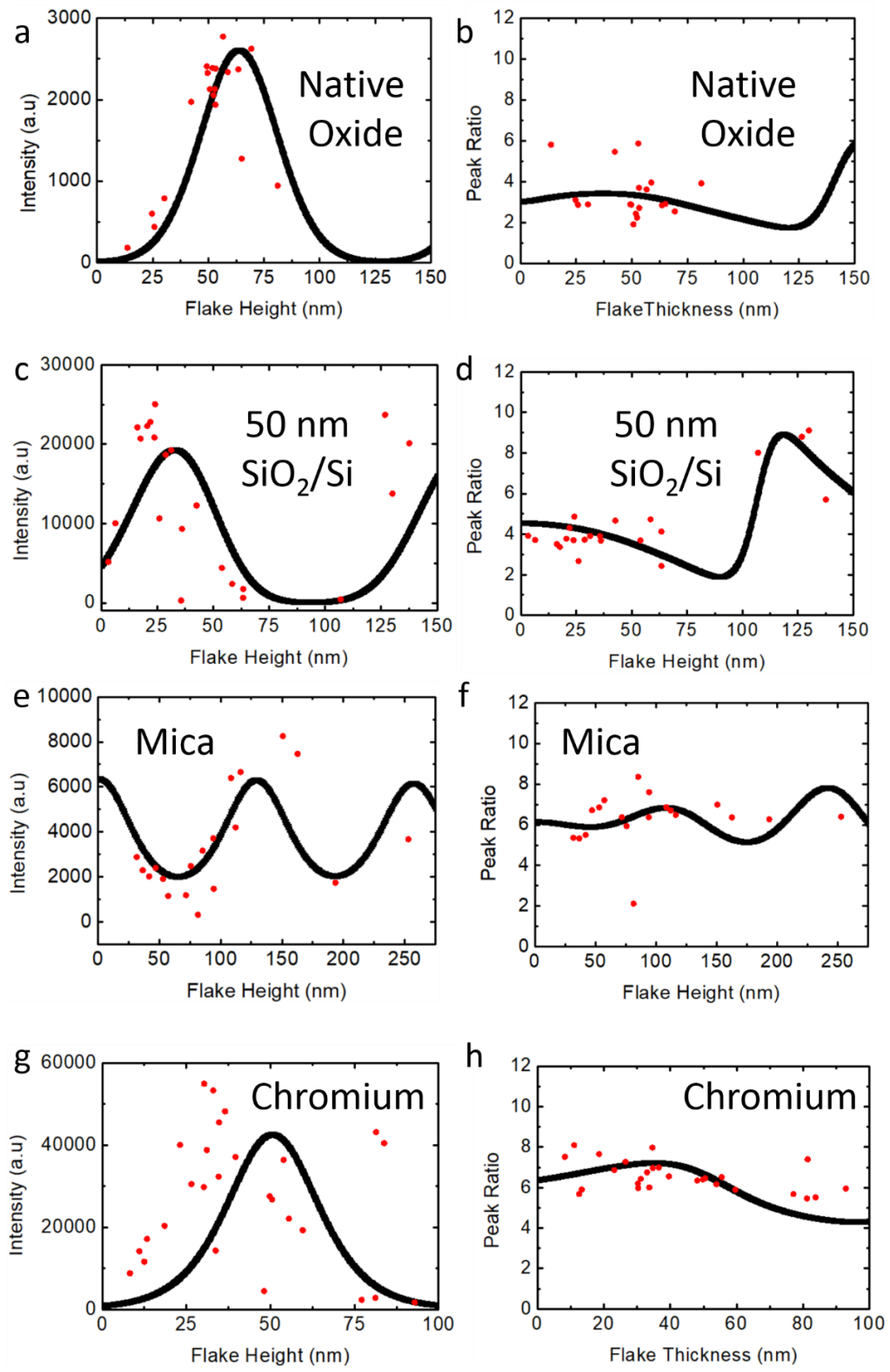


**Figure A1.2.** The variation in the intensity of the fitted 0-0 peak and the 0-0/0-1 peak ratio with hBN flake thickness are plotted for 0.4 ML coverages of PTCDI on hBN on various substrates, including; native oxide (a,b), 50 nm SiO<sub>2</sub>/Si (c,d), mica (e,f) and chromium (g,h). Interference models were also used to calculate the expected intensity and peak ratio (black) which were fitted to experimental results (red). All data was acquired using a 532 nm excitation laser.

For data acquired from 300 nm SiO<sub>2</sub>/Si substrates using both 405 nm and 532 nm excitation lasers, the experimental and calculated fluorescence intensity variations are in good agreement. This was also the case for mica, 50 nm SiO<sub>2</sub>/Si and native Si substrates, using only a 532 nm excitation laser. On chromium, the peak in the fluorescence intensity occurred at lower flake heights than in theoretical models, which included an additional phase change at the hBN/Cr interface due to the extinction coefficient of chromium [134].

This disagreement was attributed to changes to the chromium surface during furnace cleaning. After furnace cleaning, samples were darker in colour and outlines could be seen on the surface using optical microscopy, thought to arise due to the removal of hBN flakes during cleaning. This was confirmed by AFM images of an area of chromium where a hBN flake was believed to be removed during furnace cleaning, see figure A1.3, a step height on the chromium surface of approximately 5 nm was extracted. Given that the optical path includes both transmission and reflection and the refractive index of hBN, this would account for an overestimate of approximately 20 nm in the modelled flake height, in good agreement with experimental results.

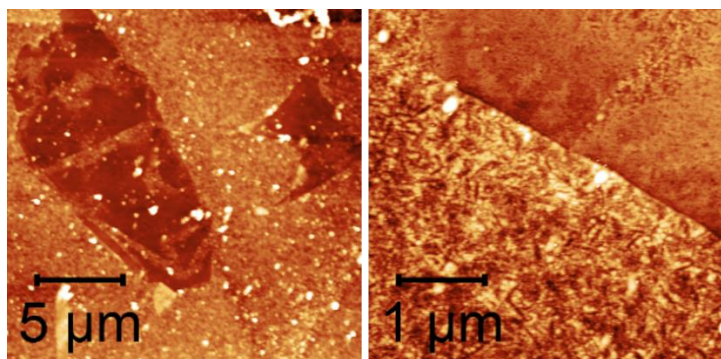


**Figure A1.3.** Images of the chromium surface after furnace cleaning were acquired using AFM. The surface topography was much rougher on areas of the surface not covered by hBN during furnace cleaning, with a step height of approximately 5 nm from uncovered areas to areas which had been covered by hBN.

The same procedure was also carried out for PTCDI-melamine on hBN on 300 nm SiO<sub>2</sub>/Si and chromium, see figure A1.4. As for PTCDI, the variation in the intensity was found to be in good

agreement for 300 nm SiO<sub>2</sub> substrates while on chromium, the flake thickness at which maximum intensity occurs was overestimated by approximately 20 nm. Comparing the variation in the fluorescence lineshape of PTCDI and PTCDI-melamine on hBN on chromium, see figure A1.2h and figure A1.4d, the relative increase in the 0-0/0-1 peak ratio in the absence of interference effects was estimated to be  $4.5 \pm 0.2$  between PTCDI-melamine and PTCDI.

This effect is discussed further in section 5.2 and 5.5.

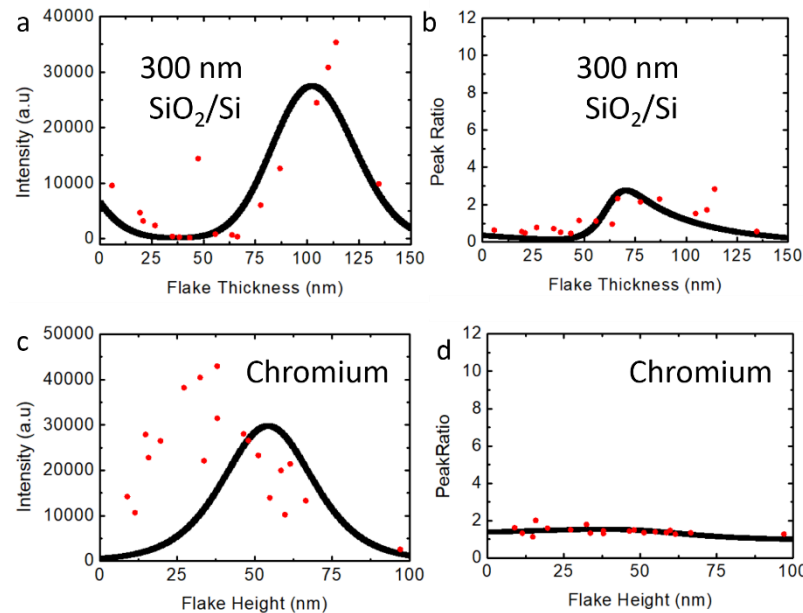


**Figure A1.4.** The variation in the 0-0 fluorescence peak intensity and the 0-0/0-1 peak ratio were plotted for PTCDI-melamine on 300 nm SiO<sub>2</sub>/Si (a,b) and chromium (c,d) substrates. Measurements were acquired with a 532 nm excitation laser.

In addition to changes in the fluorescence lineshape, the position of the 0-0 fluorescence peak was found to vary with the hBN flake thickness. The variation was found to share similar features to the variation in the fluorescence lineshape, with the maximum blue shift occurring at flake thicknesses which also gave the largest 0-0/0-1 peak ratio. The variation in the 0-0 peak position of PTCDI on hBN on 300 nm SiO<sub>2</sub>/Si with flake thickness is shown in figure A1.5, for comparison with peak ratio data from the same sample, see figure 4.3.5. The measured shift is thought to occur due to interference effects, where there is an asymmetry in the increase in the fluorescence intensity at wavelengths longer and shorter than the fluorescence

peak in the absence of interference. In chapter 5, comparison between PTCDI-melamine and PTCDI samples is drawn from hBN on chromium substrates, where interference effects are less prominent.

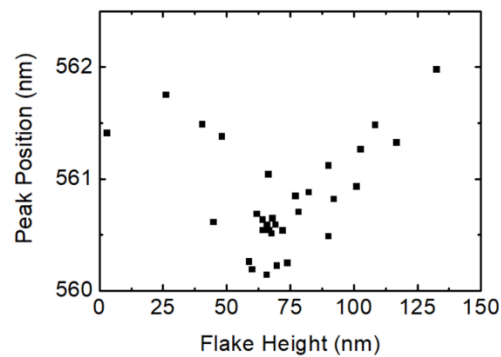


**Figure A1.4.** The position of the 0-0 fluorescence peak, extracted by fitting to a series of Lorentzian curves, of PTCDI on hBN on 300 nm SiO<sub>2</sub>/Si is plotted against the flake thickness. Spectra were acquired using a 532 nm excitation laser.

## **Appendix 2:**

# **The Fluorescence of hBN/PTCDI/hBN Heterostructures**

## A2. The Fluorescence of hBN/PTCDI/hBN Heterostructures

Currently, the Nottingham nanoscience group has been investigating van der Waals heterostructures of two dimensional materials such as hBN, graphene, black phosphorus and transition metal dichalcogenides. The electronic properties of 2D layers could be utilised in conventional device architectures, while their atomically thin structures make them ideal candidates for more sophisticated devices based on phenomena such as tunnelling [135]. In such devices, the quality of the interface between layers is important to the properties and performance of the heterostructure [136].

One way this interface could be modified or functionalised further is through molecular self-assembly. The study of fluorescent species within van der-Waals heterostructures is also interesting since the additional layer changes the chemical and dielectric environment experienced by a molecular aggregate. Exploring chromatic shifts within heterostructures gives further information about the processes which govern molecular fluorescence at interfaces. One particular aspect of molecular fluorescence which could be explored further is whether non-resonant interactions and phenomena analogous to the solvatochromic effect, seen for fluorophores in solution, lead to significant shifts [73].

Given the results presented in section 5.6, where substrate-induced fluorescence were considered, modifying the environment of PTCDI with a further hBN layer could be expected to lead to additional fluorescence shifts. By picking up mechanically exfoliated hBN flakes using poly propylene carbonate (PPC) stamps, heterostructures of PTCDI sandwiched between two hBN flakes can be produced.

PPC stamps are fabricated by first placing a small droplet of polydimethylsiloxane (PDMS) elastomer on a glass microscope slide. Once cured, the PDMS droplet enables hBN flakes to be picked up with only a small contact area between the surface and the stamp [137]. A sheet of PDMS is then placed on top of the cured droplet, giving a uniform surface on which to

deposit a poly-propylene carbonate (PPC) release layer. A solution PPC, 20 % by weight in anisole, is spin-coated onto the PDMS surface before the stamp is annealed to 80 °C for 5 minutes. The construction of a stamp is shown in figure A2.1. The resulting stamps deform under pressure, giving a flat contact area to the surface on which flakes are picked-up and dropped-off. Stamps are also transparent, which enables hBN flakes to be observed through the stamp at all stages of the fabrication process using optical microscopy.

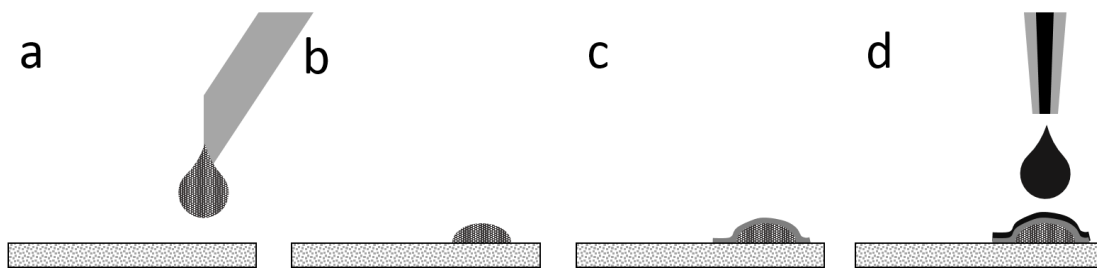


**Figure A2.1.** During the construction of a PPC stamp, PDMS is applied to a glass slide using a piece of metal wire (a) and cured to leave a circular droplet on the glass surface (b). A piece of sheet PDMS is placed over the droplet (c) before PPC is applied to the surface using a pipette and spun using a spin coater (d).

The stamping process is carried out using two micrometer stages, one for the stamp and a second for the sample, mounted beneath an optical microscope. PPC stamps are placed on a micrometer stage such that the exact placement of the PDMS droplet on the stamp can be seen using optical microscopy and controlled using the stamp micrometer. The sample is placed on a second micrometer stage and held in place using a vacuum chuck. The substrate temperature is controlled using a heater within the sample stage. The relative placement of the stamp and sample is monitored using an optical microscope. The setup of the stamping apparatus is shown in figure A2.2.

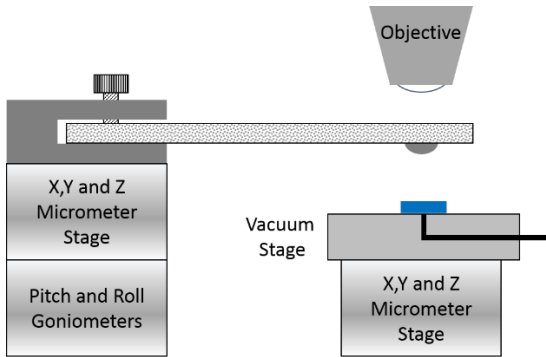


**Figure A2.2.** The configuration of the stamping apparatus is shown. A sample is placed on a heating plate on top of a micrometer stage with movement in the x, y and z directions. The sample is held in place by a vacuum chuck and can be viewed from above by an optical microscope. The stamp is held in place by a clip on top of a second micrometer stage with movement in the x, y and z directions as well as pitch and roll, enabling the stamp and sample to be fully aligned.

hBN flakes can be picked up by lowering the stamp towards substrate surface with the PDMS droplet aligned to a flake. The PPC on PDMS stamp is then brought into contact with the hBN flake, with the SiO<sub>2</sub> substrate held at approximately 40 °C. The sample is then cooled to 30 °C before the stamp is withdrawn, removing the hBN flake from the SiO<sub>2</sub> surface.

Heterostructures are produced by aligning the flake on the PPC stamp with a target flake. The sample temperature is increased and the stamp is brought into contact. During the fabrication of stamps, the PDMS surface can be placed in a plasma oven prior to spin coating PPC, giving greater adhesion between the PPC and PDMS layers [138]. The plasma treatment step leads to different results when the hBN flake is dropped-off. PPC stamps produced with and without the plasma treatment step will accordingly be referred to as plasma-treated and non-plasma-treated.

In the case of non-plasma-treated stamps, stamps with a flake attached are brought into contact with a second flake and withdrawn from the surface held at 80 °C. The PPC then delaminates from the PDMS, leaving the heterostructure and surrounding SiO<sub>2</sub> covered in a layer of PPC, which can be removed by immersion in acetone. This process is illustrated in figure A2.3.

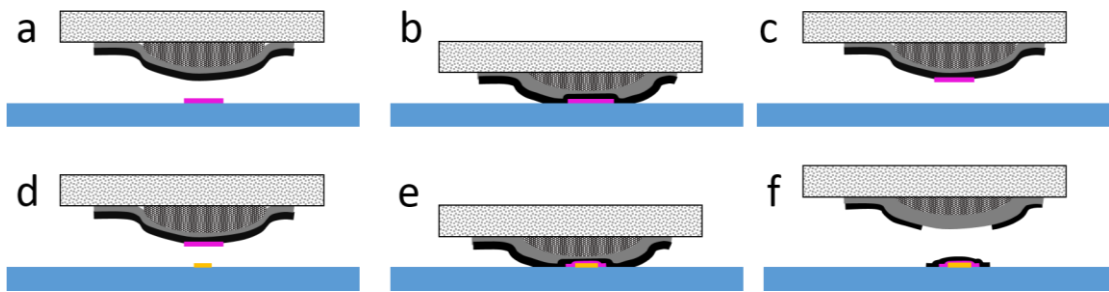


**Figure A2.3.** hBN flakes are picked up from  $\text{SiO}_2$  substrates by aligning hBN flakes underneath the centre of a PDMS droplet (a) and bringing the stamp into contact with the surface at  $40\text{ }^\circ\text{C}$  (b). The substrate is cooled to  $30\text{ }^\circ\text{C}$  before the stamp is withdrawn with the flake attached (c). The flake on the stamp is then aligned over a flake on a second substrate (d) before it is brought into contact with the substrate held at  $80\text{ }^\circ\text{C}$  (e). The stamp is then withdrawn, causing the PPC to delaminate from the PDMS (f), leaving a heterostructure covered with PPC.

In the case of plasma-treated stamps, hBN flakes on a stamp are brought into contact with a target flake. The stamp is then retracted, with the substrate temperature held at approximately  $80\text{ }^\circ\text{C}$ , to leave a heterostructure with no excess PPC on top. During the experiment, it was noted that by retracting the PPC stamp slowly; a stack of two hBN flakes were left on the surface. When the stamp was withdrawn quickly; the complete heterostructure was picked-up. The stacked hBN flakes could then be deposited on a third substrate.

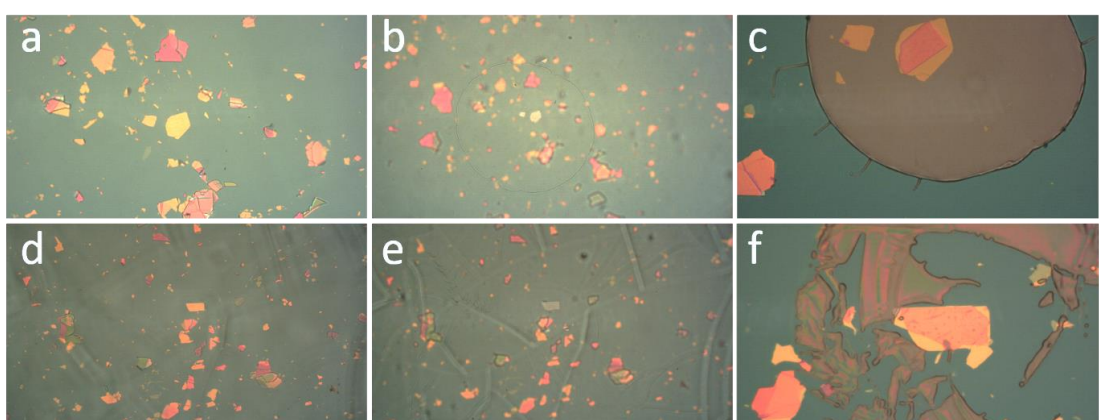


**Figure A2.4.** Heterostructures are produced using non-plasma treated stamps by aligning hBN flakes with the centre of the PDMS droplet on the stamp (a). Flakes are picked up (b) and brought into contact with a second hBN flake. The stamp is withdrawn, leaving the heterostructure and surrounding  $\text{SiO}_2$  covered with PPC (c). Plasma treated stamps work in exactly the same way to pick up flakes (d, e) but leave no visible areas of PPC on the hBN surface after dropping off the second flake (f).

Producing heterostructures using plasma-treated stamps leaves much less PPC residue on the sample surface, such that solvent cleaning is not necessary. Optical images of heterostructures produced using non-plasma treated and plasma treated PPC stamps are shown in figure A2.4. It was still possible to carry out fluorescence spectroscopy on stacked hBN/PTCDI/hBN heterostructures with PPC on the surface.

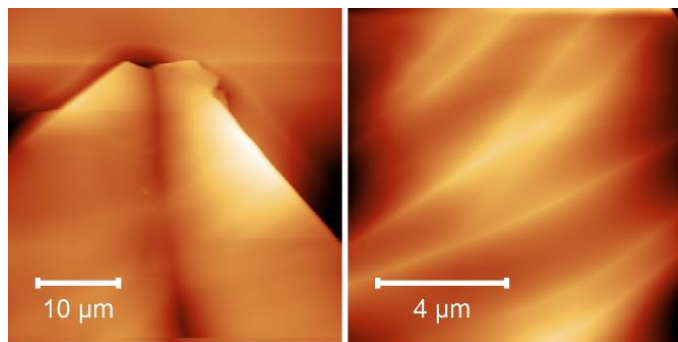


**Figure A2.5.** AFM images of a hBN flake on a PPC stamp. The side from which AFM images were acquired was the side in contact with SiO<sub>2</sub> prior to pick up, and that would be on the interior of the heterostructure after stamping.

In order to measure the fluorescence spectra of PTCDI monolayers within hBN heterostructures, a pristine interface between PTCDI and the overlying hBN is critical. hBN was deposited onto SiO<sub>2</sub>/Si by mechanical exfoliation, before flame-annealing, which was always done immediately before hBN flakes were picked up. In order to check the cleanliness of the hBN interface in contact with PTCDI monolayers, the surface morphology was determined using AFM prior to the production of heterostructures. Figure A2.5 shows the morphology a hBN flake on a PPC stamp. While creases and corrugations of the hBN surface were observed on the PPC stamp, smaller area AFM scans revealed little contamination on the hBN surface. The absence of tape residue on the side of hBN in contact with SiO<sub>2</sub> during mechanical exfoliation was unexpected and could imply better adhesion between pristine flakes and the SiO<sub>2</sub> surface onto which hBN flakes are exfoliated.

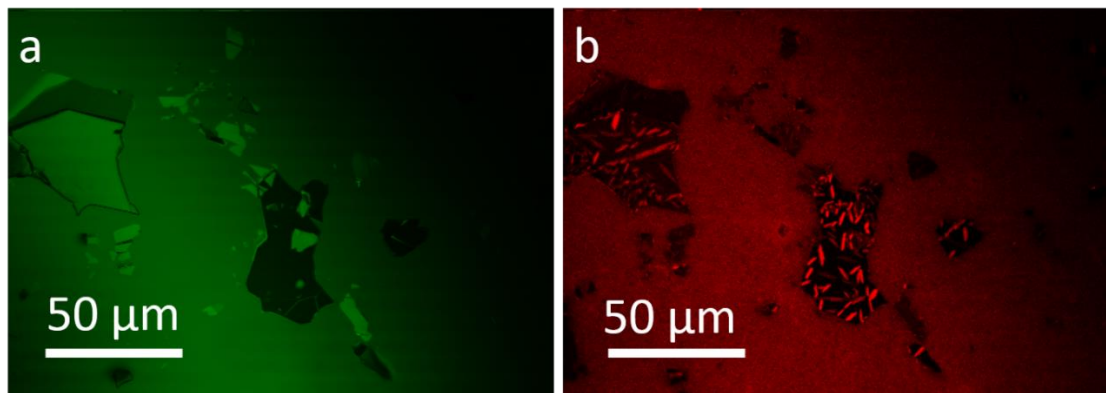


**Figure A2.6.** A 0.4 ML coverage of PTCDI was sublimed onto hBN on SiO<sub>2</sub> substrates held at 135 °C. Images of the sample were acquired using confocal scanning fluorescence microscopy with a 488 nm excitation laser. Images (a) and (b) were acquired for detection bands set at 485-490 nm and 540-580 nm respectively. The 540-580 nm band (b) contains the main fluorescence peak of monolayer PTCDI on hBN.

In order to check the effect of heterostructure formation upon the morphology of PTCDI, islands were mapped using both AFM and scanning confocal fluorescence microscopy. As in section 4.5, the fluorescence maps of PTCDI were found to be in good agreement with the island morphology seen in AFM images. Scanning confocal fluorescence microscopy images of sub-monolayer coverages of PTCDI on hBN grown at 135 °C are shown in figure A2.6 with channels set to detect the reflected laser (485 nm-490 nm) and fluorescence (540 nm-580 nm) signals. A number of hBN flakes with PTCDI monolayer islands were mapped using scanning confocal fluorescence microscopy prior to the deposition of a further hBN flake using both plasma and non-plasma treated PPC stamps. In all cases, the formation of a heterostructure did not change the size or position of PTCDI islands. Scanning confocal fluorescence microscopy images of a hBN/PTCDI/hBN heterostructure on SiO<sub>2</sub>, formed using the same flake as figure A2.6, are shown in figure A2.7.

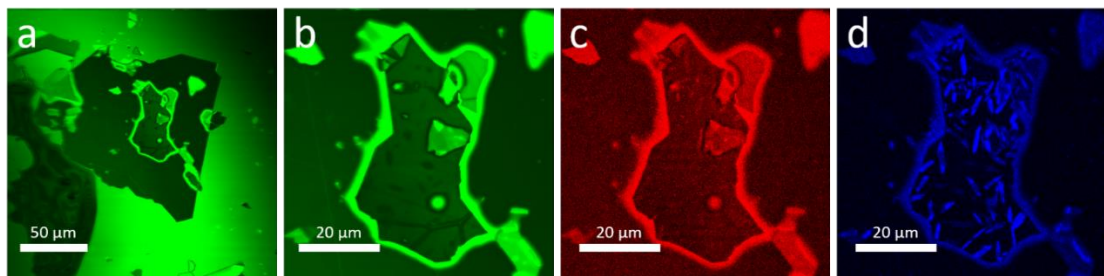


**Figure A2.7.** The same flake as figure A2.6 was used to produce a hBN/PTCDI/hBN heterostructure using a plasma-treated stamp. Scanning confocal fluorescence microscopy was used to acquire an image of the resulting heterostructure. Images a and b reveal the morphology of the heterostructure including blisters, which appear as dark spots in image b. Images c and d reveal the spatial distribution of the fluorescence signal within the given bands; green (485 nm– 490 nm), red (520 nm – 550 nm) and blue (550 nm– 580 nm).

Using scanning confocal fluorescence microscopy, it was possible to determine the presence of PTCDI islands within hBN/PTCDI/hBN heterostructures. Dark patches were also observed across the surface of heterostructures, see figure A2.7b. These dark spots were attributed to blisters within heterostructures. By comparing the images formed from the reflected laser signal (485 nm -490 nm) and the fluorescence channel (550 nm–580 nm), dark patches were found to form preferentially over PTCDI islands.

The morphology of heterostructures was determined using AFM. By comparison with AFM images, dark patches in scanning confocal fluorescence microscopy images were confirmed to be blisters within heterostructures. Above PTCDI islands, blisters had heights within the range of 10 nm to 30 nm. Off PTCDI islands, blisters had a height of 2 nm to 5 nm with much smaller lateral dimensions. Unexpectedly, PTCDI islands within heterostructures could also be observed in AFM images and height profiles, with a step height of  $0.3 \pm 0.1$  nm. An optical micrograph of a heterostructure formed using non-plasma treated stamp is shown in figure A2.8a. PPC was removed by immersion in acetone before heterostructures were investigated using AFM, see figure A2.8b and c.

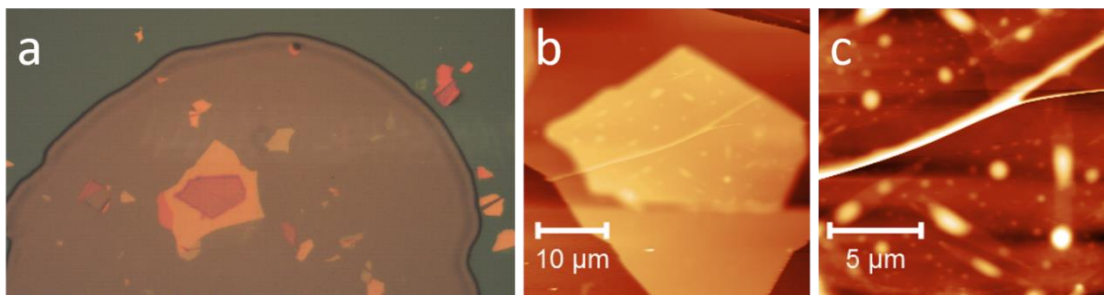


**Figure A2.8.** PTCDI on hBN was grown by sublimation in vacuum at 135 °C, a non-plasma treated PPC stamp was used to deposit a second hBN flake. Images of the heterostructure with PPC residue were acquired using optical microscopy (a). The topography of the heterostructure was then determined using AFM (b,c), blisters and step edges of PTCDI islands were observed.

The presence of blisters within van der Waals heterostructures is often observed [136], while the formation of larger blisters above PTCDI islands suggests they are able to migrate. This implies stronger adhesion between flakes than the top hBN flake and a PTCDI monolayer. In the literature, the presence of blisters is reduced through annealing procedures. This was not carried out here since annealing could cause a modification or reaction of the PTCDI monolayers, making it difficult to relate the structure and fluorescence of PTCDI within heterostructures. Heterostructures were instead loaded into a vacuum system with a base pressure of  $10^{-8}$  mbar for 12 hours, but this had no effect on the size and appearance of blisters, which were mapped using AFM before and after the pumping cycle.

The fluorescence of PTCDI monolayers within hBN/PTCDI/hBN heterostructures was first investigated using scanning confocal fluorescence microscopy. By comparing sequential images acquired with a series of 5 nm detection bandwidths, spectra could be extracted. Using this method, an intense peak was observed at  $560 \text{ nm} \pm 2.5 \text{ nm}$  ( $2.21 \pm 0.01 \text{ eV}$ ) while a very weak signal was observed at  $532.5 \text{ nm} \pm 2.5 \text{ nm}$  ( $2.33 \pm 0.01 \text{ eV}$ ). The second peak appeared as a slight shoulder in the background due to the 488 nm excitation laser. Given the weak signal-to-noise ratio of the  $532.5 \pm 2.5 \text{ nm}$  peak, it was not possible to map the spatial

distribution of this fluorescence signal. This is seen in figure A2.7c, which used a 520 nm–550 nm detection band.

Fluorescence spectra were also acquired from multiple heterostructures using the Horiba LabRAM HR spectrometer. This system used a 532 nm excitation laser with low pass filters, which allowed spectra to be taken from 533 nm. Fluorescence measurements were taken from a number of heterostructures, produced using plasma treated and non-plasma treated stamps. Two distinct peaks were measured at  $562.5 \pm 0.5$  nm ( $2.204 \pm 0.002$  eV) and  $542.6 \pm 0.5$  nm ( $2.285 \pm 0.002$  eV). The presence and relative intensity of the two peaks was different between heterostructures and was found to change laterally across the surface of a single heterostructure. There were no significant differences between heterostructures produced using plasma treated or non-plasma treated stamps with PPC residue. The fluorescence of hBN/PTCDI/hBN heterostructures produced using non-flame annealed stamps with PPC residue is shown in figure A2.9.

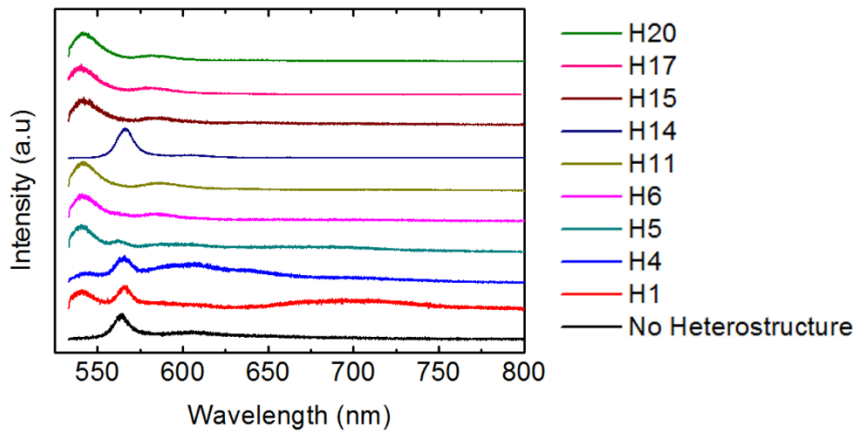


**Figure A2.9.** Fluorescence spectra were acquired from a range of hBN/PTCDI/hBN heterostructures with PPC residue using a 532 nm excitation laser. The bottom spectra (black) was acquired from an un-capped hBN flake containing monolayer islands of sublimed PTCDI.

The variation in the fluorescence spectra across all heterostructures was attributed to the presence of two peaks. The origin of the two peaks is believed to be due to two distinct environments within heterostructures, corresponding to PTCDI in contact with one

( $562.5 \pm 0.5$  nm) and two ( $542.6 \pm 0.5$  nm) hBN interfaces. The presence of a peak corresponding to PTCDI monolayers on hBN ( $562.5 \pm 0.5$  nm) is expected to correspond to PTCDI on hBN underneath blisters, which form preferentially over islands. The 0-0 transition of fully encapsulated PTCDI islands (in contact with both hBN flakes) is expected to account for the peak at  $542.6 \pm 0.5$  nm. This conclusion is supported by AFM images of the heterostructures in figure A2.8, where large bubbles are observed to coincide with intact PTCDI islands.

Since it was not possible to resolve the lateral distributions of the fluorescence signals at  $542.6 \pm 0.5$  nm and  $562.5 \pm 0.5$  nm, it was not possible to relate AFM images of heterostructures to spectral features. The possibility that the signal at  $542.6 \pm 0.5$  nm could be due to re-ordering of PTCDI within blisters of the hBN heterostructure could not be discounted. In an attempt to resolve this issue, the experiment was repeated with a greater (0.8 ML) coverage of PTCDI. This sample had larger monolayer islands, but similar results were obtained. Since it was not possible gain full monolayer coverage of PTCDI without the occurrence of additional layers, thicker sublimed films were not considered.

In this appendix, the formation of hBN/PTCDI/hBN van der Waals heterostructures was investigated. Upon formation of a heterostructure, blisters were found to form preferentially over PTCDI islands. The presence of blisters led to two fluorescence peaks, one was comparable to monolayer PTCDI on hBN without a second hBN layer while a second, blue-shifted by  $0.081 \pm 0.002$  eV, was also present. This blue shift was attributed to the encapsulation of PTCDI at the interface of two hBN flakes. Under the experimental conditions used, it was not possible to eliminate the possibility of an altered phase of PTCDI within blisters. The encapsulation of flat-lying molecular monolayers at dielectric interfaces is promising, since it could potentially be used to tune their fluorescence. The effect of parameters such as the alignment of the second layer, type of material and even further

molecular monolayers adsorbed on the second layer could be a promising way to control the dielectric environment and placement of fluorophores.

## References

- [1] J. Mei et al. Integrated materials design of organic semiconductors for field effect transistors. *J. Am. Chem. Soc.* **135**, 6724 (2013)
- [2] Y. Wang et al. A highly stretchable, transparent, and conductive polymer. *Sci. Adv.* **3**, e16020762009 (2017)
- [3] J. V. Barth et al. Engineering atomic and molecular nanostructures at surfaces. *Nature*. **437**, 671 (2005)
- [4] S. De Feyter and F. C. De Schryver. Two-dimensional supramolecular self-assembly probed by scanning tunnelling microscopy. *Chem. Soc. Rev.* **32**, 139 (2003)
- [5] J. A. Theobald et al. Controlling molecular deposition and layer structure with supramolecular surface assemblies. *Nature*. **424**, 1029 (2003)
- [6] R. Madueno et al. Functionalizing hydrogen-bonded surface networks with self-assembled monolayers. *Nature*. **454**, 618 (2008)
- [7] K. W. Hipps et al. A self-organized 2-dimensional bifunctional structure formed by supramolecular design. *J. Am. Chem. Soc.* **124**, 2126 (2002)
- [8] S. J. Griessl et al. Incorporation and manipulation of coronene in an organic template structure. *Langmuir*. **20**, 9403 (2004)
- [9] B. Karamzadeh et al. Sequential nested assembly at the liquid/solid interface. *Faraday Discuss.* **204**, 173 (2017)
- [10] T. Schmitz-Hübsch et al. Direct observation of organic–organic heteroepitaxy: perylenetetracarboxylic-dianhydride on hexa-peri-benzocoronene on highly ordered pyrolytic graphite. *Surf. Sci.* **445**, 358 (2000)
- [11] M. Gruenewald et al. Impact of a molecular wetting layer on the structural and optical properties of tin (II)-phthalocyanine multilayers on Ag(111). *Phys. Rev. B*. **93**, 115418 (2016)
- [12] L. Gross et al. The chemical structure of a molecule resolved by atomic force microscopy. *Science*. **325**, 1110 (2009).
- [13] M. Müller et al. Exciton and polarization contributions to optical transition energies in an epitaxial organic monolayer on a dielectric substrate. *Phys. Rev. B*. **83**, 241203 (2011)
- [14] T. Dienel et al. Growth-mode-induced narrowing of optical spectra of an organic adlayer. *Adv. Mater.* **20**, 959 (2008)

- [15] F. C. Spano. The spectral signatures of Frenkel polarons in H- and J-aggregates. *Acc. Chem. Res.* **43**, 429 (2010)
- [16] H. Margenau. Van der Waals forces. *Rev. Mod. Phys.* **11**, 1 (1939)
- [17] C. B. Aakeröy and K. R. Seddon. The hydrogen bond and crystal engineering. *Chem. Soc. Rev.* **22**, 397 (1993)
- [18] J. A. Venables. Introduction to surface and thin film processes (Cambridge University Press, Cambridge, 2000)
- [19] J. A. Venables and M. Hanbücken. Nucleation and growth of thin films. *Rep. Prog. Phys.*, **47**, 339 (1984).
- [20] H. Brune et al. Microscopic view of nucleation on surfaces *Phys. Rev. Lett.* **73**, 1955 (1994)
- [21] F. Loske et al. Quantitative description of C<sub>60</sub> diffusion on an insulating surface. *Phys. Rev. B.* **82**, 155428 (2010)
- [22] H.W. Kroto et al. C<sub>60</sub>: Buckminsterfullerene. *Nature.* **318**, 162 (1985)
- [23] C-Z. Li et al. Functional fullerenes for organic photovoltaics. *J. Mater. Chem.* **22**, 4161 (2012)
- [24] H. Park et al. Nanomechanical oscillations in a single-C<sub>60</sub> transistor. *Nature.* **407**, 57 (2000)
- [25] W. I. F. David et al. Crystal structure and bonding of ordered C<sub>60</sub>. *Nature.* **353**, 147 (1991)
- [26] H. I. Li et al. Surface geometry of C<sub>60</sub> on Ag(111). *Phys. Rev. Lett.* **103**, 056101 (2009)
- [27] L. Tang et al. Complex orientational ordering of C<sub>60</sub> molecules on Au(111). *J. Chem. Phys.* **135**, 114702 (2011)
- [28] P. Rahe et al. From dewetting to wetting molecular layers: C<sub>60</sub> on CaCO<sub>3</sub> (1014) as a case study. *Phys. Chem. Chem. Phys.* **14**, 6544 (2012)
- [29] F. Loske et al. Contrast inversion in non-contact atomic force microscopy imaging of C<sub>60</sub> molecules. *Nanotechnology.* **20**, 264010 (2009)
- [30] M. Korner et al. Second-layer induced island morphologies in thin-film growth of fullerenes. *Phys. Rev. Lett.* **107**, 016101 (2011)
- [31] S. A. Burke et al. C<sub>60</sub> on alkali halides: epitaxy and morphology studied by noncontact AFM. *Phys. Rev. B.* **76**, 035419 (2007)
- [32] S. A. Burke et al. Molecular dewetting on insulators *J. Phys. Condens. Matter.* **21**, 423101 (2009)

- [33] G. Ehrlich and F. G. Hudda. Atomic View of Surface Self-Diffusion: Tungsten on tungsten. *J. Chem. Phys.* **44**, 1039 (1966)
- [34] R. L. Schwoebel, and E. J. Shipsey. Step motion on crystal surfaces. *J. Appl. Phys.* **37**, 3682 (1966)
- [35] C. Li and H. Wonneberger. Perylene imides for organic photovoltaics: yesterday, today, and tomorrow. *Adv. Mater.* **24**, 613 (2012)
- [36] X. Liu et al. Seeing modularity self-assembled monolayers of  $\pi$ -conjugated perylene derivatives by scanning tunneling microscopy. *J. Phys. Chem. C.* **120**, 18607 (2016)
- [37] J. C. Swarbrick et al. Square, hexagonal, and row phases of PTCDA and PTCDI on Ag-Si(111) *J. Phys. Chem. B.* **109**, 12167 (2005)
- [38] J. B. Gustafsson et al. STM studies of thin PTCDA films on Ag/Si 111. *Phys. Rev. B.* **75**, 155414 (2007)
- [39] T. Schmitz-Hübsch et al. Epitaxial growth of 3,4,9,10-perylene-tetracarboxylic-dianhydride on Au (111): A STM and RHEED study. *Phys. Rev. B.* **55**, 12 (1997)
- [40] C. Kendrick et al. STM study of the organic semiconductor PTCDA on highly-oriented pyrolytic graphite. *Appl. Surf. Sci.* **104/105**, 586 (1996)
- [41] C. Ludwig et al. STM investigations of PTCDA and PTCDI on graphite and MoS<sub>2</sub>. A systematic study of epitaxy and STM image contrast. *Z. Phys. B.* **93**, 365 (1994)
- [42] S. A. Burke et al. Strain induced dewetting of a molecular system: bimodal growth of PTCDA on NaCl. *Phys. Rev. Lett.* **100**, 186104 (2008)
- [43] J. M. Topple et al. Thin film evolution: dewetting dynamics of a bimodal molecular system. *Phys. Rev. B.* **79**, 205414 (2009)
- [44] M. Mura et al. H-bonding supramolecular assemblies of PTCDI molecules on the Au(111) surface. *J. Phys. Chem.* **113**, 21840 (2009)
- [45] A. Saywell et al. Electrospray deposition of C<sub>60</sub> on a hydrogen-bonded supramolecular network. *J. Phys. Chem. C.* **112**, 7706 (2008)
- [46] V. V. Korolkov et al. Bimolecular porous supramolecular networks deposited from solution on layered materials: graphite, boron nitride and molybdenum disulphide. *Chem. Comm.* **50**, 8882 (2014)
- [47] L. Perdigão et al. Surface self-assembly of the cyanuric acid–melamine hydrogen bonded network. *Chem. Commun.* **0**, 538 (2006)

- [48] H. Zhang et al. One-step preparation of large-scale self-assembled monolayers of cyanuric acid and melamine supramolecular species on Au(111) surfaces. *J. Phys. Chem. C.* **112**, 4209 (2008)
- [49] P. A. Staniec et al. Honeycomb networks and chiral superstructures formed by cyanuric acid and melamine on Au(111). *J. Phys. Chem.* **111**, 886 (2007)
- [50] X. Zhang Self-assembly and aggregation of melamine and melamine–uric/cyanuric acid investigated by STM and AFM on solid surfaces. *Phys. Chem. Chem. Phys.* **11**, 7708 (2009)
- [51] K. Kannappan et al. An experimental and theoretical study of the formation of nanostructures of self-assembled cyanuric acid through hydrogen bond networks on graphite. *J. Phys. Chem. B.* **111**, 6634 (2007)
- [52] V. V. Korolkov et al. Supramolecular networks stabilise and functionalise black phosphorus. *Nat. Commun.* **8** 1385 (2017)
- [53] A.K. Geim and K. S. Novoselov. The rise of graphene. *Nat. Mater.* **6**, 183 (2007)
- [54] K. S. Novoselov et al. Electric field effect in atomically thin carbon films. *Science.* **306**, 5696 (2004)
- [55] K. S. Novoselov et al. Room-temperature quantum Hall effect in graphene. *Science.* **315**, 5817 (2007)
- [56] J. M. MacLeod and F. Rosei. Molecular self-assembly on graphene. *Small*, **10**, 1038 (2014)
- [57] J. Cai et al. Atomically precise bottom-up fabrication of graphene nanoribbons. *Nature.* **466**, 470 (2010)
- [58] Päivi Järvinen et al. Molecular self-assembly on graphene on SiO<sub>2</sub> and h-BN substrates. *Nano Lett.* **13**, 3199 (2013)
- [59] K. S. Novoselov et al. 2D materials and van der Waals heterostructures. *Science.* **353**, 6298 (2016)
- [60] A. K. Geim & I. V. Grigorieva. Van der Waals heterostructures. *Nature* **449**, 419 (2013)
- [61] A. S. Mayorov et al. Micrometer-scale ballistic transport in encapsulated graphene at room temperature. *Nano Lett.* **11**, 2396 (2011)
- [62] X. Du et al. Approaching ballistic transport in suspended graphene. *Nat. Nanotechnol.* **3**, 491 (2008)

- [63] C. R. Dean et al. Boron nitride substrates for high-quality graphene electronics. *Nat. Nanotechnol.* **5**, 722–726 (2010)
- [64] K. Watanabe et al. Direct-bandgap properties and evidence for ultraviolet lasing of hexagonal boron nitride single crystal. *Nat. mater.* **3**, 404 (2004)
- [65] B. Valeur. *Molecular Fluorescence*. (Wiley-VCH, Weinheim, 2002)
- [66] B. Kippelen and J-L. Brédas. Organic photovoltaics. *Energy Environ. Sci.* **2**, 251 (2009)
- [67] R. E. Smalley et al. Molecular optical spectroscopy with supersonic beams and Jets. *Acc. Chem. Res.* **10**, 139 (1977)
- [68] P. H. S. Fitch et al. The fluorescence excitation spectrum of free base phthalocyanine cooled in a supersonic free jet. *J. Chem. Phys.* **73**, 1064 (1980)
- [69] F. Stienkemeier and K. K. Lehmann. Spectroscopy and dynamics in helium nanodroplets. *J. Phys. B: At. Mol. Opt. Phys.* **39**, 127 (2006)
- [70] M. Wewer and F. Stienkemeier. Laser-induced fluorescence spectroscopy of 3,4,9,10-perylenetetracarboxylicdianhydrid in helium nanodroplets. *J. Chem. Phys.* **120**, 1239 (2004)
- [71] M. Wewer and F. Stienkemeier. Laser-induced fluorescence spectroscopy of N,N0-dimethyl 3,4,9,10-perylene tetracarboxylic diimide monomers and oligomers attached to helium nanodroplets. *Phys. Chem. Chem. Phys.* **7**, 1171 (2005)
- [72] R. Lehnig and A. Slenczka. Emission spectra of free base phthalocyanine in superfluid helium droplets. *J. Chem. Phys.* **118**, 8256 (2003)
- [73] N. S. Bayliss. The effect of the electrostatic polarization of the solvent on the electronic absorption spectra in solution. *J. Chem. Phys.* **18**, 292. (1950)
- [74] V. V. Korolkov et al. Van der Waals-induced chromatic shifts in hydrogen-bonded two-dimensional porphyrin arrays on boron nitride. *ACS Nano.* **9**, 10347 (2015)
- [75] A. S. Davydov. The theory of molecular excitations. *Phys. Usp.* **7**, 2 (1964)
- [76] M. Muller et al. Finite size line broadening and superradiance of optical transitions in two dimensional long-range ordered molecular aggregates. *J. Chem. Phys.* **139**, 044302 (2013)
- [77] K. Kuhnke et al. Atomic-scale imaging and spectroscopy of electroluminescence at molecular interfaces. *Chem. Rev.* **117**, 5174 (2017)
- [78] Y. Zhang et al. Visualizing coherent intermolecular dipole–dipole coupling in real space. *Nature.* **531**, 623 (2016)

- [79] H. Imada et al. Real-space investigation of energy transfer in heterogeneous molecular dimers. *Nature*. **538**, 364 (2016)
- [80] M. Kasha et al. The exciton model in molecular spectroscopy, *Pure Appl. Chem.* **11**, 371 (1965)
- [81] R. Forker et al. Optical transition energies of isolated molecular monomers and weakly interacting two-dimensional aggregates. *Phys. Rev. B*. **93**, 165426 (2016)
- [82] G. Binnig and H. Rohrer. Scanning tunnelling microscopy, *Surf. Sci.* **126**, 236 (1983)
- [83] G. Binnig and H. Rohrer. Scanning tunneling microscopy—from birth to adolescence. *Rev. Mod. Phys.* **59**, 615 (1987)
- [84] J. A. Stroscio and D. M. Eigler. Atomic and molecular manipulation with the scanning tunneling microscope. *Science*. **254**, 1319 (1991)
- [85] A. Kühnle. Self-assembly of organic molecules at metal surfaces. *Current Opinion in Colloid & Interface Science*. **14**, 157 (2009)
- [86] A. Stabe et al. Diodelike current–voltage curves for a single molecule–tunneling spectroscopy with submolecular resolution of an alkylated, *peri*-condensed hexabenzocoronene. *Angew. Chem.* **34**, 1609 (1995)
- [87] G. Binnig et al. Atomic force microscope. *Phys. Rev. Lett.* **3**, 930 (1986)
- [88] C. P. Green. Normal and torsional spring constants of atomic force microscope cantilevers. *Rev. Sci. Instrum.* **75**, 1998 (2004)
- [89] P. Eaton and P. West. *Atomic force microscopy*. (Oxford, Oxford, 2010)
- [90] G. Haugstad. *Atomic force microscopy*. (Wiley, New Jersey, 2012)
- [91] G. Y. Chen et al. Resonance response of scanning force microscopy cantilevers. *Rev. Sci. Instrum.* **65**, 2532 (1994)
- [92] A. Sharma and S. G. Schulman, *Introduction to fluorescence spectroscopy*. (Wiley, New York, 1999)
- [93] G. G. Guilbault. *Fluorescence*. (Marcel Dekker, New York, 1967)
- [94] T. Taniguchi and K. Watanabe. Synthesis of high-purity boron nitride single crystals under high pressure by using Ba–BN solvent. *J. Cryst. Growth*. **303**, 525 (2007)
- [95] D. Golla et al. Optical thickness determination of hexagonal boron nitride flakes. *Appl. Phys. Lett.* **102**, 161906 (2013)

- [96] J. Megow et al. Calculating optical absorption spectra of thin polycrystalline organic films: structural disorder and site-dependent van der Waals interaction. *J. Phys. Chem. C.* **119**, 5747 (2015)
- [97] J. Roden et al. Vibronic line shapes of PTCDA oligomers in helium nanodroplets. *J. Chem. Phys.* **134**, 054907 (2011)
- [98] Paul Eastham. Nanophotonics I: quantum theory of microcavities. Retrieved: 12/02/2018. Available:<https://www.tcd.ie/Physics/people/Paul.Eastham/nanophotonics.pdf>
- [99] F. C. Spano. The spectral signatures of Frenkel polarons in H- and J-aggregates. *Acc. Chem. Res.* **43**, 429 (2010)
- [100] A. E. Clark et al. Beyond exciton theory: a time-dependent DFT and Franck-Condon study of perylene diimide and its chromophoric dimer. *J. Am. Chem. Soc.* **129**, 7586 (2007)
- [101] H. Proehl et al. In situ differential reflectance spectroscopy of thin crystalline films of PTCDA on different substrates. *Phys. Rev. B.* **71**, 165207 (2005)
- [102] M. Buscema et al. The effect of the substrate on the Raman and photoluminescence emission of single-layer MoS<sub>2</sub>. *Nano. Res.* **7**, 561 (2014)
- [103] M. I. Alonso. Anisotropic optical properties of single crystalline PTCDA studied by spectroscopic ellipsometry. *Organic Electronics.* **3**, 23 (2003)
- [104] V. Chis et al. Vibrational and electronic structure of PTCDI and melamine–PTCDI complexes. *J. Mol. Struct.* **924**, 47 (2009)
- [105] L. Zhang et al. Growth of pentacene on  $\alpha$ -Al<sub>2</sub>O<sub>3</sub>(0001) studied by *in situ* optical spectroscopy. *Phys. Rev. Materials.* **1**, 043401 (2017)
- [106] K. G. Saw. Surface reconstruction of  $\alpha$ -(0001) sapphire: an AFM, XPS, AES and EELS investigation. *J. Mat. Sci.* **39**, 2911 (2004)
- [107] D. Schlettwein et al. Ultrathin films of Perylenedianhydride and Perylenebis(dicarboximide) dyes on (001) alkali halide surfaces. *Chem. Mater.* **10**, 601 (1998)
- [108] R. Scholz et al. Investigation of molecular dimers in  $\alpha$ -PTCDA by ab initio methods: Binding energies, gas-to-crystal shift, and self-trapped excitons. *Phys. Rev. B.* **72**, 245208 (2005)
- [109] M. Hoffmann et al. The lowest energy Frenkel and charge-transfer excitons in quasi-one-dimensional structures: application to MePTCDI and PTCDA crystals. *Chem. Phys.* **258**, 73 (2000)

- [110] M. Hochheim et al. Analysis of the vibronic spectra of perylene-3,4,9,10-tetracarboxylic dianhydride adsorbed on NaCl and KCl. *J. Phys. Chem. C*, **120**, 24240 (2016)
- [111] F. Loske et al. Deposition sequence determines morphology of C<sub>60</sub> and 3,4,9,10-perylenetetracarboxylic diimide Islands on CaF<sub>2</sub>(111), *Jpn. J. Appl. Phys.* **50**, 08LB07 (2011)
- [112] V. V. Korolkov et al. Supramolecular heterostructures formed by sequential epitaxial deposition of two-dimensional hydrogen-bonded arrays. *Nat. Chem.* **9**, 1191 (2017)
- [113] G. Decher. Fuzzy nanoassemblies: toward layered polymeric multi-composites. *Science*. **277**, 1232 (1997)
- [114] N. P. D'Costa and J. H. Hoh. Calibration of optical lever sensitivity for atomic force microscopy. *Review of Scientific Instruments* **66**, 5096 (1995)
- [115] S. Sadewasser and M. C. Lux-Steiner. Correct height measurement in noncontact atomic force microscopy. *Phys. Rev. Lett.* **91** 266101-1 (2003)
- [116] S. Freund et al. Morphology change of C<sub>60</sub> islands on organic crystals observed by atomic force microscopy. *ACS Nano*, **10**, 5782 (2016)
- [117] K. Kobayashi et al. Imaging of fullerene molecules on Si (111) surface with NC-AFM. *Appl. Surf. Sci.* **157**, 228 (2000)
- [118] Y. Yamamoto et al. Morphological change of C<sub>60</sub> monolayer epitaxial films under photoexcitation *Phys. Rev. B*. **70**, 155415 (2004)
- [119] L. A. Girifalco. Molecular properties of C<sub>60</sub> in the gas and solid phases. *J. Phys. Chem.* **96**, 858 (1992).
- [120] Ch. Girard et al. van der Waals attraction between two C<sub>60</sub> fullerene molecules and physical adsorption of C<sub>60</sub> on graphite and other substrates. *Phys. Rev. B*. **49**, 425 (1994).
- [121] Y. R. Ma et al. Disorder-order ripening of C<sub>60</sub> islands. *Phys. Rev. Lett.* **78**, 2588 (1997)
- [122] I. Jung et al. Simple approach for high-contrast optical imaging and characterization of graphene-based sheets. *Nano. Lett.* **7**, 3569 (2007)
- [123] J. Fujita et al. Spiral growth of C<sub>60</sub>. *Appl. Phys. Lett.* **63**, 1008 (1993)
- [124] Y. Kim et al. AFM study of surface phenomena based on C<sub>60</sub> film growth. *Appl. Surf. Sci.* **130**, 602 (1998)
- [125] M. B. Wieland et al. Fullerenes as adhesive layers for mechanical peeling of metallic, molecular and polymer thin films. *Beilstein J. of Nanotechnol.* **5**, 394-401. (2014)

- [126] K. L. Akers et al. Raman spectroscopy of C<sub>60</sub> solid films: a tale of two spectra. *J. Phys. Chem.* **98**, 10824 (1994)
- [127] R. Meilunas et al. Infrared and Raman spectra of C<sub>60</sub> and C<sub>70</sub> solid films at room temperature. *J. Appl. Phys.* **70**, 5128 (1991)
- [128] O. V. Mikhnenko et al. Exciton diffusion in organic semiconductors. *Energy Environ. Sci.* **8**, 1867 (2015)
- [129] J. Won Suk et al. Transfer of CVD-grown monolayer graphene onto arbitrary substrates. *ACS Nano*, **5**, 6916 (2011)
- [130] A.C. Ferrari and D. M. Basko. Raman spectroscopy as a versatile tool for studying the properties of graphene. *Nat. Nanotechnol.* **8**, 235 92013)
- [131] E. Stolyarova et al. High-resolution scanning tunneling microscopy imaging of mesoscopic graphene sheets on an insulating surface. *Proc. Natl. Acad. Sci.* **104**, 9209 (2007)
- [132] ChemBK online CAS database. Melamine cyanurate, CAS: 37640-57-6. Retreived: 14.02.18. Available: <http://www.chembk.com/en/chem/37640-57-6>
- [133] T. Ishii and T. Sato. Growth of single crystals of hexagonal boron nitride. *J. Cryst. Growth.* **61**, 689 (1983)
- [134] A. D. Rackic et al. Optical properties of metallic films for vertical-cavity optoelectronic devices. *Appl. Optics.* **37**, 5271
- [135] L. Britnell et al. Resonant tunnelling and negative differential conductance in graphene transistors. *Nat. Commun.* **4**, 1794 (2013)
- [136] A. P. Rooney et al. Observing imperfection in atomic interfaces for van der Waals heterostructures. *Nano Lett.* **17**, 5222–5228 (2017)
- [137] K. Kim et al. Van der Waals heterostructures with high accuracy rotational alignment. *Nano Lett.* **16**, 1989–1995 (2016)
- [138] F. Pizzocchero et al. The hot pick-up technique for batch assembly of van der Waals heterostructures. *Nat. Commun.* **7**, 11894 (2016)

## List of Abbreviations

**AFM** – Atomic force microscopy

**C<sub>60</sub>** – Buckminsterfullerene

**CA.M** – Cyanuric acid-melamine

**CCD** – Charge coupled device

**CVD** – Chemical vapour deposition

**DFT** – Density functional theory

**DRS** – Differential reflectance spectroscopy

**hBN** – Hexagonal boron nitride

**HOMO** – Highest occupied molecular orbital

**HOPG** – Highly oriented pyrolytic graphite

**LEED** – Low energy electron diffraction

**LUMO** – Lowest unoccupied molecular orbital

**Me-PTCDI** – Di-methyl perylene tetra carboxylic diimide

**NC-AFM** – Non-contact atomic force microscopy

**SiO<sub>2</sub>/Si** – Thermally oxidised silicon dioxide on silicon

**SNOM** – Scanning near-field optical microscopy

**SPM** – Scanning probe microscopy

**STM** – Scanning tunnelling microscopy

**STML** – Scanning tunnelling microscopy induced luminescence

**UHV** – Ultra high vacuum

**PDMS** – Poly di-methyl siloxane

**PPC** – Poly propylene carbonate

**PTCDI** – Perylene tetracarboxylic diimide

**PTCDA** – Perylene tetracarboxylic dianhydride

**PMMA** – Poly methyl methacrylate

**QCM** – Quartz crystal microbalance

**TD-DFT** – Time-dependent density functional theory